Kinetische Monte Carlo-modellering van multimodale verdelingen
in gepulseerde-laser- en mini-emulsiepolymerisatie

Kinetic Monte Carlo Modeling of Multimodal Distributions
in Pulsed Laser and Miniemulsion Polymerization

Yoshi Marien

Promotoren: prof. dr. ir. D. R. D'hooge, prof. dr. ir. G. B. Marin
Proefschrift ingediend tot het behalen van de graad van
Doctor in de ingenieurswetenschappen: chemische technologie

UNIVERSITEIT
GENT

Vakgroep Materialen, Textiel en Chemische Proceskunde
Voorzitter: prof. dr. P. Kiekens
Faculteit Ingenieurswetenschappen en Architectuur
Academiejaar 2018 - 2019

ISBN 978-94-6355-230-1
NUR 952
Wettelijk depot: D/2019/10.500/38

Promotoren

prof. dr. ir. Dagmar R. D'hooge, Universiteit Gent

prof. dr. ir. Guy B. Marin, Universiteit Gent

Examencommissie

prof. dr. ir. Filip De Turck, voorzitter, Universiteit Gent

dr. ir. Paul H.M. Van Steenberge, secretaris, Universiteit Gent

prof. dr. Richard Hoogenboom, Universiteit Gent

prof. dr. Sabine Beuermann, Clausthal University of Technology

prof. dr. Marie-Françoise Reyniers, Universiteit Gent

prof. dr. ir. Dagmar R. D'hooge, Universiteit Gent

prof. dr. ir. Guy B. Marin, Universiteit Gent

Universiteit Gent
Faculteit Ingenieurswetenschappen en Architectuur
Vakgroep Materialen, Textiel en Chemische Proceskunde
Laboratorium voor Chemische Technologie
Technologiepark 125
B-9052 Zwijnaarde, Gent
België
http://www.lct.ugent.be

Publication list

Publications related to the PhD research

1. Y.W. Marien, P.H.M. Van Steenberge, K.B. Kockler, C. Barner-Kowollik, M.-F. Reyniers, D.R. D'hooge, G.B. Marin 'An alternative method to estimate the bulk backbiting rate coefficient in acrylate radical polymerization' *Polym. Chem.* **2016**, 7, 6521 (SCI-IF 2015: 5.768)

2. Y.W. Marien, P.H.M. Van Steenberge, C. Barner-Kowollik, M.-F. Reyniers, G. B. Marin, D.R. D'hooge 'Kinetic Monte Carlo modeling extracts information on chain initiation and termination from complete PLP-SEC traces' *Macromolecules* **2017**, 50, 1371 (SCI-IF 2015: 5.554)

3. Y.W. Marien, P.H.M. Van Steenberge, K.B. Kockler, C. Barner-Kowollik, M.-F. Reyniers, G. B. Marin, D.R. D'hooge 'Estimating the photodissociation quantum yield from PLP-SEC peak heights' *Polym. Chem.* **2017**, 8, 3124 (SCI-IF 2015: 5.687)

4. G.B. Desmet, Y.W. Marien, P.H.M. Van Steenberge, D.R. D'hooge, M.F. Reyniers, G.B. Marin 'Ab initio based kinetic Monte Carlo analysis to unravel the propagation kinetics in vinyl acetate pulsed laser polymerization' *Polym. Chem.* **2017**, 8, 7143 (SCI-IF 2016: 5.375; G.B.D. and Y.W.M. shared first author)

5. A.B. Vir, Y.W. Marien, P.H.M. Van Steenberge, M.-F. Reyniers, C. Barner-Kowollik, G.B. Marin, D.R. D'hooge 'Access to the *β*-scission rate coefficient in acrylate radical polymerization by careful scanning of pulse laser frequencies' *React. Chem. Eng.* **2018,** 3, 807 (SCI-IF: 2017: 4.641; A.B.V. and Y.W.M. shared first author)

6. Y.W. Marien, P.H.M. Van Steenberge, D.R. D'hooge, G.B. Marin 'Particle by particle kinetic Monte Carlo tracking of reaction and mass transfer events in miniemulsion free radical polymerization' *Macromolecules* **2019**, 52, 1408 (SCI-IF 2017: 5.914)

7. A.B. Vir, Y.W. Marien, P.H.M. Van Steenberge, M.-F. Reyniers, C. Barner-Kowollik, G.B. Marin, D.R. D'hooge 'From *n*-butyl acrylate Arrhenius parameters for backbiting and tertiary propagation to *β*-scission via pulsed laser polymerization' *Polym. Chem.* **2019**, submitted (SCI-IF: 2017: 4.9; A.B.V. and Y.W.M. shared first author)

Dissemination of the PhD research at national and international conferences

1. Y.W. Marien, P.H.M. Van Steenberge, K.B. Kockler, C. Barner-Kowollik, M.-F. Reyniers, D. R. D'hooge, G.B. Marin
   A new method for the measurement of the backbiting rate coefficient in acrylate radical polymerization
   Belgian Polymer Group (BPG) Annual meeting
   Hasselt, Belgium, May 23-24, **2016**, poster presentation

2. Y.W. Marien, P.H.M. Van Steenberge, K.B. Kockler, C. Barner-Kowollik, M.-F. Reyniers, D. R. D'hooge, G.B. Marin
   A full exploitation of the pulsed laser polymerization technique to assess all important rate coefficients in acrylate radical polymerization
   AIChE Annual Meeting
   San Francisco, USA, November 13-18, **2016**, oral presentation

3. Y.W. Marien, P.H.M. Van Steenberge, K.B. Kockler, C. Barner-Kowollik, M.-F. Reyniers, G.B. Marin, D. R. D'hooge
   Pulsed laser polymerization revisited: from the photodissociation quantum yield to the chain initiation, propagation, backbiting and termination reactivity
   European Polymer Federation 2017
   Lyon, France, July 2-7, **2017**, poster presentation

4. Y.W. Marien, P.H.M. Van Steenberge, G.B. Desmet, M.F Reyniers, G.B. Marin, C. Barner-Kowollik, D. R. D'hooge
   A novel interpretation of measured and simulated PLP data
   Polymer Reaction Engineering (PRE) 10
   Punta Cana, Dominican Republic, May 20-25, **2018**, oral presentation

5. Y.W. Marien, P.H.M. Van Steenberge, A.B. Vir, C. Barner-Kowollik, M.F. Reyniers, G.B. Marin, D.R. D'hooge
   Exploring pulsed laser polymerization in view of reactor design and control
   23th International Conference on Chemical Reactors (ChemReactor 23)
   Ghent, Belgium, November 5-8, **2018**, poster presentation

6. Y.W. Marien, P.H.M. Van Steenberge, A.B. Vir, C. Barner-Kowollik, M.-F. Reyniers, G.B. Marin, D. R. D'hooge
   Pulsed laser (co)polymerization to determine intrinsic rate coefficients
   Mathematics in (bio)Chemical Kinetics and Engineering (MACKIE)
   Ghent, Belgium, November 8-9, **2018**, oral presentation

7. D.J.G. Devlaminck, Y.W. Marien, M.F. Reyniers, P.H.M. Van Steenberge, D. R. D'hooge
   A detailed understanding of RAFT miniemulsion polymerization
   Belgian Polymer Group (BPG) Annual meeting
   Houffalize, Belgium, May 27-28, **2019**, poster presentation

8. Y.W. Marien, A.B. Vir, P.H.M. Van Steenberge, M.-F. Reyniers, C. Barner-Kowollik, G.B. Marin, D.R. D'hooge
   Pulsed laser polymerization of acrylates: access to tertiary propagation, backbiting and β–scission rate coefficients
   Belgian Polymer Group (BPG) Annual meeting
   Houffalize, Belgium, May 27-28, **2019**, poster presentation

9. D.J.G. Devlaminck, Y.W. Marien, L. De Keer, M.F. Reyniers, P.H.M. Van Steenberge, D. R. D'hooge
   Deterministic modeling of RAFT bulk and miniemulsion polymerization up to high monomer conversion
   13th International Workshop on Polymer Reaction Engineering
   Hamburg, June 11-14, **2019**, poster presentation

10. Y.W. Marien, A.B. Vir, P.H.M. Van Steenberge, M.-F. Reyniers, C. Barner-Kowollik, G.B. Marin, D.R. D'hooge
    Arrhenius parameters for acrylate radical polymerization using low and high temperature pulsed laser polymerization data
    13th International Workshop on Polymer Reaction Engineering
    Hamburg, June 11-14, **2019**, poster presentation

Contents

Preface

I would like to thank:

Prof. Dagmar R. D'hooge and Prof. Guy B. Marin, my supervisors, for their excellent guidance,

Dr. Paul H.M. Van Steenberge for support and helpful discussions,

Prof. Marie-Françoise Reyniers for useful feedback on our PLP work,

Prof. Christopher Barner-Kowollik for valued input on our work on PLP,

Prof. Andrij Pich for providing me the opportunity to spend a very interesting time at DWI,

Prof. Filip De Turck, Prof. Sabine Beuermann and Prof. Richard Hoogenboom as jury members,

Dr. Katrin Kockler for much appreciated experimental input for our work on PLP,

Larissa Hussmann for a pleasant cooperation on miniemulsion copolymerization,

Dr. Anil Vir for our successful collaboration on PLP,

Dr. Gilles Desmet for our interesting joint work on PLP of vinyl acetate,

All (ex-)colleagues at LCT for providing a pleasant atmosphere at the lab,

My closest (ex-)colleagues Stijn, Gilles, Nils, Dries, Lies, Julio, Israel, Kyann, Anil, Francisco, Anastasia, Robert, and Alessandro for their help and friendship,

My colleagues from the class of 2015, Alexander, Alexandra, Anton, Brigitte, Florence, Jenoff, Jens, Lies, and Steffen, for sharing a long but interesting time at LCT,

All members of the Pich Group for warmly welcoming me at DWI,

My family and friends for always being there for me,

And you for reading this.

Yoshi W. Marien
Ghent, March 8, 2019.

Nederlandse samenvatting

Een brede waaier aan materialen die men in het dagelijkse leven gebruikt, gaande van eenvoudige verbruiksgoederen tot geavanceerde materialen die bv. gebruikt kunnen worden voor de gecontroleerde afgifte van medicijnen, wordt geproduceerd via radicalaire polymerisatie. Een belangrijke eigenschap van de overeenkomstige polymeermaterialen is dat de macroscopische eigenschappen zoals waargenomen door de eindgebruiker in grote mate bepaald worden door de eigenschappen op het niveau van de micro- en meso-schaal. Bijzonder is dat deze eigenschappen een verdeeld karakter hebben. Zo wordt op het niveau van de micro-schaal i.p.v. één enkele ketenlengte/molaire massa een verdeling van ketenlengtes/molaire massa's waargenomen (*i.e.* de ketenlengte-/molairemassaverdeling). In geval van gedispergeerdefasepolymerisatie (bv. emulsie- of suspensiepolymerisatie) wordt op het niveau van de meso-schaal een verdeling van deeltjesgrootten waargenomen (*i.e.* de deeltjesgrootteverdeling).

Opmerkelijk is dat bovengenoemde verdelingen vaak multimodaal zijn. Zo is de ketenlengte-/molairemassaverdeling die verkregen wordt via gepulseerdelaserpolymerisatie (PLP) – een veelgebruikte techniek voor de bepaling van (intrinsieke) snelheidscoëfficiënten – vaak multimodaal vanwege de gepulseerde creatie van radicalen. Ook bij een latex verkregen via emulsiepolymerisatie speelt multimodaliteit vaak een belangrijke rol, aangezien voor vele toepassingen enkel goed gedefinieerde multimodale deeltjesgrootteverdelingen leiden tot een hoge volumefractie aan polymeer zonder te leiden tot een te hoge viscositeit waardoor de latex niet gemakkelijk verwerkbaar meer zou zijn. Dit illustreert dat een gecontroleerde evolutie van de deeltjesgrootteverdeling in gedispergeerdefasepolymerisatie van groot industrieel belang is. Een beknopte samenvatting van de methoden beschikbaar voor het modelleren van de deeltjesgrootte- en ketenlengteverdeling in gedispergeerdefasepolymerisaties wordt gegeven in **Hoofdstuk 1**, waarmee aangetoond wordt dat de gekoppelde berekening van beide verdelingen

een cruciale uitdaging is voor dynamische gedispergeerdefasepolymerisaties zoals emulsiepolymerisatie, waarvoor een sterke correlatie tussen beide verdelingen verwacht wordt.

In deze doctoraatsthesis wordt kinetische Monte Carlo (*k*MC)-modellering, hetgeen een stochastische simulatietechniek is die toelaat individuele reacties en fasetransferfenomenen te volgen in chemische processen, toegepast en verder ontwikkeld voor de simulatie van multimodale ketenlengte- en deeltjesgrootteverdelingen in radicalaire polymerisaties.

In **Hoofdstuk 2** worden volledige log-molairemassaverdelingen (log-MMDs) verkregen via PLP gesimuleerd waardoor naast informatie over propagatie ook informatie over keteninitiatie en terminatie verkregen wordt. Een isotherm *k*MC-model (306-325 K) dat rekening houdt met diffusielimiteringen en alle relevante elementaire reacties voor *n*-butylacrylaat en 2,2-dimethoxy-2-fenylacetofenon (DMPA) wordt beschouwd. Er wordt aangetoond dat de sterk verschillende reactiviteiten van de DMPA-gebaseerde initiatorfragmenten t.o.v. vinyllische bindingen cruciaal zijn voor het verkrijgen van gestructureerde multimodale log-MMDs die toelaten opeenvolgende buigpunten te identificeren. Het wordt ook aangetoond dat log-MMDs gebruikt kunnen worden om de accuraatheid van modellen voor de ketenlengteafhankelijkheid van de geobserveerde terminatiesnelheidscoëfficiënt te testen en dat *k*MC-modellering een bijzonder interessante techniek is om de ketengroei van de verschillende radicaaltypes tussen de laserpulsen te volgen en om dominante elementaire reacties te identificeren.

In **Hoofstuk 3** wordt een snelle en betrouwbare methode voor de bepaling van de fotodissociatiekwantumopbrengst Φ_{diss} voorgesteld. PLP-experimenten worden uitgevoerd met variërende pulsenergiën (1.5 – 6 mJ) en regressieanalyse aan de verhouding van de piekhoogten zoals waargenomen in de overeenkomstige log-MMDs wordt uitgevoerd. De accuraatheid van de methode wordt *in silico* aangetoond voor DMPA-geïnitieerde PLP-experimenten door het beschouwen van grote theoretische fouten (tot 20%). De methode wordt bovendien succesvol toegepast voor isotherme PLP van *n*-butylacrylaat (306 K), hetgeen een geschatte Φ_{diss} = 0.42

$\pm$ 0.04 oplevert. Op langere termijn zal de aangebrachte methode de evaluatie van huidige en de ontwikkeling van nieuwe efficiënte fotoinitiatoren vergemakkelijken.

Op basis van PLP-SEC wordt een nieuwe alternatieve methode voor de bepaling van de backbitingsnelheidscoëfficiënt k_{bb} in radicalaire polymerisatie van acrylaten voorgesteld in **Hoofdstuk 4**. Regressieanalyse wordt uitgevoerd aan de locatie van de buigpunten verkregen via PLP-experimenten bij variërende solventvolumefracties (0-0.75), gebruikmakend van het gesatureerde analoog van het monomeer als solvent om mogelijke solventeffecten te vermijden, en lage pulsfrequenties (*ca*. < 100 s^{-1}), hetgeen het gebruik van goedkopere PLP-toestellen mogelijk maakt. Variatie van de solventvolumefractie laat toe de gemiddelde levensduur van tertiaire radicalen te variëren, waardoor de sensitiviteit van de methode voor de schatting van k_{bb} toeneemt. *In silico* data wordt gebruikt om de robuustheid van de methode aan grote experimentele fouten aan te tonen en om de gezamenlijke schatting van k_{bb} en de tertiairepropagatiesnelheidscoëfficiënt te illustreren. De methode wordt bovendien toegepast voor de regressie aan experimentele data van DMPA-geïnitieerde PLP-experimenten van *n*-butylacrylaat, met butylpropionaat als solvent. Een k_{bb} waarde van 171 $\pm$ 21 s^{-1} (303 K) wordt verkregen, hetgeen in overeenstemming is met literatuurwaarden.

In **Hoofdstuk 5** wordt een methodologie analoog aan degene gebruikt in Hoofdstuk 4 toegepast voor de bepaling van de β-scissiesnelheidscoëfficiënt k_β, op voorwaarde dat de Arrheniusparameters voor backbiting reeds geschat werden bij voldoende lage temperaturen (<< 350 K; *cf*. Hoofstuk 4). De methode is gebaseerd op de sensitiviteit van k_β aan wijzigingen in de pulsfrequentie (<< 200 s^{-1}) in isotherme PLP-experimenten (*ca*. 350 tot 415 K), hetgeen leidt tot een voldoende grote variatie van de tijdschalen van de verschillende radicaaltypes. Belangrijk is dat deze waarnemingen niet significant beïnvloed worden door macropropagatie en thermische zelfinitiatie, hetgeen respectievelijk *in silico* en experimenteel aangetoond wordt. Het wordt bovendien aangetoond dat het gebruik van een solvent (*e.g*. butylpropionaat) nodig

is bij lagere temperaturen (350-410 K); voor hogere temperaturen (410-415 K) volstaat het gebruik van data opgemeten onder bulk condities. Regressie aan bulk experimentele data voor *n*-butylacrylaat leidt tot een schatting van $k_\beta = (4.26 \pm 1.8)\ 10^2\ s^{-1}$ bij 413 K, een waarde die eerder gerapporteerde waarden overschrijdt ($k_\beta = 6\ 10^0 - 1.45\ 10^2\ s^{-1}$) en aangeeft dat er in radicalaire polymerisatie van acrylaten bij hoge temperaturen een grote neiging is tot de vorming van macromonomeren.

In het tweede deel van deze doctoraatsthesis verschuift de aandacht naar gedispergeerdefasepolymerisatie. Rekening houdend met de verwachte sterkere interactie tussen de micro- en meso-schaal in emulsiepolymerisatie t.o.v. suspensiepolymerisatie wordt enkel emulsiepolymerisatie beschouwd met in het bijzonder aandacht voor miniemulsiepolymerisatie in de afwezigheid van morfologische aspecten zoals faseseparatie in de deeltjes.

In **Hoofdstuk 6** wordt een nieuwe *k*MC-modelleringstechniek ontwikkeld die de simulatie van vrijeradicalairepolymerisatie in miniemulsie toelaat en expliciet rekening houdt met de evolutie van de deeltjesgrootteverdeling en de interactie met de evolutie van de ketenlengteverdeling. In dit model wordt het aantal radicalen en de monomeerconcentratie in elk individueel deeltje opgevolgd. Bijgevolg maakt het model geen gebruik van een gemiddelde monomeerconcentratie in de deeltjes, hetgeen wel het geval is in eerdere studies, inclusief degene die de conventionele Smith-Ewart-modelleringstechniek toegepast hebben. Bovendien houdt het model rekening met absorptie en desorptie van zowel radicalen als monomeer op basis van een diffusie-gebaseerde beschrijving. Er wordt aangetoond dat door gebruik te maken van een gereduceerd *k*MC-model waarin de werkelijke monomeerconcentratie in individuele deeltjes overschreven wordt door de gemiddelde monomeerconcentratie in de deeltjes, de evolutie van de monomeerconversie en gemiddelde ketenlengte-eigenschappen zoals verkregen door een conventioneel Smith-Ewart-model gesimuleerd wordt. Bovendien wordt door gebruik

te maken van het volledige *k*MC-model, met fysisch relevante waarden voor de modelparameters, een zeer dynamische en gecorreleerde evolutie van de deeltjesgrootte- en ketenlengteverdeling gesimuleerd.

In **Hoofdstuk 7** wordt het *k*MC-model ontwikkeld in Hoofstuk 6 uitgebreid en toegepast voor miniemulsiecopolymerisatie van styreen en N-vinylcaprolactam (VCL). Het wordt aangetoond dat de initiële deeltjesgrootteverdeling een grote invloed heeft op de evolutie van de miniemulsiekarakteristieken, met lagere polymerisatiesnelheden indien de initiële deeltjesgrootteverdeling naar grotere deeltjesgrootten verschuift. Een opeenvolgend dominant verbruik van styreen en VCL wordt gesimuleerd, in overeenstemming met de sterk verschillende reactiviteitsverhoudingen. Bovendien tonen de *k*MC-simulaties een zeer dynamische deeltjesgrootteverdeling aan, hetgeen wederom de noodzaak van een gekoppelde berekening van de ketenlengte- en deeltjesgrootteverdeling aantoont. Deze inzichten zullen de ontwikkeling van VCL-gebaseerde nanogels voor bv. de gecontroleerde afgifte van medicijnen vergemakkelijken.

In **Hoofdstuk 8** worden de belangrijkste conclusies samengevat en wordt een toekomstperspectief gegeven over de beide delen van dit doctoraatsonderzoek.

English summary

A wide variety of polymer products used in every-day life, ranging from commodity materials to high-tech materials for *e.g.* drug delivery applications, are produced via radical polymerization. A key feature of the associated polymer products is that the macroscopic properties as observed by the end-user are strongly determined by micro- and meso-scale characteristics. These characteristics have a distributed nature, for example on the micro-scale (*i.e.* the level of molecules) rather than a single chain length or molar mass, a distribution of chain lengths/molar masses (*i.e* the chain length/molar mass distribution, CLD/MMD) is influencing the polymer material behavior. In case dispersed phase polymerization is performed (*e.g.* emulsion or suspension polymerization), at the meso-scale (*i.e.* the level of the particles) a distribution of particle sizes is obtained (*i.e.* the particle size distribution, PSD).

Notably, the distributions encountered in radical polymerizations often display multimodality. For example, the CLD (or MMD) obtained via pulsed laser polymerization (PLP) – a frequently used technique for the determination of (intrinsic) rate coefficients – typically is multimodal due to the pulsed creation of radicals. Another example in which multimodality plays a key role relates to latexes obtained via emulsion polymerization, for which in several cases only well-designed multimodal PSDs allow to obtain high solid contents while maintaining a sufficiently low viscosity for processability. Hence, it is clear that the regulated growth of the PSD in dispersed phase polymerization is of great industrial importance. A brief overview of the state-of-the-art for the modeling of the PSD and CLD evolution in dispersed phase polymerizations is given **Chapter 1**, from which it becomes evident that the joint and interactive calculation of these distributions remains a major challenge for dynamic dispersed phase polymerizations such as emulsion polymerization in which a strong correlation between the PSD and CLD evolution is expected.

In this PhD thesis, kinetic Monte Carlo (*k*MC) modeling, which is a powerful stochastic technique allowing to track individual reaction and phase transfer events in chemical processes, is applied and further developed to the simulation of multimodal chain length/molar mass and particle size distributions encountered in radical polymerizations.

In **Chapter 2**, complete PLP log-molar mass distributions (log-MMDs) are accurately simulated to gain not only knowledge on the propagation but also on the chain initiation and termination reactivity. An isothermal *k*MC model (306-325 K) accounting for diffusional limitations and all relevant elementary reactions for *n*-butyl acrylate and 2,2-dimethoxy-2-phenylacetophenone (DMPA) is considered. The disparate reactivities towards vinylic bonds of the DMPA fragments are shown to be essential to ensure the well-defined multimodality of the log-MMDs necessary to identify consecutive inflection points. It is also illustrated that PLP log-MMD data can be used to test the validity of models for apparent termination rate coefficients at low monomer conversions and that *k*MC simulations are a powerful tool to track the chain growth of the different radical types between laser pulses and to identify dominant elementary reactions.

In **Chapter 3**, a fast method for the reliable estimation of the photodissociation quantum yield Φ_{diss} is presented. PLP experiments are performed at various pulse energies (1.5 – 6 mJ) and regression analysis is performed to the ratio of the peak heights identified in the size exclusion chromatography (SEC) trace. The high accuracy of the method is demonstrated for PLP initiated by DMPA, considering *in silico* generated data including large theoretical errors (up to 20%). The method is also successfully applied to experimental data of DMPA based isothermal PLP of *n*-butyl acrylate at 306 K, with an estimated Φ_{diss} of 0.42 ± 0.04. In the long term, the method will facilitate the evaluation of current and the design of new highly efficient photoinitiators.

Based on a PLP-SEC analysis, a novel alternative method to estimate the bulk backbiting rate coefficient k_{bb} in acrylate radical polymerization is presented in **Chapter 4**. For different solvent volume fractions (0-0.75), using the saturated analogue of the monomer as solvent to rule out solvent effects, regression analysis is applied to inflection point data in the low frequency range (< *ca.* 100 s^{-1}) only, which can be scanned with less expensive PLP equipment. Variation of the solvent volume fraction allows to independently alter the average mid-chain radical life time and to improve the sensitivity of the method to estimate k_{bb} confidently. The robustness of the method is verified considering *in silico* generated data including large artifical errors and also illustrated for a joint estimation of k_{bb} and the mid-chain radical propagation rate coefficient $k_{p,m}$. The method is applied to experimental data of DMPA initiated PLP of *n*-butyl acrylate, taking butyl propionate as the solvent. A k_{bb} value of 171 ± 21 s^{-1} (303 K) is found, in good agreement with literature data.

In **Chapter 5**, an analogous methodology as in Chapter 4 is applied for the estimation of the *β*-scission rate coefficient from high temperature PLP experiments, provided that the backbiting rate coefficient has already been determined at sufficiently low temperatures at which *β*-scission is negligible (<< 350 K; *cf.* Chapter 4). The method relies on the sensitivity of k_β upon a change of the pulse laser frequency (<< 200 Hz) under isothermal pulsed laser polymerization (PLP) conditions in the temperature range between *ca.* 350 and 415 K, leading to a sufficient variation of the times scales of the radicals involved. These observations are not significantly influenced by macropropagation and thermal self-initiation, as respectively confirmed by *in silico* testing and experimental data. Solution inflection point data (*e.g.* solvent butyl propionate) are needed at the lower temperature range (350-410 K), whereas bulk inflection point data suffice at the higher temperature range (410-415 K). The proposed method leads to an estimated k_β value of (4.26 ± 1.8)×10^2 s^{-1} at 413 K with bulk PLP data, suggesting a high propensity of macromonomer formation in acrylate polymerization under high temperature radical

polymerization conditions, exceeding the previously suggested levels (k_β = 6 x 10^0-1.45 x10^2 s^{-1}).

In the second part of this PhD thesis, focus is shifted to dispersed phase radical polymerization. In view of the expected stronger interaction between the micro- and meso-scale in emulsion polymerization compared to suspension polymerization, focus is on the former polymerization technique. For illustration purposes focus is restricted to miniemulsion polymerization in the absence of morphological aspects such as phase separation in polymer particles.

In **Chapter 6**, a novel *k*MC modeling tool allowing the simulation of miniemulsion free radical polymerization (FRP) is developed, explicitly taking into account the evolution of the PSD and its interaction with the evolution of the CLD. In this model, the number of radicals and the monomer concentration in each individual particle are tracked. Hence, the model does not make use of an average particle monomer concentration at any time as done in previous studies, including those based on the conventional Smith-Ewart approach. Moreover, exit/entry of both radicals and monomer is accounted for between the particles and the aqueous phase, considering a diffusion-based approach. In addition to a successful benchmark to a conventional Smith-Ewart model using a downsized *k*MC model that overwrites the actual particle monomer concentration with the average one, a dynamic PSD and CLD evolution is simulated using the full *k*MC model and physically reasonable values for all model parameters.

In **Chapter 7**, the *k*MC model is extended and applied to miniemulsion copolymerization of styrene and N-vinylcaprolactam (VCL). The initial PSD is demonstrated to have a large effect on the evolution of the copolymerization characteristics, with lower polymerization rates as the initial PSD shifts to higher particle sizes. A consecutive dominant incorporation of styrene and VCL is simulated simulated, in agreement with the disparate monomer reactivity ratios. Moreover, the *k*MC simulations indicate a very dynamic evolution of the PSD, again highlighting the need for the simultaneous simulation of both CLD and PSD. Importantly, the

obtained insights will aid the design of copolymer VCL nanogel particles for *e.g.* drug livery applications in the near future, also taking into account the experimental knowledge acquired during a research stay in the group of Prof. Pich at DWI Leibniz Institute for Interactive Materials/ RWTH Aachen University.

In **Chapter 8** the main conclusions are highlighted and an outlook is given on future research activities regarding both parts of the PhD thesis.

List of symbols

Greek symbols

α_{gel}	Parameter of the composite k_t-model for the gel regime	-
α_L	Parameter of the composite k_t-model for long chains	-
α_S	Parameter of the composite k_t-model for short chains	-
Γ	Partition coefficient	-
$\Delta[R_0]$	Concentration of radicals generated by each laser pulse	mol L^{-1}
ε	Molar absorptivity	L mol^{-1} m^{-1}
λ	Wave length	m
ν	Laser pulse frequency	s^{-1}
τ_e	Average life time of an end-chain radical	s
τ_m	Average life time of a mid-chain radical	s
Φ_{diss}	Photodissociation quantum yield	-
Φ_S	Solvent volume fraction	-
Ω	Optical cross-sectional area	m^2

Roman symbols

$b\sigma_v$	SEC broadening parameter	-
c	Speed of light	m s^{-1}
C_{entry}	Proportionality constant for calculating the entry rate coefficient	-

C_{exit}	Proportionality constant for calculating the exit rate coefficient	-
d_p	Particle diameter	m
D_p	Diffusion coefficient in a particle, *i.e.* in the organic phase	$m^2\ s^{-1}$
D_w	Diffusion coefficient in water	$m^2\ s^{-1}$
E_{pulse}	Energy of one laser pulse	J
f_A	Molar fraction of monomer A in the monomer phase	-
F_A	Molar fraction of monomer A in the polymer	-
f_B	Molar fraction of monomer B in the monomer phase	-
F_B	Molar fraction of monomer B in the polymer	-
h	Planck constant	J s
i	Chain length	-
i_{sol}	Maximum chain length for solubility in water	-
I_2	Initiator molecule	-
i_{SL}	Crossover chain length in the composite k_t-model corresponding to a shift between termination controlled by center-of-mass diffusion (shorter radicals) and segmental diffusion (longer radicals)	-
i_{gel}	Crossover chain length in the composite k_t-model for the gel regime	-
k_β	Rate coefficient for β-scission	s^{-1}
k_{bb}	Rate coefficient for backbiting	s^{-1}
k_{diss}	Rate coefficient for initiator dissociation	s^{-1}

k_{entry}	Rate coefficient for entry	L mol^{-1} s^{-1}
k_{exit}	Rate coefficient for exit	s^{-1}
k_i	Rate coefficient for chain initiation	L mol^{-1} s^{-1}
k_{iA}	Rate coefficient for addition of an initiator radical fragment to monomer molecule A	L mol^{-1} s^{-1}
k_{iB}	Rate coefficient for addition of an initiator radical fragment to monomer molecule B	L mol^{-1} s^{-1}
$k_{p,AA}$	Rate coefficient for addition of a radical with terminal unit A to monomer molecule A	L mol^{-1} s^{-1}
$k_{p,AB}$	Rate coefficient for addition of a radical with terminal unit A to monomer molecule B	L mol^{-1} s^{-1}
$k_{p,app}$	Apparent propagation rate coefficient	L mol^{-1} s^{-1}
$k_{p,BA}$	Rate coefficient for addition of a radical with terminal unit B to monomer molecule A	L mol^{-1} s^{-1}
$k_{p,BB}$	Rate coefficient for addition of a radical with terminal unit B to monomer molecule B	L mol^{-1} s^{-1}
$k_{p,e}$	Propagation rate coefficient of an end-chain radical	L mol^{-1} s^{-1}
$k_{p,eMM}$	Rate coefficient for addition of an end-chain radical to a macromonomer	L mol^{-1} s^{-1}
$k_{p,m}$	Propagation rate coefficient of a mid-chain radical	L mol^{-1} s^{-1}
$k_{p,mMM}$	Rate coefficient for addition of a mid-chain radical to a macromonomer	L mol^{-1} s^{-1}

$k_{t,AA}$	Rate coefficient for termination of two radicals with terminal unit A	L mol^{-1} s^{-1}
$k_{t,AB}$	Rate coefficient of termination of two radicals with terminal unit A and B respectively	L mol^{-1} s^{-1}
$k_{t,BB}$	Rate coefficient of termination of two radicals with terminal unit B	L mol^{-1} s^{-1}
$k_{t,ee}$	Rate coefficient for termination of two end-chain radicals	L mol^{-1} s^{-1}
$k_{t,em}$	Rate coefficient for termination of an end-chain and a mid-chain radical	L mol^{-1} s^{-1}
$k_{t,mm}$	Rate coefficient for termination of two mid-chain radicals	L mol^{-1} s^{-1}
$k_t(i,j)$	Chain length dependent rate coefficient corresponding to termination of a macroradical with chain length i and j	L mol^{-1} s^{-1}
$k_{trM,AA}$	Rate coefficient chain transfer to monomer A from an A unit	L mol^{-1} s^{-1}
$k_{trM,AB}$	Rate coefficient chain transfer to monomer B from an A unit	L mol^{-1} s^{-1}
$k_{trM,BA}$	Rate coefficient chain transfer to monomer A from a B unit	L mol^{-1} s^{-1}
$k_{trM,BB}$	Rate coefficient chain transfer to monomer B from a B unit	L mol^{-1} s^{-1}
$k_{trM,e}$	Rate coefficient chain transfer from an end-chain radical to a monomer molecule	L mol^{-1} s^{-1}
$k_{trM,m}$	Rate coefficient chain transfer from a mid-chain radical to a monomer molecule	L mol^{-1} s^{-1}
L	Optical path length	m
L_i	Chain length corresponding to the i^{th} inflection point	-
M	Monomer molecule	-
MM_i	Macromonomer with chain length i	-
N_A	Avogadro constant	-
P_i	'Dead' polymer molecule with chain length i	-
r_A	Monomer reactivity ratio for A	-

r_B	Monomer reactivity ratio for B	-
$R_{i,e}$	End-chain radical with chain length *i*	-
$R_{i,m}$	Mid-chain radical with chain length *i*	-
t_0	Time between two laser pulses	s
$w(\log M)$	Logarithmic mass weighted molar mass distribution	-
$w(M)$	Mass weighted molar mass distribution	-
x_n	Number average chain length	-
x_m	Mass average chain length	-

Abbreviations

CLD	Chain length distribution
CRP	Controlled radical polymerization, also known as RDRP
CTA	Chain transfer agent
DMPA	2,2-dimethoxy-2-phenylacetophenone
ECR	End-chain radical
EPR	Electron paramagnetic resonance
FRP	Free radical polymerization
GC	Gas chromatography
GPC	Gel permeation chromatography, also known as SEC
*k*MC	kinetic Monte Carlo
MCR	Mid-chain radical
MMA	Methyl methacrylate

MMD	Molar mass distribution
*n*BuA	*n*-butyl acrylate
PLP	Pulsed laser polymerization
PSD	Particle size distribution
RAFT	Reversible addition-fragmentation chain transfer
RDRP	Reversible deactivation radical polymerization
SEC	Size exclusion chromatography
THF	Tetrahydrofuran
VCL	N-vinylcaprolactam

Chapter 1: Multimodality in radical polymerization

1.1 From chain length to particle size distribution

A wide variety of polymer products used in everyday life is produced via radical polymerization.[1-3] A key feature of the associated polymer products is that the macroscopic properties as observed by the end-user are strongly determined by micro- and meso-scale characteristics.[1, 4-8] These characteristics have a distributed nature, for example on the micro-scale (*i.e.* the level of molecules; Figure 1: left) rather than a single chain length, a distribution of chain lengths (*i.e* the chain length distribution, CLD) is influencing the polymer material behavior.[9-12] In case dispersed phase polymerization is performed (*e.g.* emulsion or suspension polymerization), at the meso-scale (*i.e.* the level of the particles) a distribution of particle sizes is obtained (*i.e.* the particle size distribution, PSD; Figure 1: middle: case of emulsion polymerization).[13-15]

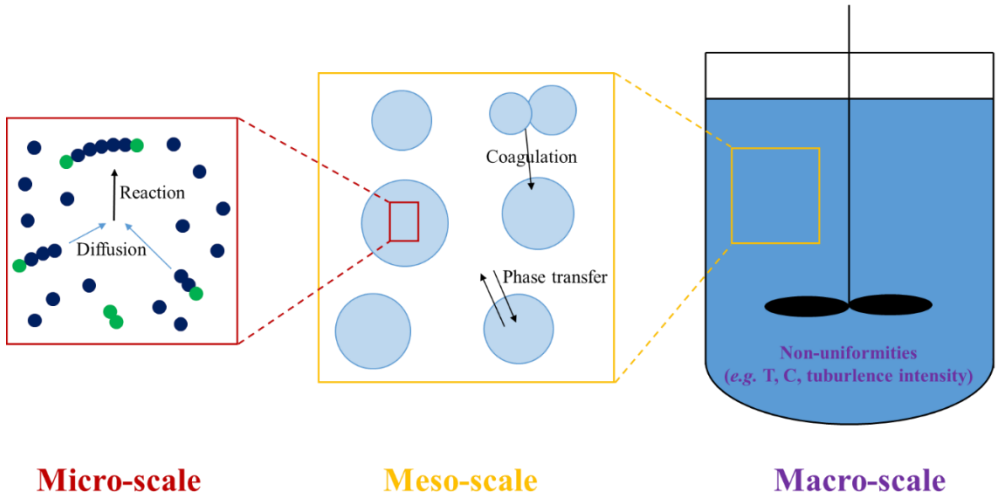

Figure 1. Multi-scale character of dispersed phase radical polymerization (case with reaction loci of nm scale). At the micro-scale, the reaction probabilities and diffusion characteristics determine the evolution of the chain length distribution (CLD). At the meso-scale, which transcends a local single phase kinetic variation, particle dynamics such as particle growth, coagulation and breakage determine the evolution of the particle size distribution (PSD). Due to the occurrence of particle size dependent interphase mass transfer phenomena, *e.g.* radical exit and entry, and compartmentalization of radicals, the micro- and meso-scale are in general coupled. At the reactor or macro-scale, non-uniformities such as temperature and concentration gradients and differences in turbulence intensity lead to a non-uniform evolution of the CLD (micro-scale) and PSD (meso-scale).[1, 16, 17]

Notably the distributions encountered in radical polymerizations often display multimodality. For example, the CLD (or the molar mass distribution; MMD) obtained via pulsed laser polymerization (PLP)[18, 19] – a frequently used technique for the determination of (intrinsic) rate coefficients – typically is multimodal due to the pulsed creation of radicals.[20, 21] The origin of the multimodality of the CLD/MMD in PLP and the possibilities this offers for the determination of individual rate coefficients will be explained in detail in Chapter 2-5. Diffusional limitations on termination can also result in a multimodal MMD. For instance in radical polymerization of styrene toward the production of expandable styrene, a multimodal character for the log-MMD results at low temperatures as chain transfer to monomer cannot prevent the formation of longer chains once the number average chain lengths increases.[22] Another example in which multimodality plays a key role relates to latexes obtained via emulsion polymerization, for which in several cases only well-designed multimodal PSDs allow to obtain high solid contents while maintaining a sufficiently low viscosity for processability.[23, 24] Hence, it is clear that the regulated growth of the PSD in dispersed phase polymerization is of great industrial importance.

In this chapter, focus is on the fundamental aspects related to radical dispersed phase polymerizations and the implications they have on the modeling of the relevant distributions. Upon the consideration of one "large" particle the conventional homogeneous case results, explaining why focus is on the heterogeneous case.

1.2 Radical dispersed phase polymerization: state-of-the-art and challenges

One of the outstanding industrial challenges for radical polymerization in dispersed systems is the regulated growth of the PSD. The PSD, which depending on the polymerization technique can be in the μm (suspension polymerization) or nm (emulsion polymerization) size range,[2] determines strongly the polymer processability and therefore the final properties of a polymeric material.[23, 25-27] For example, the PSD influences the impregnability of suspension

polymerization beads and, hence, the insulation capability of the polymer foam upon expansion with a blowing agent (*e.g.* expandable polystyrene process).[25] Another example relates to the coating industry, in which only well-shaped multimodal acrylic emulsion PSDs result in a high solid content and consequently in a low film formation time and a high film quality.[26, 27]

Currently, a limited control over the temporal evolution of the PSD can unfortunately be obtained, which can be explained by (i) the absence of reliable sensors for the on-line measurement of the PSD under industrially relevant conditions of a high solid content,[28] which inherently leads to too low signal-to-noise ratios; (ii) the limited fundamental knowledge on important meso-scale phenomena such as particle nucleation, breakage, and coalescence;[29, 30] and (iii) the complex interplay between the effect of the particle size on the polymerization kinetics and polymer molecular structure.[31-33] The latter is particularly relevant in the nm size range, in which radicals can, depending on the time scale of the reactions, easily enter and exit nanoparticles, perturbing the desired chain growth pattern.[34-36] A strong interaction between the temporal evolution of the CLD at the micro-scale and the PSD at the meso-scale can thus result for reaction loci of nm size, taking into account the additional influence of the reaction temperature, initial concentrations, and reactor operation mode (*e.g.* (semi-)batch). This interaction becomes even stronger if advanced functional nanoparticles[37] are targeted via *e.g.* reversible deactivation radical polymerization, for which a high product quality implies often a narrow unimodal PSD.[38]

Hence, depending on the application a unimodal or multimodal PSD is required. Since many process parameters at different length and time scales determine the industrial feasibility of radical polymerization in dispersed systems, a multi-scale modeling approach is clearly indispensable to fully regulate the entire CLD and PSD during polymer synthesis. [1, 16, 17, 31] Such approach will not only allow an accurate simulation of these distributions but will also facilitate

the identification of the best industrial protocols, taking into account environmental and economic constraints.

A logical question to ask is whether simplifications can be made such as the decoupling of the CLD and PSD calculation. Next to that one needs to identify in a multiphase reactive polymerization the reactive "particle" types.

In suspension polymerization (Figure 2: left), monomer droplets of µm size are created upon stirring in the presence of surfactant. While polymerization progresses, these droplets undergo breakage and coalescence events. A dynamic evolution of the PSD results on the µm scale, which is affected by many parameters such as the surface tension, dynamic viscosity and turbulence intensity, and which can be studied as a good as decoupled from the polymerization kinetics.[17, 39, 40] Since at higher monomer conversions more viscous "droplets" are however formed, coalescence is favored at one point, until eventually, also coalescence ceases to occur and the final PSD is established.[2]

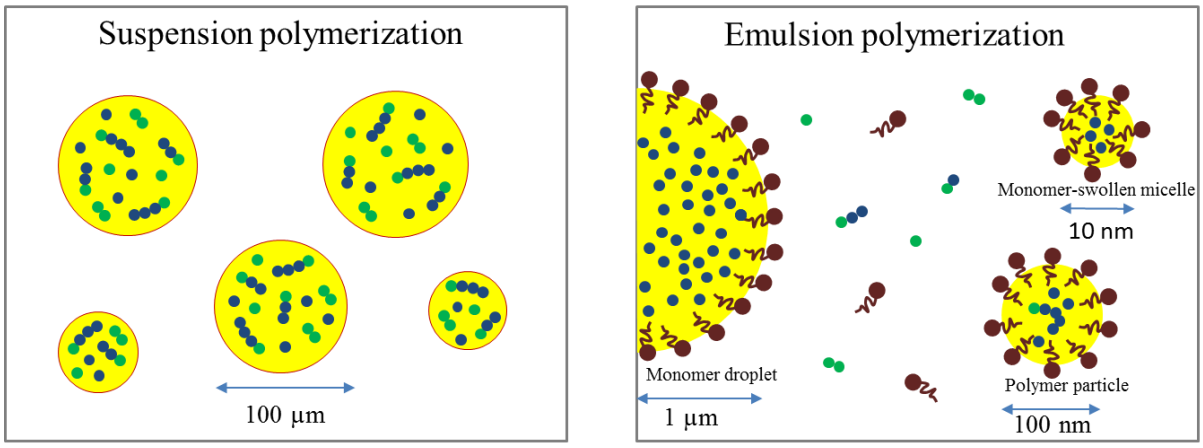

Figure 2. Comparison of suspension (left) and emulsion (right) polymerization. In suspension polymerization, the droplets/particles are in the µm size range and the evolution of the polymerization kinetics (micro-scale) and particle size distribution (meso-scale) are as good as decoupled. In emulsion polymerization, particles are in the nm size range and the evolution of the micro- and meso-scale are inherently coupled due to particle size dependent entry/exit events.[14, 31]

Much effort has been dedicated to obtaining a quantitative multi-scale description of radical suspension polymerization processes.[17, 39, 41-43] For example, Kalfas *et al.*[39] developed a population balance model for suspension homo-and copolymerizations. In this work, the polymerization kinetics simulations were fully decoupled from the PSD evolution simulations. To account for differences in turbulence intensity inside suspension polymerization reactors (*cf.* the higher turbulence intensity near the impeller), Kiparissides and coworkers[41, 42] developed a two-compartment population balance model. These authors used computational fluid dynamics (CFD) simulations to determine the size of and exchange flows between the two compartments. More recently, Xie *et al.*[17] developed a CFD-population balance model for suspension atom transfer radical polymerization (ATRP). In this work, a CFD model for the calculation of the turbulence intensity field was combined with a model for the polymerization kinetics (method of moments), particle dynamics (population balance model accounting for growth, aggregation and coalescence), and interphase monomer mass transfer (thermodynamic model). The simulation of the polymerization kinetics was partially decoupled from the PSD simulation as an iterative approach was used.

In (conventional macro-) emulsion polymerization (Figure 2: right), large monomer droplets (> 1 μm), (monomer-swollen) micelles (5-10 nm) and polymer nanoparticles (10-500 nm) are present, making it a much more dynamic process than suspension polymerization, as also illustrated in Figure 3.[44-49] As a result, most focus has either been on the simulation of the polymerization kinetics (*i.e.* the micro-scale) while assuming an average (constant) particle size,[11, 32, 33, 50-53] or on the evolution of the PSD (*i.e.* the meso-scale) via population balance models, assuming a simplified model for the polymerization kinetics (*e.g.* zero-one or pseudo-bulk model and typically ignoring chain length dependent termination kinetics).[13, 16, 54-56] It should however be stressed that from a fundamental point of view a strong coupling between

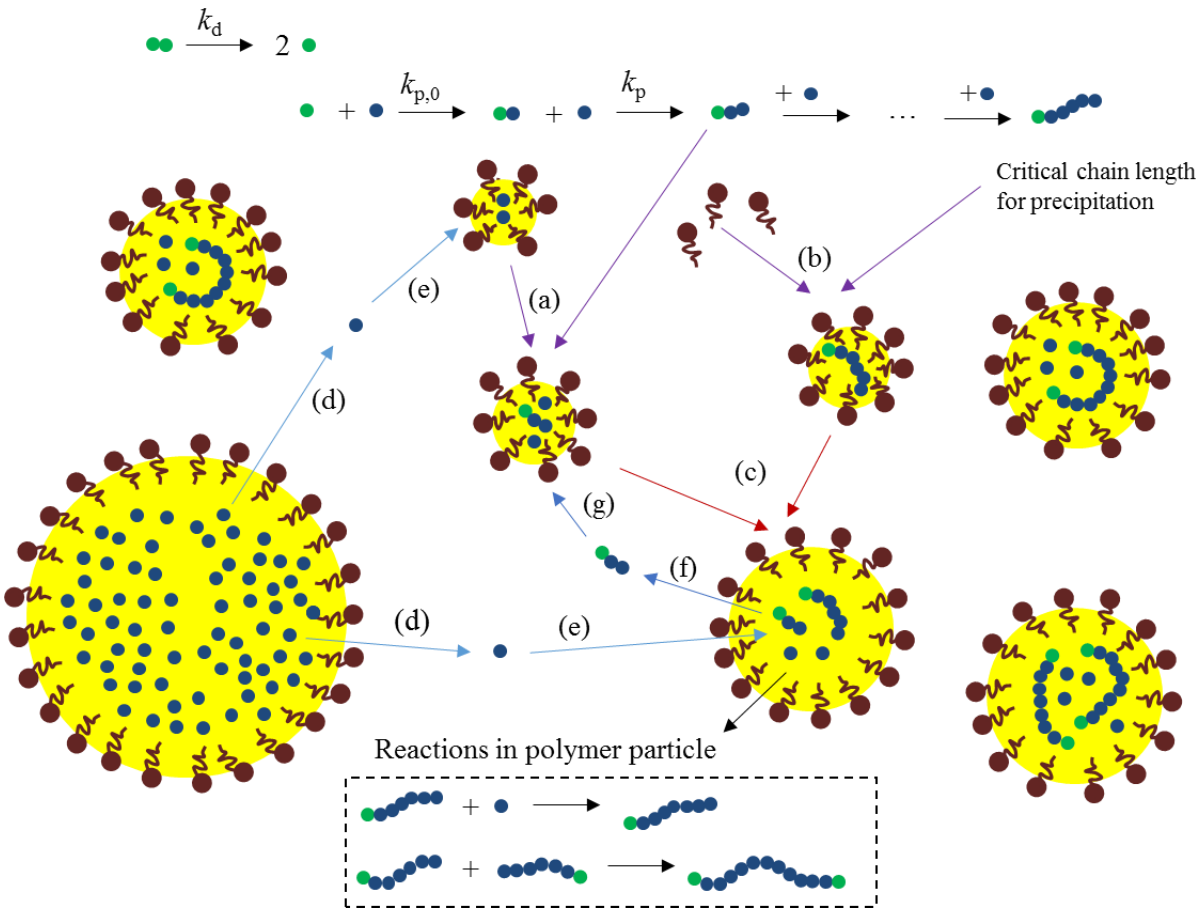

Figure 3. Micro- and meso-scale events occurring in (conventional macro-) emulsion polymerization initiated by a water-soluble initiator: dissociation in the aqueous phase, where the radical propagates a few times before undergoing heterogeneous (a) or homogeneous (b) nucleation; (c) nucleation of colloidally unstable particles; (d,e) interphase monomer mass transfer, (f) radical exit; (g) radical entry.

the micro- and meso-scale is expected for emulsion polymerization. Hence, an important research task is to develop multi-scale models that address this explicit coupling of particle and chain growth.

1.3 Outline

In this PhD thesis, kinetic Monte Carlo (*k*MC) modeling is applied to accurately simulate multimodal distributions in radical polymerization. In a first part, *k*MC modeling is applied to pulsed laser polymerization (PLP), starting from model developments in earlier work.[12, 57, 58] As demonstrated in **Chapter 2**, *k*MC modeling of the complete multimodal PLP MMD allows to extract information on chain initiation and termination alongside propagation rate

coefficients that follow from the inspection of inflection point data only. Next, the developed *k*MC model for PLP is applied in **Chapter 3** to design PLP experiments allowing the estimation of the less known photodissociation quantum yield. The PLP *k*MC model is also used to estimate for acrylate radical polymerization the backbiting rate coefficient from low temperature PLP experiments (**Chapter 4**) and the β-scission rate coefficient from high temperature PLP (**Chapter 5**).

In the second part of this PhD thesis, focus is shifted to dispersed phase radical polymerization. In view of the expected stronger interaction between the micro- and meso-scale in emulsion polymerization compared to suspension polymerization, focus is on the former polymerization technique. For illustration purposes focus is on miniemulsion polymerization in the absence of morphological aspects such as phase separation in the polymer particles. In **Chapter 6**, a novel detailed *k*MC model in which reaction and interphase mass transfer events are tracked particle by particle is developed for isothermal batch miniemulsion free radical homopolymerization. A joint and interactive prediction of the CLD and PSD evolution is highlighted for the first time, considering literature parameters for all model parameters. This model is extended and applied to miniemulsion copolymerization of styrene and N-vinylcaprolactam (VCL) in **Chapter 7**, leading to new insights for the design of tailored VCL-based nanoparticles in view of drug delivery applications, benefiting from the experimental knowledge acquired during a research stay in the group of Prof. Pich at DWI Leibniz Institute for Interactive Materials/RWTH Aachen University.

Finally, an outlook is presented in **Chapter 8**, with focus on the possibilities of the developed *k*MC model for (i) future PLP studies and (ii) the model-based design of nanoparticles with a nanoengineered morphology.

1.4 References

1. D. R. D'hooge, P. H. M. Van Steenberge, M. F. Reyniers and G. B. Marin, *Prog. Polym. Sci.*, 2016, **58**, 59-89.
2. J. Asua, *Polymer Reaction Engineering*, John Wiley & Sons, 2008.
3. A. M. van Herk, *Chemistry and technology of emulsion polymerisation*, John Wiley & Sons, 2013.
4. J. M. Asua, *J. Polym. Sci. Pol. Chem.*, 2004, **42**, 1025-1041.
5. A. K. Tripathi, J. G. Tsavalas and D. C. Sundberg, *Macromolecules*, 2015, **48**, 184-197.
6. D. Meimaroglou and C. Kiparissides, *Ind. Eng. Chem. Res.*, 2014, **53**, 8963-8979.
7. J. Jennings, G. He, S. M. Howdle and P. B. Zetterlund, *Chem. Soc. Rev.*, 2016, **45**, 5055-5084.
8. F. A. L. Janssen, M. Kather, L. C. Kroger, A. Mhamdi, K. Leonhard, A. Pich and A. Mitsos, *Ind. Eng. Chem. Res.*, 2017, **56**, 14545-14556.
9. F. Brandl, M. Drache and S. Beuermann, *Polymers*, 2018, **10**, 16.
10. A. Nasresfahani and R. A. Hutchinson, *Ind. Eng. Chem. Res.*, 2018, **57**, 9407-9419.
11. A. Butte, G. Storti and M. Morbidelli, *Macromol. Theory Simul.*, 2002, **11**, 37-52.
12. P. H. M. Van Steenberge, D. R. D'hooge, M. F. Reyniers and G. B. Marin, *Chem. Eng. Sci.*, 2014, **110**, 185-199.
13. H. M. Vale and T. F. McKenna, *Prog. Polym. Sci.*, 2005, **30**, 1019-1048.
14. M. Drache, K. Brandl, R. Reinhardt and S. Beuermann, *Phys. Chem. Chem. Phys.*, 2018, **20**, 10796-10805.
15. D. Meimaroglou, A. I. Roussos and C. Kiparissides, *Chem. Eng. Sci.*, 2006, **61**, 5620-5635.
16. A. H. Alexopoulos, P. Pladis and C. Kiparissides, *Ind. Eng. Chem. Res.*, 2013, **52**, 12285-12296.
17. L. Xie and Z. H. Luo, *Ind. Eng. Chem. Res.*, 2017, **56**, 4690-4702.
18. O. F. Olaj, I. Bitai and F. Hinkelmann, *Die Makromolekulare Chemie*, 1987, **188**, 1689-1702.
19. S. Beuermann and M. Buback, *Prog. Polym. Sci.*, 2002, **27**, 191-254.
20. Y. W. Marien, P. H. M. Van Steenberge, C. Barner-Kowollik, M. F. Reyniers, G. B. Marin and D. R. D'hooge, *Macromolecules*, 2017, **50**, 1371-1385.
21. A. N. Nikitin, I. Lacık, R. A. Hutchinson, M. Buback and G. T. Russell, *Macromolecules*, 2019, **52**, 55-71.
22. L. De Keer, P. H. M. Van Steenberge, M. F. Reyniers, G. B. Marin, K. D. Hungenberg, L. Seda and D. R. D'hooge, *Aiche J.*, 2017, **63**, 2043-2059.
23. M. Do Amaral, S. Van Es and J. M. Asua, *J. Polym. Sci. Pol. Chem.*, 2004, **42**, 3936-3946.

24. M. do Amaral, A. Roos, J. M. Asua and C. Creton, *J. Colloid Interface Sci.*, 2005, **281**, 325-338.
25. J. Alvarez, J. Alvarez and M. Hernandez, *Chem. Eng. Sci.*, 1994, **49**, 99-113.
26. A. Guyot, F. Chu, M. Schneider, C. Graillat and T. F. McKenna, *Prog. Polym. Sci.*, 2002, **27**, 1573-1615.
27. A. Peters, G. C. Overbeek, A. J. P. Buckmann, J. C. Padget and T. Annable, *Progress in Organic Coatings*, 1996, **29**, 183-194.
28. G. E. Fonseca, M. A. Dube and A. Penlidis, *Macromol. React. Eng.*, 2009, **3**, 327-373.
29. C. Kiparissides, *J. Process Control*, 2006, **16**, 205-224.
30. M. Morbidelli, G. Storti and S. Carra, *J. Appl. Polym. Sci.*, 1983, **28**, 901-919.
31. Y. W. Marien, P. H. M. Van Steenberge, D. R. D'hooge and G. B. Marin, *Macromolecules*, 2019, **52**, 1408-1423.
32. D. J. G. Devlaminck, P. H. M. Van Steenberge, M. F. Reyniers and D. R. D'hooge, *Macromolecules*, 2018, **51**, 9442-9461.
33. P. H. M. Van Steenberge, D. R. D'hooge, M. F. Reyniers, G. B. Marin and M. F. Cunningham, *Macromolecules*, 2014, **47**, 7732-7741.
34. M. F. Cunningham, *Prog. Polym. Sci.*, 2008, **33**, 365-398.
35. B. Charleux and J. Nicolas, *Polymer*, 2007, **48**, 5813-5833.
36. J. Qiu, B. Charleux and K. Matyjaszewski, *Prog. Polym. Sci.*, 2001, **26**, 2083-2134.
37. M. J. Monteiro and M. F. Cunningham, *Macromolecules*, 2012, **45**, 4939-4957.
38. H. A. Zayas, N. P. Truong, D. Valade, Z. F. Jia and M. J. Monteiro, *Polym. Chem.*, 2013, **4**, 592-599.
39. G. Kalfas, H. Yuan and W. H. Ray, *Ind. Eng. Chem. Res.*, 1993, **32**, 1831-1838.
40. C. Kotoulas and C. Kiparissides, *Chem. Eng. Sci.*, 2006, **61**, 332-346.
41. D. Maggioris, A. Goulas, A. H. Alexopoulos, E. G. Chatzi and C. Kiparissides, *Chem. Eng. Sci.*, 2000, **55**, 4611-4627.
42. A. H. Alexopoulos, D. Maggioris and C. Kiparissides, *Chem. Eng. Sci.*, 2002, **57**, 1735-1752.
43. J. Wieme, T. De Roo, G. B. Marin and G. J. Heynderickx, *Ind. Eng. Chem. Res.*, 2007, **46**, 1179-1196.
44. S. C. Thickett and R. G. Gilbert, *Polymer*, 2007, **48**, 6965-6991.
45. C. S. Chern, *Prog. Polym. Sci.*, 2006, **31**, 443-486.
46. H. F. Hernandez and K. Tauer, *Macromol. React. Eng.*, 2009, **3**, 375-397.
47. T. G. T. Jansen, J. Meuldijk, P. A. Lovell and A. M. van Herk, *J. Polym. Sci. Pol. Chem.*, 2016, **54**, 2731-2745.
48. T. G. T. Jansen, J. Meuldijk, P. A. Lovell and A. M. van Herk, *Macromol. React. Eng.*, 2015, **9**, 19-31.
49. L. Hlalele, D. R. D'hooge, C. J. Durr, A. Kaiser, S. Brandau and C. Barner-Kowollik, *Macromolecules*, 2014, **47**, 2820-2829.

50. P. B. Zetterlund and M. Okubo, *Macromolecules*, 2006, **39**, 8959-8967.
51. C. Autran, J. C. de la Cal and J. M. Asua, *Macromolecules*, 2007, **40**, 6233-6238.
52. G. Lichti, R. G. Gilbert and D. H. Napper, *J. Polym. Sci. Pol. Chem.*, 1980, **18**, 1297-1323.
53. L. Bentein, D. R. D'hooge, M. F. Reyniers and G. B. Marin, *Polymer*, 2012, **53**, 681-693.
54. N. Sheibat-Othman, H. M. Vale, J. M. Pohn and T. F. L. McKenna, *Macromol. React. Eng.*, 2017, **11**, 32.
55. O. Kammona, P. Pladis, C. E. Frantzikinakis and C. Kiparissides, *Macromol. Chem. Phys.*, 2003, **204**, 983-999.
56. A. Hosseini, A. E. Bouaswaig and S. Engell, *Chem. Eng. Sci.*, 2012, **72**, 179-194.
57. P. H. M. Van Steenberge, D. R. D'hooge, Y. Wang, M. J. Zhong, M. F. Reyniers, D. Konkolewicz, K. Matyjaszewski and G. B. Marin, *Macromolecules*, 2012, **45**, 8519-8531.
58. D. R. D'hooge, P. H. M. Van Steenberge, P. Derboven, M. F. Reyniers and G. B. Marin, *Polym. Chem.*, 2015, **6**, 7081-7096.

Chapter 2: Kinetic Monte Carlo modeling of complete PLP-SEC traces extracts information on chain initiation and termination

Summary

Complete pulsed laser polymerization (PLP) log-molar mass distributions (log-MMDs) are accurately simulated using kinetic Monte Carlo (*k*MC) modeling to gain not only knowledge on the propagation but also on the chain initiation and termination reactivity. The isothermal *k*MC model (306-325 K) accounts for diffusional limitations and all relevant elementary reactions, considering *n*-butyl acrylate, 2,2-dimethoxy-2-phenylacetophenone (DMPA), and a frequency of 500 s^{-1}. The disparate reactivities towards vinylic bonds of the DMPA fragments are essential to ensure the well-defined multimodality of the log-MMDs necessary to identify consecutive inflection points. It is also illustrated that PLP log-MMD data can be used to test the validity of models for apparent termination rate coefficients at low monomer conversions and that *k*MC simulations are a powerful tool to track the chain growth of the different radical types between laser pulses and to identify dominant elementary reactions.

2.1 Introduction

Many polymer products in everyday life stem from free radical polymerization (FRP), which is characterized by a chain-growth mechanism involving initiation, propagation and termination as the basic reactions. A large variety of vinyl monomers, *e.g.* styrene, methyl (meth)acrylate, vinyl acetate, vinyl chloride, and acrylamide can be (co)polymerized under FRP conditions to synthesize high molar mass polymers under mild conditions and with a high tolerance toward impurities.[1, 2]

Despite the high industrial importance of radical polymerization, no complete quantitative understanding of the reaction kinetics is yet obtained.[3] The design of the polymer microstructure requires the consideration of a detailed reaction scheme, including side reactions which can lead to the formation of defects that can influence the polymer macroscopic properties.[4-6] Identification of the most suited polymerization conditions is complicated as many competitive phenomena are simultaneously occurring, including diffusional limitations[7-10] due to viscosity changes along the polymerization. A model-based strategy, supported by experimental validation, is recommendable as it allows a facile and fast screening of a broad range of reactant candidates and polymerization conditions.[11-13] A prerequisite for a successful model-based design is the availability of reliable kinetic parameters.[6, 10, 14, 15] For many reaction steps, the values of the intrinsic/chemical reactivities and the Arrhenius parameters are still uncertain, which hampers the design of radical polymerization processes, particularly when conducted in large-scale reactors in which temperature control is very relevant.

One of the most established experimental techniques to measure intrinsic rate coefficients is pulsed laser polymerization (PLP).[3, 16, 17] This technique, as originally introduced by Aleksandrov *et al.*[18] and Olaj *et al.*,[19] is the method of choice to determine the intrinsic propagation rate coefficient k_p, as illustrated in Figure 1. In PLP, photoinitiator radical fragments (*I*) are formed via laser pulses, *j*, with a frequency ν (dark time: $\Delta t = \nu^{-1}$). Part of the *I* radicals propagate until they are terminated with fresh radicals generated at the next pulse(s) on the time scale $j\Delta t$ (j = 1, 2, …). Under well-defined PLP conditions, these time scales are reflected in the size exclusion chromatography (SEC) trace via inflection points at chain lengths equal to L_j (j = 1, 2, …) so that k_p can be determined:

$$k_p = \frac{L_j}{[M]_0 (j\Delta t)} \tag{1}$$

in which $[M]_0$ is the initial monomer concentration.

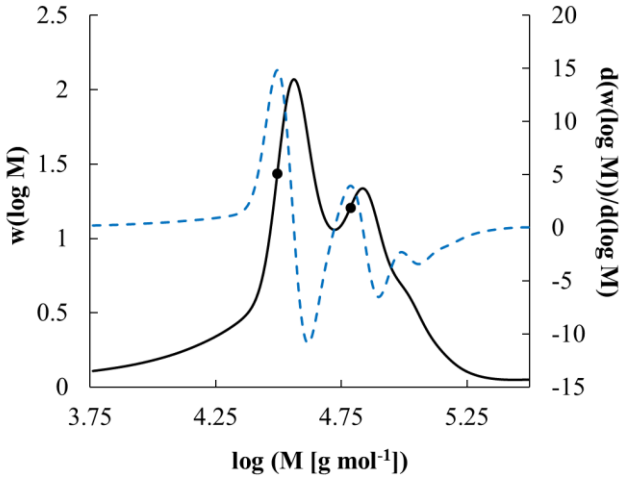

Figure 1. Principle of pulsed laser polymerization (PLP) to measure the intrinsic propagation reactivity k_p from the inflection points (black dots) in the size exclusion chromatography (SEC) trace (full black line; log molar mass distribution (MMD)). These inflection points correspond to maxima for the corresponding derivative (dashed blue line).

Currently, the PLP technique has been used to accurately measure a wide range of k_p values, mostly for standard monomers such as styrene and methyl methacrylate[20-28] and as facilitated by the foundation of the IUPAC working party on 'Modeling of kinetics and processes of polymerization'. Based on the measured k_p data, reliable propagation Arrhenius parameters have been extracted, which are a major input in kinetic modeling studies and allow to study the impact of the chemical structure on the propagation reactivity, including an evaluation of the possible existence of solvent effects.[29-40]

A direct application of Equation (1) can however lead to a biased kinetic analysis. Specifically for acrylates, depending on the polymerization temperature and laser frequency, the position of the PLP inflection points can be influenced by both the propagation of secondary end-chain radicals (ECRs) and tertiary mid-chain radicals (MCRs), the latter dominantly formed via backbiting reactions.[17, 41-48] By dedicated analysis, considering several experimental conditions, both the ECR and MCR propagation reactivity for acrylate polymerization can be determined.[49, 50] The determination of k_p values for the radical polymerization of acrylamides in aqueous media has also shown to be challenging. A concentration dependency has been reported which has been attributed to dimer formation[51] on the one hand and the formation of a pre-reactive

complex[52, 53] prior to acrylamide propagation on the other hand. Recently, Kattner and Buback[54] used single pulse–PLP–electron paramagnetic resonance (SP-PLP-EPR) to perform a detailed kinetic analysis of acrylamide polymerization in aqueous solution. Based on a comparison with experimental data, rate coefficients for reactions with ECRs and MCRs could be assessed, opening the pathway to a more complete picture on the propagation kinetics of acrylamides in aqueous media.[55] Also for other monomers polymerizable in water, *e.g.* acrylic acid[56] and N-vinylpyrrolidone,[57] a strongly improved understanding of the propagation kinetics has been obtained by combining PLP experimental and modeling research. Furthermore, PLP allows to elucidate radical copolymerization kinetics.[58-65] For example, Rooney *et al.*[62] studied the copolymerization of *n*-butyl cyanoacrylate and MMA and demonstrated that a strongly alternating comonomer incorporation can be obtained.

It is important to realize that the PLP-SEC trace is inherently a reflection of all reactions taking place and, hence, the application of the PLP-technique is not restricted to the measurement of k_p values. For instance, Arzamendi *et al.*[43] illustrated that for acrylate radical polymerization backbiting strongly influences the shape of the PLP-SEC trace at high temperatures and low frequencies, even leading to the disappearance of the typical multimodality of the PLP-SEC trace, as visible in Figure 1. In the past decades, various PLP-based methods have been developed to determine the backbiting rate coefficient k_{bb}.[49, 50, 66-68] Several research groups performed frequency tuned PLP-SEC experiments with *n*-butyl acrylate (*n*BuA) as monomer to determine k_{bb} from inflection point data. In addition, Nikitin *et al.*[69] highlighted that in the presence of a chain transfer agent the PLP-SEC trace contains information regarding the corresponding chain transfer reactivity. Furthermore, it is known that the termination reactivity has a pronounced impact on the PLP-SEC trace, as for instance reviewed by Drawe *et al.*[70] Very recently, Ballard *et al.*[71] reminded that information on the mode of termination can also be

deduced from PLP-SEC traces, again illustrating that the PLP technique can be used for a detailed kinetic analysis of radical polymerization as such.

Albeit that kinetic information on all relevant reaction steps is hidden in PLP-SEC traces, a limited number of kinetic modeling studies[50, 61, 70-72] have focused on the complete PLP molar mass distribution (MMD), combined with a kinetic analysis transcending the localization of only the inflection points (or peak maxima). Analytical MMD models[18, 19, 73-75] can unfortunately not be relied on as they are only valid under strong simplifications with respect to the size of the reaction scheme and/or the treatment of the apparent termination kinetics. Even at the very low monomer conversions encountered under PLP conditions, a strong chain length dependency exists for the observed termination reactivity, which has been mainly attributed to diffusional limitations. This requires accounting for the chain length dependency of the apparent termination rate coefficients $k_{t,}^{app}$ which can greatly influence the PLP MMD characteristics.[76-78] More advanced mathematical methods such as the Galerkin method, as implemented in the deterministic PREDICI software package,[50, 78, 79] or the kinetic Monte Carlo (*k*MC) method[43, 47, 61, 80-84] have been applied to that purpose. For example, Willemse *et al.*[61] implemented chain length dependent $k_{t,}^{app}$ values in a *k*MC model for pulsed laser copolymerization and obtained a good correspondence between chemical composition distributions obtained by simulation and matrix assisted laser desorption and ionization time-of-flight mass spectrometry (MALDI-TOF-MS). Despite such advances, in many kinetic modeling studies on PLP MMDs, for simplicity, chain length independent termination kinetics have been assumed.[43, 47, 50, 79, 80]

In the present work, *k*MC modeling is applied to perform a more accurate simulation of experimental PLP log-MMDs of poly(*n*BuA) as obtained at polymerization temperatures between 306 and 325 K,[85] considering the commonly used photoinitiator 2-dimethoxy-2-phenylacetophenone (DMPA) and literature based kinetic parameters. The novelty lies in the

combined fundamental description of both the PLP chemistry and molecular diffusion so that not only the inflection points but also the peak heights and tail of experimental log-MMDs are accurately described. An extensive reaction scheme including acrylate specific polymerization reactions, such as backbiting and β-scission, is therefore combined with a detailed and explicit description of the photodissociation and chain initiation process, and of the chain length dependency of the apparent termination kinetics.

Based on earlier SP-PLP results,[86] the difference in reactivity of the DMPA radical fragments is explicitly accounted for via elementary reactions and its impact is shown to be a prerequisite for a good description of the heights of the log-MMD peak maxima. Moreover, the strength of PLP-SEC experiments to confirm the accuracy of k_t^{app} models at low monomer conversions is illustrated. A detailed tracking of the chain growth of the different radical types between consecutive pulses is also performed, highlighting the strength of *k*MC modeling to further improve the kinetic understanding of PLP. The *k*MC modeling study thus allows a further comprehension of the relation between the PLP reactions and their impact on the MMD.

Table 1. Reactions and literature based Arrhenius parameters to simulate log-MMDs for PLP of *n*BuA initiated by DMPA; initiator radicals (I and II) defined in Figure 2; macromonomer addition and intermolecular chain transfer can be neglected under the investigated conditions.

Entry	Reaction	Equation	A [(L mol^{-1}) s^{-1}]	E_a [kJ mol^{-1}]	k (306 K) [(L mol^{-1}) s^{-1}]	ref
1	Photodissociation	$I_2 \xrightarrow{h\nu} R^{\mathrm{I}}_{0,\mathrm{e}} + R^{\mathrm{II}}_{0,\mathrm{e}}$	-	-	[a]	-
2	Chain initiation[b]	$R^{\mathrm{I/III}}_{0,\mathrm{e}} + M \xrightarrow{k_{\mathrm{p,I/III}}} R_{1,\mathrm{e}}$	2.4 10^8	17.9	2.1 10^5	24
3	Propagation[c]	$R_{\mathrm{i,e}} + M \xrightarrow{k_{\mathrm{p,e}}} R_{\mathrm{i+1,e}}$	2.2 10^7	17.9	1.9 10^4	24
4		$R_{\mathrm{i,m}} + M \xrightarrow{k_{\mathrm{p,m}}} R_{\mathrm{i+1,e}}$	9.2 10^5	28.3	1.4 10^1	67
5	Backbiting	$R_{\mathrm{i,e}} \xrightarrow{k_{\mathrm{bb}}} R_{\mathrm{i,m}}$, i ≥ 3	1.6 10^8	34.7	1.9 10^2	67
6	β-scission	$R_{\mathrm{i,m}} \xrightarrow{k_{\mathrm{\beta s}}} MM_3 + R_{\mathrm{i-3,e}}$	1.5 10^9	63.9	1.8 10^{-2}	87
7		$R_{\mathrm{i,m}} \xrightarrow{k_{\mathrm{\beta s}}} MM_{\mathrm{i-2}} + R_{2,\mathrm{e}}$	1.5 10^9	63.9	1.8 10^{-2}	87
8	Chain transfer to monomer	$R_{\mathrm{i,e}} + M \xrightarrow{k_{\mathrm{trM,e}}} P_{\mathrm{i}} + R^{\mathrm{III}}_{0,\mathrm{e}}$	2.9 10^5	32.6	7.8 10^{-1}	88
9		$R_{\mathrm{i,m}} + M \xrightarrow{k_{\mathrm{trM,m}}} P_{\mathrm{i}} + R^{\mathrm{III}}_{0,\mathrm{e}}$	2.0 10^5	46.1	2.7 10^{-3}	88
10	Termination[d]	$R_{\mathrm{i,e}} + R_{\mathrm{j,e}} \xrightarrow{k^{\mathrm{app}}_{\mathrm{t,ee}}(i,j)} P_{\mathrm{i(+j)}}(+P_{\mathrm{j}})$	2.6 10^{10}	8.4	9.6 10^8	67
11		$R_{\mathrm{i,e}} + R_{\mathrm{j,m}} \xrightarrow{k^{\mathrm{app}}_{\mathrm{t,em}}(i,j)} P_{\mathrm{i(+j)}}(+P_{\mathrm{j}})$	2.8 10^9 [e]	6.6	2.1 10^8	67
12		$R_{\mathrm{i,m}} + R_{\mathrm{j,m}} \xrightarrow{k^{\mathrm{app}}_{\mathrm{t,mm}}(i,j)} P_{\mathrm{i(+j)}}(+P_{\mathrm{j}})$	1.8 10^7	5.6	2.0 10^6	67
13		$R^{\mathrm{I/II/III}}_{0,\mathrm{e}} + R^{\mathrm{I/II/III}}_{0,\mathrm{e}} \xrightarrow{k^{\mathrm{app}}_{\mathrm{t,oo}}} P_0$	2.6 10^{10}	8.4	9.6 10^8	[f]
14		$R^{\mathrm{I/II/III}}_{0,\mathrm{e}} + R_{\mathrm{i,e}} \xrightarrow{k^{\mathrm{app}}_{\mathrm{t,oe}}(i)} P_{\mathrm{i}}(+P_0)$	2.6 10^{10}	8.4	9.6 10^8	[g]
15		$R^{\mathrm{I/II/III}}_{0,\mathrm{e}} + R_{\mathrm{i,m}} \xrightarrow{k^{\mathrm{app}}_{\mathrm{t,om}}(\mathrm{i})} P_{\mathrm{i}}(+P_0)$	2.8 10^9 [e]	6.6	2.1 10^8	[h]

[a]: $\Delta[R_0]$ is calculated via Equation (2); for $\lambda = 351\ 10^{-9}$ m, $E_{\mathrm{pulse}} = 2.5\ 10^{-3}$ J and $V = 2\ 10^{-7}\ m^3$ and L = 5.2 10^{-3} m (*cf.* experiments in ref. [85]), and a Φ of 0.8 based on Figure 3, $\Delta[R_0]$ at the first laser pulse is equal to 4.8 10^{-5} mol L^{-1}.

[b]: increased reactivity of $k_{\mathrm{p,I/III}}$ taken into account (see Appendix A); no propagation of $R_{0,\mathrm{II}}$ (*cf* . discussion Figure 2).

[c]: chain length dependencies for propagation accounted for according to Equation (S.11)[89] in Appendix A; only the plateau value for propagation with long ECRs is reported here.

[d]: chain length dependent apparent termination rate coefficients are considered (parameters: ref. [67]); only $k^{\mathrm{app}}_{\mathrm{t}}(1,1)$ is reported here, taking into account a correction with a factor 2, as indicated by *e.g.* Derboven *et al*;[90] fraction of termination by recombination (0.9 (entry 10), 0.3 (entry 11) and 0.1 (entry 12)) in agreement with literature data;[87, 91] strictly one of the disproportionation products is also a MM.

[e]: *A* slightly lowered (1.4 10^9 L mol^{-1} s^{-1}) based on comparison with experimental data in Figure 3.

[f]: assumed equal to $k^{\mathrm{app}}_{\mathrm{t,ee}}(1,1)$.

[g]: assumed equal to $k_{\mathrm{t,ee}}$ (i,1); $k^{\mathrm{app}}_{\mathrm{t,ee}}(1,1)$ is reported here.

[h]: assumed equal to $k_{\mathrm{t,em}}$ (i,1); $k^{\mathrm{app}}_{\mathrm{t,em}}(1,1)$ is reported here.

2.2 Kinetic model

Kinetic Monte Carlo (*k*MC) modeling of isothermal PLP of *n*-butyl acrylate (*n*BuA; 306-325 K and $\nu = 500\ s^{-1}$; simulation volume = $5\ 10^{-12}$ L, *i.e.* an initial number of monomer molecules of $2\ 10^{13}$) is performed according to the well-established Gillespie algorithm,[92] as also considered in previous modeling studies on polymerization in general[11, 13, 93-97] and PLP in particular.[43, 47, 61, 80-84] In contrast to deterministic modeling, detailed microstructural information is more easily accessible with stochastic modeling, explaining the recent boost in the development and application of *k*MC modeling tools to simulate and design polymerization processes. An overview of the reactions considered in the *k*MC PLP model is given in Table 1. The associated Arrhenius parameters, which are all literature based,[24, 67, 87, 88] with only one very small and thus acceptable modification after comparison with experimental data, and the values for the rate coefficients at 306 K are listed as well. Since *n*BuA is selected as monomer, next to the classical PLP reactions such as photodissociation, chain initiation and termination, reactions such as backbiting, tertiary propagation, and β-scission are included.[87, 91, 98, 99]

An important novelty taken up in the present work is the explicit description of the photodissociation kinetics (entry 1 in Table 1), for which the concentration of the photoinitiator radical fragments per pulse ($\Delta[R_0]$) is calculated based on theoretical concepts. Hence, $\Delta[R_0]$ is no longer seen as an adjustable parameter, in contrast to most previous PLP kinetic modeling studies. It should be stressed that the latter studies typically only aim at an accurate simulation of inflection point data for which the assumed value of $\Delta[R_0]$ is less critical. As demonstrated in the present work, for an accurate representation of the complete PLP MMD a more detailed description is required. Taking into account the decrease in light intensity along the optical path according to the Beer-Lambert law,[100] it follows from previous theoretical work[101, 102] (see Appendix A) that:

$$\Delta[R_0] = 2\Phi \frac{E_{\text{pulse}}\lambda}{hcN_A V}[1 - \exp(-2.303\varepsilon[I_2]L)] \quad (2)$$

in which Φ is the quantum yield for photodissociation, λ the wavelength of the laser, E_{pulse} the energy of a laser pulse, h the Planck constant, c the speed of light, N_A the Avogadro constant, V the volume of the sample, $[I_2]$ the photoinitiator concentration, ε the molar absorptivity, and L the optical path length. Note that the chemical initiator efficiency is given a value of 1 and is thus not included in Equation (2). This is allowed since all termination reactions are explicitly accounted for (entry 13-15 in Table 1) and for the DMPA radical fragments no side reactions take place in the considered temperature range (306-325 K).[86]

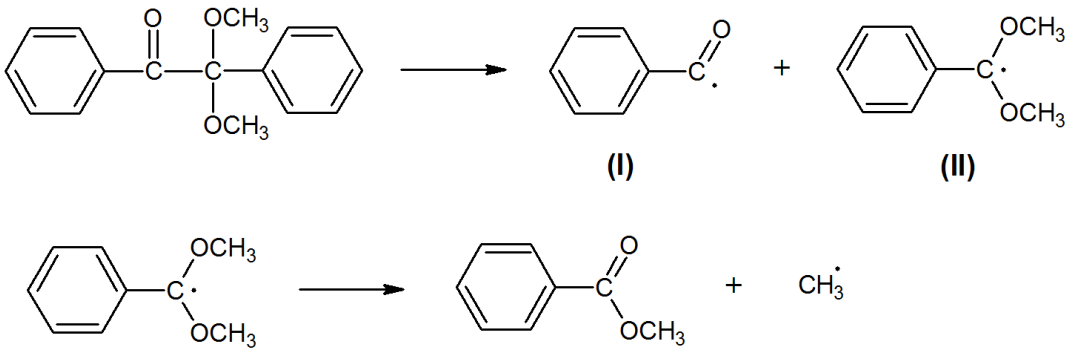

Figure 2. Top: UV-induced decomposition of 2,2-dimethoxy-2-phenylacetophenone (DMPA), yielding a benzoyl (I) and dimethoxy benzyl (II) radical. Bottom: β-scission of the dimethoxy benzyl radical at temperatures higher than those considered in the present study (> 325 K);[86] chain initiation can be neglected for radical II.[86, 103-106]

In contrast to previous *k*MC studies of PLP but in agreement with earlier kinetic analysis with SP-PLP,[86] in the present work, the difference in chain initiation reactivity of the DMPA radical initiator fragments (entry 2 in Table 1) is explicitly taken into account starting from elementary reactions, allowing a more detailed description of the chain initiation process. As indicated by Fischer *et al.*,[103] upon irradiation with UV light, DMPA decomposes into a benzoyl and dimethoxy benzyl radical (Figure 2; top; radical I and II) which are characterized by a strongly different reactivity. By means of electron spin resonance (ESR) spectroscopy Fischer *et al.*[103] observed that the benzoyl radical readily adds to acrylonitrile ($k_{p,I} \neq 0$ L mol^{-1} s^{-1}) while the

dimethoxy benzyl does not initiate chain growth ($k_{p,II}$ = 0 L mol^{-1} s^{-1}). In the reported ESR spectrum, the signal of the dimethoxy benzyl radical remained unvaried whereas the benzoyl signal was clearly replaced by its adduct formed upon monomer addition. By means of photolysis product analysis Fischer and coworkers[103] demonstrated that the dimethoxy benzyl radical (radical II in Figure 2) can participate in termination reactions (entry 13-15 in Table 1), thus having an inhibiting effect. Kowollik *et al.*[86] exploited these observations by extending their kinetic scheme for SP-PLP of methyl acrylate and styrene to describe the unusual behavior of a decreasing monomer conversion with increasing initial DMPA concentration. The Barner-Kowollik team[104] also confirmed the presence of an initiating and inhibiting species in laser-induced polymerization of methyl methacrylate by means of end-group analysis via MALDI mass spectrometry. Inhibition was further confirmed by Barner-Kowollik and coworkers,[105, 106] who reported the detection of dimethoxy benzyl radical based termination products via electrospray ionization-mass spectrometry. These authors concluded that the dimethoxy benzyl radical must be much more effective in termination than in chain initiation. Notably also other acetophenone-type photoinitiators such as benzoin are known to yield an inhibiting species upon photodecomposition.[107]

Despite the experimental observations that acetophenone-type photoinitiators such as DMPA and benzoin yield an initiating and an inhibiting radical fragment, in previous PLP modeling studies[43, 47, 61, 80-84] it was assumed that both photoinitiator radical fragments have the same reactivity toward chain initiation. As will be shown further, this simplification leads to an overestimation of the chain initiation rate and thus a less accurate description of the complete PLP-SEC trace. It should be noted that to represent the inhibition with DMPA also an alternative approach has been proposed in which additional (unknown) inhibitor radical species are introduced in the reaction scheme with tunable rate coefficients.[108] Such approach is however less generally applicable than the one proposed in the present work. In addition, it has

been indicated that the dimethoxy benzyl radical can also undergo β-scission, leading to the formation of a methyl benzoate molecule and a very reactive methyl radical (bottom of Figure 2). Given that the thermal decomposition of the dimethoxy benzyl radical is very slow at the temperatures considered in this *k*MC study (306-325 K) and that UV-initiated decomposition of this radical can be neglected due to the very limited duration of the laser pulses,[86] β-scission of the dimethoxy benzyl radical can assumed to be insignificant, explaining its absence in Table 1.

Furthermore, in Table 1, a distinction is made between ECRs and MCRs. Backbiting (entry 5 in Table 1) transforms ECRs into MCRs, which are more stable and, hence, less reactive. Upon propagation of MCRs, *i.e.* tertiary propagation (entry 4 in Table 1), rate retardation takes place and short chain branches (SCBs) are formed. Even for very low SCB amounts, as for instance encountered under well-defined controlled radical polymerization (CRP) conditions, this rate retardation is relevant. For example, Van Steenberge *et al.*[109] recently demonstrated in their simulation of miniemulsion nitroxide mediated polymerization of *n*BuA that an accurate description of the polymerization rate requires the consideration of SCB formation.

As shown in Appendix A the concentration of macromonomers (MMs) formed via β-scission and disproportionation is small and macromonomer addition can, at least in a first approximation, be neglected. Note that, in principle, in addition to intramolecular chain transfer, *i.e.* backbiting, also intermolecular chain transfer or so-called chain transfer to polymer may occur.[42] However, this process is kinetically insignificant at low to moderate monomer conversions.[110-113] Since in PLP experiments the monomer conversion is very limited (< 5%), intermolecular chain transfer can be neglected as a reaction possibility.

Both termination by recombination and disproportionation have been taken into account, with the fractional contributions taken from literature.[87, 91] Recent kinetic studies[71, 114] have although

indicated that a more detailed determination of these fractions is recommended but under typical acrylate PLP conditions of a high frequency and/or low temperature, leading to a dominant ECR formation, termination by recombination can be expected as the dominant termination mode. The influence of chain length dependent termination kinetics on the PLP-SEC trace, either caused intrinsically or due to diffusional limitations, is evaluated via the so-called composite k_t model,[9, 115, 116] which is implemented in the *k*MC model in the same way as previously reported[92] and which can be applied for both low and high monomer conversions, *i.e.* low and high viscosities.[117] Since in PLP only the lower monomer conversions are relevant, it suffices to consider only the first two equations of this piecewise defined model to calculate the apparent termination reactivities, *i.e.* the apparent termination reactivities between radicals with the same chain length:

$$k_t^{app}(i,i) = k_t^{app}(1,1)i^{-\alpha_S} \qquad i \leq i_c \tag{3}$$

$$k_t^{app}(i,i) = k_t^{app}(1,1)i_c^{-\alpha_S+\alpha_L}i^{-\alpha_L} \qquad i > i_c \tag{4}$$

in which α_S and α_L express the chain length dependence for short and long radicals and i_c is the cross-over chain length, describing the shift between termination controlled by center-of-mass diffusion (shorter radicals) and segmental diffusion (longer radicals). In the present work, the SP-PLP-EPR based values as reported by Barth *et al.*[67] are used, *i.e.* $\alpha_S = 0.85$, $\alpha_L = 0.16$, and $i_c = 30$.

For the apparent cross-termination or short-long termination reactivity, *i.e.* the apparent termination reactivity of radicals with differing chain lengths *i* and *j*, the geometric mean is considered:[118-120]

$$k_t^{app}(i,j) = [k_t^{app}(i,i)k_t^{app}(j,j)]^{0.5} \tag{5}$$

Recent work of Derboven *et al.*[90] highlighted that ideally a direct measurement of short-long apparent rate coefficients *e.g.* via the reversible addition fragmentation chain transfer – chain

length dependent - termination (RAFT-CLD-T) is needed to obtain highly accurate $k_t^{app}(i,j)$ values. However, these authors also indicated that to a first approximation it is allowed to use simplified models such as Equation (5), at least under diluted conditions as in PLP.

Finally, the simulated PLP log-MMDs account for non-idealities during sample preparation and analysis. At the end of a PLP experiment quenching is performed which is non-instantaneous and thus slightly changes the shape of the PLP-SEC trace at the higher chain lengths, as also theoretically highlighted by Nikitin.[121] This effect is accounted for by adding ten extra seconds to the simulation time after the final pulse. For higher delays no effect is observed, explaining the selection of this threshold value. Next to that, during experimental analysis SEC broadening can take place. For the simulated MMDs, this broadening is accounted for, following the method proposed by Buback *et al.*[79] and as described in Appendix A.

2.3 Results and discussion

In this section, it is first demonstrated that the developed *k*MC model allows an accurate representation of the complete log-MMD for PLP of *n*BuA with DMPA as photoinitiator. To allow for a direct comparison with experimental data, modeling is performed for a frequency of 500 s^{-1} and a polymerization temperature of 306 and 325 K.[85] Isothermal PLPs are considered, assuming an excellent temperature control at any position in the reaction mixture. Next, the *k*MC model is used to obtain a better understanding of several key reactions taking place during PLP of acrylates. A differentiation is made between photodissociation, chain initiation, and termination. For each reaction, its impact on the description of the complete MMD is highlighted.

2.3.1 Model validation up to high molar masses

Figure 3 shows a comparison between log-MMDs as simulated with the *k*MC model (dashed green lines), considering the reactions and kinetic parameters listed in Table 1, and as

experimentally recorded by Barner-Kowollik *et al.*[85] (black full lines), including error bars based on the lowest molar mass. The generated amount of photoinitiator radical fragments per pulse ($\Delta[R_0]$) is calculated explicitly via Equation (2). For both plots, $[DMPA]_0$ amounts to 5 10^{-3} mol L^{-1} and the number of pulses (N_{pulse}) is equal to 100. The initial monomer concentration ($[n\text{BuA}]_0$) is equal to 6.92 (306 K) and 6.76 mol L^{-1} (325 K).

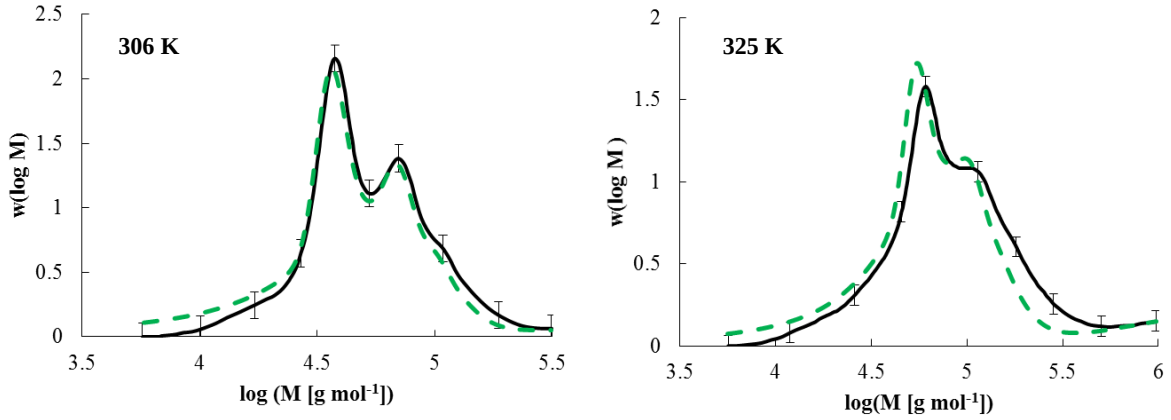

Figure 3. Comparison of simulated (dashed green line) and experimentally recorded[85] (black full line) log-MMD for DMPA initiated PLP of *n*BuA at 306 K (left) and 325 K (right); $[DMPA]_0$ = 5 10^{-3} mol L^{-1}, $[n\text{BuA}]_0$ = 6.92 mol L^{-1} (306 K; left) and 6.76 mol L^{-1} (325 K; right), number of pulses N_{pulse} = 100; model parameters: Table 1; quenching accounted for.

It follows from Figure 3 that at both temperatures a good description of the log-MMD is obtained with the *k*MC model. Compared to previous modeling studies in particular the peak heights and the high molar mass region are described much better, which can be related to the more representative model assumptions in the present work. At the highest temperature (325 K), a less characteristic PLP trace is obtained, in agreement with the recent simulation results of Ballard *et al.*[71] This again confirms the stronger influence of MCRs on the chain growth pattern at higher temperatures.[17, 43, 45, 48] At 325 K, the time scale for backbiting (2.4 10^{-3} s vs. 5.2 10^{-3} s at 306 K) becomes closer to the dark time (2 10^{-3} s). Hence, on average, backbiting requires ECRs surviving only one laser pulse. The increased importance of backbiting at 325 K is also reflected in the increase of the simulated SCB amount with temperature (0.14 to 0.21 % from 306 to 325 K; monomer basis; molar).

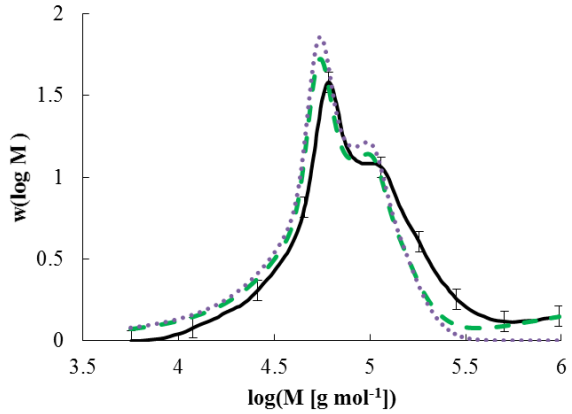

Figure 4. Effect of non-instantaneous quenching on simulated PLP log-MMD (325 K); instantaneous quenching (purple dotted line) vs. non-instantaneous quenching with 10 seconds (green dashed line as in Figure 3 (right)). Experimentally recorded log-MMD (full black line) also included; model parameters: Table 1; other conditions: see caption Figure 3; effect most important for the highest temperature considered.

In addition, in Figure 3 (right; 325 K) at high molar masses (log M > 5.5) a significant increase in w(log M) is observed. This can be attributed to non-instantaneous quenching, *i.e.* it takes in practice some time to add a radical scavenger to the reaction mixture. To illustrate this the simulated log-MMD with a purely theoretical instantaneous quenching at 325 K is depicted in Figure 4 (purple dotted line) and compared to the log-MMD as shown in Figure 3 (right; dashed green line). Clearly, the assumption of instantaneous quenching affects the description of the high molar mass region of the experimental log-MMD (black full line), as was also analytically demonstrated by Nikitin.[121] Hence, for a proper kinetic interpretation of experimental PLP-SEC traces it is recommended to account for the time scale of quenching.

2.3.2 Importance of photoinitiator decomposition

In Figure 5, *k*MC simulations results for the PLP SEC trace are displayed in which, in contrast to before, $\Delta[R_0]$ is assumed time independent and equal to a value of 2.4 10^{-5} mol L^{-1} (purple dotted line) and 9.6 10^{-5} mol L^{-1} (blue dashed-dotted line). Hence, with respect to the first pulse value as obtained based on Equation (2) ($\Delta[R_0]$ = 4.8 10^{-5} mol L^{-1}; SEC trace: dashed green line in Figure 5; same as in Figure 3 (left)) a decrease and increase with a factor of 2 is considered. Such a variation of $\Delta[R_0]$ falls within the variation of the input values proposed in previous

modeling studies (*ca.* $\Delta[R_0] = 10^{-6}$-10^{-3} mol L^{-1}; $\nu = 500\ s^{-1}$) and allows to highlight the relevance of the explicit and fundamental calculation of $\Delta[R_0]$. To not overload the discussion, focus is restricted to the lowest temperature of 306 K for which more classical PLP behavior is to be expected.

In agreement with the recent work of Drawe *et al.*[70] it follows that on an overall basis the PLP log-MMD is highly sensitive to $\Delta[R_0]$. For a higher $\Delta[R_0]$, the intensity of the first peak increases and the one of the second peak decreases because the termination rate increases more than the propagation rate, taking into account the reaction orders (propagation: first order in the radical concentration; termination: second order) and the strong apparent chain length dependency for termination (higher reactivity in case of shorter chains). Note that depending on the PLP experiment a different level of accuracy for $\Delta[R_0]$ is required. Small deviations from the actual value can be afforded in case for instance only the inflection points are required (almost coinciding symbols in Figure 5 for various $\Delta[R_0]$ values), reconfirming the accuracy of previous PLP studies aiming at the determination of the propagation reactivity. On the other hand, in case focus is on the accurate representation of the complete SEC trace, as in the present work, $\Delta[R_0]$ needs to be known very accurately (clearly different lines in Figure 5) and $\Delta[R_0]$ should not be seen an adjustable parameter.

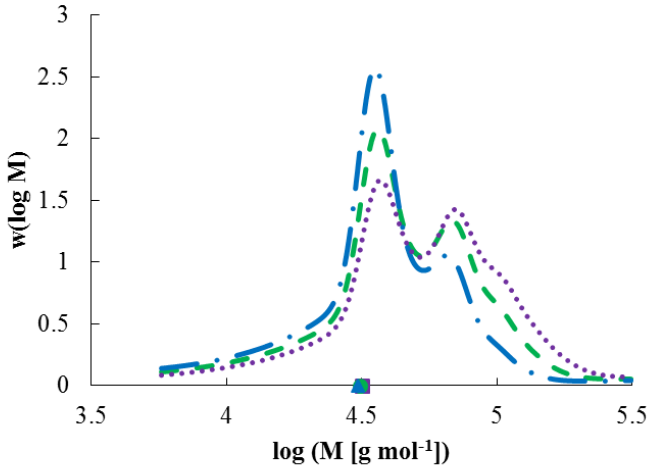

Figure 5. Sensitivity of simulated PLP log-MMD to variation of $\Delta[R_0]$; reference case: green dashed line as in Figure 3 (left; 306 K), *i.e.* full model with Equation (2) and initial $\Delta[R_0]$ of 4.8 10^{-5} mol L^{-1} (inflection point: green circle); purple dotted line: constant $\Delta[R_0]$ of 2.4 10^{-5} mol L^{-1} (factor 2 lower compared to 4.8 10^{-5} mol L^{-1}; inflection point: purple square) and blue dashed dotted line line: constant $\Delta[R_0]$ of 9.6 10^{-5} mol L^{-1} (factor 2 higher compared to 4.8 10^{-5} mol L^{-1}; inflection point: blue triangle); model parameters: Table 1; inflection points are coinciding, whereas peak heights not.

The results in Figure 5 also indicate that in practice an optimal $\Delta[R_0]$ exists, as very recently also indicated by Noble *et al.*[122] For a too low $\Delta[R_0]$, the laser pulses no longer have a modulating effect, while a too high $\Delta[R_0]$ leads to an unclear second peak, which is not desired for k_p determination according to IUPAC rules. In agreement with earlier literature reports,[70, 123] the first step in the design of a PLP experiment should be the identification of the correct order of magnitude for $\Delta[R_0]$. In a second step, adequate values for E_{pulse} and $[I_2]_0$ have to be determined via Equation (2).

It should be mentioned for completeness that the photoinitiator concentration decreases as a function of the reaction time (Figure 6 (left; full blue line) and, hence, $\Delta[R_0]$ is not constant as it decreases for later pulses (Equation (2); Figure 6 (left; purple line)). As a result, the total radical concentration $[R_{tot}]$ does not become periodic after a few pulses (Figure 6 (right)). For the calculation of the overall PLP characteristics, it is however allowed to consider the average $\Delta[R_0]$ value over the different pulses in case of a limited consumption of the photoinitiator, *i.e.* in case of a limited number of pulses, as also indicated by Buback *et al.*[79] and Castignolles *et*

al.[102] A constant yet average $\Delta[R_0]$ can thus be used at least to a first approximation, in agreement with previous studies.[50, 78, 79]

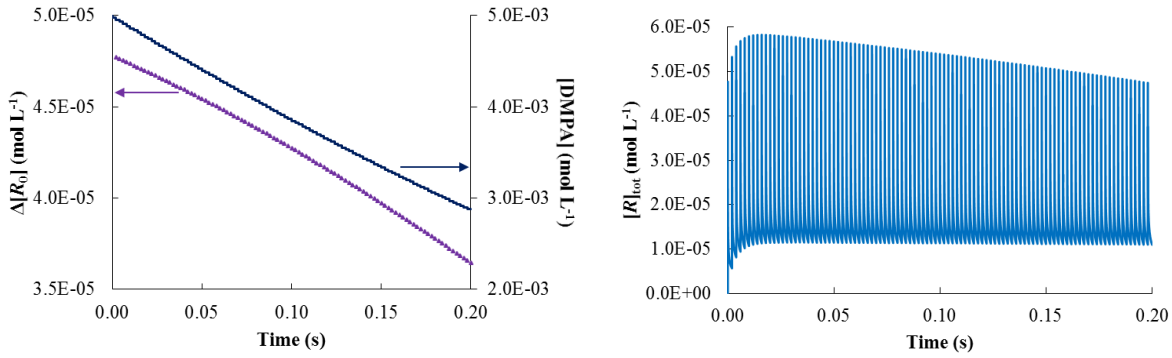

Figure 6. Left: Photoinitiator (DMPA; full blue line) and generated photoinitiator radical (purple line) concentration as a function of time (Equation (2)); Right: Corresponding evolution of the total radical concentration; conditions correspond to Figure 3 (left; 306 K); model parameters; Table 1.

The *k*MC model also allows to further differentiate between the contributions of the different radical types to $[R_{tot}]$. For example, in Figure 7, for the first 10 dark periods (*i.e.* $t < 10\Delta t$), the concentration of the ECRs (top left; dotted orange line; $[R_{i,e}]$), MCRs (top left; full grey line; $[R_{i,m}]$) and the two photoinitiator radical fragments (top right; dashed-dotted yellow and purple line; $[R_{0,I}]$ and $[R_{0,II}]$)) are depicted, focusing on the lowest temperature of 306 K. The concentration traces during the course of the entire experiment are provided in Appendix A.

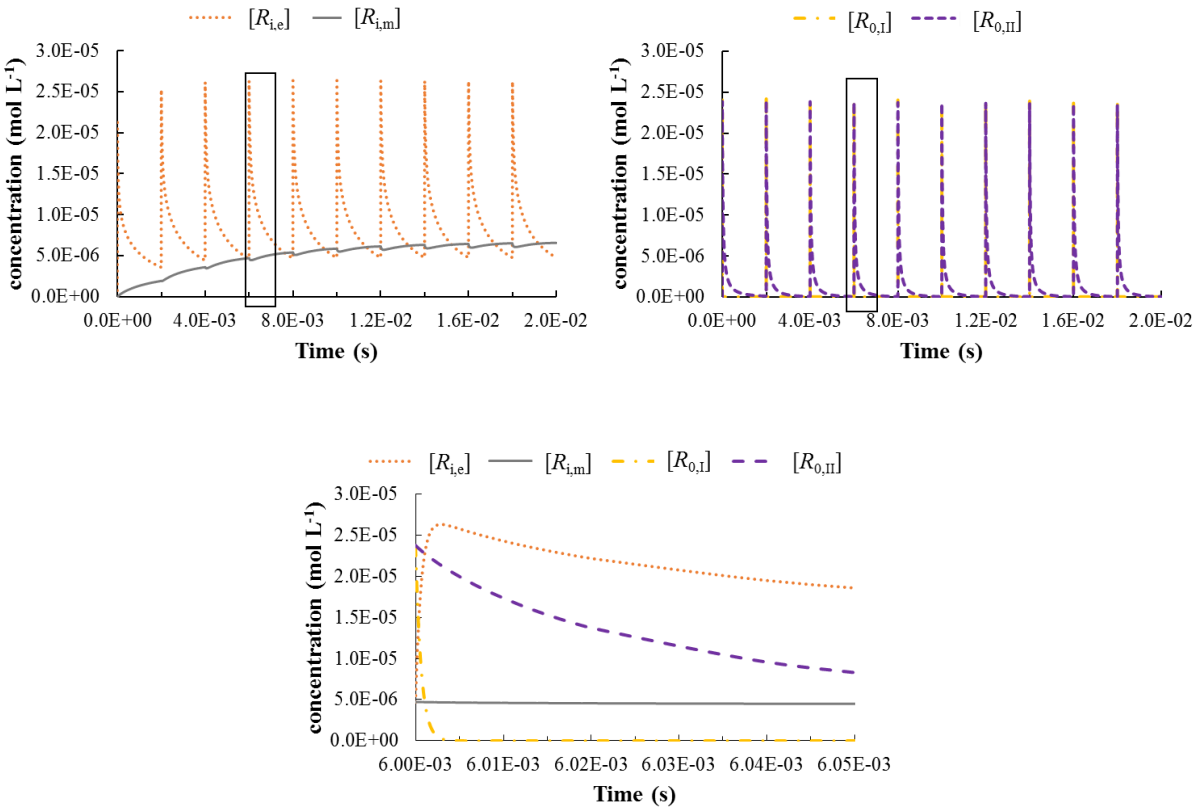

Figure 7. Top: Temporal evolution of the concentrations of the different radical types (ECRs/MCRs (left; dotted orange/fully grey line), and the two photoinitiator radical fragments (right): dashed dotted yellow (I) and purple (II) line) for the first 10 dark periods; Bottom: inset for a small part of a dark period (see boxes above); conditions correspond to Figure 3 (left; 306 K); model parameters in Table 1.

In Figure 7 (top left) it can be seen that the ECRs are the dominant macrospecies in the radical population, which can be expected based on the relatively low reaction temperature and relatively high frequency (500 s^{-1}). It further follows that during each dark period [R_e] quickly decreases to approximately 20% of its maximal value as reached after a new laser pulse. It can be also deduced that during $0 < t < 6\ \Delta t$, [R_m] globally increases, although just after each pulse [R_m] slightly decreases due to the increased MCR termination probability upon the generation of new initiator radicals at each pulse. From Figure 7 (top right), it can be inferred that $R_{0,I}$ almost immediately reacts via chain initiation ([$R_{0,I}$] ≈ 0 mol L^{-1}), while $R_{0,II}$ disappears much more slowly via termination reactions, indicating the different role of both photoinitiator radicals in the PLP kinetics. This is even more clear in Figure 7 (bottom), which focuses only on a small part of the dark period just after a new pulse is applied.

It should be further noted that the concentrations in Figure 7 are absolute and can be helpful to validate the accuracy of experimental measurements by for instance EPR. In addition, these simulations allow to assess whether the ECR and MCR concentrations can be obtained by equating the backbiting and tertiary propagation rate as sometimes done in literature. The latter corresponds to applying the pseudo-steady state approximation (PSSA) under the assumption of negligible termination. As shown in Appendix A, the relatively high frequency of 500 s^{-1} prevents the PSSA based concentrations from being reached and, hence, in the present work the PSSA cannot be applied.

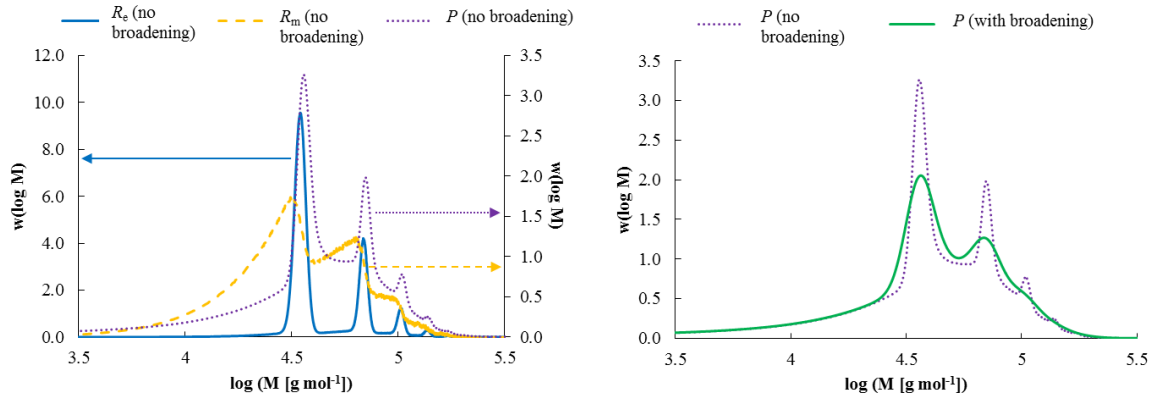

Figure 8. Left: Simulated log-MMD without SEC broadening for the ECRs (full blue line), MCRs (dashed yellow line) and termination products (dotted purple line) at t = 0.1 s. Right: log-MMD for the termination products without SEC broadening (dotted purple line, same as left) and with a correction for SEC broadening as described in Appendix A (full green line, same as in Figure 3 (left; 306 K); also same conditions); model parameters are listed in Table 1.

The dominance of ECRs in Figure 7 (306 K) is also reflected in Figure 8, in which the log-MMD of these radicals without SEC broadening (full blue line) is shown along with the corresponding log-MMD for the termination products (dotted purple line; dead polymer) just before a new pulse (t = 0.1 s). The peak maxima of the log-MMD of the ECRs correspond to the inflection points of the log-MMD of the dead polymer, which highlights the limited importance of backbiting and thus MCR formation under the selected PLP conditions (306 K; ν = 500 s^{-1}). It thus confirms that under these conditions in the so-called low termination limit[49]

the ECR propagation rate coefficient can be evaluated either via the peak maxima of the ECR log-MMD or the inflection points of dead polymer log-MMD (Equation (1)).

For completeness in Figure 8 (left) the MCR log-MMD is also included (dashed yellow line). It follows that the peaks in the MCR distribution show a significant fronting compared to the well-defined peaks of the ECR log-MMD (full blue line), which is due to the slower propagation of tertiary radicals. Furthermore, the chain growth of the different radical types can be visualized by plotting the simulated log-MMDs at different times between the pulses. For example, Figure S4 in Appendix A shows the chain growth of the different radical types in between the 50^{th} and 51^{st} pulse, from which the rate retardation taking place due to backbiting can be inferred.

Finally, from Figure 8 (right; 306 K) it follows that SEC broadening leads to less sharp peaks, in agreement with earlier reports,[70, 79] In the high molar mass region, peaks can even disappear. For instance, the third peak of the uncorrected simulated SEC trace (dotted purple line) is no longer distinguishable in case SEC broadening is taken into account (dashed green line). It is thus reconfirmed that SEC broadening needs to be accounted for upon the modeling of PLP experimental data. Reversely it can be in principle stated that the removal of SEC broadening from experimental traces instead of a correction of simulated log-MMDs allows a more confident kinetic parameter determination, as *e.g.* more inflection points can be identified (Figure 8; right). However, in practice this requires complex mathematical inversion methods, which can be also noise-sensitive. Hence, it can be expected that a correction of the simulated SEC traces with SEC broadening, as currently performed, is still the preferred data treatment method.

2.3.3 Importance of different chain initiation reactivity of the DMPA radical fragments

As explained above (*cf.* Table 1 and Figure 2), the *k*MC model accounts for the different chain initiation capability of the DMPA fragments. One of these fragments, *i.e.* the dimethoxy benzyl radical (Figure 2; radical II) cannot, or only in a very limited fashion, lead to chain initiation, which affects the overall PLP kinetics. To illustrate the impact of this incapability of chain initiation, in Figure 9, a comparison is made between the simulation results for the monomer conversion (left) and the log-MMD (right) in case inhibition is ignored, *i.e.* both initiator radicals are equally reactive (dotted red lines), and those in which the inhibition effect is included (dashed green lines). Again focus is for simplicity only on a polymerization temperature of 306 K. For completeness, the experimental SEC trace (black full line) and the experimentally recorded monomer conversion after quenching (black symbol; average error bar) are added as well. For comparison, all log-MMDs are normalized within the same selected range of experimentally covered molar masses.

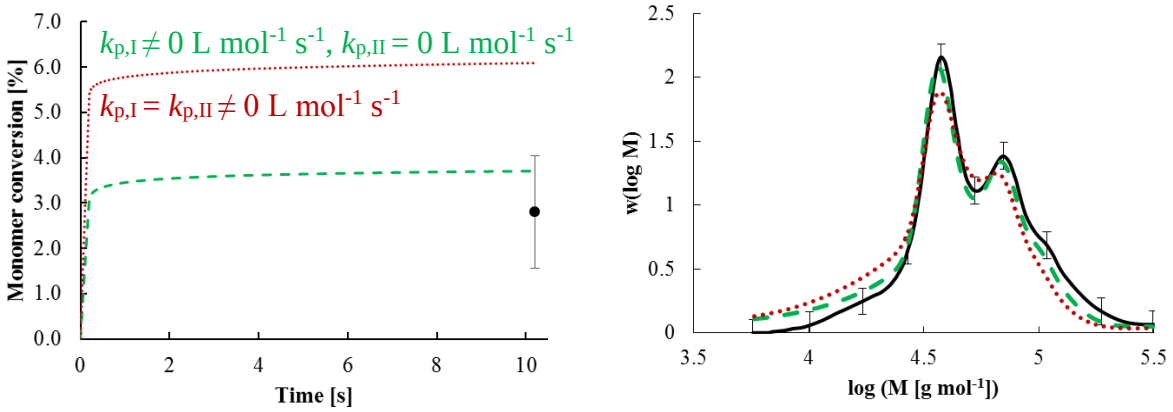

Figure 9. Left: Comparison between simulation results of the monomer conversion in case both DMPA radical fragments (Figure 2; radical I and II) are equally reactive (dotted red line), and those in which the inhibition effect of the dimethoxy benzyl radical (radical II) is included (dashed green line). Experimentally recorded monomer conversion after quenching is indicated by a black symbol. Right: corresponding simulation results of the log-MMD (dashed green line as in Figure 3 (left)). Model parameters in Table 1 (with inhibition).

Inspection of Figure 9 (left) allows to deduce that the polymerization rate is too high if the chain initiation reactivity of the dimethoxy benzyl radicals is overestimated. A too high monomer

conversion of *ca.* 6% would be simulated after quenching instead of the expected monomer conversion of *ca.* 3%. Furthermore, it is observed in Figure 9 (right) that the chain initiation kinetics have a noticeable effect on the intensity of the peaks of the log-MMD. In case the different chain initiation reactivity of the DMPA radical fragments is taken into account, sharper simulated peaks are observed (green dashed line), in agreement with the experimental curve (black full line). In contrast, for equally reactive photoinitiator radical fragments, a less characteristic PLP-SEC trace is obtained (dotted red line), *i.e.* the higher order peaks are less distinguishable. Since the inflection point of the second PLP peak is used as a consistency test for the determination of k_p according to IUPAC rules[20] (Equation (1) for $j = 2$), a clear second peak is required for an elegant application of the PLP technique. Hence, in this case, the inhibition effect of the dimethoxy benzyl radical is beneficial, explaining the success of PLP studies with DMPA as photoinitiator. In other words, the non-ideality of DMPA makes it an ideal photoinitiator for PLP.

The inhibition effect is also reflected in the overall termination behavior. Due the chain initiation incapability of the dimethoxy benzyl radicals, termination with benzoyl initiated macroradicals originating from previous pulses is enhanced compared to the case of equal chain initiation reactivities. Hence, a more defined termination pattern is obtained compared to the case of equal chain initiation reactivities, in which for termination a broader range of chain lengths is available. The latter is illustrated in Figure 10 (top left and right), which shows the individual termination fractions limiting the chain length *i* and *j* to 600. In particular from the insets (bottom of Figure 10), for which the chain length range *i* and *j* is limited to 30 and 320, it follows that the chain initiation incapability of the dimethoxy benzyl radicals results in a larger fraction located at the *i*- and *j*-axis. This indicates that termination reactions with at least one radical of chain length 0 (*i.e.* an initiator radical fragment) occur more, which leads to

termination products having a narrower range of chain lengths around L_1 and L_2 and thus sharper peaks in the log-MMD, as highlighted in Figure 9 (right).

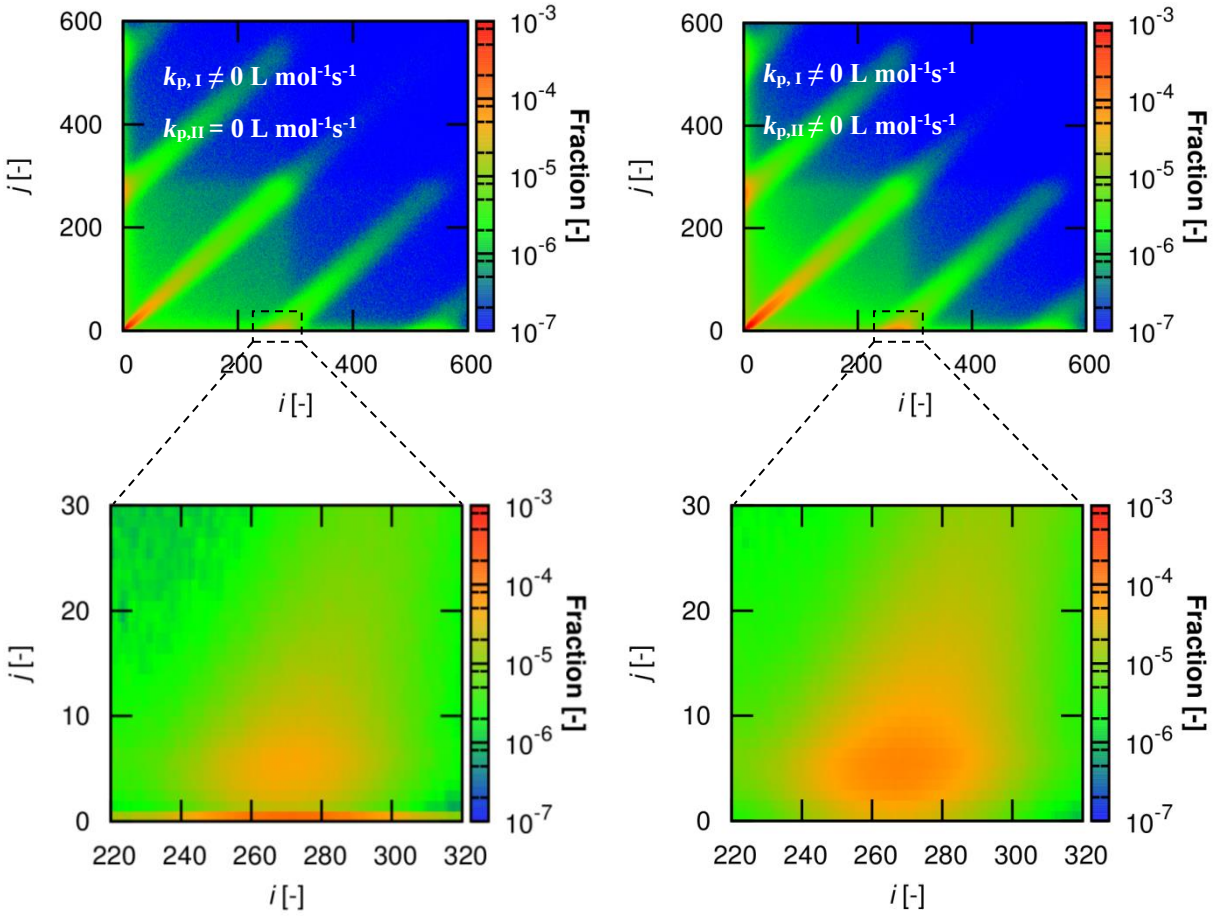

Figure 10. Fraction of termination reactions between radicals of chain length i and j in case inhibition accounted for (left) and neglected (right); in the top figures symmetry exists about the diagonal as there is no difference between $R_i + R_j$ and $R_j + R_i$ termination; initiator radical: chain length of 0; initial conditions: Figure 3 (left; 306 K); model parameters: Table 1.

Finally, it should be noted that the termination events between radicals originating from the same laser pulse are displayed around the diagonal, while the terminating radicals belonging to the same narrow chain length distribution of radicals centered around $i = k_{p,e}\,[M]\,t$, with t typically going from 0 to Δt. Spots of an increased termination behavior very close to the i and j-axis can also be identified. They emerge from the termination of chains with a length very close to 0 and to L_1 (270) or L_2 (540). These spots thus relate to the formation of dead polymer chains upon the generation of new pulses and initiator radicals, *i.e.* the relevance of short-long

termination is again observed. On the other hand, a part of the radicals only terminate later on, *i.e.* between one and two/three dark times, as witnessed by the parallel green regions to the diagonal.

2.3.4 Importance of chain length dependent termination

Figure 11 illustrates the impact of the chain length dependency of the apparent termination reactivity (Equation (3)-(4)) on the shape of the log-MMD under PLP conditions. At a temperature of 306 K a comparison is first made between the results as obtained with the full *k*MC model (dashed green line; same line as in Figure 3 (left)) and those obtained in case chain length independent termination rate coefficients are considered (dash-dotted red line; $k_{\mathrm{t}}^{\mathrm{app}} = k_{\mathrm{t}}^{\mathrm{app}}(1,1)$). Again for comparison the experimentally recorded log-MMD is included (full black line; same as in Figure 3 (left)). Also, the *k*MC simulation results are depicted with a simplified diffusion model (dotted blue line) with only one exponent α for the apparent homotermination rate coefficient:

$$k_t^{app}(i,i) = k_t^{app}(1,1)i^{-\alpha} \tag{6}$$

Both the simulation results for $\alpha = \alpha_L$ (dotted blue line) and $\alpha = \alpha_S$ (long purple dashes) are shown. For comparison, all log-MMDs in Figure 11 are again normalized within the same selected range of molar masses as experimentally recorded.

It can be seen in Figure 11 that termination is overestimated in case no (apparent) chain length dependency is taken into account. Under such premise the fraction of long chains is strongly underestimated and a unimodal distribution results, as easily observable by comparing the simulated log-MMD (red dashed-dotted line) with the experimental one (black full line). On the other hand, by accounting for the decrease in k_t^{app} with increasing chain length, longer chains may be theoretically formed and the simulated log-MMD has a more pronounced tail. This tail formation, which is in agreement with experimental observations, is however limited in case

the chain length dependence of k_t^{app} is expressed by the simplified diffusion model with $\alpha = \alpha_L$ (Equation (6); dotted blue line). The simplified diffusion model with $\alpha = \alpha_S$ (Equation (6); purple long dashes) on the other hand leads to an overestimation of longer chains ($\alpha_S > \alpha_L$; stronger dependence of k_t^{app}). Only with the more advanced composite k_t model (Equation (3) and (4); parameters determined by SP-PLP-EPR;[67] dashed green line) an excellent match with the experimentally recorded log-MMD (full black line) is obtained up to high molar masses. It should however be mentioned that a better description with Equation (6) is possible if the exponent is seen as a free parameter, as for instance demonstrated by Moad *et al.*[72] for PLP of styrene and MMA.

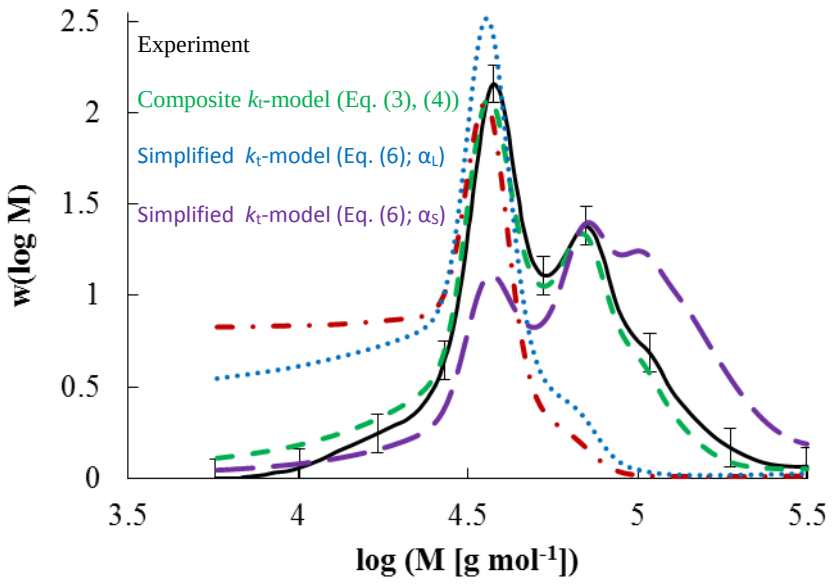

Figure 11. Comparison between simulation results of the log-MMD in case the chain length dependence of k_t^{app} is expressed by the composite k_t model (Equation (3) and (4); dashed green line, as in Figure 3 (left)), by a simplified k_t model (Equation (6), dotted blue line: $\alpha = \alpha_L$, long purple dashes: $\alpha = \alpha_S$), and in case the chain length dependence of k_t is ignored (dashed-dotted red line). Experimentally recorded log-MMD also included; other model parameters in Table 1; normalization in same range of molar masses for visualization purposes.

In general, it is thus clear that differentiation between termination involving shorter chains, as controlled by center-of-mass diffusion (α_S; Equation (3)), and termination involving longer chains as controlled by segmental diffusion (α_L: Equation (4)), is of key importance. Hence, as

for photoinitiation, an accurate description is needed of the termination events to accurately represent the PLP kinetics.

In agreement with earlier literature reports,[72] PLP-SEC data can thus be also used to validate the accuracy of k_t^{app} models at low monomer conversions, highlighting for instance the importance of SP-PLP-EPR studies.[67] Alternatively, these PLP data are relevant to test composite k_t models as constructed based on *e.g.* RAFT-CLD-T measurements. With RAFT-CLD-T it is inherently difficult to scan the conditions of high chain lengths and very diluted conditions (very low monomer conversions) so that the associated RAFT-CLD-T parameters are mostly based on the extrapolation of the experimental results recorded in the more concentrated regions (higher monomer conversions). Based on the results in Figure 11, it follows that additional PLP measurements allow to improve RAFT-CLD-T based composite k_t models and therefore contribute to a better mapping of the effect of the chain length and monomer mass fraction on the apparent termination reactivity. Both from an academic and industrial point of view,[6, 9, 90, 124] such improvements are beneficial for a better understanding of all radical polymerization processes, further highlighting the relevance of a detailed kinetic analysis as performed in Figure 11.

2.4 Conclusions

Kinetic Monte Carlo (*k*MC) modeling is successfully applied to accurately represent the complete experimental PLP-SEC trace, considering *n*BuA as monomer, DMPA as photoinitiator, and a detailed reaction scheme including chain transfer reactions. It is shown that a detailed description of both the photoinitiation process and the apparent termination kinetics are indispensable to obtain accurate simulation results. Reversely, PLP-SEC data can be used to tune or test the related fundamental parameters for photoinitiation and termination.

Importantly, the non-ideality of DMPA as a photoinitator, *i.e.* generating a chain initiating and non-initiating fragment, results in sharper peaks and thus better defined inflection points, allowing a more reliable k_p determination according to IUPAC rules. Hence, it has been explained why DMPA is a very efficient photoinitiator for PLP kinetic studies. The sharpness and number of peaks can also be controlled by tuning the radical generation rate, starting from fundamental concepts.

In case the complete SEC trace is the simulation target, it is recommended in future PLP simulation studies to explicitly calculate the radical generation rate to avoid a biased interpretation of the PLP kinetics. For such simulations, a correction for non-instantaneous quenching is also needed to accurately represent the high molar mass range. On the other hand, if the focus is only the accurate representation of the inflection points, a less detailed kinetic model can be safely used.

Furthermore, it has been theoretically indicated that it is worthwhile to make experimental PLP log-MMD data SEC broadening free rather than correcting simulated data for this broadening. Such treatment of experimental SEC traces, although computationally intensive, allows to retrieve a higher amount of kinetic information on the polymerization kinetics, for instance the identification of a higher number of inflection points.

It has been also highlighted that *k*MC modeling allows to study the chain growth of the different radical types. In particular, a differentiation between the behavior of the end- and mid-chain radicals (ECRs/MCRs) allows to quantify the complex radical log-MMD as a superposition of narrow and broad peaks. Such *in silico* information allows to corroborate experimental measurements on for instance the ECR and MCR concentration and to improve the mechanistic understanding of the radical polymerization kinetics with several radical types.

2.5 References

1. J. M. Asua, in *Polymer Reaction Engineering*, ed. J. M. Asua, Blackwell Pub., Oxford, 2007, pp. 1-28.
2. M. F. Cunningham and R. Hutchinson, in *Handbook of Radical Polymerization*, eds. K. Matyjaszewski and T. P. Davies, Wiley Interscience, New York, 2002, pp. 333-359.
3. S. Beuermann and M. Buback, *Prog. Polym. Sci.*, 2002, **27**, 191-254.
4. J. Purmova, K. F. D. Pauwels, M. Agostini, M. Bruinsma, E. J. Vorenkamp, A. J. Schouten and M. L. Coote, *Macromolecules*, 2008, **41**, 5527-5539.
5. P. H. M. Van Steenberge, J. Vandenbergh, D. R. D'hooge, M. F. Reyniers, P. J. Adriaensens, L. Lutsen, D. J. M. Vanderzande and G. B. Marin, *Macromolecules*, 2011, **44**, 8716-8726.
6. D. R. D'hooge, P. H. M. Van Steenberge, M.-F. Reyniers and G. B. Marin, *Prog. Polym. Sci.*, 2016, **58**, 59-89.
7. D. R. D'hooge, M. F. Reyniers and G. B. Marin, *Macromol. React. Eng.*, 2013, **7**, 362-379.
8. P. Derboven, D. R. D'hooge, M. M. Stamenovic, P. Espeel, G. B. Marin, F. E. Du Prez and M. F. Reyniers, *Macromolecules*, 2013, **46**, 1732-1742.
9. C. Barner-Kowollik and G. T. Russell, *Prog. Polym. Sci.*, 2009, **34**, 1211-1259.
10. A. D. Peklak, A. Butte, G. Storti and M. Morbidelli, *J. Polym. Sci. Pol. Chem.*, 2006, **44**, 1071-1085.
11. D. R. D'hooge, P. H. M. Van Steenberge, P. Derboven, M. F. Reyniers and G. B. Marin, *Polym. Chem.*, 2015, **6**, 7081-7096.
12. E. Mastan, X. Li and S. Zhu, *Progr. Polym. Sci.*, 2015, **45**, 71-101.
13. A. L. T. Brandao, J. B. P. Soares, J. C. Pinto and A. L. Alberton, *Macromol. React. Eng.*, 2015, **9**, 141-185.
14. P. Vana, T. P. Davis and C. Barner-Kowollik, *Macromol. Theory Simul.*, 2002, **11**, 823-835.
15. C. Kiparissides, P. Seferlis, G. Mourikas and A. J. Morris, *Ind. Eng. Chem. Res.*, 2002, **41**, 6120-6131.
16. M. L. Coote, M. D. Zammit and T. P. Davis, *Trends Polym. Sci.*, 1996, **4**, 189-196.
17. K. B. Kockler, A. P. Haehnel, T. Junkers and C. Barner-Kowollik, *Macromol. Rapid Commun.*, 2016, **37**, 123-134.
18. A. Aleksandrov, V. N. Genkin, M. Kitaĭ, I. Smirnova and V. Sokolov, *Sov. J. Quantum Electron.*, 1977, **7**, 547-550.
19. O. F. Olaj, I. Bitai and F. Hinkelmann, *Macromol. Chem. Phys.*, 1987, **188**, 1689-1702.
20. M. Buback, R. G. Gilbert, R. A. Hutchinson, B. Klumperman, F. D. Kuchta, B. G. Manders, K. F. O'Driscoll, G. T. Russell and J. Schweer, *Macromol. Chem. Phys.*, 1995, **196**, 3267-3280.

21. S. Beuermann, M. Buback, T. P. Davis, R. G. Gilbert, R. A. Hutchinson, O. F. Olaj, G. T. Russell, J. Schweer and A. M. van Herk, *Macromol. Chem. Phys.*, 1997, **198**, 1545-1560.
22. S. Beuermann, M. Buback, T. P. Davis, R. G. Gilbert, R. A. Hutchinson, A. Kajiwara, B. Klumperman and G. T. Russell, *Macromol. Chem. Phys.*, 2000, **201**, 1355-1364.
23. S. Beuermann, M. Buback, T. P. Davis, N. Garcia, R. G. Gilbert, R. A. Hutchinson, A. Kajiwara, M. Kamachi, I. Lacik and G. T. Russell, *Macromol. Chem. Phys.*, 2003, **204**, 1338-1350.
24. J. M. Asua, S. Beuermann, M. Buback, P. Castignolles, B. Charleux, R. G. Gilbert, R. A. Hutchinson, J. R. Leiza, A. N. Nikitin, J. P. Vairon and A. M. van Herk, *Macromol. Chem. Phys.*, 2004, **205**, 2151-2160.
25. S. Beuermann, M. Buback, P. Hesse, F. D. Kuchta, I. Lacik and A. M. Van Herk, *Pure and Applied Chemistry*, 2007, **79**, 1463-1469.
26. C. Barner-Kowollik, S. Beuermann, M. Buback, P. Castignolles, B. Charleux, M. L. Coote, R. A. Hutchinson, T. Junkers, I. Lacik, G. T. Russell, M. Stach and A. M. van Herk, *Polym. Chem.*, 2014, **5**, 204-212.
27. B. Dervaux, T. Junkers, M. Schneider-Baumann, F. E. Du Prez and C. Barner-Kowollik, *J. Polym. Sci. Pol. Chem.*, 2009, **47**, 6641-6654.
28. C. Barner-Kowollik, S. Beuermann, M. Buback, R. A. Hutchinson, T. Junkers, H. Kattner, B. Manders, A. N. Nikitin, G. T. Russell and A. M. van Herk, *Macromol. Chem. Phys.*, 2017, **218**, 1600357.
29. A. P. Haehnel, M. Schneider-Baumann, K. U. Hiltebrandt, A. M. Misske and C. Barner-Kowollik, *Macromolecules*, 2013, **46**, 15-28.
30. R. X. E. Willemse and A. M. van Herk, *Macromol. Chem. Phys.*, 2010, **211**, 539-545.
31. A. P. Haehnel, M. Schneider-Baumann, L. Arens, A. M. Misske, F. Fleischhaker and C. Barner-Kowollik, *Macromolecules*, 2014, **47**, 3483-3496.
32. K. B. Kockler, A. P. Haehnel, F. Fleischhaker, M. Schneider-Baumann, A. M. Misske and C. Barner-Kowollik, *Macromol. Chem. Phys.*, 2015, **216**, 1573-1582.
33. K. B. Kockler, F. Fleischhaker and C. Barner-Kowollik, *Polym. Chem.*, 2016, **7**, 4342-4351.
34. S. Harrisson, S. R. Mackenzie and D. M. Haddleton, *Macromolecules*, 2003, **36**, 5072-5075.
35. I. Woecht, G. Schmidt-Naake, S. Beuermann, M. Buback and N. Garcia, *J. Polym. Sci. Pol. Chem.*, 2008, **46**, 1460-1469.
36. A. P. Haehnel, B. Wenn, K. Kockler, T. Bantle, A. M. Misske, F. Fleischhaker, T. Junkers and C. Barner-Kowollik, *Macromol. Rapid Commun.*, 2014, **35**, 2029-2037.
37. M. Buback, *Macromol. Rapid Commun.*, 2015, **36**, 1979-1983.
38. A. P. Haehnel, B. Wenn, K. Kockler, T. Bantle, A. M. Misske, F. Fleischhaker, T. Junkers and C. Barner-Kowollik, *Macromol. Rapid Commun.*, 2015, **36**, 1984-1986.

39. L. Couvreur, G. Piteau, P. Castignolles, M. Tonge, B. Coutin, B. Charleux and J. P. Vairon, *Macromolecular Symposia*, 2001, **174**, 197-207.
40. S. Beuermann, *Macromol. Rapid Commun.*, 2009, **30**, 1066-1088.
41. A. M. van Herk, *Macromol. Rapid Commun.*, 2009, **30**, 1964-1968.
42. T. Junkers and C. Barner-Kowollik, *J. Polym. Sci. Pol. Chem.*, 2008, **46**, 7585-7605.
43. G. Arzamendi, C. Plessis, J. R. Leiza and J. M. Asua, *Macromol. Theory Simul.*, 2003, **12**, 315-324.
44. C. Plessis, G. Arzamendi, J. M. Alberdi, A. M. van Herk, J. R. Leiza and J. M. Asua, *Macromol. Rapid Commun.*, 2003, **24**, 173-177.
45. C. Plessis, G. Arzamendi, J. R. Leiza, H. A. S. Schoonbrood, D. Charmot and J. M. Asua, *Macromolecules*, 2000, **33**, 4-7.
46. T. Junkers, M. Schneider-Baumann, S. P. S. Koo, P. Castignolles and C. Barner-Kowollik, *Macromolecules*, 2010, **43**, 10427-10434.
47. Y. Reyes, G. Arzamendi, J. M. Asua and J. R. Leiza, *Macromolecules*, 2011, **44**, 3674-3679.
48. R. X. E. Willemse, A. M. van Herk, E. Panchenko, T. Junkers and M. Buback, *Macromolecules*, 2005, **38**, 5098-5103.
49. B. Wenn and T. Junkers, *Macromol. Rapid Commun.*, 2016, **37**, 781-787.
50. A. N. Nikitin, R. A. Hutchinson, M. Buback and P. Hesse, *Macromolecules*, 2007, **40**, 8631-8641.
51. F. Ganachaud, R. Balic, M. J. Monteiro and R. G. Gilbert, *Macromolecules*, 2000, **33**, 8589-8596.
52. B. De Sterck, R. Vaneerdeweg, F. Du Prez, M. Waroquier and V. Van Speybroeck, *Macromolecules*, 2010, **43**, 827-836.
53. M. Vachaudez, D. R. D'hooge, M. Socka, J. Libiszowski, O. Coulembier, M. F. Reyniers, A. Duda, G. B. Marin and P. Dubois, *React. Funct. Polym.*, 2013, **73**, 484-491.
54. H. Kattner and M. Buback, *Macromolecules*, 2015, **48**, 7410-7419.
55. C. Preusser, A. Chovancová, I. Lacík and R. A. Hutchinson, *Macromol. React. Eng.*, 2016.
56. N. F. G. Wittenberg, C. Preusser, H. Kattner, M. Stach, I. Lacik, R. A. Hutchinson and M. Buback, *Macromol. React. Eng.*, 2016, **10**, 95-107.
57. S. Santanakrishnan, L. Tang, R. A. Hutchinson, M. Stach, I. Lacik, J. Schrooten, P. Hesse and M. Buback, *Macromol. React. Eng.*, 2010, **4**, 499-509.
58. M. L. Coote, M. D. Zammit, T. P. Davis and G. D. Willett, *Macromolecules*, 1997, **30**, 8182-8190.
59. M. L. Coote, L. P. M. Johnston and T. P. Davis, *Macromolecules*, 1997, **30**, 8191-8204.
60. R. A. Hutchinson, J. H. McMinn, D. A. Paquet, S. Beuermann and C. Jackson, *Ind. Eng. Chem. Res.*, 1997, **36**, 1103-1113.

61. R. X. E. Willemse and A. M. van Herk, *J. Am. Chem. Soc.*, 2006, **128**, 4471-4480.
62. T. R. Rooney, E. Mavroudakis, I. Lacik, R. A. Hutchinson and D. Moscatelli, *Polym. Chem.*, 2015, **6**, 1594-1603.
63. R. Ferrari, T. R. Rooney, M. Lupi, P. Ubezio, R. A. Hutchinson and D. Moscatelli, *Macromol. Biosci.*, 2013, **13**, 1347-1357.
64. E. Mavroudakis, K. Liang, D. Moscatelli and R. A. Hutchinson, *Macromol. Chem. Phys.*, 2012, **213**, 1706-1716.
65. R. A. Cockburn, R. Siegmann, K. A. Payne, S. Beuermann, T. F. L. McKenna and R. A. Hutchinson, *Biomacromolecules*, 2011, **12**, 2319-2326.
66. A. N. Nikitin, P. Castignolles, B. Charleux and J. P. Vairon, *Macromol. Rapid Commun.*, 2003, **24**, 778-782.
67. J. Barth, M. Buback, P. Hesse and T. Sergeeva, *Macromolecules*, 2010, **43**, 4023-4031.
68. Y. W. Marien, P. H. M. Van Steenberge, K. B. Kockler, C. Barner-Kowollik, M.-F. Reyniers, D. R. D'hooge and G. B. Marin, *Polym. Chem.*, 2016, **7**, 6521-6528.
69. A. N. Nikitin, R. A. Hutchinson, M. Buback and P. Hesse, *Macromol. Chem. Phys.*, 2011, **212**, 699-707.
70. P. Drawe and M. Buback, *Macromol. Theory Simul.*, 2016, **25**, 74-84.
71. N. Ballard, S. Hamzehlou, F. Ruipérez and J. M. Asua, *Macromol. Rapid Commun.*, 2016, **37**, 1364-1368.
72. D. A. Shipp, D. H. Solomon, T. A. Smith and G. Moad, *Macromolecules*, 2003, **36**, 2032-2040.
73. A. Kornherr, G. Zifferer and O. F. Olaj, *Macromol. Theory Simul.*, 1999, **8**, 260-271.
74. A. V. Evseev and A. N. Nikitin, *Laser Chem.*, 1995, **16**, 83-99.
75. A. N. Nikitin, P. Castignolles, B. Charleux and J. P. Vairon, *Macromol. Theory Simul.*, 2003, **12**, 440-448.
76. O. F. Olaj, A. Kornherr and G. Zifferer, *Macromol. Theory Simul.*, 1997, **6**, 655-666.
77. O. F. Olaj, A. Kornherr and G. Zifferer, *Macromol. Theory Simul.*, 1998, **7**, 501-508.
78. K. D. Hungenberg, K. Knoll and M. Wulkow, *Macromol. Theory Simul.*, 1997, **6**, 393-426.
79. M. Buback, M. Busch and R. A. Lammel, *Macromol. Theory Simul.*, 1996, **5**, 845-861.
80. J. P. He, H. D. Zhang and Y. L. Yang, *Macromol. Theory Simul.*, 1995, **4**, 811-819.
81. K. F. O'Driscoll and M. E. Kuindersma, *Macromol. Theory Simul.*, 1994, **3**, 469-478.
82. J. M. Lu, H. D. Zhang and Y. L. Yang, *Makromolekulare Chemie-Theory and Simulations*, 1993, **2**, 747-760.
83. H. J. Liang, W. Jiang and X. H. He, *European Polymer Journal*, 2000, **36**, 2527-2530.
84. B. G. Manders, A. M. Vanherk and A. L. German, *Macromol. Theory Simul.*, 1995, **4**, 325-333.
85. C. Barner-Kowollik, F. Gunzler and T. Junkers, *Macromolecules*, 2008, **41**, 8971-8973.
86. M. Buback, M. Busch and C. Kowollik, *Macromol. Theory Simul.*, 2000, **9**, 442-452.

87. A. N. Nikitin, R. A. Hutchinson, W. Wang, G. A. Kalfas, J. R. Richards and C. Bruni, *Macromol. Reac. Eng.*, 2010, **4**, 691-706.
88. S. Maeder and R. G. Gilbert, *Macromolecules*, 1998, **31**, 4410-4418.
89. J. P. A. Heuts and G. T. Russell, *European Polymer Journal*, 2006, **42**, 3-20.
90. P. Derboven, D. R. D'hooge, M.-F. Reyniers, G. B. Marin and C. Barner-Kowollik, *Macromolecules*, 2015, **48**, 492-501.
91. S. Hamzehlou, N. Ballard, Y. Reyes, A. Aguirre, J. M. Asua and J. R. Leiza, *Polym. Chem.*, 2016.
92. D. T. Gillespie, *Abstr. Pap. Am. Chem. Soc.*, 1977, **173**, 128-128.
93. P. H. M. Van Steenberge, D. R. D'hooge, M. F. Reyniers and G. B. Marin, *Chem. Eng. Sci.*, 2014, **110**, 185-199.
94. S. K. Fierens, D. R. D'hooge, P. H. M. Van Steenberge, M. F. Reyniers and G. B. Marin, *Chem. Eng. J.*, 2015, **278**, 407-420.
95. H. Y. Gao, L. H. Oakley, I. A. Konstantinov, S. G. Arturo and L. J. Broadbelt, *Ind. Eng. Chem. Res.*, 2015, **54**, 11975-11985.
96. M. Drache, B. Hosemann, T. Laba and S. Beuermann, *Macromol. Theory Simul.*, 2015, **24**, 301-310.
97. A. K. Tripathi, J. G. Tsavalas and D. C. Sundberg, *Macromolecules*, 2015, **48**, 184-197.
98. W. Wang, A. N. Nikitin and R. A. Hutchinson, *Macromol. Rapid Commun.*, 2009, **30**, 2022-2027.
99. T. Junkers and C. Barner-Kowollik, *Macromol. Theory Simul.*, 2009, **18**, 421-433.
100. R. W. Ricci, M. A. Ditzler and L. P. Nestor, *J. Chem. Educ.*, 1994, **71**, 983-985.
101. G. Odian, *Principles of Polymerization*, Wiley, 2004.
102. P. Castignolles, A. N. Nikitin, L. Couvreur, G. Mouraret, B. Charleux and J. P. Vairon, *Macromol. Chem. Phys.*, 2006, **207**, 81-89.
103. H. Fischer, R. Baer, R. Hany, I. Verhoolen and M. Walbiner, *J. Chem. Soc.-Perkin Trans. 2*, 1990, 787-798.
104. C. Barner-Kowollik, P. Vana and T. P. Davis, *J. Polym. Sci. Pol. Chem.*, 2002, **40**, 675-681.
105. Z. Szablan, T. M. Lovestead, T. P. Davis, M. H. Stenzel and C. Barner-Kowollik, *Macromolecules*, 2007, **40**, 26-39.
106. Z. Szablan, T. Junkers, S. P. S. Koo, T. M. Lovestead, T. P. Davis, M. H. Stenzel and C. Barner-Kowollik, *Macromolecules*, 2007, **40**, 6820-6833.
107. C. Barner-Kowollik, T. P. Davis and M. H. Stenzel, *Polymer*, 2004, **45**, 7791-7805.
108. O. Monyatsi, A. N. Nikitin and R. A. Hutchinson, *Macromolecules*, 2014, **47**, 8145-8153.
109. P. H. M. Van Steenberge, D. R. D'Hooge, M. F. Reyniers, G. B. Marin and M. F. Cunningham, *Macromolecules*, 2014, **47**, 7732-7741.

110. J. Barth, M. Buback, P. Hesse and T. Sergeeva, *Macromol. Rapid Commun.*, 2009, **30**, 1969-1974.
111. C. Farcet, J. Belleney, B. Charleux and R. Pirri, *Macromolecules*, 2002, **35**, 4912-4918.
112. P. Derboven, P. H. M. Van Steenberge, J. Vandenbergh, M. F. Reyniers, T. Junkers, D. R. D'hooge and G. B. Marin, *Macromol. Rapid Commun.*, 2015, **36**, 2149-2155.
113. N. Ballard, S. Hamzehlou and J. M. Asua, *Macromolecules*, 2016, **49**, 5418-5426.
114. Y. Nakamura, R. Lee, M. L. Coote and S. Yamago, *Macromol. Rapid Commun.*, 2016, **37**, 506–513.
115. G. B. Smith, G. T. Russell and J. P. A. Heuts, *Macromol. Theory Simul.*, 2003, **12**, 299-314.
116. G. Johnston-Hall and M. J. Monteiro, *J. Polym. Sci. Pol. Chem.*, 2008, **46**, 3155-3173.
117. J. B. L. de Kock, B. Klumperman, A. M. van herk and A. L. German, *Macromolecules*, 1997, **30**, 6743-6753.
118. O. F. Olaj, G. Zifferer and G. Gleixner, *Macromolecules*, 1987, **20**, 839-850.
119. O. F. Olaj, G. Zifferer and G. Gleixner, *Macromol. Chem. Phys.*, 1986, **187**, 977-994.
120. H. K. Mahabadi, *Macromolecules*, 1985, **18**, 1319-1324.
121. A. N. Nikitin, *Macromol. Theory Simul.*, 1996, **5**, 957-967.
122. B. B. Noble, A. C. Mater, L. M. Smith and M. L. Coote, *Polym. Chem.*, 2016, **7**, 6400-6412.
123. M. Busch and A. Wahl, *Macromol. Theory Simul.*, 1998, **7**, 217-224.
124. L. De Keer, P. H. M. Van Steenberge, M.-F. Reyniers, K. D. Hungenberg, L. Seda, D. R. D'hooge and G. B. Marin, *AIChE J.*, 2017, 63, 2043-2059.

Chapter 3: Estimating the photodissociation quantum yield from PLP-SEC peak heights

Summary

A fast method for the reliable estimation of the photodissociation quantum yield Φ_{diss} is presented. Pulsed laser polymerization (PLP) experiments are performed at various pulse energies (1.5 – 6 mJ) and regression analysis is performed to the ratio of the peak heights identified in the size exclusion chromatography (SEC) trace. The high accuracy of the method is demonstrated for PLP initiated by 2,2-dimethoxy-2-phenylacetophenone (DMPA), considering *in silico* generated data including large theoretical errors (up to 20%). The method has also been successfully applied to experimental data of DMPA based isothermal PLP of *n*-butyl acrylate at 306 K, with an estimated Φ_{diss} of 0.42 ± 0.04. In the long term, the method will facilitate the evaluation of current and the design of new highly efficient photoinitiators.

3.1 Introduction

Pulsed laser polymerization (PLP) is currently seen as the preferred method to determine the propagation rate coefficient k_p in radical polymerization.[1, 2] Upon irradiation with a frequency ν, initiator radical fragments (R_0) are generated upon the dissociation of a photoinitiator, which is typically 2,2-dimethoxy-2-phenylacetophenone (DMPA). These R_0 species add to monomer (M) until they are transformed into dead polymer species, typically via termination. Characteristic points of the resulting PLP - size exclusion chromatogram (SEC) trace are inflection points at chain lengths L_j (j = 1, 2, …). Under well-defined PLP conditions with a negligible monomer conversion, the inflection points can be directly linked to k_p:[3, 4]

$$k_p = L_j [M]_0^{-1} (j\Delta t)^{-1} \quad (1)$$

in which $[M]_0$ and Δt are the initial monomer concentration and the dark time between pulses, the latter equal to the reciprocal of ν.

More recently, PLP experiments have also been conducted to determine other rate coefficients than k_p. For example, the backbiting rate coefficient, k_{bb}, in acrylate radical polymerization has been measured, considering nuclear magnetic resonance (NMR) data on the branching amounts[5] and PLP inflection point data at various ν.[6-8] In addition, an accurate description of the complete PLP-size exclusion chromatography (SEC) trace has been targeted, as it contains information on all kinetically relevant reactions.[9-11] Very recently Marien *et al.*[9] demonstrated that the disparate chain initiation reactivities of the DMPA fragments strongly affect the heights of the PLP peaks. These authors demonstrated that the existence of a non-initiating DMPA fragment is essential to ensure the multimodality required for the identification of consecutive inflection points in the SEC trace, in agreement with earlier modeling efforts of Kowollik *et al.*[12] for single pulse PLP.

A crucial input parameter for the detailed kinetic description of PLP is the concentration of the R_0 species generated at each laser pulse ($\Delta[R_0]$), which upon consideration of the Bouguer-Lambert-Beer law can be calculated from:[9, 13, 14]

$$\Delta[R_0] = 2\Phi_{\text{diss}} \frac{E_{\text{pulse}}\lambda}{hcN_{\text{A}}V}[1 - \exp(-2.303\varepsilon[I_2]L)] \quad (2)$$

in which Φ_{diss} is the photodissociation quantum yield, E_{pulse} the energy of a laser pulse, λ the laser wavelength, c the speed of light, h the Planck constant, N_{A} the Avogadro constant, V the volume of the sample, ε the molar absorptivity of the photoinitiator, L the optical path length, and $[I_2]$ the photoinitiator concentration at the considered reaction time.

The photodissociation quantum yield Φ_{diss} takes into account that only a fraction of the photoinitiator molecules that are excited via photon absorption results in dissociation, as illustrated in Figure 1 displaying the energy level diagram for an acetophenone photoinitiator type. Photon absorption results in a transfer from the singlet ground state S_0 to a singlet excited state S_1. The created singlet excited state can undergo intersystem crossing (ISC) to a triplet

state T_2 and an internal conversion (IC) to a triplet state T_1. A further lowering of the excited energy of the molecule can occur via α-cleavage, leading to the generation of the desired benzoyl (I) and dimethoxy benzyl radical ($R_1 = R_2 = OCH_3$ in II) for DMPA. An excited singlet or triplet sate can however be converted back into a singlet ground state (red arrows), therefore leading to a Φ_{diss} smaller than 1.

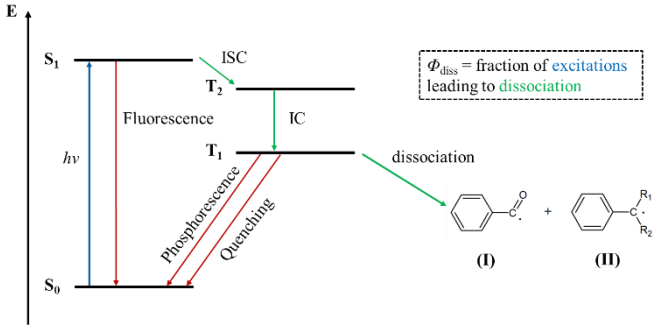

Figure 1. Energy level diagram for photodissociation of an acetophenone photoinitiator type;[15] ISC: intersystem crossing, IC: internal conversion; excitation to higher singlet states as well as vibrational and rotational energy levels not shown for clarity.

By using Equation (2) one assumes that the PLP photodissociation process is quasi-instantaneous. This assumption is valid in view of the relevant time scales, which have been investigated using time-resolved laser spectroscopy by Allonas *et al.*[16] for photodissociation of DMPA in benzene. Intersystem crossing from S_1 to T_1 has been observed to occur within 15 ps, *i.e.* the response time of the apparatus, and a triplet lifetime of 250 ps has been identified. Since the duration of the laser pulse is close to 5 ns, excitation of DMPA molecules takes place in a time interval much smaller than the time scale for chain initiation, which is *ca.* 0.7 µs for *n*-butyl acrylate (*n*BuA) monomer at 306 K.[17, 18]

It should be noted that the actual fraction of radicals leading to chain initiation is lower than $\Delta[R_0]$ as defined by Equation (2). Typically in kinetic studies a chemical initiator efficiency f is introduced to reflect this reduction in concentration with respect to an accurate description of the monomer addition rates. However, a more detailed modeling strategy involves the explicit consideration of all phenomena disturbing chain initiation.[9] For DMPA, this implies that in the kinetic model, as shown in Table S2 in Appendix B, the termination reactions for the DMPA

radical fragments are explicitly accounted for and only one fragment is allowed to initiate chain growth, with no other side reactions needed in case the laser duration is limited (as is typically the case in PLP) and the reaction temperature is kept sufficiently low (*e.g.* 306 K).[9, 12]

Despite the importance of a correct calculation, in most PLP kinetic modeling studies, $\Delta[R_0]$ is given a typical, yet arbitrary value or even seen as an adjustable parameter. Such a formal model strategy unfortunately does not explicitly take into account that $\Delta[R_0]$ is related to E_{pulse} and $[I_2]$, which makes a consistent kinetic analysis for varying reaction conditions challenging. The popularity of the formal modeling approach can be explained by the difficulties encountered during the Φ_{diss} measurement.[19, 20] Although the method of Allonas *et al.*[19] - which uses a combination of *ab initio* calculated bond dissociation energies and experimental calorimetric data to assess Φ_{diss} - provides certain insights, quantitative information on Φ_{diss} remains limited, hampering the use of Equation (2) to reliably determine $\Delta[R_0]$ and to accurately describe PLP-SEC traces. It should be noted that the experimental determination of k_p via Equation (1) does not require knowledge of Φ_{diss}. Such knowledge is on the other hand required *e.g.* for the *in silico* determination of an E_{pulse} and an $[I_2]_0$ that give rise to a multimodal PLP-SEC trace possessing at least two inflection points fulfilling the consistency check $L_2 \approx 2L_1$.

In the present work, a reliable and fast method is presented to reliably estimate Φ_{diss}. Regression analysis is performed based on the PLP-SEC peak heights, considering E_{pulse} as the independent variable. The method is applied under well-chosen PLP conditions, including a low temperature and high frequency to avoid side reactions (*e.g.* chain transfer to monomer). For illustration purposes, DMPA is considered as photoinitiator and *n*BuA as monomer in view of its extensively studied radical polymerization kinetics.[8, 17, 21, 22]

3.2 Experimental section

3.2.1 Materials

n-Butyl acrylate (*n*BuA) was provided by BASF and freed from inhibitor via distillation. 2,2-Dimethoxy-2-phenylacetophenone (DMPA) was obtained from VWR International and used as received.

3.2.2 PLP experiments

0.2 mL solutions of *n*BuA containing 3 mmol L^{-1} DMPA were transferred into sample vials (optical path length L = 0.52 cm). These vials were placed into a stainless steel sample holder that was brought to 306 K employing a VWR 1196D thermostat. The reaction temperature measured at the sample did not exceed a deviation larger than 0.1 K. As low monomer conversions (≤ 0.03) were recorded it can thus be expected that isothermicity is obtained at least to a first approximation,[23] also taking into account the low initial temperature (306 K) and the small sample volume (0.2 mL).

An overview of all the conditions is provided in Table S1 in Appendix B. Photopolymerization was initiated by laser pulsing (ν = 500 s^{-1}) with a Xantos XS-500 system operated at the XeF line (λ = 351 nm). The laser beam uniformly reached the sample from the bottom with an energy that was varied between 1.5 and 6 mJ. At the end of the polymerization, hydroquinone dissolved in THF was directly added to the samples. Via evaporation solvent and remaining monomer were subsequently removed. Two samples at identical conditions were always combined before SEC analysis to increase the detector reliability.

3.2.3 Characterization

Size exclusion chromatography (SEC) measurements were conducted on a PL-SEC 50 Plus Integrated System with an autosampler and a PL-gel 5 μm bead-size guard column (50 × 7.5 mm), followed by a PL-gel 5 μm mixed E column (300 × 7.5 mm), three PL-gel 5 μm mixed C

columns (300 × 7.5 mm), and a differential refractive index (RI) detector with THF as eluent, a flow rate of 1 mL min^{-1}, and an analysis temperature of 308 K. The GPC system was calibrated with linear polystyrene standards (4.8 10^2 to 2.5 10^6 g mol^{-1}) and linear poly(methyl methacrylate) standards (8.0 10^2 to 1.6 10^6 g mol^{-1}). To obtain the absolute poly(*n*BuA) molar masses polymer specific Mark-Houwink-Kuhn-Sakurada (MHKS) parameters were used.[17]

3.3 Simulation section

3.3.1 Modeling technique

To simulate the SEC trace for low temperature PLP with *n*BuA and thus to identify the corresponding peak heights, kinetic Monte Carlo (*k*MC) modeling is performed. In agreement with work of Marien *et al.*[6, 9] and as discussed in Appendix B, for low temperature PLP, a basic model consisting of photodissociation, chain initiation, propagation, backbiting, and chain length dependent termination can accurately predict the ratio of PLP-SEC peak heights. Hence, side reactions such as chain transfer to monomer and β-scission do not need to be considered. The concentration of radicals generated at each pulse is calculated via Equation (2). The decrease of the photoinitiator concentration as a function of time is thus explicitly accounted for.

The *k*MC solution strategy in general is based on previous modeling efforts on the stochastic description of radical polymerization processes.[24-26] For the actual estimation, all model parameters except Φ_{diss} are taken from literature and provided in Appendix B (Table S2). In particular, in Appendix B, attention is focused on the relevance of the correct (apparent) chain length dependent termination reactivities. SEC broadening is accounted for as discussed in previous work,[27] with the SEC broadening parameter equal to 0.05, in agreement with typical values reported in literature.[8, 9, 28]

3.3.2 Regression analysis procedure

In the present work, the following objective function S is considered for the regression analysis:

$$S = \sum_{i=1}^{N} (y_i - \hat{y}_i)^2 \tag{3}$$

in which y_i corresponds to the measured ratio of the first two PLP-SEC peak heights of the i^{th} experiment (N experiments in total) and $\hat{y}_i$ to the corresponding model predicted value. This regression analysis is performed using the Levenberg-Marquardt algorithm (ODRPACK v2.01). All independent variables are assumed to be error-free. In addition to the 95% confidence interval, the F value for the global significance of the regression is calculated, which needs to be sufficiently higher than the corresponding tabulated value (F_{tab}). For more details on the estimation procedure as such, the reader is referred to previous work.[29-31]

3.4 Results and discussion

3.4.1 Model development and theoretical evaluation

In agreement with previous simulation results,[9, 28] the peak heights of a PLP-SEC trace are highly sensitive to $\Delta[R_0]$ and thus to E_{pulse} (Equation (2)). This is demonstrated in Figure 2 in which for various pulse energies the log-molar mass distribution (log-MMD) is shown as simulated for a theoretical Φ_{diss} of 0.5 and all other model parameters as in Table S2 in Appendix B (3th column; values equal to orders of magnitude). For a higher $\Delta[R_0]$, the height of the first peak (h_1 in Figure 2) increases and the height of the second peak (h_2 in Figure 2) decreases, *i.e.* h_1/h_2 increases.

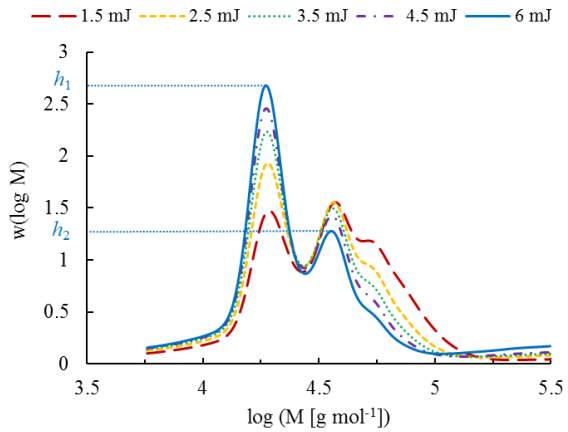

Figure 2. Simulated PLP-SEC traces at various pulse energies and a theoretical Φ_{diss} of 0.5; other model parameters as specified in Table S2 in Appendix B (column 3; values equal to orders of magnitude); ν = 500 s^{-1}, number of pulses *cf.* Table S1 (Appendix B), $[DMPA]_0$ = 5 10^{-3} mol L^{-1}, $[M]_0$ = 7 mol L^{-1}.

This trend for the ratio of the peak heights in Figure 2 can be explained by the larger increase in the termination rate compared to the propagation rate as a result of the corresponding differences in the reaction orders (propagation: first order in the radical concentration; termination: second order) and the strong chain length dependence of the (apparent) termination reactivity with a higher reactivity for shorter chains.[32] An increase of E_{pulse} promotes termination and suppresses the formation of longer chains, resulting in a larger h_1/h_2. Hence, it can be expected that Φ_{diss} can be estimated based on experimental h_1/h_2 data and a reliable PLP kinetic model, explicitly considering Equation (2). This can be theoretically demonstrated by performing regression analysis to simulated h_1/h_2 data, as obtained with a *k*MC model with given input parameters that are deliberately superimposed with random Gaussian error.[6]

For example Figure 3 shows such regression results, considering DMPA as photoinitiator and all model parameter values equal to orders of magnitude with in particular an input value of 0.5 for Φ_{diss}. In a first test case (left), a Gaussian error with a standard deviation (σ) of 0.06 is selected, corresponding to an experimental error (2σ) of *ca.* 10%. In a second test case (right), a σ of 0.12 is selected reflecting a large experimental error of ca. 20%. For both test cases, an excellent fit is obtained, as evidenced by the full green lines in Figure 3 (left and right). The corresponding estimates for Φ_{diss} are respectively 0.520 ± 0.065 and 0.523 ± 0.116 (95%

confidence intervals). These are both very close to the implemented and thus to be estimated value of Φ_{diss}, highlighting the accuracy of the proposed method. Even for the very large (theoretical) experimental error of 20%, an accurate estimate is obtained, indicating the method is robust toward experimental outliers. Similar conclusions can be made based on *in silico* testing with methyl methacrylate (MMA), as shown in Appendix B.

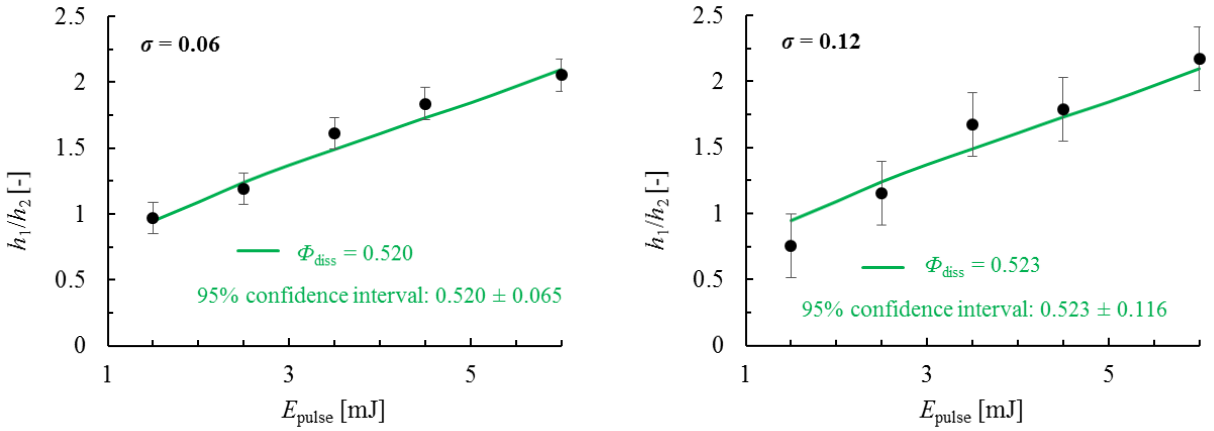

Figure 3. *In silico* validation of the proposed method for the estimation of Φ_{diss} from h_1/h_2 data; symbols: data generated using a *k*MC model with an input value of 0.5 for Φ_{diss} and all other model parameters as in Table S2 in Appendix B (column 3; values: orders of magnitude; *cf.* Figure 2), superimposed with a random error (Gaussian sampling with standard deviation σ = 0.06 (left) and σ = 0.12 (right)); full line: model after regression analysis; conditions: caption Figure 2; model parameters: Table S2 in Appendix B.

3.4.2 Application to DMPA based PLP of nBuA

In the previous section, the high accuracy and robustness of the developed method has been theoretically illustrated for two monomer types. In what follows, the strength of the method is further demonstrated by applying it to experimental data for DMPA based PLP of *n*BuA for various E_{pulse} values. An overview of the experimental conditions covered is given in Table S1 in Appendix B. The model parameters of the PLP kinetic model are provided in Table S2 (column 4) in Appendix B and are all taken from literature.

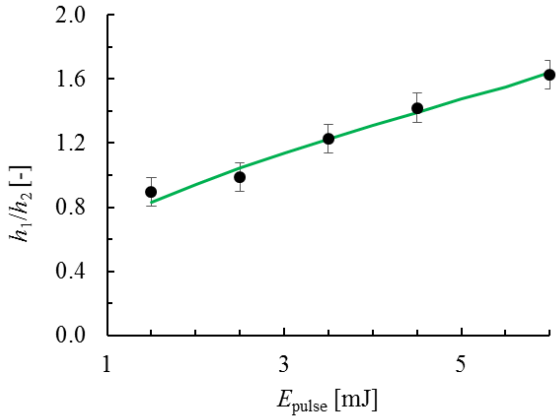

Figure 4. Application of the proposed method to DMPA based PLP of *n*BuA; symbols: experimentally measured ratio of PLP-SEC peak heights (Table S1 in Appendix B); error bars determined from duplicate experiments; full line: fit with $\Phi_{diss} = 0.42$ (95% confidence interval: 0.42 ± 0.04; $F = 3816 >> F_{tab} = 8$); conditions: Table S1 (Appendix B); model parameters: Table S2 (Appendix B).

For the experimental PLP system, regression analysis yields a parameter estimate of 0.42 for Φ_{diss} with a narrow 95% confidence interval ($\Phi_{diss} = 0.42 \pm 0.04$) and an excellent fit to the experimental data, as shown in Figure 4. A significantly lower value is obtained compared to the work of Allonas *et al.*[19] ($\Phi_{diss} = 0.95$). On the other hand, taking into account the obtained confidence interval, a slightly lower value as reported by Müller and Vallejos[20] ($\Phi_{diss} = 0.52$) is obtained. It should however be stressed that both studies did not include a robustness check of their method or a detailed regression analysis.

The potential of the method has thus been demonstrated both theoretically and experimentally. It should be further noted that in case accurate monomer-specific model parameters are used and solvent effects can be ruled out, the obtained estimate for Φ_{diss} does not depend on the selected monomer. Hence, the correctness of the obtained estimate can always be verified by selecting another monomer for which benchmarked model parameters are available.

3.5 Conclusions

For the estimation of the photodissociation quantum yield Φ_{diss}, a simple and fast method using only the ratio of PLP-SEC peak heights has been presented. Based on regression analysis to *in silico* data the method has been shown to be very accurate and robust, even if rather large

theoretical experimental errors are considered. The method has also been successfully applied to experimental data of DMPA based PLP of *n*BuA.

On a longer term, the method allows the fast determination of Φ_{diss} for a wide range of photoinitiators, which is required for the evaluation of current and the design of new photoinitiators.

3.6 References

1. S. Beuermann and M. Buback, *Prog. Polym. Sci.*, 2002, **27**, 191-254.
2. K. B. Kockler, A. P. Haehnel, T. Junkers and C. Barner-Kowollik, *Macromol. Rapid Commun.*, 2016, **37**, 123-134.
3. A. Aleksandrov, V. N. Genkin, M. Kitaĭ, I. Smirnova and V. Sokolov, *Sov. J. Quantum Electron.*, 1977, **7**, 547-550.
4. O. F. Olaj, I. Bitai and F. Hinkelmann, *Macromol. Chem. Phys.*, 1987, **188**, 1689-1702.
5. C. Plessis, G. Arzamendi, J. M. Alberdi, A. M. van Herk, J. R. Leiza and J. M. Asua, *Macromol. Rapid Commun.*, 2003, **24**, 173-177.
6. Y. W. Marien, P. H. M. Van Steenberge, K. B. Kockler, C. Barner-Kowollik, M.-F. Reyniers, D. R. D'hooge and G. B. Marin, *Polym. Chem.*, 2016, **7**, 6521-6528.
7. B. Wenn and T. Junkers, *Macromol. Rapid Commun.*, 2016, **37**, 781-787.
8. A. N. Nikitin, R. A. Hutchinson, M. Buback and P. Hesse, *Macromolecules*, 2007, **40**, 8631-8641.
9. Y. W. Marien, P. H. M. Van Steenberge, C. Barner-Kowollik, M.-F. Reyniers, G. B. Marin and D. R. D'hooge, *Macromolecules*, 2017, **50**, 1371-1385.
10. N. Ballard, S. Hamzehlou, F. Ruipérez and J. M. Asua, *Macromol. Rapid Commun.*, 2016, **37**, 1364-1368.
11. D. A. Shipp, D. H. Solomon, T. A. Smith and G. Moad, *Macromolecules*, 2003, **36**, 2032-2040.
12. M. Buback, M. Busch and C. Kowollik, *Macromol. Theory Simul.*, 2000, **9**, 442-452.
13. G. Odian, *Principles of Polymerization*, Wiley, 2004.
14. P. Castignolles, A. N. Nikitin, L. Couvreur, G. Mouraret, B. Charleux and J. P. Vairon, *Macromol. Chem. Phys.*, 2006, **207**, 81-89.
15. B. B. Noble, A. C. Mater, L. M. Smith and M. L. Coote, *Polym. Chem.*, 2016, **7**, 6400-6412.
16. X. Allonas, J. Lalevee, F. Morlet-Savary and J. P. Fouassier, *Polimery*, 2006, **51**, 491-498.

17. J. M. Asua, S. Beuermann, M. Buback, P. Castignolles, B. Charleux, R. G. Gilbert, R. A. Hutchinson, J. R. Leiza, A. N. Nikitin, J. P. Vairon and A. M. van Herk, *Macromol. Chem. Phys.*, 2004, **205**, 2151-2160.
18. J. J. Haven, J. Vandenbergh, R. Kurita, J. Gruber and T. Junkers, *Polym. Chem.*, 2015, **6**, 5752-5765.
19. X. Allonas, J. Lalevee and J. P. Fouassier, *Journal of Photochemistry and Photobiology a-Chemistry*, 2003, **159**, 127-133.
20. U. Muller and C. Vallejos, *Angew. Makromol. Chem.*, 1993, **206**, 171-191.
21. S. Maeder and R. G. Gilbert, *Macromolecules*, 1998, **31**, 4410-4418.
22. J. Barth, M. Buback, P. Hesse and T. Sergeeva, *Macromolecules*, 2010, **43**, 4023-4031.
23. A. N. Nikitin, I. Lacík and R. A. Hutchinson, *Macromolecules*, 2016, **49**, 9320-9335.
24. P. H. M. Van Steenberge, D. R. D'hooge, Y. Wang, M. Zhong, M.-F. Reyniers, D. Konkolewicz, K. Matyjaszewski and G. B. Marin, *Macromolecules*, 2012, **45**, 8519-8531.
25. P. H. M. Van Steenberge, D. R. D'hooge, M. F. Reyniers and G. B. Marin, *Chem. Eng. Sci.*, 2014, **110**, 185-199.
26. P. H. M. Van Steenberge, J. Vandenbergh, D. R. D'hooge, M. F. Reyniers, P. J. Adriaensens, L. Lutsen, D. J. M. Vanderzande and G. B. Marin, *Macromolecules*, 2011, **44**, 8716-8726.
27. M. Buback, M. Busch and R. A. Lammel, *Macromol. Theory Simul.*, 1996, **5**, 845-861.
28. P. Drawe and M. Buback, *Macromol. Theory Simul.*, 2016, **25**, 74-84.
29. T. De Roo, J. Wieme, G. J. Heynderickx and G. B. Marin, *Polymer*, 2005, **46**, 8340-8354.
30. C. Toloza Porras, D. R. D'hooge, P. H. M. Van Steenberge, M. F. Reyniers and G. B. Marin, *Ind. Eng. Chem. Res.*, 2014, **53**, 9674-9685.
31. S. K. Fierens, D. R. D'hooge, P. H. M. Van Steenberge, M. F. Reyniers and G. B. Marin, *Chem. Eng. J.*, 2015, **278**, 407-420.
32. C. Barner-Kowollik and G. T. Russell, *Prog. Polym. Sci.*, 2009, **34**, 1211-1259.

Chapter 4: Estimating the backbiting rate coefficient from low temperature PLP experiments

Summary

Based on a pulsed laser polymerization – size exclusion chromatography (PLP-SEC) analysis, an alternative method to estimate the bulk backbiting rate coefficient k_{bb} in acrylate radical polymerization is presented. For different solvent volume fractions (0-0.75), using the saturated analogue of the monomer as solvent to rule out solvent effects, regression analysis is applied to inflection point data in the low frequency range (< *ca.* 100 s^{-1}) only, which can be scanned with less expensive PLP equipment. Variation of the solvent volume fraction allows to independently alter the average mid-chain radical life time and to improve the sensitivity of the method to estimate k_{bb} confidently. The robustness of the method is verified considering *in silico* generated data including large artificial errors. The method is applied to experimental data of 2,2-dimethoxy-2-phenylacetophenone (DMPA) initiated PLP of *n*-butyl acrylate, taking butyl propionate as the solvent. A k_{bb} value of 171 ± 21 s^{-1} (303 K) is found, in good agreement with literature data. The method presents a generic approach for the estimation of k_{bb} for other acrylate monomers, allows a complete statistical analysis, and can be used as a complementary tool to existing methods. On a longer term, the method can even be extended for the simultaneous estimation of the bulk k_{bb} and mid-chain radical propagation rate coefficient $k_{p,m}$.

4.1 Introduction

One of the most prominent reactions in chain-growth polymerization is propagation, as it is the main contributor to the final chain length of each macrospecies. For radical polymerization, which contributes significantly to the production of macromolecular materials via a chain-growth mechanism, pulsed laser polymerization (PLP) has evolved as the preferred experimental technique to measure the intrinsic propagation rate coefficient k_p.[1, 2] Accurate k_p

values for a broad temperature range are essential for an optimal polymer product design and a reliable polymerization reactor control, in view of the high amount of heat generated during monomer incorporation. The latter is particularly relevant upon the establishment of the so-called Trommsdorff or gel-effect, leading to a strong increase in polymerization rate due to unavoidable diffusional limitations on termination.[3-6]

Depending on the nature of the monomer and the reaction medium a direct or more dedicated PLP analysis can be required.[7, 8] For bulk and solution radical polymerizations with one dominant macroradical type, k_p can be reliably obtained by generating multiple photoinitiated radical pulses with a frequency ν (or dark time $\Delta t = \nu^{-1}$) so that in the corresponding size exclusion chromatography (SEC) trace - after a limited monomer conversion (< 5 mol%) - repetitive inflection points L_j (j = 1, 2, …) can be identified that are directly linked to k_p:

$$L_j = k_p[M]_0(j\Delta t) \quad (1)$$

in which $[M]_0$ is the initial monomer concentration. On the other hand, for polymerizations with several dominant macroradical types, it has been postulated that Equation (1) needs to be modified to:[9-12]

$$L_j = k_{p,app}[M]_0(j\Delta t) \quad (2)$$

in which $k_{p,app}$ is an apparent rate coefficient reflecting the mixed propagation behavior of the different macroradical types. For example, in acrylate PLP in general secondary end-chain radicals (ECRs) and tertiary mid-chain radicals (MCRs) are present (Scheme 1), leading to a SEC trace with at least one inflection point L_1 controlled by the extent of chain growth between pulses as defined by Equation (2).[13-15] At very high frequencies, however, the radical population is restricted to ECRs so that Equation (2) can be directly applied to determine the ECR

propagation reactivity ($k_{p,app} = k_{p,e}$). In a next step, the MCR reactivity ($k_{p,m}$) can be assessed from the $k_{p,app}$ values at the lower frequencies.[11, 12]

Currently, the PLP technique has been successfully applied to obtain mostly bulk $k_{p,e}$ values for a wide range of commercially relevant monomers and to study the impact of the chemical structure on the propagation reactivity.[16-24] Many focus has been on (meth)acrylate monomers. For instance, in a IUPAC benchmark paper[18] based on earlier data[25-27] it has been reported that in bulk for linear alkyl methacrylates, k_p increases for longer ester side chains. The observation has been underpinned by additional data provided by Haehnel *et al.*[28] and a PLP - matrix assisted laser desorption ionization - time of flight - mass spectroscopy study of Willemse *et al.*[29] This later trend has also been observed for linear alkyl acrylates.[2, 30] It has been further indicated that the bulk k_p values of branched alkyl methacrylates can be described by a joint Arrhenius fit.[30] In contrast, this family type behavior was not detected for branched alkyl acrylates. Based on literature data provided,[27, 31, 32] the IUPAC group[19] reported a family type behavior also for the bulk k_p of methacrylates with cyclic ester side chains; an observation also supported by recent additional data.[33, 34]

Attention has also been focused on the existence of a solvent effect on k_p. For non-conventional solvents such as ionic liquids a very strong solvent effect has been measured.[35-37] In contrast, for the more common organic solvents the situation is less clear. Barner-Kowollik, Junkers and colleagues[38] reported that only a weak solvent effect is present for linear alkyl acrylates, selecting toluene and butyl acetate as solvents. Their claim, which is in agreement with the earlier contribution of Beuermann,[37] is based on the observation that the deviations between solution and bulk k_p values are generally within the expected experimental error of the PLP technique. Later on, Buback[39] pointed out that an opposite trend exists for k_p with increasing size of the ester side chain in bulk (increasing k_p values) and toluene (decreasing k_p values), questioning the formulated claim of a weak solvent effect for common organic solvents. In a

reply, Barner-Kowollik, Junkers and colleagues[40] emphasized that Buback[39] is only focusing on a small part of the investigated dataset. These authors put forward that globally an increasing trend for k_p with increasing size of the ester side chain remains the expectation both in bulk and solution and therefore the impact of the solvent on k_p can assumed to be limited for common organic solvents.

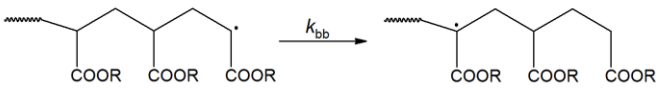

Scheme 1. Backbiting leading to a transformation of the radical nature from secondary (end-chain radical; ECR) to tertiary (mid-chain radical; MCR) in acrylate radical polymerization; dominant path via six-membered transition state.

In addition to the determination of k_p, the PLP technique has also been applied for the measurement of other important intrinsic rate coefficients. In particular, the backbiting rate coefficient k_{bb} for acrylate radical polymerization, which reflects the tendency of ECRs to switch to MCRs (Scheme 1), has been extensively measured. Since propagation of MCRs is slower than propagation of ECRs, backbiting can result in a pronounced rate retardation besides the formation of short chain branches (SCBs), making k_{bb} a key kinetic parameter in the model-based design of acrylate synthesis procedures.

Several PLP-based methods are available to determine k_{bb} in acrylate radical polymerization. These methods all allow to achieve isothermicity, favoring them over the traditional method of multiresponse regression analysis[41-43] of acrylate polymerization data on monomer conversion, average molar masses, and/or branching density. In batch operation mode, these data are typically recorded under strongly non-isothermal conditions. By considering a shift to a semibatch operation mode this non-isothermicity can be partially avoided.[41] Very recently Hamzehlou *et al.*[44] explicitly accounted for this non-isothermicity in their regression analysis, using bulk and solution batch free radical *n*-butyl acrylate (*n*BuA) polymerization data. Although more activated reactivities have been obtained compared to a series of isothermal

PLP studies, this study highlights the importance of dedicated kinetic analysis to obtain more reliable acrylate specific kinetic parameters. It should be stressed that such carefully determined kinetic parameters are indispensable to enable a quantitative understanding of the relation between the reaction conditions and the final polymer properties.[44, 45]

Under the isothermal PLP conditions one of the first methods to obtain k_{bb} was developed by Plessis *et al.*[46] who measured the amount of SCBs in bulk and solution PLP of *n*BuA via ^{13}C nuclear magnetic resonance (NMR) analysis. By applying the pseudo-steady state assumption (PSSA) for the calculation of the MCR concentration and subsequent regression analysis, these authors determined k_{bb}, although a qualitative ^{13}C NMR analysis is known to be difficult.[47] On the other hand, k_{bb} has also been determined by fitting the concentration traces of ECRs and MCRs as measured by electron spin resonance (ESR) spectroscopy after applying a single laser pulse, which is also known as single pulse-PLP (SP-PLP).[48] However, a reliable ESR analysis is often cost-intensive as it requires complex calibration procedures.[48, 49]

Furthermore, Nikitin *et al.*[11] determined the k_{bb} Arrhenius parameters by conducting at different temperatures so-called frequency tuned PLP-SEC experiments, which yield S-shaped $k_{p,app}$ curves as a function of the frequency. From the specific frequency ν_0 corresponding to the sharp decrease of $k_{p,app}$ with decreasing ν, these authors proposed to obtain k_{bb} via the semi-empirical relationship:[11]

$$\nu_0 = \alpha\, k_{bb} \tag{3}$$

in which α is an *in silico* based proportionality coefficient, and ν_0 the frequency at which a shift from two inflection points to one could be identified in the PLP-SEC traces when going from high to low frequency. The first inflection point, which is also appearing at the lowest frequencies, is associated with the mixed propagation behavior of ECRs and MCRs (Equation (2)), whereas the second one is related to the propagation of ECRs which did not backbite before

undergoing termination at a next pulse (Equation (2) with $k_{p,app} = k_{p,e}$). Nikitin *et al.*[11] further indicated that based on the obtained k_{bb} (Equation (3)) and the reliable measurement of $k_{p,e}$ at high frequencies, in a next step, $k_{p,m}$ can be obtained at very low frequencies, using the following relation:

$$k_{p,app} = k_{p,e} - \frac{k_{p,e} - k_{p,m}}{1 + \frac{k_{p,m}[M]_0}{k_{bb}}} \quad (4)$$

in which the PSSA is assumed for the calculation of the MCRs,[9, 11, 12] termination reactions are neglected and it is assumed that $k_{p,app}$ can be considered frequency independent and equal to the average propagation reactivity as defined based on the overall polymerization rate.

It should although be stressed that a reliable determination of k_{bb} and $k_{p,m}$ via Equation (3) and (4) is not always straightforward. Firstly, the unambiguous determination of v_0 and α in Equation (3) can be complicated, as recently also pointed out by Wenn and Junkers.[12] A conventional regression analysis for the estimation of k_{bb} is thus not straightforward. To partially resolve this issue, Wenn and Junkers[12] recently suggested a more feasible tuning procedure based on the sideward shift of the simulated S-shaped curves by a variation of k_{bb} and considering arbitrary $k_{p,app}$ testing values.[12] Secondly, in practice, $k_{p,app}$ does not reach a constant value in the low frequency range but continues to lower with decreasing frequency. Hence, $k_{p,m}$ can only be assessed via Equation (4), as also indicated by Wenn and Junkers.[12]

It is thus clear that the aforementioned PLP-based methods for the determination of k_{bb} (and $k_{p,m}$) can be further improved, either by the development of more accurate analysis techniques or the refinement of the model assumptions to facilitate a more accurate regression analysis.

In the present work, an alternative method is presented and applied to estimate the bulk k_{bb} from inflection point PLP-SEC data (Equation 2; $j = 1$). On a longer term, this method allows for the simultaneous estimation of k_{bb} and $k_{p,m}$, including a complete statistical analysis. The presented

method is related to the one of Nikitin *et al.*[11] and Wenn and Junkers[12] but focuses only on the regime of low frequencies, which can be easily scanned with less expensive PLP equipment and which is most sensitive to variations in the propagation rates relative to the backbiting rate. For these low frequencies, in contrast to the method of Nikitin *et al.*[11] and Wenn and Junkers,[12] PLP experiments with various solvent volume fractions (Φ_S) are considered, which leads to a significant data variation and allows for a reliable regression analysis, even in the presence of large experimental errors as confirmed by a robustness check. To safely rule out potential solvent effects the saturated analogue of the monomer is chosen as the solvent and the polymerization temperature is set sufficiently low to avoid any kinetically significant impact of chain transfer to solvent reactions.

4.2 Experimental section

4.2.1 Materials

n-Butyl acrylate (*n*BuA; monomer) was provided by BASF and freed from inhibitor via distillation. Butyl propionate (solvent), which can be seen as the saturated analogue of the monomer, was purchased from TCI Europe and 2,2-dimethoxy-2-phenylacetophenone (DMPA) from VWR International. Both chemicals were used as received.

4.2.2 PLP experiments

0.3 mL solutions of *n*BuA and butyl propionate (solvent volume fraction (Φ_S) of 0, 0.5, and 0.75), containing 2.5 10^{-3} mol L^{-1} DMPA, were transferred into sample vials. These vials were placed into a stainless steel sample holder that was brought to 303 K by a VWR 1196D thermostat. The temperature was directly measured at the sample and did not exceed a deviation larger than 0.1 K during the experiments so that isothermicity can be safely assumed. An overview of all the initial conditions is provided in Table S1 in Appendix C.

Photopolymerization was initiated by laser pulsing with a Xantos XS-500 system operated at the XeF line (351 nm). The laser beam was adjusted to hit the sample from the bottom with an energy of 1.5 10^{-3} J per pulse. For each Φ_S, experiments with a varying frequency were performed, with a minimal value of 10 s^{-1} and a maximal value of 60 s^{-1}. This v range was determined in such a way that PLP-SEC traces with an inflection point corresponding to the mixed propagation behavior of ECRs and MCRs (*cf.* Equation (2)) were obtained.

At the end of the polymerization, hydroquinone dissolved in THF was directly added to the samples. Subsequently, solvent and remaining monomer were removed by evaporation.

4.2.3 Characterization

Size exclusion measurements (SEC) measurements were performed on a PL-SEC 50 Plus Integrated System with an autosampler and a PL-gel 5 μm bead-size guard column (50 × 7.5 mm), followed by a PL-gel 5 μm mixed E column (300 × 7.5 mm), three PL-gel 5 μm mixed C columns (300 × 7.5 mm), and a differential refractive index (RI) detector with THF as eluent, an analysis temperature of 308 K, and a flow rate of 1 mL min^{-1}.

The GPC system was calibrated using linear polystyrene standards ranging from 4.8 10^2 to 2.5 10^6 g mol^{-1} and linear poly(methyl methacrylate) standards ranging from 8.0 10^2 to 1.6 10^6 g mol^{-1}. Polymer specific Mark-Houwink-Kuhn-Sakurada (MHKS) parameters were used to obtain the absolute poly(*n*BuA) molar masses.[20]

4.3 Simulation section

4.3.1 Modeling technique

Kinetic Monte Carlo (*k*MC) modeling is applied for the calculation of the inflection points of the SEC trace for isothermal PLP of acrylates, using a basic PLP reaction scheme consisting of photodissociation, chain initiation, propagation, backbiting and termination, and considering

chain-length dependent termination kinetics (see Appendix C). The entire PLP experiment is always simulated with the number of pulses listed in Table S1 in Appendix C. More details on the *k*MC modeling technique as such can be found in previous work.[50-52]

It should be stressed that a basic PLP reaction scheme can be considered for the determination of the position of the inflection points, as explained in Appendix C. A sensitivity analysis (also Appendix C) indicates that no dedicated kinetic parameter selection is required, except for $k_{p,e}$ similar to other methods. Hence, the method can be reliably applied for less studied acrylate monomers as well.

It should also be noted that the PLP-SEC technique is sensitive to SEC broadening. An explanation on how SEC broadening is accounted for, in accordance with the procedure introduced by Buback *et al.*,[53] is given in Appendix C. Alternatively, analysis via matrix assisted laser desorption/ionization-time of flight (MALDI-TOF) mass spectroscopy can be applied.[54]

4.3.2 Regression analysis procedure

Regression analysis is performed using the Levenberg-Marquardt algorithm (ODRPACK v2.01), considering the minimization of the following objective function:

$$S = \sum_{i=1}^{N} (y_i - \hat{y}_i)^2 \tag{5}$$

in which y_i corresponds to the i^{th} experimental $k_{p,app}$ (N measured points in total; Equation (2) with j=1) and $\hat{y}_i$ is the corresponding model predicted value. The individual confidence intervals and the global significance of the regression are calculated. The latter is reflected by a F value which needs to be sufficiently higher than the corresponding tabulated value (F_{tab}).[55, 56] For more details on the estimation procedure as such, the reader is referred to previous work.[57-59]

In a first stage, regression analysis is performed based on *in silico* inflection point data generated with the *k*MC model using given input values for the to be estimated parameter(s) and including artificial error with a given standard deviation σ. This *in silico* testing is used to verify the robustness of the method. Attention is focused both on the sole estimation of k_{bb} and the simultaneous estimation of k_{bb} and $k_{p,m}$.

In a second stage, regression analysis is performed based on actual experimental data selecting *n*BuA as monomer and butyl propionate as solvent (*cf.* Experimental section and Appendix C). Here, focus is restricted to the estimation of k_{bb} only. For a reliable joint estimation of k_{bb} and $k_{p,m}$, a sufficient number of experimental data points need to be available, which is however outside the scope of the present work.

4.4 Results and discussion

In what follows, the principle and advantages of the alternative method to estimate bulk k_{bb} values are first elaborated, followed by a demonstration of the accuracy and robustness of the method through simulations accounting for various degrees of artificial error. Next, based on experimentally recorded inflection point data for PLP of *n*BuA in butyl propionate at 303 K, regression analysis is successfully performed to estimate k_{bb}, for illustration purposes using $k_{p,e}$ and $k_{p,m}$ values from literature. The reported k_{bb} value is compared with literature data.

4.4.1 Principle and advantages of the method

In agreement with the method of Nikitin *et al.*[11] and Wenn and Junkers,[12] in the present work, PLP $k_{p,app}$ data (Equation (2); $j = 1$) at different frequencies are considered to determine k_{bb}. The novel aspect is the consideration of $k_{p,app}$ data at a varying solvent volume fraction Φ_S and this only in the low frequency range, which is accessible with less expensive PLP equipment. Note that the use of solution PLP for a reliable parameter estimation has also been put forward by Plessis *et al.*[46] and that the saturated analogue of the monomer is chosen as the solvent so that

a possible impact of the reaction medium on the intrinsic reactivities can be safely ruled out. Such absence can always be verified by comparing bulk and solution PLP data at conditions leading to conventional PLP behavior (*i.e.* at low temperatures and/or high frequencies).

Table 1. Principle of the method to estimate k_{bb} in acrylate radical polymerization for $\Delta t = \nu^{-1} = 10^{-2}$ s; an increase of Φ_S leads to an increased MCR average life time τ_m within Δt; solvent: saturated analogue of the monomer.

	Equation	**Bulk ($\Phi_S = 0$)**	**Solution ($\Phi_S = 0.75$)**
τ_e **[s]**	$\frac{1}{k_{bb}}$	10^{-3}	10^{-3}
τ_m **[s]**	$\frac{1}{k_{p,m}(1-\Phi_S)[M]_{0,bulk}}$	$1.4\ 10^{-3}$	$5.7\ 10^{-3}$

The principle of the method is illustrated in Table 1, selecting typical orders of magnitude for $k_{p,e}$, $k_{p,m}$, and k_{bb} (10^4 L mol^{-1} s^{-1}, 10^2 L mol^{-1} s^{-1}, and 10^3 s^{-1}) and the initial bulk monomer concentration $[M]_{0,bulk}$ (7 mol L^{-1}). For a frequency of 100 s^{-1}, it follows that a variation of Φ_S allows to alter the average MCR life time (τ_m) within Δt, in agreement with the NMR studies of Ahmad *et al.*[47] and Plessis *et al.*[46] An increase in Φ_S from 0 to 0.75 leads to a strongly increased τ_m, while the average ECR life time (τ_e) remains unchanged. Hence, an increase in Φ_S leads to an increased contribution of the more stable tertiary radicals and thus lowers $k_{p,app}$. In other words, by altering Φ_S the impact of k_{bb} on $k_{p,app}$ can be regulated in a highly sensitive manner, allowing reliable regression analysis if $k_{p,m}$ is accurately known or simultaneously estimated.

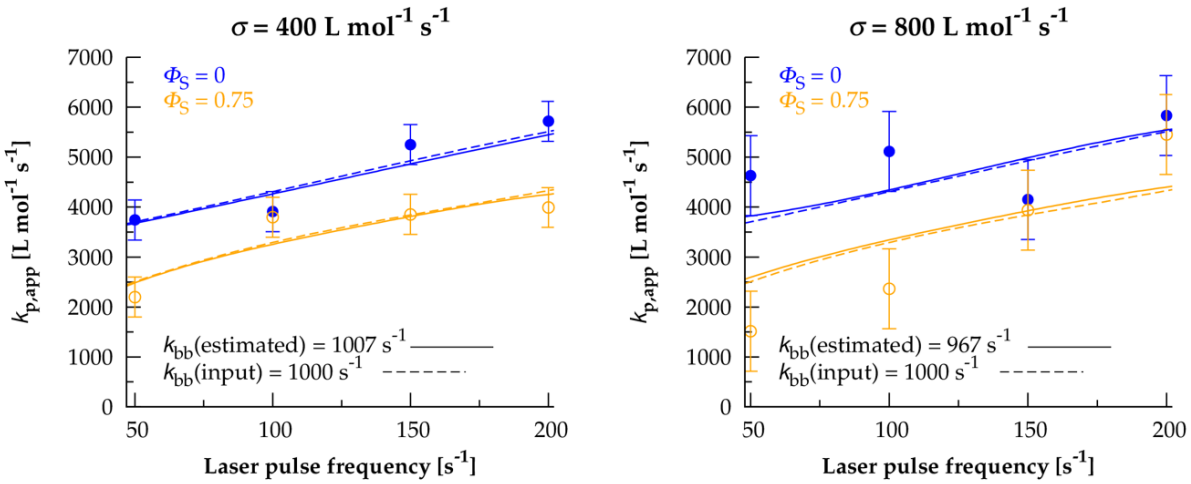

Figure 1. *In silico* validation of the proposed alternative method to determine k_{bb} for acrylate radical polymerization from $k_{p,app}$ data (Equation 2; j = 1) with a known $k_{p,e}$ and $k_{p,m}$; symbols: generated data with the *k*MC model (dashed lines), superimposed with an artificial random error (Gaussian sampling with a standard deviation σ); error bars correspond to a correction with ± σ (input value); model parameters: Table S2 in Appendix C; fits after regression analysis: full lines. Analogous figure for the estimation of both k_{bb} and $k_{p,m}$ in Appendix C (Figure S6); both for Figure 1 and Figure S6 the estimated parameters are very close to the implemented ones and for the full frequency range the correct inflection points are obtained, highlighting the high robustness of the method.

4.4.2 Accuracy and robustness of the method

The high accuracy of the method to estimate bulk k_{bb} values is demonstrated in a first instance theoretically, assuming that both $k_{p,e}$ and $k_{p,m}$ are known. Regression analysis is performed with $k_{p,app}$ data (Equation (2); j = 1) obtained from simulated PLP-SEC traces (see details in Appendix C). These *in silico* generated data (dashed lines in Figure 1) are perturbed by random noise based on Gaussian sampling (with standard deviation σ) to mimic experimental error (symbols in Figure 1). Φ_S values of 0 (bulk situation) and 0.75 (solvent-rich situation) are selected and for all rate coefficients in the basic PLP model typical orders of magnitude are used (Table S2 in Appendix C).

Two theoretical test cases are considered with the input k_{bb} value for the PLP *k*MC model equal to 1000 s^{-1} (same as in Table 1) and considering frequencies of 50, 100, 150 and 200 s^{-1}. The maximum frequency value is consistent with the reported time scales in Table 1 to allow for an efficient regression analysis. In the first theoretical test case, the $k_{p,app}$ data are

perturbed by a Gaussian error with an acceptable σ of 400 L mol^{-1} s^{-1}, emulating an experimental error of *ca.* 10% as can be judged from the error bars for the symbols in Figure 1. This σ is doubled to 800 L mol^{-1} s^{-1} for the second theoretical test case, resulting in a double relative error of *ca*. 20%.

The corresponding estimates for k_{bb} are 1007 ± 157 s^{-1} and 967 ± 262 s^{-1} (95% confidence intervals) with the corresponding fits shown in Figure 1 (full lines). The obtained estimates for k_{bb} are thus very close to the implemented and therefore to be estimated value of 1000 s^{-1}, highlighting the potential of the proposed method. Even for an artificial experimental error of 20% (second theoretical test case) the method is still sufficiently accurate, as a mismatch of less than 4% results for the estimated k_{bb} value, although the confidence interval is much broader. The high robustness towards experimental outliers is also confirmed by the closely matching dashed and full lines in Figure 1, which are obtained by simulation with respectively k_{bb} input values (noise-free) and estimated values (from noisy inflection point data).

The robustness is further confirmed in case the regression analysis aims at a higher number of parameter estimates. This is theoretically illustrated in Appendix C in which the updated Figure 1 is presented (Figure S6), aiming at the simultaneous estimation of both k_{bb} and $k_{p,m}$. As indicated in Table 1, the relative importance of the time scales for ECRs and MCRs depends on $k_{p,m}$ and, hence, it can be expected that an error on this rate coefficient can have a kinetically significant impact on the reliability of the regression results focusing only on the estimation of k_{bb}. Importantly, the results in Appendix C (Figure S6) allow to conclude that in addition to k_{bb}, $k_{p,m}$ can also be accurately estimated, as a good match with the implemented value (100 L mol^{-1} s^{-1}) is obtained.

Since regression analysis to a limited amount of *in silico* $k_{p,app}$ data (8 *in silico* generated points as in Figure 1) is performed, broader individual 95% confidence intervals result as compared to the case of a sole estimation of k_{bb}. Hence, in practice, a sufficient large set of PLP-SEC

inflection point data is required before the simultaneous estimation of k_{bb} and $k_{p,m}$ can be reliably performed with the proposed method.

4.4.3 Application of the method with nBuA at 303 K

Based on the theoretical results in the previous section, it can be deduced that the presented method is robust and is also complementary to the already available methods to determine k_{bb}. In this section, the potential of the method is further illustrated by considering experimentally measured inflection point PLP data for the radical polymerization of *n*BuA.

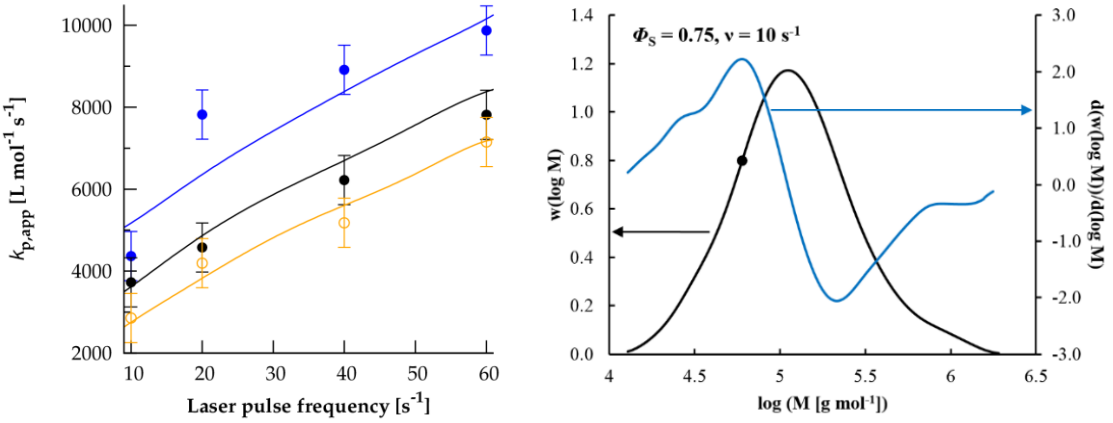

Figure 2. Top: application of the alternative method for DMPA photoinitiated PLP of *n*BuA; initial conditions: 303 K, $[DMPA]_0$ = 2.5 10^{-3} mol L^{-1}, and E_{pulse} = 1.5 10^{-3} J; experimental data: symbols; error bars correspond to an error of 10% on the average recorded $k_{p,app}$ value;[17] lines: fits with k_{bb} = 171 s^{-1} (95% confidence interval: 171 s^{-1} ± 21 s^{-1}; F = 1084 >> F_{tab} = 4.84); Bottom: typical experimental SEC trace (black full line) and corresponding derivative (blue full line), allowing the determination of $k_{p,app}$ (Equation (2); j = 1) via the indicated inflection point (black symbol); initial conditions: ν = 10 s^{-1}, Φ_S = 0.75 (additional SEC traces are included in Appendix C).

As indicated above, the considered experimental data set is restricted to the estimation of k_{bb} only. Regression analysis (full lines in Figure 2; left) to experimental bulk (Φ_S = 0) and solution (Φ_S = 0.5 and 0.75) $k_{p,app}$ data (symbols in Figure 2) in the low frequency range (ν ≤ 60 s^{-1}) is performed to estimate the bulk k_{bb} at 303 K. The maximal v of 60 s^{-1} is identified based on preliminary simulations in which the existence of an inflection point corresponding to the mixed propagation behavior of ECRs and MCRs as defined by Equation (2) (j = 1) can be guaranteed. For illustration purposes, a typical experimental SEC trace (full black line) and the

corresponding derivative (full blue line) are provided in Figure 2 (bottom; $\nu = 10\ s^{-1}$, $\Phi_S = 0.75$). The full range of experimental initial conditions is provided in Appendix C (Table S1).

In Appendix C it is also shown that for the determination of the position of the simulated inflection points that serve as input values in the regression analysis, a dedicated kinetic parameter selection is not required and a basic PLP model can be reliably used. In particular, it is demonstrated that chain transfer to monomer and solvent can be neglected at the considered low temperature, *i.e.* they do not influence the position of the inflection points. The impact of an acceptable uncertainty on the apparent termination reactivities is also shown to be very limited, highlighting the generic potential of the proposed method.

A bulk k_{bb} value of $171 \pm 21\ s^{-1}$ (95% confidence interval; see Figure 2 for the corresponding fit) is obtained, which is in very good agreement with the value reported by Nikitin *et al.*[11] ($167\ s^{-1}$) and Barth *et al.* ($168\ s^{-1}$).[48] Hence, the robustness of the proposed method can be claimed not only theoretically but also experimentally.

4.5 Conclusions

For the estimation of the bulk backbiting rate coefficient in acrylate radical polymerization, an alternative method using PLP inflection point data and allowing a complete statistical analysis is presented, selecting the saturated analogue of the monomer as the solvent. A key feature is the variation of the solvent volume fraction in the low frequency range, which allows to independently change the average MCR life time and to obtain a high sensitivity towards k_{bb} using less expensive PLP equipment.

Regression analysis of *in silico* generated data shows that the method is robust, even if large artificial errors are introduced and $k_{p,m}$ needs to be also estimated. Additionally, the method has been successfully applied to $k_{p,app}$ data of *n*BuA at 303 K, yielding a k_{bb} value in agreement with literature data.

On a long term, the method will contribute to the determination of k_{bb} values for a wide monomer range and the obtained parameter values can be compared with those obtained with the already reported methods to further improve the fundamental understanding of acrylate radical polymerization kinetics in general.

4.6 References

1. O. F. Olaj, I. Bitai and F. Hinkelmann, *Macromol. Chem. Phys.*, 1987, **188**, 1689-1702.
2. S. Beuermann and M. Buback, *Prog. Polym. Sci.*, 2002, **27**, 191-254.
3. D. R. D'hooge, M. F. Reyniers and G. B. Marin, *Macromol. React. Eng.*, 2013, **7**, 362-379.
4. P. Derboven, D. R. D'hooge, M. M. Stamenovic, P. Espeel, G. B. Marin, F. E. Du Prez and M. F. Reyniers, *Macromolecules*, 2013, **46**, 1732-1742.
5. C. Barner-Kowollik and G. T. Russell, *Prog. Polym. Sci.*, 2009, **34**, 1211-1259.
6. M. Buback, H. Schroeder and H. Kattner, *Macromolecules*, 2016, **49**, 3193-3213.
7. K. B. Kockler, A. P. Haehnel, T. Junkers and C. Barner-Kowollik, *Macromol. Rapid Commun.*, 2016, **37**, 123-134.
8. P. Drawe and M. Buback, *Macromol. Theory Simul.*, 2016, **25**, 74-84.
9. A. N. Nikitin, P. Castignolles, B. Charleux and J. P. Vairon, *Macromol. Rapid Commun.*, 2003, **24**, 778-782.
10. M. Buback, P. Hesse and I. Lacik, *Macromol. Rapid Commun.*, 2007, **28**, 2049-2054.
11. A. N. Nikitin, R. A. Hutchinson, M. Buback and P. Hesse, *Macromolecules*, 2007, **40**, 8631-8641.
12. B. Wenn and T. Junkers, *Macromol. Rapid Commun.*, 2016, **37**, 781-787.
13. A. M. van Herk, *Macromol. Rapid Commun.*, 2009, **30**, 1964-1968.
14. T. Junkers and C. Barner-Kowollik, *J. Polym. Sci. Pol. Chem.*, 2008, **46**, 7585-7605.
15. G. Arzamendi, C. Plessis, J. R. Leiza and J. M. Asua, *Macromol. Theory Simul.*, 2003, **12**, 315-324.
16. M. Buback, R. G. Gilbert, R. A. Hutchinson, B. Klumperman, F. D. Kuchta, B. G. Manders, K. F. O'Driscoll, G. T. Russell and J. Schweer, *Macromol. Chem. Phys.*, 1995, **196**, 3267-3280.
17. S. Beuermann, M. Buback, T. P. Davis, R. G. Gilbert, R. A. Hutchinson, O. F. Olaj, G. T. Russell, J. Schweer and A. M. van Herk, *Macromol. Chem. Phys.*, 1997, **198**, 1545-1560.

18. S. Beuermann, M. Buback, T. P. Davis, R. G. Gilbert, R. A. Hutchinson, A. Kajiwara, B. Klumperman and G. T. Russell, *Macromol. Chem. Phys.*, 2000, **201**, 1355-1364.
19. S. Beuermann, M. Buback, T. P. Davis, N. Garcia, R. G. Gilbert, R. A. Hutchinson, A. Kajiwara, M. Kamachi, I. Lacik and G. T. Russell, *Macromol. Chem. Phys.*, 2003, **204**, 1338-1350.
20. J. M. Asua, S. Beuermann, M. Buback, P. Castignolles, B. Charleux, R. G. Gilbert, R. A. Hutchinson, J. R. Leiza, A. N. Nikitin, J. P. Vairon and A. M. van Herk, *Macromol. Chem. Phys.*, 2004, **205**, 2151-2160.
21. S. Beuermann, M. Buback, P. Hesse, F. D. Kuchta, I. Lacik and A. M. Van Herk, *Pure and Applied Chemistry*, 2007, **79**, 1463-1469.
22. C. Barner-Kowollik, S. Beuermann, M. Buback, P. Castignolles, B. Charleux, M. L. Coote, R. A. Hutchinson, T. Junkers, I. Lacik, G. T. Russell, M. Stach and A. M. van Herk, *Polym. Chem.*, 2014, **5**, 204-212.
23. F. Ganachaud, R. Balic, M. J. Monteiro and R. G. Gilbert, *Macromolecules*, 2000, **33**, 8589-8596.
24. B. Dervaux, T. Junkers, M. Schneider-Baumann, F. E. Du Prez and C. Barner-Kowollik, *J. Polym. Sci. Pol. Chem.*, 2009, **47**, 6641-6654.
25. M. Buback, U. Geers and C. H. Kurz, *Macromol. Chem. Phys.*, 1997, **198**, 3451-3464.
26. R. A. Hutchinson, S. Beuermann, D. A. Paquet and J. H. McMinn, *Macromolecules*, 1997, **30**, 3490-3493.
27. M. D. Zammit, M. L. Coote, T. P. Davis and G. D. Willett, *Macromolecules*, 1998, **31**, 955-963.
28. A. P. Haehnel, M. Schneider-Baumann, K. U. Hiltebrandt, A. M. Misske and C. Barner-Kowollik, *Macromolecules*, 2013, **46**, 15-28.
29. R. X. E. Willemse and A. M. van Herk, *Macromol. Chem. Phys.*, 2010, **211**, 539-545.
30. A. P. Haehnel, M. Schneider-Baumann, L. Arens, A. M. Misske, F. Fleischhaker and C. Barner-Kowollik, *Macromolecules*, 2014, **47**, 3483-3496.
31. R. A. Hutchinson, S. Beuermann, D. A. Paquet, J. H. McMinn and C. Jackson, *Macromolecules*, 1998, **31**, 1542-1547.
32. M. Buback and C. H. Kurz, *Macromol. Chem. Phys.*, 1998, **199**, 2301-2310.
33. K. B. Kockler, A. P. Haehnel, F. Fleischhaker, M. Schneider-Baumann, A. M. Misske and C. Barner-Kowollik, *Macromol. Chem. Phys.*, 2015, **216**, 1573-1582.
34. K. B. Kockler, F. Fleischhaker and C. Barner-Kowollik, *Polym. Chem.*, 2016, **7**, 4342-4351.
35. S. Harrisson, S. R. Mackenzie and D. M. Haddleton, *Macromolecules*, 2003, **36**, 5072-5075.

36. I. Woecht, G. Schmidt-Naake, S. Beuermann, M. Buback and N. Garcia, *J. Polym. Sci. Pol. Chem.*, 2008, **46**, 1460-1469.
37. S. Beuermann, *Macromol. Rapid Commun.*, 2009, **30**, 1066-1088.
38. A. P. Haehnel, B. Wenn, K. Kockler, T. Bantle, A. M. Misske, F. Fleischhaker, T. Junkers and C. Barner-Kowollik, *Macromol. Rapid Commun.*, 2014, **35**, 2029-2037.
39. M. Buback, *Macromol. Rapid Commun.*, 2015, **36**, 1979-1983.
40. A. P. Haehnel, B. Wenn, K. Kockler, T. Bantle, A. M. Misske, F. Fleischhaker, T. Junkers and C. Barner-Kowollik, *Macromol. Rapid Commun.*, 2015, **36**, 1984-1986.
41. A. N. Nikitin, R. A. Hutchinson, W. Wang, G. A. Kalfas, J. R. Richards and C. Bruni, *Macromol. Reac. Eng.*, 2010, **4**, 691-706.
42. D. R. D'hooge, M. F. Reyniers, F. J. Stadler, B. Dervaux, C. Bailly, F. E. Du Prez and G. B. Marin, *Macromolecules*, 2010, **43**, 8766-8781.
43. C. Plessis, G. Arzamendi, J. R. Leiza, H. A. S. Schoonbrood, D. Charmot and J. M. Asua, *Ind. Eng. Chem. Res.*, 2001, **40**, 3883-3894.
44. S. Hamzehlou, N. Ballard, Y. Reyes, A. Aguirre, J. M. Asua and J. R. Leiza, *Polym. Chem.*, 2016, **7**, 2069-2077.
45. D. R. D'hooge, P. H. M. Van Steenberge, P. Derboven, M. F. Reyniers and G. B. Marin, *Polym. Chem.*, 2015, **6**, 7081-7096.
46. C. Plessis, G. Arzamendi, J. M. Alberdi, A. M. van Herk, J. R. Leiza and J. M. Asua, *Macromol. Rapid Commun.*, 2003, **24**, 173-177.
47. N. M. Ahmad, F. Heatley and P. A. Lovell, *Macromolecules*, 1998, **31**, 2822-2827.
48. J. Barth, M. Buback, P. Hesse and T. Sergeeva, *Macromolecules*, 2010, **43**, 4023-4031.
49. R. X. E. Willemse, A. M. van Herk, E. Panchenko, T. Junkers and M. Buback, *Macromolecules*, 2005, **38**, 5098-5103.
50. P. H. M. Van Steenberge, D. R. D'hooge, Y. Wang, M. Zhong, M.-F. Reyniers, D. Konkolewicz, K. Matyjaszewski and G. B. Marin, *Macromolecules*, 2012, **45**, 8519-8531.
51. P. H. M. Van Steenberge, D. R. D'hooge, M. F. Reyniers and G. B. Marin, *Chem. Eng. Sci.*, 2014, **110**, 185-199.
52. P. H. M. Van Steenberge, J. Vandenbergh, D. R. D'hooge, M. F. Reyniers, P. J. Adriaensens, L. Lutsen, D. J. M. Vanderzande and G. B. Marin, *Macromolecules*, 2011, **44**, 8716-8726.
53. M. Buback, M. Busch and R. A. Lammel, *Macromol. Theory Simul.*, 1996, **5**, 845-861.

54. R. X. E. Willemse, B. B. P. Staal, A. M. van Herk, S. C. J. Pierik and B. Klumperman, *Macromolecules*, 2003, **36**, 9797-9803.
55. K. Levenberg, *Q. Appl. Math.*, 1944, **2**, 164.
56. D. W. Marquardt, *SIAM Soc. Ind. Appl. Math. J. Sci.*, 1963, **11**, 431.
57. T. De Roo, J. Wieme, G. J. Heynderickx and G. B. Marin, *Polymer*, 2005, **46**, 8340-8354.
58. C. T. Porras, D. R. D'hooge, P. H. M. Van Steenberge, M. F. Reyniers and G. B. Marin, *Ind. Eng. Chem. Res.*, 2014, **53**, 9674-9685.
59. S. K. Fierens, D. R. D'hooge, P. H. M. Van Steenberge, M. F. Reyniers and G. B. Marin, *Chem. Eng. J.*, 2015, **278**, 407-420.

Chapter 5: Estimating the β-scission rate coefficient from high temperature PLP experiments

Summary

A novel method to estimate the β-scission rate coefficient (k_β) in radical polymerization of acrylates is introduced, provided that the backbiting and tertiary propagation rate coefficient have already been determined at sufficiently low temperatures at which β-scission is negligible (<< 350 K). The method relies on the sensitivity of k_β upon a change of the pulse laser frequency (<< 200 Hz) under isothermal pulsed laser polymerization (PLP) conditions in the temperature range between *ca.* 350 and 415 K, leading to a sufficient variation of the times scales of the radicals involved. These observations are not significantly influenced by macropropagation and thermal self-initiation, as respectively confirmed by *in silico* testing and experimental data. Solution inflection point data (*e.g.* solvent butyl propionate) are needed at the lower temperature range (350-410 K), whereas bulk inflection point data suffice at the higher temperature range (410-415 K). The proposed method leads to an estimated k_β value of $(4.26 \pm 1.8)\times10^2$ s^{-1} at 413 K with bulk PLP data, suggesting a high propensity of macromonomer formation in acrylate polymerization under high temperature radical polymerization conditions, exceeding the previously suggested levels (k_β = 6 x 10^0-1.45 x10^2 s^{-1}).

5.1 Introduction

Pulsed laser polymerization (PLP) combined with size exclusion chromatography (SEC) analysis is a versatile technique for the determination of rate coefficients in radical polymerization processes. These rate coefficients are the core of any kinetic and process control model and are essential for the understanding of the relation of chemical structure and reactivity.[1–3]

Most focus has been on the determination of the intrinsic propagation rate coefficient k_p, with IUPAC supported benchmark results for radical polymerization of standard monomers such as styrene and methyl methacrylate,[4–9] in which under pulsation one dominant macroradical type is obtained so that:[10,11]

$$k_p = L_i[[M]_0(i\Delta t)]^{-1} \quad (1)$$

in which $[M]_0$ is the initial monomer concentration, L_i the chain length associated with the i^{th} (i=1,2,…) inflection point of the PLP-SEC trace, and Δt the dark time between pulses, *i.e.* the reciprocal of the pulse laser frequency (*e.g.* 100 Hz).

For polymerizations with more than one macroradical type, Equation (1) needs to be written with an apparent propagation rate coefficient ($k_{p,app}$),[12–16] highlighting that the positions of the inflection points are not uniquely correlated with the chain growth pattern of one active species. As the ultimate goal is the determination of elementary intrinsic rate coefficients, an elegant variation of the PLP conditions is required to alter the relative importance of the radical types and to obtain limiting conditions with only one macroradical type so that the original Equation (1) can be applied.

For example, in acrylate radical polymerization, both secondary end-chain radicals (ECRs) and tertiary mid-chain radicals (MCRs) exist with the latter being formed from the former by transfer reactions such as intermolecular H-abstraction (chain transfer to polymer) or backbiting (left part of Scheme 1).[16–20] Upon addition of monomer to a MCR, *i.e.* tertiary propagation, a short chain branch (SCB) results and the conventional chain growth pattern can continue as again an ECR is obtained. Under high frequency PLP conditions, backbiting can however be suppressed so that only ECRs exist, giving access the secondary intrinsic propagation rate coefficient $k_{p,e}$. Several methods have been developed to retrieve the intrinsic tertiary propagation rate coefficient $k_{p,m}$ along with the intrinsic backbiting rate coefficient k_{bb}.[14–16,21]

As SCBs are generated upon tertiary propagation, quantitative ^{13}C-nuclear magnetic resonance (NMR) measurements can be performed, comparing the contribution of quaternary and tertiary carbon atoms in the polymer backbone of the dead polymer chains.

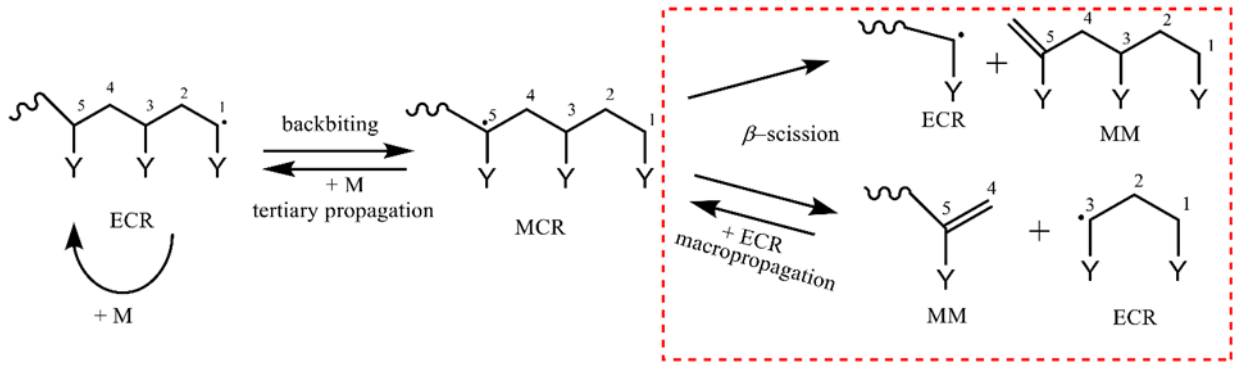

Scheme 1. End-chain radicals (ECRs) and mid-chain radicals (MCRs) in acrylate radical polymerization as formed due to intramolecular H-abstraction or backbiting. Dashed box: at elevated temperature (*e.g.* above 350 K[17,23–27]), *β*-scission of a MCR leads to the formation of macromonomers (MMs); these MMs compete with conventional monomer for chain growth; here case with addition of ECR only shown for one the MMs; Y=COOR (*n*BuA: R: butyl group); not shown for simplicity: intermolecular H-abstraction or chain transfer to polymer and radical migration.

A detailed kinetic model can subsequently be employed to obtain the desired rate coefficients. Alternatively, the frequency dependence of $k_{p,app}$ can be exploited under PLP conditions, with the steepness of the decay from higher to lower pulse laser frequencies providing information on the difference in $k_{p,e}$ and $k_{p,m}$, and k_{bb}.[14,15,20,22,23]

Recently, Marien *et al.*[16] highlighted that to increase the sensitivity toward $k_{p,m}$ and k_{bb}, parameter estimation of $k_{p,app}$ data at different pulse laser frequencies under both bulk and solution conditions should be considered. To avoid solvent effects, these authors recommend to utilize the saturated analogue of the monomer as solvent (*e.g.* butyl propionate as solvent for *n*-butyl acrylate *n*BuA as monomer). By including a variation of the solvent volume fraction next to a frequency variation, a broader span of PLP time scales for the ECRs and MCRs can be achieved, taking into account that backbiting is a unimolecular and tertiary propagation a

bimolecular reaction. A broader span of time scales implies a larger sensitivity and therefore contributes to a more facile and reliable parameter estimation.

It should be stressed that for acrylate radical polymerization at elevated temperature (> *e.g.* 350 K), additional reactions play a role (right part of Scheme 1; dashed box). Specifically, MCRs can under high temperature conditions undergo *β*-scission,[17,23,24,26–28] lowering the average chain length and leading to the formation of macromonomers (MMs). As MMs contain unsaturations, they can compete with conventional monomer for further chain growth, resulting in the formation of MCRs through so-called macropropagation (example in Scheme 1 only for one MM/ECR pair). More recent research has also indicated that MCRs can migrate so that the radical is shuffled along the lateral chain.[29–34] In case backbiting is the dominant trigger for MCR formation, a specific chain growth pattern can be detected after *β*-scission, *i.e.* the short unsaturated fragments with respect to the original terminal unit are different with a chain length of 2 and not 1.[33] With a dominance of chain transfer to polymer, the random nature of the H-abstraction is further enhanced by consecutive migration.[31]

Reliable intrinsic rate coefficients for high temperature acrylate radical polymerization reactions are, however, scarce as no dedicated methods are available yet as is the case for the determination of k_{bb} and $k_{p,m}$.[30] Currently, the common method for the assessment of the intrinsic *β*-scission and macropropagation rate coefficient (k_{β} and k_{mac}) is parameter tuning to (semi-)batch bulk/solution polymerization data, with the additional complexity of non-isothermicity.[25,27,28,35,36] A strong correlation of parameters is expected with the additional interference of (less studied) side reactions such as thermal self-initiation.[30,37–39] The majority of existing experimental literature data can also not be used as such, as no temperature history has been recorded. The issue of non-isothermicity could be resolved by switching to a micro-reactor set-up,[40] but still a detailed kinetic model is required with the need of multi-parameter estimation. Overall, it is therefore worthwhile to further explore – at elevated temperature – the

time scale ranges for ECRs and MCRs as accessible with PLP and to further extent frequency based methods based on Equation (1).

In the present work, such an extension is introduced that is capable to reliably extract k_β from inflection point data under PLP conditions at which macropropagation and thermal-self initiation can be neglected. The potential of the method is first illustrated *in silico* using literature values for all rate coefficients. It is theoretically illustrated that in the 'lower' temperature range (< 410 K) k_β needs to be determined based on solution inflection point data, whereas bulk inflection point data suffice in the 'higher' temperature range (≥ 410 K). The latter is illustrated for *n*-butyl acrylate (*n*BuA) polymerization at 413 K, showcasing a successful regression analysis under bulk conditions.

5.2 Experimental details

5.2.1 Materials

n-Butyl acrylate (*n*BuA, monomer, ≥99%) purchased from Sigma-Aldrich was used after passing over an alumina oxide bed for removing the inhibitor. The photoinitiator 2,2-dimethoxy-2-phenylacetopheneone (DMPA, 99%) was used as received from Sigma-Aldrich. Tetrahydrofuran (THF, ≥99.8%) obtained from Chem-Lab and hydroquinone (HQ, ≥99.5%) from Sigma-Aldrich were also used as received.

5.2.2 Experimental procedure

A monomer solution in a 50 mL round bottom flask was loaded with photoinitiator DMPA (2.5×10^{-3} mol L^{-1}). The solution was degassed for 45 minutes by purging with nitrogen. In parallel 0.7 mL PLP vials were degassed under argon atmosphere for 30 minutes. After degassing 0.4 mL monomer solutions were added to the vials. These vials were placed into the reaction chamber of the PLP setup for which the temperature was increased from ambient

temperature to the polymerization temperature (413 K). Since the number of pulses is limited (≤ 60), leading to monomer conversions below 3%, isothermicity can be assumed.[41]

PLP was performed with a Xantos XS-500 system operated at the XeF line (351 nm). The laser hit the sample from the bottom with a pulse energy of 1.5×10^{-3} J. A frequency range from 1 to 50 Hz was covered, which was determined based on a sensitivity analysis of simulation results covering a wider range of frequencies and literature values for the kinetic parameters. After a PLP experiment, the sample vial was immediately removed from the reaction chamber and a mixture of THF and HQ added to the sample to avoid further polymerization. The solvent and remaining monomer were removed by evaporation by maintaining the mixture in the oven overnight (temperature: 343 K).

5.2.3 Analysis

The conversion of monomer to polymer was measured gravimetrically. Size exclusion chromatography (SEC) was performed on a PL-GPC 50 Plus instrument with an autosampler and a refractive index (RI) detector. A 50×7.5 mm Resipore guard column and two Reispore 300×7.5 mm columns were used in series. THF was used as eluent with a flow rate of 1 ml min^{-1} and the temperature of the oven was maintained at 303 K. Calibration was performed using polystyrene standards (Medium EasiVials kit, Agilent Technologies) in the 1.62×10^{2} to 4.83×10^{5} g mol^{-1} range. Absolute molar masses were obtained employing the Mark-Houwink-Kuhn-Sakurada (MHKS) parameters of poly(*n*BuA) in THF, *i.e.* $K= 7.4\times10^{-5}$ dL g^{-1} and $\alpha = 0.75$,[42] and polystyrene in THF, *i.e.* $K=11.4\times10^{-5}$ dL g^{-1} and $\alpha = 0.716$.[43]

5.3 Kinetic model: reactions and regression analysis

The simulations to test the proposed method were carried out using a kinetic Monte Carlo (*k*MC) model as previously developed,[16,44–46] allowing the simulation of both the inflection points and the complete SEC trace. In agreement with literature data, ECRs and MCRs are

considered.[12–16,20,22,23] Essential for the current model are DMPA photodissociation, chain initiation, propagation of ECRs/MCRs, chain length dependent apparent termination, backbiting of ECRs, and *β*-scission of MCRs (k_β).

The complete set of elementary reactions and the corresponding literature based kinetic parameters [35,45,47–50] are shown in Table 1. As *β*-scission can occur to the 'left' and to the 'right' (*cf.* Scheme 1), two elementary *β*-scission reactions are considered for the MCRs with to a first approximation the same rate coefficient k_β. As elevated temperatures are considered (> 350 K), the dimethoxy benzyl radicals resulting from DMPA photodissociation can also undergo *β*-scission ($k_{\beta 0}$), leading to the formation of methyl radicals[47,51] as an additional source of chain carriers.

In agreement with previous work, chain transfer to polymer can be ignored.[52] Furthermore, thermal self-initiation can be neglected based on experimental analysis in the present work (Figure 1; left). Under conventional free radical polymerization (FRP) conditions it has been suggested that the monomer *n*BuA can initiate radical polymerization at elevated temperature.[39,53] Hence, experiments – without pulsation – were carried out at 413 K using the sample vials from actual PLP experiments. The sample vials were filled with 0.4 mL oxygen free *n*BuA (after purging with argon for 30 minutes) and placed in the reaction chamber for several minutes to evoke thermal self-initiation, bearing in mind that the time frame for a PLP experiment is only one minute as it takes about 50 seconds to reach the desired temperature (*e.g.* 413 K) and the pulsation time is very short.

As shown in Figure 1, there is negligible monomer conversion for the initial first minute at which the temperature is at the set-point, which is relevant for the PLP experiment. Subsequently, the monomer conversion increases gradually along with the temperature, confirming that under conventional FRP conditions thermal self-initiation is indeed relevant.

Preliminary modeling analysis (refer to Appendix D for details: Figure S2-4 in Section S3.2) also revealed that macropropagation, *i.e.* the addition of the macromonomers formed out of *β*–scission, is kinetically insignificant under the selected PLP conditions. Figure 1 (right) depicts the theoretical SEC traces (413 K; 5 pulses) if macropropagation is also considered. Even with a macropropagation rate coefficient (k_{mac}) that is deliberately higher than the propagation rate coefficient of ECRs ($k_{p,e}$), the resulting SEC trace is practically identical as in the case without macropropagation.

It should be stressed that the current work focuses on the determination/estimation of k_{β} only with the other kinetically relevant rate coefficients already determined by other techniques under low temperature conditions.[35,47–49]

Table 1 Reactions and Arrhenius parameters for PLP of *n*-butyl acrylate (photoinitiator DMPA) at elevated temperature (> 350 K) and used to test the proposed method (Figure 1, 2 and 3); for Figure 4 (413 K; application of method to bulk experimental data in the present work) all parameters are maintained except the one for β-scission which is estimated at a higher value (4.26×10^2 s^{-1}) than the literature value reported in this table.

Reaction	Equation	A [(L mol^{-1})s^{-1}]	E_A. [kJ mol^{-1}]	k [(L mol^{-1}) s^{-1}] at 413 K	Ref
Photodissociation[i]	$I_2 \xrightarrow{h\nu} R_{0,e}^{I} + R_{0,e}^{II}$			*a*	45
Chain initiation	$R_{0,e}^{I/III/IV} + M \xrightarrow{k_{p,I/III/IV}} R_{1,e}$	2.4×10^8	17.9	1.3×10^6	*b*
Propagation[c]	$R_{i,e} + M \xrightarrow{k_{p,e}} R_{i+1,e}$	2.2×10^7	17.9	1.2×10^5	48
	$R_{i,m} + M \xrightarrow{k_{p,m}} R_{i+1,e}$	9.2×10^5	28.3	2.4×10^2	49
Backbiting	$R_{i,e} \xrightarrow{k_{bb}} R_{i,m}$ i ≥ 3	1.6×10^8	34.7	6.6×10^3	49
β-scission of MCR[k]	$R_{i,m} \xrightarrow{k_\beta} MM_3 + R_{i-3,e}$	1.5×10^9	63.9	1.2×10^1	35
	$R_{i,m} \xrightarrow{k_\beta} MM_{i-2} + R_{2,e}$	1.5×10^9	63.9	1.2×10^1	35
β-scission of dimethoxy benzyl radical	$R_{0,e}^{II} \xrightarrow{k_{\beta o}} R_{0,e}^{III} + \text{MeBez}^h$	2.0×10^{13}	61.8	3.1×10^5	47
Chain transfer to monomer[j]	$R_{i,e} + M \xrightarrow{k_{trM,e}} P_i + R_{0,e}^{IV}$	2.9×10^5	32.6	2.2×10^1	50
	$R_{i,m} + M \xrightarrow{k_{trM,m}} P_i + R_{0,e}^{IV}$	2.0×10^5	46.1	3.0×10^{-1}	50
Termination[d]	$R_{i,e} + R_{j,e} \xrightarrow{k_{t,ee}^{app}(i,j)} P_{i(+j)}\left(+P_j\right)$	1.3×10^{10}	8.4	1.1×10^9	49
	$R_{i,e} + R_{j,m} \xrightarrow{k_{t,em}^{app}(i,j)} P_{i(+j)}\left(+P_j\right)$	4.2×10^9	6.6	6.1×10^8	49
	$R_{i,m} + R_{j,m} \xrightarrow{k_{t,mm}^{app}(i,j)} P_{i(+j)}\left(+P_j\right)$	9.0×10^6	5.6	1.8×10^6	49
	$R_{0,e}^{I/II/III/IV} + R_{0,e}^{I/II/III/IV} \xrightarrow{k_{t,00}^{app}} P_0$	1.3×10^{10}	8.4	1.1×10^9	*e*
	$R_{0,e}^{I/II/III/IV} + R_{i,e} \xrightarrow{k_{t,0e}^{app}(i)} P_i\left(+P_0\right)$	1.3×10^{10}	8.4	1.1×10^9	*f*
	$R_{0,e}^{I/II/III/IV} + R_{i,m} \xrightarrow{k_{t,0m}^{app}(i)} P_i\left(+P_0\right)$	4.2×10^9	6.6	6.1×10^8	*g*

[a] $\Delta[R_0]$ is calculated via Equation S2 in Appendix D for $\lambda = 351 \times 10^{-9}$ m, $E_{pulse} = 1.5 \times 10^{-3}$ J, $V = 4\times10^{-7}$ m^3, $l = 1.04 \times 10^{-2}$ m, and Φ of 0.42[45]; $\Delta[R_0]$ at the first laser pulse is equal to 1.04×10^{-5} mol L^{-1} (initial DMPA concentration= 2.5 x 10^{-3} mol L^{-1}). [b] higher chain initiation rate because of reaction 8, as a higher number of initiator radical prone to chain initiation.[47,56] [c]Chain length dependent propagation considered (refer to Appendix D Section S3.3).[57,58] [d]Chain length dependent (apparent) termination rate coefficients considered with $k_t^{app}(1,1)$ reported here, taking into account correction factor 2[40] and literature based fraction of termination by recombination (for other chain lengths refer to Appendix D Section S3.3).[27,35] [e]Assumed equal to $k_{t,ee}^{app}(1,1)$; [f]Assumed equal to $k_{t,ee}^{app}(i,1)$; $k_{t,ee}^{app}(1,1)$is reported here. [g]Assumed equal to $k_{t,em}^{app}(i,1)$; $k_{t,em}^{app}(1,1)$ is reported here. [h]MeBez= methyl benzoate formed during β-scission of dimethoxybenzyl radical; [i]radicals derived from the photoinitiator DMPA (I to III): benzoyl radical, dimethoxybenzyl radical, and methyl radical; [k]mid-chain radical; [j]radical formed by H-abstraction from *n*BuA.

Regression analysis is performed based on PLP inflection point data, driven by the Marquardt-Levenberg algorithm following the procedure as detailed in previous work.[16,54,55] Previous PLP work[22] also highlights that parameter variations within experimental margins have a limited impact in case the target is only the representation of inflection point data instead of complete SEC traces.

Note that under PLP conditions, migration is virtually non-existent. Based on the currently available data on migration rate coefficients,[31,34] it follows that on average migration occurs once after backbiting. Hence, the shorter chain length fraction of the *β*-scission product is only altered to a very limited extent, with a negligible effect on the inflection point – at least to a first approximation.

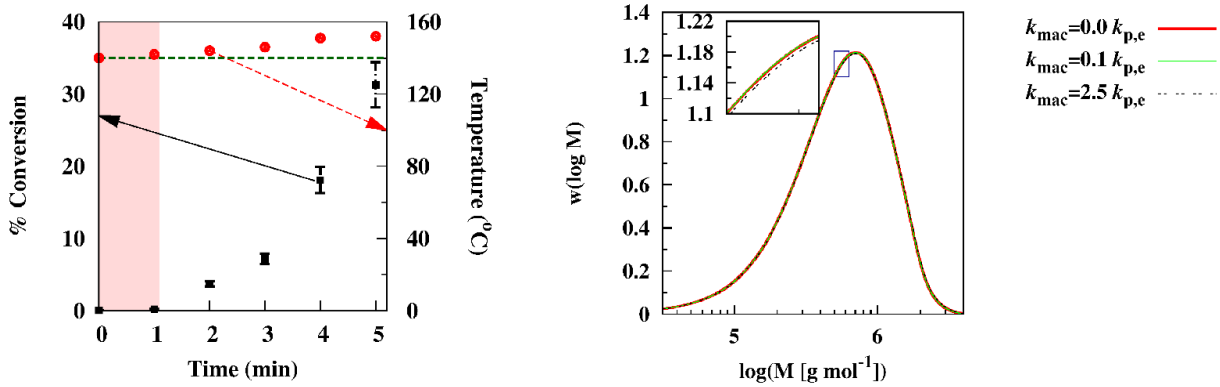

Figure 1. Left: Thermal self-initiation of *n*-butyl acrylate (*n*BuA) leading to increased monomer conversion, after heating toward 413 K in a PLP vial without pulsation in the laser set-up (average values from repeat experiments); for PLP experiments only the first minute is relevant at which the contribution is negligible shown by pink region; also given is the temperature change; Right: negligible impact of macropropagation as illustrated by as good as identical theoretical SEC traces, even if the macropropagation rate coefficients are higher than the propagation rate coefficient for ECRs: reaction conditions: 413 K and frequency 10 Hz; other parameters from Table 1.

5.4 Results and discussion

In the following section, the effect of k_β on the relation of the first inflection point ($k_{p,app}$; i=1; Equation (1)) and the laser pulse frequency is first theoretically evaluated in bulk at 413 K and in solution at temperatures below or equal to 413 K. Sufficient sensitivity in view of parameter

determination is illustrated so that the proposed method can be applied to *n*BuA experimental data in the next step.

5.4.1 Effect of k_β on the relation laser pulse frequency and inflection point in bulk at 413 K

Using the literature values collated in Table 1, it is initially tested *in silico* if k_β sufficiently affects the relation between the laser pulse frequency and the first inflection point (Equation (1) with $k_{p,app}$ and i=1). Focus is placed on bulk conditions and a high polymerization temperature of 413 K (boiling point of *n*BuA: 418 K) as it is known that *β*-scission is only relevant at higher temperatures.[17,23–27,59–61] Figure 2(top) shows the change in $k_{p,app}$ with the laser pulse frequency with k_β halved and doubled with respect to the reference value in Table 1. A 5 to 35 % change in $k_{p,app}$ is observed in the frequency range of 1-50 Hz, highlighting the potential of the method proposed toward parameter determination. Note that a higher k_β leads to a lower $k_{p,app}$ at a given frequency as the regular chain growth less favourable, in agreement with the lowering of the position of the inflection point.

The log-MMDs and corresponding derivatives at laser pulse frequencies of 10 and 50 Hz are shown in Figure 2 (bottom). The MMD shifts towards the left with increasing k_β with the shift being more pronounced for the lower frequency of 10 Hz (left figure). By considering very low pulse laser frequencies, it is therefore possible to ensure sufficient sensitivity at the selected high temperature. Further inspection of Figure 2 (bottom) shows that a secondary inflection point can be identified for the covered range of theoretical k_β. This inflection point is, however, less clear for a higher k_β and thus the theory suggests that for a strong relevance of *β*-scission only one inflection point is visible. In contrast, under conditions with no relevance of *β*-scission, it is likely that such second inflection points exist. Indeed, previous experimental reports at both lower[14,16]and higher[62] frequencies do mention the existence of two inflection points.

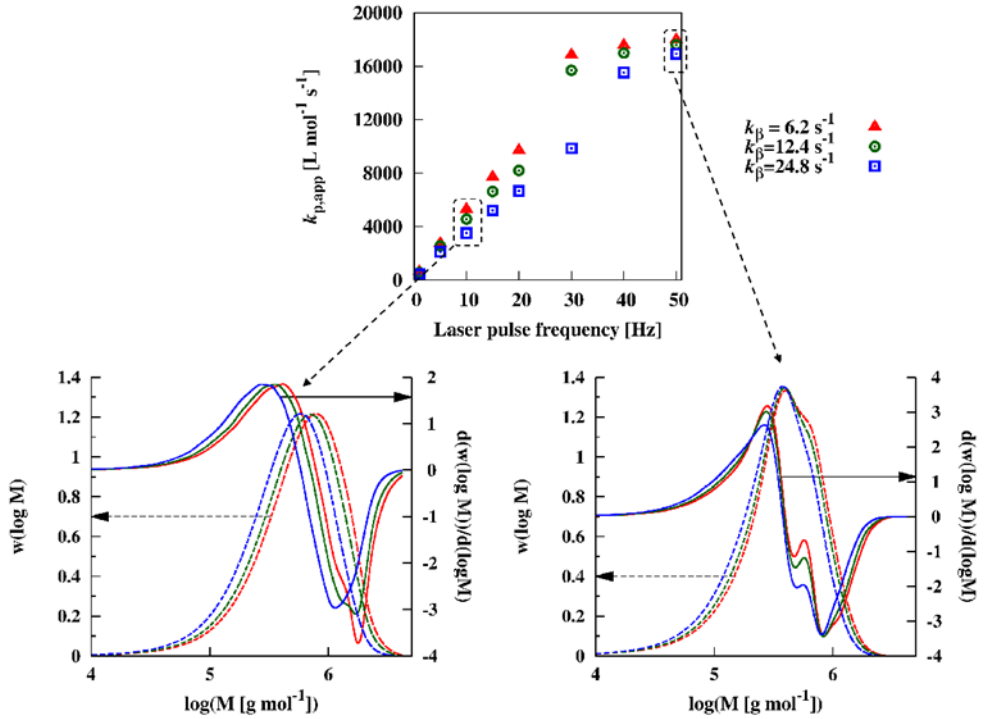

Figure 2. Top: Simulated effect of the *β*-scission rate coefficient (k_β) on the shift of the first inflection point with changing pulse laser frequency (Equation (1) with $k_{p,app}$ and i=1) in bulk PLP of *n*-butyl acrylate at 413 K by kinetic Monte Carlo (*k*MC) simulations using the reference parameters in Table 1; k_β is halved and doubled with respect to the reference value (k_β =12.4 s^{-1}): k_β = 6.2 s^{-1} (red), k_β = 12.4 s^{-1} (green) and k_β = 24.8 s^{-1} (blue); for a higher k_β the symbols globally shift to lower $k_{p,app}$, highlighting the sensitivity of the proposed method. Bottom: simulated log MMD (dashed lines) and corresponding derivative (solid lines) at laser pulse frequency of 10 Hz (bottom left) and 50 Hz (bottom right).

5.4.2 Effect of k_β on the relation laser pulse frequency and inflection point: solution and at temperatures below 413 K

It is well-accepted that k_β is important at higher polymerization temperatures[17,23–27,59–61]but the actual temperature window is not reliably known and is dependent on a number of factors such as concentration of initiator, concentration of monomer, and solvent amount.[27,28,61] Thus, a sensitivity analysis based on the kinetic parameters in Table 1 was carried out at alternative temperatures than 413 K in bulk (Figure 3: top) and in solution (Figure 3:bottom; 383 and 413 K), implicitly assuming the absence of a solvent effect. The latter can in practice be mimicked employing the saturated analogue of the monomer (*e.g.* butyl propionate for *n*-butyl acrylate).[16]

Figure 3 (top; bulk) highlights a too low sensitivity of k_β at lower temperatures of 353 and 383 K in the laser pulse frequency from 1-200 Hz, as the results show negligible change (< 5%; red and green bars) in $k_{p,app}$ by a doubling of k_β versus it reference value in Table 1. Sensitivities above 5% are recommended to avoid the impact of experimental error. Hence, under bulk conditions a high temperature (> 410 K) can only be considered for application of the method as at lower temperatures it is very likely that the regression analysis will not be significant.

The same laser pulse frequency range is used in Figure 3 (bottom left; 413 K) in order to assess the influence of the solvent fraction. The highest solvent fraction (ϕ_s=0.75; black bars) is most sensitive to a change in $k_{p,app}$, including a very high sensitivity (> 10%) at the lower frequencies and still an acceptable sensitivity (10%) at the higher frequencies, *i.e.* up to 200 Hz. Lower solvent fractions (ϕ_s=0.5 and ϕ_s=0; purple bar and blue bar, the latter the same as the blue bar in the top figure) show in contrast only sufficient sensitivity in the lower frequency range (below 50 Hz). Raw log-MMD data to further support these conclusions are provided in Appendix D; Figure S5-S8 in Section S4). Furthermore, a similar trend is repeated for the lower temperature Figure 3 (bottom right; 383 K). Only by considering a sufficiently high solvent fraction (ϕ_s=0.5; yellow bar) it is possible to obtain at least an acceptable sensitivity for certain (lower) frequencies, as e.g. opposed to the bulk case (bulk green bar in Figure 3 (bottom right); same green bar as in Figure 3; top) for which even at the lower frequencies it is difficult to have a sufficient sensitivity.

Thus, in order to deduce k_β with the proposed method, one needs to perform experiments in the lower frequency range, preferably below 50 Hz. In case a rate coefficient is targeted at a lower temperature solution conditions are necessary. In the present work, for illustration purposes, focus is on the high temperature of 413 K so that bulk PLP experiments suffice.

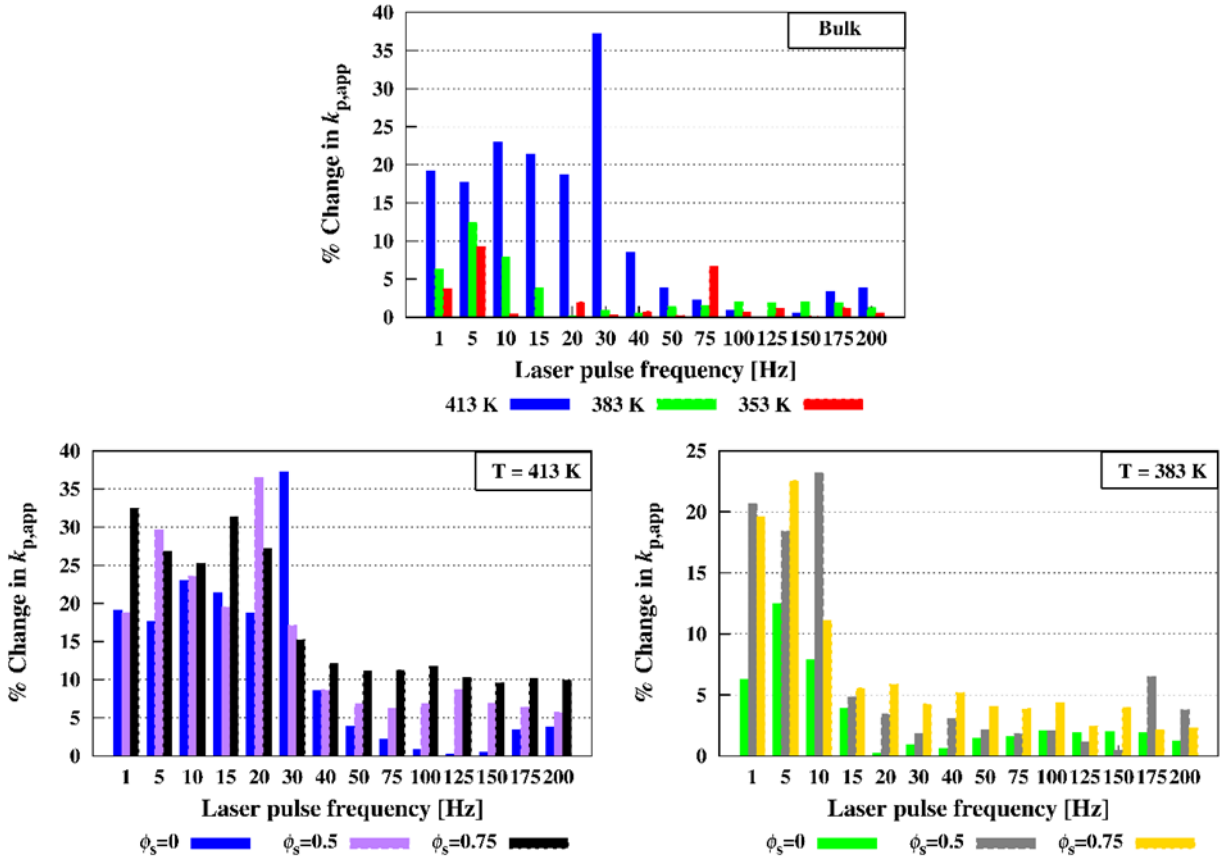

Figure 3. Simulated change in the first inflection point (Equation (1) with $k_{p,app}$ and i=1) vs. laser pulse frequency if the β-scission rate coefficient (k_β) is doubled with respect to reference value (Table 1) in PLP of *n*-butyl acrylate by kinetic Monte Carlo (*k*MC) simulations. Top: temperature influence at solvent volume fraction ϕ_s of 0 (bulk) and reference k_β of 0.52 sec^{-1} (353 K), 2.9 sec^{-1} (383 K), and 12.4 sec^{-1} (413 K); Bottom (left): solvent fraction effect at 413 K, with reference k_β of 12.4 sec^{-1}; Bottom (right): solvent fraction effect at 383 K, with reference k_β of 2.9 sec^{-1}; these results are complementary to the one in Figure 2 where focus only on bulk and 413 K; same colour relates to the same conditions (always bulk).

5.4.3 Application of method to bulk experimental data at 413 K

Figure 4 depicts the $k_{p,app}$ data as obtained from the experimentally recorded first inflection point data for bulk PLP of *n*BuA at 413 K (experimental SEC traces in Figure S1 of Appendix D). The full line represents the model description, using the estimated value of 4.26×10^2 s^{-1} for k_β and the literature values for the other reaction steps as specified in Table 1. Good agreement can be observed between experiment and model, underpinned by the high value for the global significance of the regression (F value of 4.57×10^2 much higher than the tabulated one of 6.61). The dashed lines in Figure 4 are the simulations results upon changing k_β according

to the edges of the 95% confidence interval $(4.26\pm1.8)\times10^2$ s^{-1}, again confirming the aforementioned sensitivity.

Notably the estimated value is higher than previously reported values ($6\cdot10^0$-$1.45\cdot10^2$ s^{-1}; all *ca.* 140°C),[27,28,35,36] which could be attributed to the use of a data set under well-defined conditions, in particular obtained without the interference of other higher temperature reactions such as macropropagation and thermal self-initiation. Furthermore, the SEC trace data in Figure S1 in Appendix D show one inflection point and not two as in Figure 2 (bottom right), where a considerably lower k_β is employed. Hence, the findings based on Figure 2, Figure 4, and Figure S1 in Appendix D, highlight the relevance of the developed method in the future understanding of high temperature acrylate kinetics.

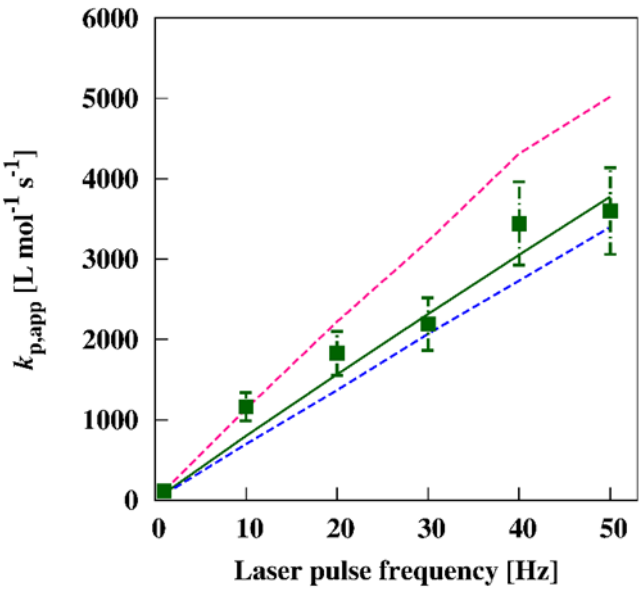

Figure 4. Comparison of experimental and simulated $k_{p,app}$ (first inflection point) for bulk PLP of *n*BuA at 413 K. For the simulation line, the estimated value of 4.26×10^2 s^{-1} is used, as determined in the present work. To highlight the relevance of the parameter estimation also the simulation lines according to the edges of the confidence interval are included: $(4.26\pm1.8) \times 10^2$ s^{-1}. Experimental data are averaged values for three repeat experiments.

5.5 Conclusions

Access to the *β*-scission rate coefficient can be provided in the kinetically significant range for acrylate radical polymerization by the proposed inflection point based PLP method. The method focuses on the lower pulse laser frequencies at elevated temperature and can additionally consider experimental data as obtained by varying the solvent volume fraction using the saturated analogue of the monomer. Rate coefficients of backbiting and tertiary propagation need to be determined *a priori* at sufficiently low temperatures at which *β*-scission can be ignored.

The potential of the method has been demonstrated based on bulk PLP data at 413 K, leading to the kinetic insight that *β*-scission proceeds faster than currently anticipated. The present work therefore contributes to a better global understanding of acrylate kinetics and is essential in future work regarding the relation of the polyacrylate molecular structure and the macroscopic properties at higher temperatures.

5.6 References

1 D. R. D'hooge, P. H. M. Van Steenberge, M. F. Reyniers and G. B. Marin, *Prog. Polym. Sci.*, 2016, **58**, 59–89.

2 J. E. S. Schier, D. Cohen-Sacal and R. A. Hutchinson, *Polym. Chem.*, 2017, **8**, 1943–1952.

3 J. Y. Jiang, L. M. Smith, J. H. Tyrell and M. L. Coote, *Polym. Chem.*, 2017, **8**, 5948–5953.

4 M. Buback, R. G. Gilbert, R. A. Hutchinson, B. Klumperman, F. Kuchta, B. G. Manders, K. F. O'Driscoll, G. T. Russell and J. Schweer, *Macromol. Chem. Phys.*, 1995, **196**, 3267–3280.

5 S. Beuermann, M. Buback, T. P. Davis, R. G. Gilbert, R. A. Hutchinson, O. F. Olaj, G. T. Russell, J. Schweer and A. M. van Herk, *Macromol. Chem. Phys.*, 1997, **198**, 1545–1560.

6 S. Beuermann, M. Buback, T. P. Davis, R. G. Gilbert, R. A. Hutchinson, A. Kajiwara, B. Klumperman and G. T. Russell, *Macromol. Chem. Phys.*, 2000, **201**, 1355–1364.

7 S. Beuermann, M. Buback, T. P. Davis, N. García, R. G. Gilbert, R. A. Hutchinson, A. Kajiwara, M. Kamachi, I. Lacík and G. T. Russell, *Macromol. Chem. Phys.*, 2003, **204**,

1338–1350.

8 S. Beuermann, M. Buback, P. Hesse, F.-D. Kuchta, I. Lacík and A. M. van Herk, *Pure Appl. Chem.*, 2007, **79**, 1463–1469.

9 C. Barner-Kowollik, S. Beuermann, M. Buback, P. Castignolles, B. Charleux, M. L. Coote, R. A. Hutchinson, T. Junkers, I. Lacik, G. T. Russell, M. Stach and A. M. Van Herk, *Polym. Chem.*, 2014, **5**, 204–212.

10 A. P. Aleksandrov, V. N. Genkin, M. S. Kitai, I. M. Smirnova and V. V Sokolov, *Sov. J. Quantum Electron.*, 1977, **7**, 547–550.

11 O. F. Olaj, I. Bitai and F. Hinkelmann, *Makromol. Chem*, 1987, **188**, 1689–1702.

12 A. N. Nikitin, P. Castignolles, B. Charleux and J. P. Vairon, *Macromol. Rapid Commun.*, 2003, **24**, 778–782.

13 M. Buback, P. Hesse and I. Lacík, *Macromol. Rapid Commun.*, 2007, **28**, 2049–2054.

14 A. N. Nikitin, R. A. Hutchinson, M. Buback and P. Hesse, *Macromolecules*, 2007, **40**, 8631–8641.

15 B. Wenn and T. Junkers, *Macromol. Rapid Commun.*, 2016, **37**, 781–787.

16 Y. W. Marien, P. H. M. Van Steenberge, K. B. Kockler, C. Barner-Kowollik, M.-F. Reyniers, D. R. D'hooge and G. B. Marin, *Polym. Chem.*, 2016, **7**, 6521–6528.

17 J. Chiefari, J. Jeffery, R. T. A. Mayadunne, G. Moad, E. Rizzardo and S. H. Thang, *Macromolecules*, 1999, **32**, 7700–7702.

18 S. Liu, S. Srinivasan, M. C. Grady, M. Soroush and A. M. Rappe, *Int. J. Quantum Chem.*, 2014, **114**, 345–360.

19 C. Quan, M. Soroush, M. C. Grady, J. E. Hansen and W. J. Simonsick, *Macromolecules*, 2005, **38**, 7619–7628.

20 T. Junkers and C. Barner-Kowollik, *J. Polym. Sci. Part A Polym. Chem.*, 2008, **46**, 7585–7605.

21 C. Plessis, G. Arzamendi, J. M. Alberdi, a. M. Van Herk, J. R. Leiza and J. M. Asua, *Macromol. Rapid Commun.*, 2003, **21**, 173–177.

22 A. M. Van Herk, *Macromol. Rapid Commun.*, 2009, **30**, 1964–1968.

23 G. Arzamendi, C. Plessis, J. R. Leiza and J. M. Asua, *Macromol. Theory Simulations*, 2003, **12**, 315–324.

24 R. X. E. Willemse, A. M. Van Herk, E. Panchenko, T. Junkers and M. Buback, *Macromolecules*, 2005, **38**, 5098–5103.

25 A. N. F. Peck and R. A. Hutchinson, *Macromolecules*, 2004, **37**, 5944–5951.

26 W. Wang and R. A. Hutchinson, *Chem. Eng. Technol.*, 2010, **33**, 1745–1753.

27 S. Hamzehlou, N. Ballard, Y. Reyes, A. Aguirre, J. M. Asua and J. R. Leiza, *Polym. Chem.*, 2016, **7**, 2069–2077.

28 T. Junkers and C. Barner-Kowollik, *Macromol. Theory Simulations*, 2009, **18**, 421–433.

29 A. Kajiwara, in *Controlled/Living Radical Polymerization: Progress in ATRP*, 2009, vol. 1023, pp. 49–59.

30 N. Ballard and J. M. Asua, *Prog. Polym. Sci.*, 2018, **79**, 40–60.
31 N. Ballard, A. Veloso and J. Asua, *Polymers (Basel).*, 2018, **10**, 765.
32 D. Cuccato, E. Mavroudakis and D. Moscatelli, *J. Phys. Chem. A*, 2013, **117**, 4358–4366.
33 J. Vandenbergh and T. Junkers, *Macromolecules*, 2012, **45**, 6850–6856.
34 P. H. M. Van Steenberge, J. Vandenbergh, M. F. Reyniers, T. Junkers, D. R. D'hooge and G. B. Marin, *Macromolecules*, 2017, **50**, 2625–2636.
35 A. N. Nikitin, R. A. Hutchinson, W. Wang, G. A. Kalfas, J. R. Richards and C. Bruni, *Macromol. React. Eng.*, 2010, **4**, 691–706.
36 D. Cuccato, E. Mavroudakis, M. Dossi and D. Moscatelli, *Macromol. Theory Simulations*, 2013, **22**, 127–135.
37 M. Soroush, M. C. Grady and G. A. Kalfas, *Comput. Chem. Eng.*, 2008, **32**, 2155–2167.
38 F. S. Rantow, M. Soroush, M. C. Grady and G. A. Kalfas, *Polymer (Guildf).*, 2006, **47**, 1423–1435.
39 A. Shamsabadi, N. Moghadam, S. Srinivasan, P. Corcoran, M. Grady, A. Rappe and M. Soroush, *Processes*, 2016, **4**, 26.
40 P. Derboven, P. H. M. Van Steenberge, J. Vandenbergh, M. F. Reyniers, T. Junkers, D. R. D'hooge and G. B. Marin, *Macromol. Rapid Commun.*, 2015, **36**, 2149–2155.
41 A. N. Nikitin, I. Lacík and R. A. Hutchinson, *Macromolecules*, 2016, **49**, 9320–9335.
42 E. Penzel and N. Goetz, *Die Angew. Makromol. Chem.*, 1990, **178**, 191–200.
43 S. Beuermann, D. A. Paquet, J. H. McMinn and R. A. Hutchinson, *Macromolecules*, 1996, **29**, 4206–4215.
44 Y. W. Marien, P. H. M. Van Steenberge, C. Barner-Kowollik, M. F. Reyniers, G. B. Marin and D. R. D'hooge, *Macromolecules*, 2017, **50**, 1371–1385.
45 Y. W. Marien, P. H. M. Van Steenberge, K. B. Kockler, C. Barner-Kowollik, M.-F. Reyniers, G. B. Marin and D. R. D'hooge, *Polym. Chem.*, 2017, **8**, 3124–3128.
46 G. B. Desmet, Y. W. Marien, P. H. M. Van Steenberge, D. R. D'hooge, M. F. Reyniers and G. B. Marin, *Polym. Chem.*, 2017, **8**, 7143–7150.
47 H. Fischer, R. Baer, R. Hany, I. Verhoolen and M. Walbiner, *J. Chem. Soc. Perkin Trans. II*, 1990, 787–798.
48 J. M. Asua, S. Beuermann, M. Buback, P. Castignolles, B. Charleux, R. G. Gilbert, R. A. Hutchinson, J. R. Leiza, A. N. Nikitin, J. P. Vairon and A. M. Van Herk, *Macromol. Chem. Phys.*, 2004, **205**, 2151–2160.
49 J. Barth, M. Buback, P. Hesse and T. Sergeeva, *Macromolecules*, 2010, **43**, 4023–4031.
50 S. Maeder and R. G. Gilbert, *Macromolecules*, 1998, **31**, 4410–4418.
51 M. Buback, M. Busch and C. Kowollik, *Macromol. Theory Simulations*, 2000, **9**, 442–452.
52 C. Farcet, J. Belleney, B. Charleux and R. Pirri, *Macromolecules*, 2002, **35**, 4912–4918.
53 H. Riazi, A. A. Shamsabadi, P. Corcoran, M. C. Grady, A. M. Rappe and M. Soroush,

Processes, 2018, **6**, 3.

54 I. Chavez-Sumarriva, P. H. M. Van Steenberge and D. R. D'hooge, *Ind. Eng. Chem. Res.*, 2016, **55**, 9387–9396.

55 C. Toloza Porras, D. R. D'hooge, P. H. M. Van Steenberge, M. F. Reyniers and G. B. Marin, *Ind. Eng. Chem. Res.*, 2014, **53**, 9674–9685.

56 C. Barner-Kowollik, P. Vana and T. P. Davis, *J. Polym. Sci. Part A Polym. Chem.*, 2002, **40**, 675–681.

57 J. P. A. Heuts and G. T. Russell, *Eur. Polym. J.*, 2006, **42**, 3–20.

58 J. J. Haven, J. Vandenbergh, R. Kurita, J. Gruber and T. Junkers, *Polym. Chem.*, 2015, **6**, 5752–5765.

59 N. Ballard, S. Hamzehlou and J. M. Asua, *Macromolecules*, 2016, **49**, 5418–5426.

60 S. P. S. Koo, T. Junkers and C. Barner-kowollik, *Macromolecules*, 2009, **42**, 62–69.

61 W. Wang, A. N. Nikitin and R. A. Hutchinson, *Macromol. Rapid Commun.*, 2009, **30**, 2022–2027.

62 C. Barner-Kowollik, F. Günzler and T. Junkers, *Macromolecules*, 2008, **41**, 8971–8973.

Chapter 6: Particle by particle kinetic Monte Carlo tracking of reaction and mass transfer events in miniemulsion free radical homopolymerization

Summary

In many studies on emulsion polymerization emphasis is on a constant average particle size and an average monomer concentration for all particles, and the zero-one or pseudo-bulk approximation is applied. Based on kinetic Monte Carlo simulations it is demonstrated that the kinetics need to be followed particle by particle while acknowledging the difference in radical and monomer concentration per particle in contrast to the conventional Smith-Ewart methodology. Focus is on miniemulsion free radical polymerization, with physically reasonable values for all parameters and considering interphase mass transfer of initiator and monomer molecules and initiator-derived, monomeric and oligomeric radicals, following a diffusion-based approach. The temporal evolutions of the chain length distribution (CLD) and the particle size distribution (PSD) are correlated and affected by radical exit/entry and monomer mass transfer. The results unveil unprecedented insight in dispersed phase radical polymerizations and open the pathway to a joint PSD and CLD control and design.

6.1 Introduction

Emulsion radical polymerizations are extensively used to synthesize dry polymers for rubber production or waterborne latexes with applications such as paints, coatings, adhesives and drug delivery.[1-7] These polymerizations are characterized by an organic phase that is dispersed in an aqueous medium in the presence of emulsifier or surfactant. In the industrial (macro)emulsion process large monomer droplets (> 1 μm), (monomer swollen) micelles (5-10 nm), and polymer nanoparticles (d_p = 10-500 nm) are present, making it a much more dynamic process than

conventional bulk polymerization, due to the existence of several reaction loci and interphase interactions.[8-11]

A special class of emulsion radical polymerization is miniemulsion radical polymerization in which only small monomer droplets/particles (< 500 nm), as formed under high shear conditions with (co)stabilizer, are initially present. The miniemulsion kinetics converting these monomer droplets/particles into polymer particles are complicated and characterized by many competing phenomena taking place on different length and time scales.[12] For example, radicals can enter and exit the particles, strongly affecting the chain growth pattern per particle. Depending on the initiator type, radicals are generated upon initiator dissociation in the organic and/or aqueous phase. In case initiator dissociation takes place in the aqueous phase, polymer particles containing a single radical are created upon entry of a radical to a monomer droplet/particle or an inactive polymer particle. In case initiator dissociation takes place in a particle, two radicals are created simultaneously in a small volume leading to large termination probabilities, the so called confined space or single molecule concentration effect[13-18], at least if exit of radicals is unlikely. However, if exit of one radical occurs, the remaining radical can grow significantly and termination is delayed, changing the miniemulsion kinetics and polymer properties. It is therefore not surprising that several contradictory postulations have been made related to the faith of radicals generated in miniemulsion polymerization.[19-26]

In order to resolve this issue kinetic modeling has been applied, in most cases focusing only on the calculation of the evolution of the monomer conversion (X_M) and the average particle radical concentration or equivalently the average number of radicals per particle, $\bar{n}$. Often deterministic models describing the temporal evolution of the number of particles containing certain numbers of one or more radical types have been considered. These models assume an average particle size and an average particle monomer concentration which is updated at each integration step.[14, 25, 27-34] Such deterministic description has been originally introduced in the pioneering work of

Smith and Ewart[35] for emulsion free radical polymerization (FRP) with a water-soluble initiator, leading to textbook limiting cases for $\bar{n}$. With negligible exit and instantaneous termination in small particles, zero-one kinetics (maximally one radical per particle) are obtained and $\bar{n}$ approaches a limiting value of 0.5. With larger particles (*e.g.* d_p > 200 nm), high initiator concentrations and/or low (apparent) termination rates, *e.g.* due to a strong gel effect, $\bar{n}$ becomes much higher than 0.5 and the pseudo-bulk kinetic limit is obtained.[12]

For zero-one-two systems (maximally two radicals per particle), Smith-Ewart models have been also extended to so-called doubly distinguished particle models to calculate next to the monomer conversion evolution the variation of the chain length distribution (CLD). Specifically for particles with 2 radicals population balances are integrated accounting for the variation of the (two) chain lengths.[27-30] Population balance equations describing the temporal evolution of the particle size distribution (PSD) due to particle nucleation, coagulation and growth have been also considered.[36-40] To avoid numerical difficulties these intractable multidimensional population balances have been constructed assuming zero-one or pseudo-bulk kinetics and ignoring the chain length dependent nature of apparent termination kinetics. The potential of Smith-Ewart based models has been further highlighted for the more recently developed reversible deactivation radical polymerization (RDRP) techniques. For example, Zetterlund *et al*.[14, 41, 42] investigated the relevance of compartmentalization for nitroxide mediated polymerization (NMP), differentiating between nanoparticles with *x* macroradicals and *y* nitroxide radicals so that conventional population balances needed to be extended to two-dimensional Smith-Ewart equations. Further extensions were made by Van Steenberge *et al*.[34] covering more NMP radical types, leading to 4-dimensional Smith-Ewart equations, and toward the calculation of average polymer properties such as the end-group functionality, the number average chain length x_n, the dispersity, and the short branching content, with the average chain length characteristics approximated under the validity of the pseudo-bulk approximation.[33]

Alternatively, stochastic or kinetic Monte Carlo (*k*MC) modeling has been applied to simulate the monomer conversion evolution, $\bar{n}$, and the chain length distribution in FRP (mini)emulsion polymerization.[18, 43-49] For example, for miniemulsion polymerization with water-soluble initiators and a single radical type, Tobita *et al.*[18, 44] simulated the reaction events of a single particle up to a certain time, calculating the aqueous phase radical concentration based on the pseudo-steady state approximation (PSSA). Noise-free results are then obtained by repeating the single particle simulation *e.g.* 200 times. A downside is that the interaction between particles due to exit and re-entry phenomena is not fundamentally captured. The concept of single particle simulations has been also considered by Arzamendi and Leiza,[45] who additionally accounted for semi-batch operation modes and the presence of both end- and mid-chain radicals with *n*-butyl acrylate as monomer. Within the field of RDRP, Tobita and Yanase[18] developed a basic *k*MC model for reversible addition fragmentation chain transfer (RAFT) polymerization and NMP miniemulsion polymerization, considering a single particle size and focusing on the effect of this particle size on the polymerization rate, neglecting radical exit, chain transfer reactions and chain length dependent termination and again simulating one particle at a time. Also Luo *et al.*[47] developed a *k*MC model for RAFT miniemulsion polymerization, focusing on the effect of the RAFT agent on droplet nucleation, however only simulating one particle. Furthermore, only a very limited number of *k*MC studies have focused on the calculation of the PSD.[46, 50] For instance, Nie *et al.*,[46] developed a *k*MC model for microemulsion FRP, which is commenced with small monomer droplets and micelles, taking into account the PSD variation but assuming zero-one kinetics *a priori*, limiting the applicability of the model.

Despite the significant progress in the (mini)emulsion modeling field major challenges persist as several simplifications are still commonly applied. A first simplification, as highlighted above, is that most models assume a limited maximum number of radicals per particle (*e.g.* 2) combined with an average (constant) particle diameter and, hence, do not consider the entire

PSD, although this distribution is a key and dynamic emulsion property.[37, 51-53] A second simplification is that typical models consider an average particle monomer concentration, whilst monomer fluctuations along reaction loci are expected as a function of time.[54] A third simplification relates to the calculation method for mass transfer phenomena. For radical exit and entry diffusion-based models are often considered in which the entry and exit rate coefficients are a function of the diffusion coefficients and the reaction locus diameter,[6, 33, 34, 55-58] with as a constraint a constant, hence, simplified partitioning coefficient. For monomer mass transfer, a diffusion-based approach has also been applied. For example, Rodriguez *et al.*[59] considered monomer mass balances describing the evolution of the average monomer concentration in the monomer droplets/particles and in the polymer particles while assuming an average size for both populations and solving the Smith-Ewart equations for $\bar{n}$, taking into account monomer mass transfer via diffusion from the droplets and via the aqueous phase to the particles or via collisions between droplets and particles. Mostly thermodynamic models based on the Morton equation have been considered for the description of monomer mass transfer, in which the equilibrium state that is strived for is a function of hard to determine Flory-Huggins interaction parameters and the particle diameter.[54, 60-65] In these models, focus is restricted to the description of the evolution of the PSD as a result of monomer mass transfer, *e.g.* due to Ostwald ripening, either in the absence of polymerization or with simplified reaction kinetics. For example, by assuming equal monomer chemical potentials in all droplets/particles at each simulation step, neglecting the surface energy contribution, *i.e.* the size dependent term of the Morton equation, and by formally describing $\bar{n}$, Jansen *et al.*[54] theoretically showed that monomer mass transfer can lead to droplet disappearance and a narrowing of the PSD. Very recently Asua[65] theoretically described mass transfer of a reactive costabilizer, *e.g.* comonomer, due to Ostwald ripening from small to large nanoparticles (PSD with initially two peaks). In this work, a film diffusion model with artificial Flory-Huggins interaction parameters was

considered, describing mass transfer of the reactive costabilizer either in the absence of polymerization or for different artificial values of the polymerization rate.

The aforementioned three types of simplifications limit the correctness of (mini)emulsion polymerization kinetic simulations. At the micro-scale (Figure 1; top),[9] which is conceptually defined as an ensemble of molecules so that for a given phase local concentration changes can be calculated and local restrictions due to diffusivity changes can be captured, the reaction probabilities depend on the monomer concentration. At the meso-scale (Figure 1; top), which transcends a local single phase kinetic variation, interphase mass transfer phenomena, *e.g.* radical exit and entry, are particle size dependent.[35, 58, 66-68] Hence, from a fundamental point of view the (mini)emulsion kinetics and particle growth are coupled in contrast to what is assumed upon the consideration of particle averages.

As computing power grows exponentially over time, it has become worthwhile to develop more detailed *k*MC (mini)emulsion kinetic models avoiding the previously mentioned simplifications. Main computational focus has however been on improving the description of bulk/solution polymerization benefiting from the introduction of composite binary trees and matrix-based representations.[69-77] Very recently, Drache *et al.*[50] developed a *k*MC model for the seeded radical emulsion polymerization of styrene initiated by a water-soluble initiator. While in that work the entire PSD is taken into account, which allows to assign higher probabilities for entry to larger particles, the Maxwell-Morrison or so-called propagation controlled mechanism[78] is assumed. This means that radical entry is only allowed once a radical reaches a critical chain length and this entry takes place instantaneously and irreversibly, *i.e.* exit of radicals is ignored. For oil-soluble initiators the Maxwell-Morrison approach cannot be applied.

In the present work, a novel *k*MC modeling tool is presented allowing the simulation of isothermal batch miniemulsion radical polymerization, explicitly taking into account the evolution of the PSD and its correlation with the CLD. In contrast to previous work, the *k*MC

modeling tool does not rely on the simplification of an average particle monomer concentration, a maximum number of radicals per particle, a Maxwell-Morrison entry mechanism, chain length independent termination kinetics or a pseudo-bulk approximation for the calculation of chain length characteristics. The *k*MC model has of course the possibility to include these simplifications. Indeed, in the first part of this work an average particle monomer concentration, a Mawell-Morrison entry mechanism and chain length independent termination kinetics are considered to benchmark the *k*MC model to a conventional Smith-Ewart model. In the second part of this work, the *k*MC modeling tool is applied in its full detail, *i.e.* all the aforementioned simplifications are avoided. As such, it is demonstrated that the developed model opens the window to a much more detailed understanding of miniemulsion FRP kinetics and particle growth and that the interaction of micro- and meso-scale phenomena is essential to fully design radical dispersed phase polymerizations.

6.2 Model development

In the present work, a novel *k*MC tool is developed to describe the kinetics and particle growth for dispersed phase radical polymerization involving nanosized reaction loci. For illustration purposes focus is on isothermal batch miniemulsion FRP in which the initial state is a distribution of small monomer droplets (< 500 nm) with conventional radical initiator that can thermally decompose. The novelty lies in the explicit consideration of kinetic non-uniformities due to differences in particle size, such as the temporal evolution of the number of radicals and chain growth, and of the interaction of micro- and meso-scale phenomena.

This implies that the micro-scale reaction events in the organic and aqueous phase and meso-scale mass transfer phenomena between those phases are sampled - for the first time - particle by particle, as conceptually illustrated in Figure 1 (top). In contrast to previous modeling studies,[14, 25, 27-34, 44, 46, 48] the particle kinetics are not tracked assuming a constant average particle size and an average particle monomer concentration that is updated per integration step,

and no zero-one or pseudo-bulk approximation is needed to assess the average chain length characteristics. Instead, at each time the interplay of the complete CLD and the complete PSD is captured (Figure 1; bottom). Hence, observed chain length and particle size averages can be retrieved *a posteriori* as the actual individual distributions are always available. The core of the model is the Gillespie algorithm[79] as commonly applied to stochastically describe the kinetics of bulk/solution polymerization, with storage and execution of events conducted based on composite binary trees as introduced by Van Steenberge *et al.*[34] More details on the *k*MC modeling tool are provided in Appendix E, including a flow chart (Figure S1) with the essential model implementations and extensions with respect to bulk/solution *k*MC models as previously developed.

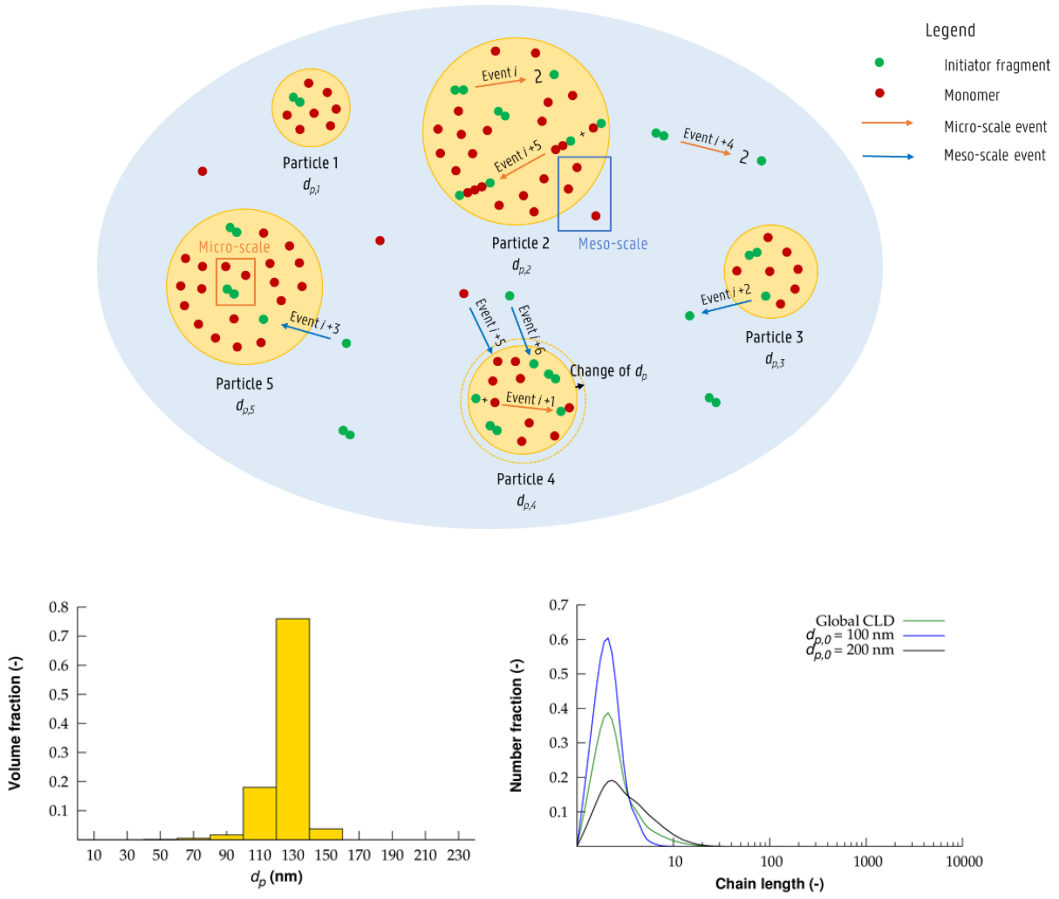

Figure 1. Top: illustration of the principle of the novel kinetic Monte Carlo (*k*MC) modeling tool to account for consecutive reaction and mass transfer events in miniemulsion free radical polymerization explicitly accounting for differences in particle size and composition (e.g. number of radicals and monomer concentration). Six consecutive events are shown, starting at event *i* (at a certain time *t*): dissociation in particle 2; chain initiation in particle 4; initiator radical exit from particle 3; initiator radical entry to particle 4; termination in particle 2; several (lumped) monomer entries to particle 4 altering the particle size; and entry of an initiator radical; after each event the time step is stochastically increased, *i.e.* steps 2 – 6 in Figure S1 of Appendix E are executed; Bottom: examples of model output, including the particle size distribution (PSD) and the chain length distribution (CLD) per particle size (next to the global one) as a function of time (here simplified case with initially only two particle diameters: 100 and 200 nm). The strength lies in the interactive calculation of CLD and PSD, *i.e.* the interplay between micro- and meso-scale phenomena.

An overview of the reactions and mass transfer events is shown in Table 1, with diffusional limitations on the micro-scale captured by apparent rate coefficients[9, 80-84] and meso-scale mass transfer coefficients calculated with a diffusion-based approach. [6, 33, 34, 55-58] Most important are diffusional limitations on termination for which chain length and monomer conversion dependent apparent rate coefficients are used,[85] as calculated based on the RAFT-CLD-T technique (Equation (S5)-(S9) in Appendix E). At each time step, each termination possibility

between a radical of chain length *i* and chain length *j* ($k_{t,app}$ (*i*,*j*)) in a certain particle is considered explicitly. For simplicity, only termination by recombination is considered. For all model parameters, typical orders of magnitude are employed, with some simplifications in view of the conceptual framework of the work, *e.g.* the same (intrinsic) reactivity for organic and aqueous phase reactions. For simplicity diffusional limitations on propagation are ignored as even under bulk conditions these are likely only relevant at very high monomer conversion (> 0.95).[81]

First the *k*MC tool is benchmarked to a conventional Smith-Ewart model, which assumes an average particle size and an average monomer concentration per particle (formally no monomer fluctuations over the particles) at each integration step (case of a water soluble initiator). Next an oil-soluble initiator is considered, as envisaged by a high partition coefficient (Γ_{I2} = 100 = $[I_{2,org}]_{eq}/[I_{2,w}]_{eq}$). Exit and entry propensities are calculated as outlined in the emulsion research field.[6, 37, 55-58] Partitioning of all radical types is allowed, with the exception of macroradicals with a chain length larger than the critical one for solubility in the aqueous phase (i_{sol} = 5; typical value[37]). For illustration purposes, a bimodal initial monomer droplet size distribution is assumed, consisting of two monodisperse peaks relating to an initial diameter ($d_{p,0}$) of 100 nm and 200 nm leading to an equal total volume of both particle types. The difference in density between monomer and polymer is neglected for simplicity.

Table 1. Reactions and mass transfer events for the simulation of isothermal miniemulsion FRP (Figure 3-11); for benchmark to Smith-Ewart model (Figure 2): no mass transfer events except entry of R_4. For illustration purposes, orders of magnitude for all parameters[24, 25, 31, 85-87] and the same (intrinsic) reactivity for reactions in the organic and aqueous phase; initiator efficiency of 1 for simplicity; the reported k for entry and exit events corresponds to a particle diameter of 100 nm (general formulas: see footnotes). Also specified are the time scales at t = 0 min for a particle diameter of 100 and 200 nm (formulas for these scales: Table S1 in Appendix E); the partition coefficients (organic over water) are literature based: Γ_{I_2} = 100, Γ_{I} = 10, Γ_{M} = 800, Γ_{M^*} = 800, Γ_{R} ($i \le i_{\mathrm{sol}}$) = 10, and Γ_{R} ($i > i_{\mathrm{sol}}$) = ∞ with i_{sol} the maximum chain length of a radical present in the aqueous phase (5).

Event	Equation	k (d_p = 100 nm)	τ_0 [s] (d_p= 100 nm)	τ_0 [s] (d_p= 200 nm)
Reactions in particles				
Dissociation	$I_{2,p} \xrightarrow{k_{d,p}} 2\, I_p$	10^{-5} s^{-1}	10^{5}	10^{5}
Chain initiation	$I_p + M_p \xrightarrow{k_{i,p}} R_{1,p}$	10^{3} L mol^{-1} s^{-1}	1.3 10^{-4}	1.3 10^{-4}
	$M_p^* + M_p \xrightarrow{k_{i,p}} R_{1,p}$	10^{3} L mol^{-1} s^{-1}	1.3 10^{-4}	1.3 10^{-4}
Propagation	$R_{i,p} + M_p \xrightarrow{k_{p,p}} R_{i+1,p}$	10^{2} L mol^{-1} s^{-1}	1.3 10^{-3}	1.3 10^{-3}
Chain transfer to monomer	$R_{i,p} + M_p \xrightarrow{k_{trM,p}} M_p^* + P_{i,p}$	10^{-2} L mol^{-1} s^{-1}	1.3 10^{1}	1.3 10^{1}
Termination [a]	$R_{i,p} + R_{j,p} \xrightarrow{k_{t,app,p}} P_{i+j,p}$	10^{9} L mol^{-1} s^{-1} [b]	3.2 10^{-4}	2.5 10^{-3}
Reactions in water				
Dissociation	$I_{2,w} \xrightarrow{k_{d,w}} 2\, I_w$	10^{-5} s^{-1}	10^{5}	10^{5}
Chain initiation	$I_w + M_w \xrightarrow{k_{i,w}} R_{1,w}$	10^{3} L mol^{-1} s^{-1}	1.0 10^{-1}	1.0 10^{-1}
	$M_w^* + M_w \xrightarrow{k_{i,w}} R_{1,w}$	10^{3} L mol^{-1} s^{-1}	1.0 10^{-1}	1.0 10^{-1}
Propagation	$R_{i,w} + M_w \xrightarrow{k_{p,w}} R_{i+1,w}$	10^{2} L mol^{-1} s^{-1}	1.0 10^{0}	1.0 10^{0}
Chain transfer to monomer	$R_{i,w} + M_w \xrightarrow{k_{trM,w}} M_w^* + P_{i,w}$	10^{-2} L mol^{-1} s^{-1}	1.0 10^{4}	1.0 10^{4}
Termination [a]	$R_{i,w} + R_{j,w} \xrightarrow{k_{t,app,w}} P_{i+j,w}$	10^{9} L mol^{-1} s^{-1} [a]	1.6 10^{-1}	1.6 10^{-1}
Phase transfer events				
Entry of I_2 [b]	$I_{2,w} \xrightarrow{k_{entry,I_2}} I_{2,p}$	6 10^{5} L mol^{-1} s^{-1}	2.7 10^{2}	1.4 10^{2}
Entry of I [b]	$I_w \xrightarrow{k_{entry,I}} I_p$	6 10^{5} L mol^{-1} s^{-1}	2.7 10^{2}	1.4 10^{2}
Entry of M [b]	$M_w \xrightarrow{k_{entry,M}} M_p$	6 10^{5} L mol^{-1} s^{-1}	2.7 10^{2}	1.4 10^{2}
Entry of M^* [b]	$M_w^* \xrightarrow{k_{entry,M^*}} M_p^*$	6 10^{5} L mol^{-1} s^{-1}	2.7 10^{2}	1.4 10^{2}
Entry of R_i [b,c]	$R_{i,w} \xrightarrow{k_{entry,R}} R_{i,p}$	6 10^{5} L mol^{-1} s^{-1} [c]	2.7 10^{2}	1.4 10^{2}
Exit of I_2 [d]	$I_{2,p} \xrightarrow{k_{exit,I_2}} I_{2,w}$	2 10^{-2} s^{-1}	5.2 10^{1}	2.1 10^{2}
Exit of I [d]	$I_p \xrightarrow{k_{exit,I}} I_w$	2 10^{-1} s^{-1}	5.2 10^{0}	2.1 10^{1}
Exit of M [d]	$M_p \xrightarrow{k_{exit,M}} M_w$	2 10^{-3} s^{-1}	4.2 10^{2}	1.7 10^{3}
Exit of M^* [d]	$M_p^* \xrightarrow{k_{exit,M^*}} M_w^*$	2 10^{-3} s^{-1}	4.2 10^{2}	1.7 10^{3}
Exit of R_i [c,d]	$R_{i,p} \xrightarrow{k_{exit,R}} R_{i,w}$	2 10^{-1} s^{-1} [c]	5.2 10^{0}	2.1 10^{1}

[a] apparent termination coefficients (RAFT-CLD-T): Equation (S5)-(S9) in Appendix E;[85] α_S = 0.5 , α_L = 0.15, $\alpha_{gel} = m_p$–0.1; i_{SL} = 30, i_{gel} = 3 m_p^{-2}; $k_{t,app}$ for $i = j$ = 1 and m_p = 0 (no polymer) is only reported here.

[b] $k_{entry,I/M^*/R} = C_{entry,I/M^*/R}\, N_A\, D_{I/M^*/R,w}\, d_p$ with $C_{entry,I/M^*/R} = 10^{-5}$ and $D_{I/M^*,} = D_{R,w}$ (i = 1) = 10^{-7} dm^2 s^{-1}; $D_{R,w}$(i): Equation (S10) in Appendix E.

[c] value for i = 1 is reported here.

[d] $k_{exit,I/M^*/R} = C_{exit,I/M^*/R}\, D_{I/M^*/R,p}\, d_p^{-2}$ with $C_{exit,I/M^*/R} = 6\, C_{entry,I/M^*/R}\, D_{I/M^*/R,w}\, \pi^{-1}\, \Gamma_{I/M^*/R}^{-1}\, D_{I/M^*/R,p}^{-1}$ (references[6, 33, 34, 55-58]); $D_{R,p}$ (i = 1) = 10^{-7} dm^2 s^{-1}; $D_{R,p}(i)$: Equation (S10) in Appendix E.[87]

6.3 Results and Discussion

6.3.1 Benchmark to a conventional Smith-Ewart model: average polymerization characteristics based on the simplification of one particle size and an average particle monomer concentration

A benchmark of the novel *k*MC modeling tool is first performed to a conventional Smith-Ewart based model for miniemulsion FRP with a basic reaction scheme considering a water-soluble initiator, and assuming intrinsic kinetics, a constant particle diameter (50 nm), an average particle monomer concentration (no monomer fluctuations over particles), and a Maxwell-Morrison entry mechanism. The basic reaction scheme implies that only dissociation, chain initiation and propagation in the aqueous phase, entry of macroradicals to the particles (i=4) and propagation and termination in the particles are taken in account. Hence, in Table 1, the rate coefficients for chain transfer to monomer (both in the aqueous and organic phase), for termination in the aqueous phase and for exit and entry of initiator and monomeric radicals as well as initiator and monomer molecules are given a zero value.

Focus is on the simulation of temporal evolution of $\bar{n}$, X_M, and the 'dead' polymer number and the mass average chain length x_n and x_m. For the *k*MC model the flowsheet (Figure S1 of Appendix E) is used but with the simplification that the particles are overruled by average monomer concentrations each stochastic time step. The deterministic equations of the Smith-Ewart model (Equation (S11)-(S21)), in addition to the associated moment equations for the determination of x_n and x_m (Equation (S22)-(S29)), are given in Appendix E.

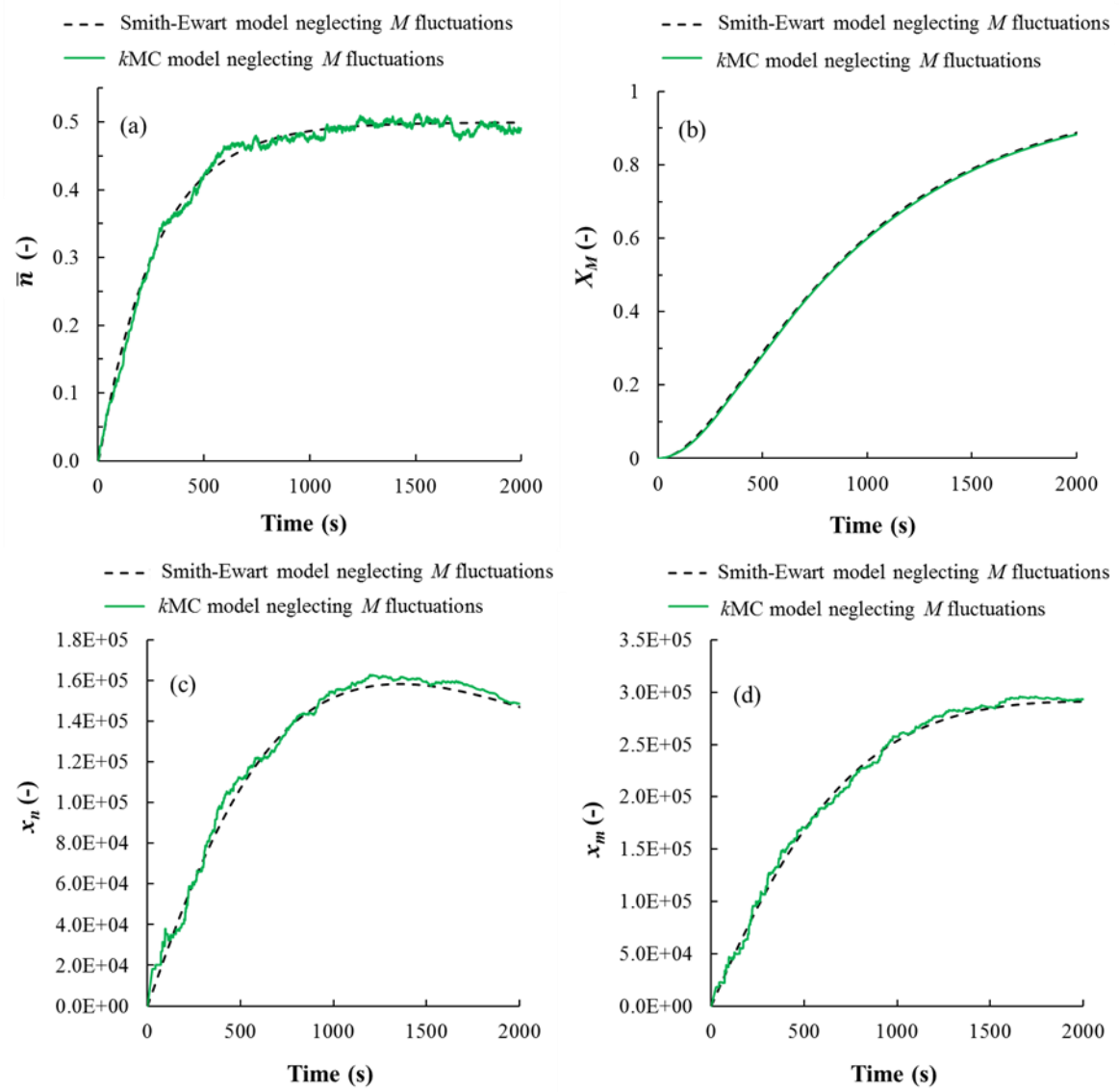

Figure 2. Successful benchmark with the conventional Smith-Ewart based model (details in Appendix E) under the constraint/simplification of the absence of monomer fluctuations over the particles (average monomer concentration), a single particle size (50 nm), and intrinsic kinetics: comparison of the average number of radicals per particle $\bar{n}$ (a), monomer conversion X_M (b), the 'dead' polymer number average chain length x_n (c), and the mass average chain length x_m (d) for an oil-in-water miniemulsion free radical polymerization with a water-soluble initiator ; $[I_2]_w = 10^{-3}$ mol L^{-1}, $[I_2]_p = 0$ mol L^{-1}, $[M]_w = 10^{-2}$ mol L^{-1}, $[M]_p = 8$ mol L^{-1}; $k_{d,w} = 10^{-5}$ s^{-1}, $k_{i,w} = 10^3$ L mol^{-1} s^{-1}, $k_{p,w} = 10^2$ L mol^{-1} s^{-1}, $C_{entry,R} = 10^{-5}$, $k_{p,p} = 10^3$ L mol^{-1} s^{-1}, $k_{t,p} = 10^9$ L mol^{-1} s^{-1}; all other rate coefficients listed in Table 1 are given a value equal to zero: 1023 particles are stochastically simulated; Smith-Ewart model (black dashed lines): Equation (S11)-(S29) in Appendix E; *k*MC model (green full lines): the flowsheet (Figure S1 of Appendix E) is used but with the simplification that the particles are overruled by average monomer concentrations. Figure S2 of Appendix E shows the evolution of X_M, x_n and x_m if monomer fluctuations are accounted for (*i.e.* no average particle monomer concentration assumed): deviations are observed, highlighting the relevance of the developed model.

The excellent benchmark between the simplified *k*MC model (green full lines) and the Smith-Ewart model (dashed black lines) results are shown in Figure 2 under typical initial conditions:

$[I_2]_w = 10^{-3}$ mol L^{-1}, $[I_2]_p = 0$ mol L^{-1}, $[M]_w = 10^{-2}$ mol L^{-1}, and $[M]_p = 8$ mol L^{-1}. From Figure 2 (a) it follows that $\bar{n}$ initially increases as a function of time as entry more and more creates active particles with one radical. This increase converges toward a limiting value of 0.5, consistent with the large termination rate coefficient (no diffusional limitations) and the absence of radical exit, *i.e.* a miniemulsion is obtained in which as soon as a particle contains two radicals termination takes place. The low x_n (Figure 2 (c)) and x_m (Figure 2 (d)) values at low reaction times ($t < 200$ s) imply that radicals that entered a same particle only had a limited time for chain growth. At higher times ($t > 200$ s), active particles with one radical had more time for chain growth before entry causes termination, consistent with the higher x_n and x_m values. From Figure 2 (b) it can be observed that the increase in $\bar{n}$ for $t < 750$ s leads to a fast increase in X_M. For $t > 750$ s the increase in X_M becomes lower as the decrease in monomer concentration in the particles becomes dominant, which also explains the maximum observed in the evolution of x_n (Figure 2 (c) and x_m (Figure 2 (d)).

It is important to note that a different evolution of X_M, x_n and x_m are obtained if the monomer fluctuations over the particles are accounted for in the *k*MC model, as shown in Figure S2 of Appendix E (blue lines). This clearly indicates the need for the novel modeling methodology with an explicit consideration of monomer mass transfer.

6.3.2 Beyond the conventional description: interaction of CLD and PSD with monomer fluctuations

To illustrate the importance of exit and entry of the radical species (*e.g.* initiator and vinyl radicals) and non-radical species (*e.g.* monomer and initiator) in isothermal miniemulsion FRP initiated by an oil-soluble initiator (model parameters: Table 1), a stepwise extension of the *k*MC model is considered, as illustrated in Table 2. In a first step (case 1 in Table 2), initiator dissociation, chain initiation, propagation, chain transfer to monomer, and termination are considered in both the organic and aqueous phase, assuming intrinsic kinetics. In the next three

steps (case 2-4 in Table 2), respectively exit/entry of initiator radicals, monomeric radicals formed via chain transfer to monomer and macroradicals are consecutively added as reaction possibility. In case 5 and 6 in Table 2, also exit/entry of respectively monomer, and monomer and initiator is considered. Finally, chain length and monomer conversion dependent apparent termination kinetics are taken into account (case 7 in Table 2). Note that for the cases with monomer transport (case 5-7 in Table 2) a time dependent PSD is obtained, whereas in the other cases (cases 1-4 in Table 2) the initial bimodality is theoretically maintained.

Table 2. Theoretical cases to illustrate in a step-wise manner the relevance of each exit/entry in Table 1, and the apparent chain length and monomer conversion dependence for termination; hence, only in the last case (case 7) all phenomena of Table 1, including apparent termination kinetics, are accounted for: Figure 3-11 gradually capture this increase in complexity.

Case	Dissociation	Chain initiation	Propagation	Chain transfer to monomer	Termination	Exit/entry of I	Exit/entry of M^*	Exit/entry of R_i	Exit/entry of M	Exit/entry of I_2	CLD-T[a]
1	✓	✓	✓	✓	✓	×	×	×	×	×	×
2	✓	✓	✓	✓	✓	✓	×	×	×	×	×
3	✓	✓	✓	✓	✓	✓	✓	×	×	×	×
4	✓	✓	✓	✓	✓	✓	✓	✓	×	×	×
5	✓	✓	✓	✓	✓	✓	✓	✓	✓	×	×
6	✓	✓	✓	✓	✓	✓	✓	✓	✓	✓	×
7	✓	✓	✓	✓	✓	✓	✓	✓	✓	✓	✓

[a]chain length dependent termination.

Importance of exit and entry of initiator radicals

The effect of exit and entry of initiator radicals on the miniemulsion FRP kinetics, starting from a bimodal PSD with peaks at 100 nm and 200 nm (equal volume fraction for both particle types) and an oil-soluble initiator, is illustrated in Figure 3. This figure shows for case 1 in Table 2 (no exit/entry of any species; red lines) and case 2 in Table 2 (exit/entry of only initiator radicals; green lines) the temporal evolution of the concentration of initiator (a), 'dead' polymer (b), monomer (c), and the 'dead' polymer number average chain length x_n (d) for particles having a $d_{p,0}$ of 100 nm (full lines) and 200 nm (dotted lines). Note that in the remainder of the text this line type distinction (full lines for $d_{p,0}$ = 100 nm and dotted line for $d_{p,0}$ = 200 nm) is always followed.

As initiator dissociation is an irreversible unimolecular reaction, the decrease of the initiator concentration is the same for both particle sizes and the temporal evolution of the initiator concentration is unaffected by exit/entry of initiator radicals (coinciding lines for case 1 and case 2 in Figure 3 (a)). On the other hand, the temporal evolution of x_n (Figure 3 (d)) is strongly affected by exit/entry of initiator radicals. In case 1 (without exit/entry) much lower x_n values are obtained compared to case 2 (with exit/entry of I). The effect also depends on the particle size. In case 1 (without exit/entry) a smaller particle size leads to lower x_n values whereas the opposite is true for case 2.

To understand these observations for x_n focus should be on the number of radicals in a particle of 100 and 200 nm (Figure S3 and S4 in Appendix E) and on the time scales for reactions and phase transfer events. Due to the slow rates of initiator dissociation - in the absence of exit/entry (case 1) - in both particle types it is very likely that two radicals generated by a dissociation event are terminated before two new radicals are generated at a next dissociation event. Hence, the number of radicals can expected to be zero or two (Figure S3 of Appendix E).

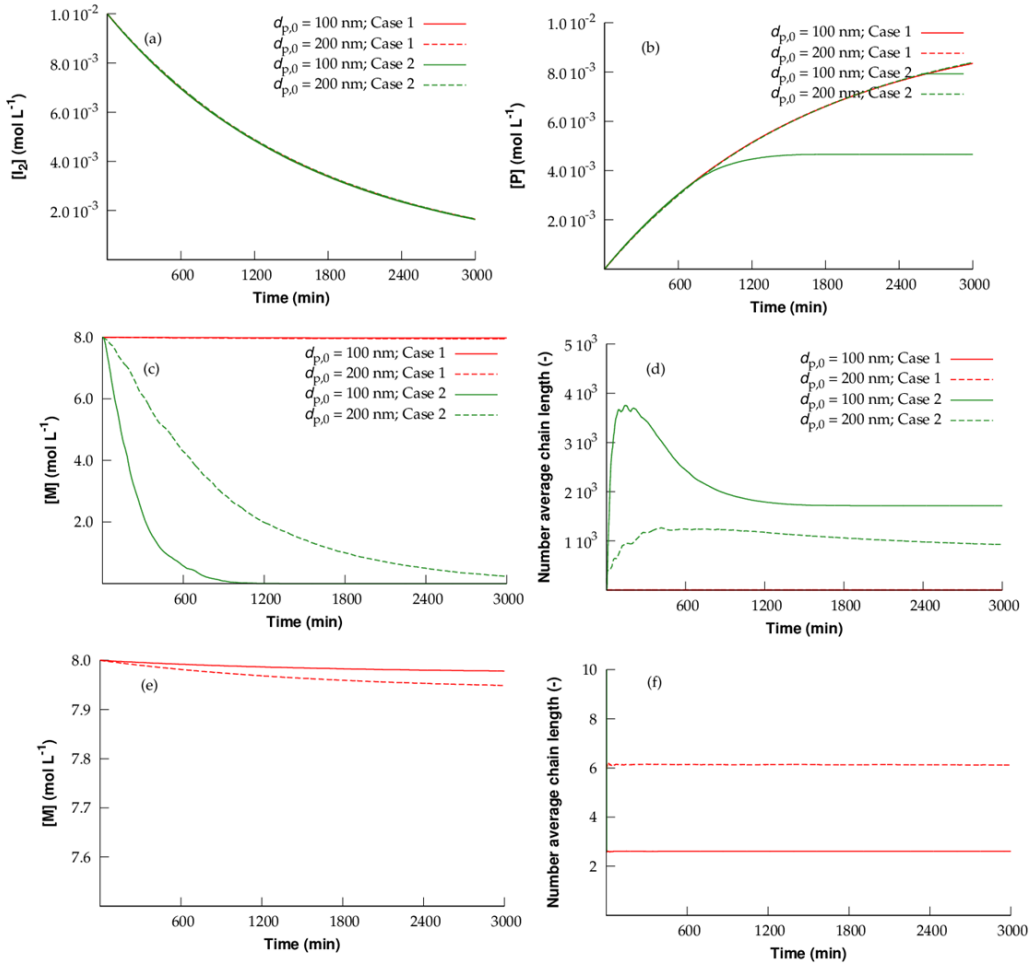

Figure 3. Importance of exit and entry of initiator radicals by comparing results for case 1 (red lines; no exit/entry) and 2 (green lines; exit/entry of initiator radicals) in Table 2 with initially a bimodal particle size distribution with two peaks at $d_{p,0}$ = 100 and 200 nm; temporal evolution of (a) the initiator concentration, (b) concentration of 'dead' polymer, (c) monomer concentration, (d) 'dead' polymer number average chain length; lower graphs of (e) monomer concentration and (f) number average chain length are also shown; model parameters: Table 1; $[I_2]_{p,0} = 10^{-2}$ mol L^{-1}, $[I_2]_{w,0} = 10^{-4}$ mol L^{-1}, $[M]_{p,0}$ = 8 mol L^{-1}, $[M]_{w,0} = 10^{-2}$ mol L^{-1}; number of particles in simulation volume: 126; volume fraction of aqueous phase = 0.7, volume fraction of 100 nm particles is equal to volume fraction of 200 nm particles = 0.15; 112 particles of 100 nm and 14 particle of 200 nm initially; the simulation lines are the averages over the particles with that size; full lines: $d_{p,0}$ = 100 nm; dashed lines: $d_{p,0}$ = 200 nm.

Furthermore, the time scales in the beginning of the miniemulsion polymerization ($[M] \approx [M]_0$; column 4 and 5 in Table 1) for dissociation, chain initiation, propagation, and chain transfer to monomer are the same for both particle sizes. However, if two radicals are present in a 100 and 200 nm particle, the time scale for termination is 8 times smaller in the 100 nm particle due to the so-called confined space effect or single molecule concentration effect,[13-18]

leading to a lower x_n in those particles. This also explains the slower decrease in monomer concentration in the 100 nm particles for case 1 (Figure 3 (c) and Figure 3 (e)).

With exit/entry of initiator radicals (case 2) the situation is different. If one of the two initiator radicals generated upon initiator dissociation can exit the particle or if an initiator radical in the aqueous phase can enter an empty particle, particles can contain only one radical, as illustrated in Figure S4 in Appendix E. Since this radical cannot terminate until another radical enters the particle or radicals are formed through a dissociation event in the particle, chain stoppage is delayed. This leads to much higher x_n values in case 2 (with exit/entry of *I*) compared to case 1 (without exit/entry of *I*). Since the time in between two individual dissociation reaction events is smaller in 200 nm particles than in 100 nm particles, due to the higher initial amount of initiator molecules, and radical entry to 200 nm particles is faster than to 100 nm particles, termination occurs faster in a 200 nm particle and x_n is now lower in a larger particle. Consistently, for case 2, a slower decrease of the monomer concentration is observed for 200 nm particles (Figure 3 (c)) than for 100 nm particles.

Note that in case 2 (with exit/entry of *I*) chain initiation can no longer occur in the 100 nm particles after *ca.* 1200 min, as all monomer has been already consumed (Figure 3 (c); full green line). Hence, in those particles macroradicals are no longer generated and termination can no longer occur, leading to a stagnation of the 'dead' polymer concentration (full green line in Figure 3 (b)).

Close inspection of Figure 3 (d) reveals that in case 2 (*i.e.* case with entry/exit of *I*; green lines) at one point a maximum is obtained for x_n, with this maximum being more pronounced for the particles with a $d_{p,0}$ of 100 nm. The existence of this extremum can be rationalized as follows. In the very beginning of the polymerization, the only termination events taking place are between radicals originating from the same particle. Hence, initially only 'dead' polymers of very short chain length result, due to a very strong confined space effect. For larger times, also

termination after entry of a radical to a particle containing only one radical can take place, leading to the formation of 'dead' polymer with a much higher chain length (*cf.* delayed termination), leading to an increase of the (cumulative) x_n value. This increase in x_n is however counteracted by the decreasing monomer concentration which lowers the propagation rate and, hence, the additional chain lengths, explaining the observed maximum.

The developed modeling methodology also allows to access CLDs per particle and, hence, also the overall (average) CLD per particle size. For a time of 3000 min, the overall (number) CLD for particles with a $d_{p,0}$ of 100 (full line) and 200 nm (dashed line) are shown in Figure 4 (a) for case 1 (no exit/entry; red lines). In agreement with the higher x_n observed for the 200 nm particles compared to the 100 nm particles (Figure 3 (d); full versus dashed red line) the CLD of the 200 nm particles displays a more extended tail. Upon switching to case 2 (with exit/entry of initiator radicals; green lines), as shown in Figure 4 (b), both the CLDs of the 100 and 200 nm particles display a pronounced tail, as also envisaged by the much lower cumulative number fractions at the lower chain lengths for case 2 (Figure 4 (d); cumulative distributions of Figure 4 (b)) compared to case 1 (Figure 4 (c); cumulative distributions of Figure 4 (a)). This is also consistent with the significantly higher x_n values in case 2 compared to case 1, as observed in Figure 3 (d), both for $d_{p,0}$ = 100 nm and $d_{p,0}$ = 200 nm. Also note for case 2 (Figure 4 (d)) the lower cumulative number fractions for the high chain lengths (10^3 – 10^4) for $d_{p,0}$ = 100 nm compared to 200 nm, explaining again the higher x_n values for the former particles (Figure 3 (d)).

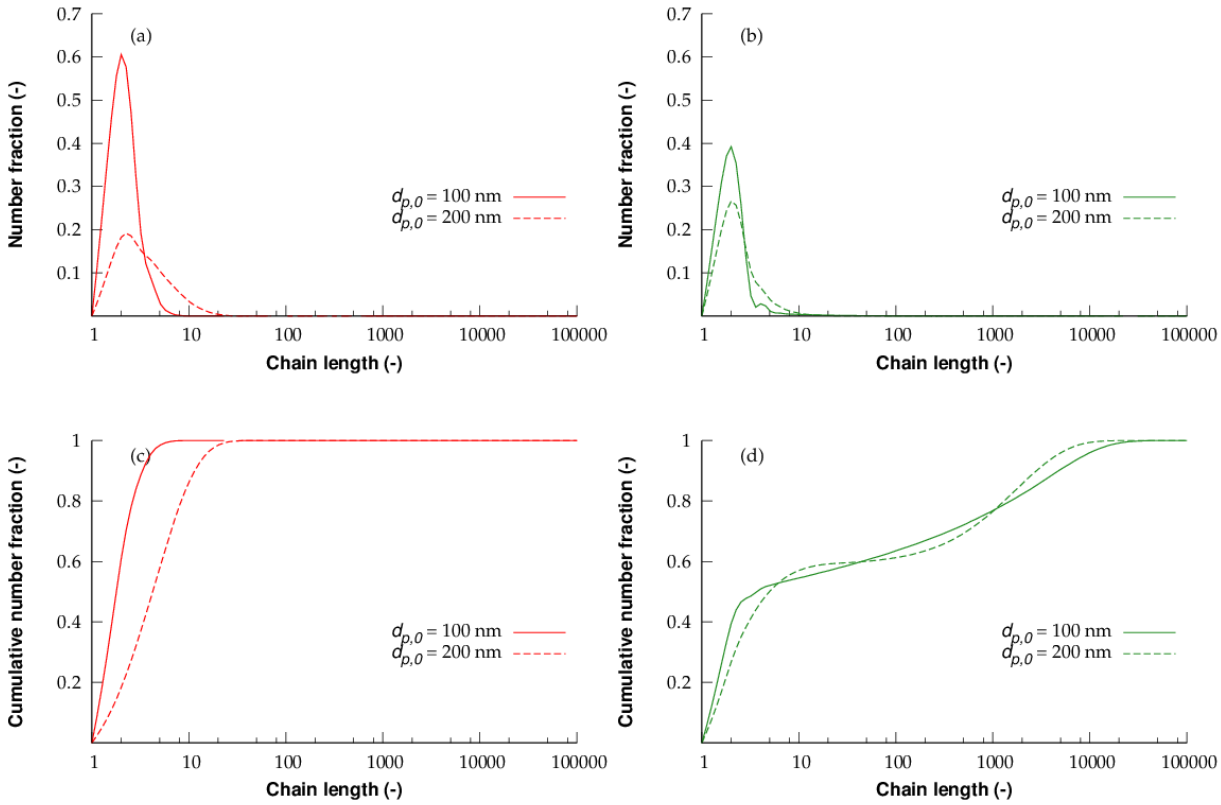

Figure 4. (a) Overall chain length distribution (CLD) for $d_{p,0}$ = 100 nm (full line; average for all those particles) and 200 nm (dashed line) at t = 3000 min for case 1 (no exit/entry) in Table 2; initial conditions: caption Figure 3; (b) corresponding figure for case 2 (again t = 3000 min; with exit/entry of initiator radicals); (c) cumulative distributions of (a); (d) cumulative distributions of (b).

Importance of exit and entry of monomeric radicals

In dispersed phase systems the importance of chain transfer to monomer and the associated exit of the monomeric radical fragment, may affect the chain growth.[88-90] As indicated in Table 2, in case 3 (blue lines) also exit and entry of monomeric radicals formed via chain transfer to monomer are included next to exit and entry for initiator radicals (case 2; green lines). Since initiator dissociation is unimolecular and irreversible, inclusion of these two phase transfer events does not affect the temporal evolution of the initiator concentration (Figure 5 (a)). Figure 5 (b)-(c) indicate that the temporal evolution of the concentration of 'dead' polymer and monomer is almost unaffected. The same is true for x_n (Figure 5 (d)). These similarities can be explained by the larger time scale for exit of monomeric radicals than for chain initiation (Table 2; column 4 and 5).

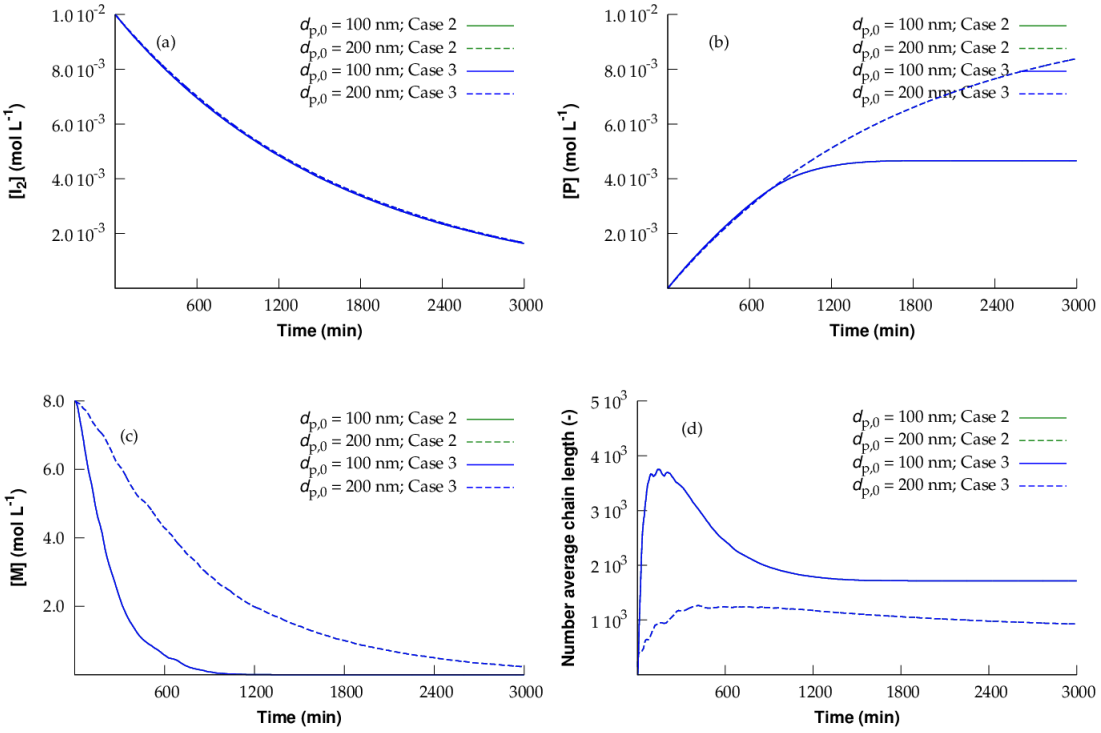

Figure 5. Importance of exit and entry of monomeric radicals formed via chain transfer to monomer by comparing case 2 (green lines; only exit and entry of initiator radicals) and case 3 (blue lines; case 2 + exit and entry of the monomeric radicals) in Table 2; temporal evolution of (a) the initiator concentration, (b) concentration of 'dead' polymer, (c) monomer concentration, and (d) 'dead' polymer number average chain length; model parameters: Table 1; initial conditions: see caption Figure 3; coinciding of blue and green lines.

Importance of exit and entry of macroradicals

In case 4 in Table 2 also exit and entry of macroradicals are included next to exit and entry of initiator and monomeric radicals as formed by chain transfer to monomer. A critical chain length i_{sol} of 5 above which macroradicals can no longer exit a particle is considered ($i > i_{sol}$: $C_{exit,R}(i) = 0$, $\Gamma_R(i) = \infty$; Table 1). Both for exit ($i \leq i_{sol}$) and entry (all i) of macroradicals chain length dependent diffusion coefficients are calculated based on Equation (S10) in Appendix E.

In Figure 6, a comparison is made between case 3 (blue lines; exit and entry of initiator radicals and monomeric radicals) and case 4 (purple lines; case 3 + exit/entry of macroradicals), again considering the initial miniemulsion characteristics as covered in Figure 3 and 5. Analogously to the previous cases, the temporal evolution of the initiator concentration (Figure 6 (a)) is not

affected, again reminding that initiator dissociation is unimolecular and irreversible. Since the time scale for radical exit is smaller for smaller particles, exit of macroradicals is more important for the 100 nm particles. Hence, the effect of additionally considering exit and entry of macroradicals will be the largest for the 100 nm particles. This explains the slightly faster decrease of the monomer concentration in the 100 nm particles for case 4 (Figure 6 (c)) and the slightly higher x_n values (Figure 6 (d)), as exit of a macroradical (next to an initiator radical) from a particle containing two radicals leads to a particle containing only one radical in which bimolecular termination cannot occur. It can also be observed that the stagnation of the 'dead' polymer concentration evolution (Figure 6 (b)) for the 100 nm particles, due to the absence of monomer (Figure 6 (c)), is partially counteracted if macroradicals can enter the 100 nm particles (t > 1200 (blue line) vs. 1500 min (purple line)).

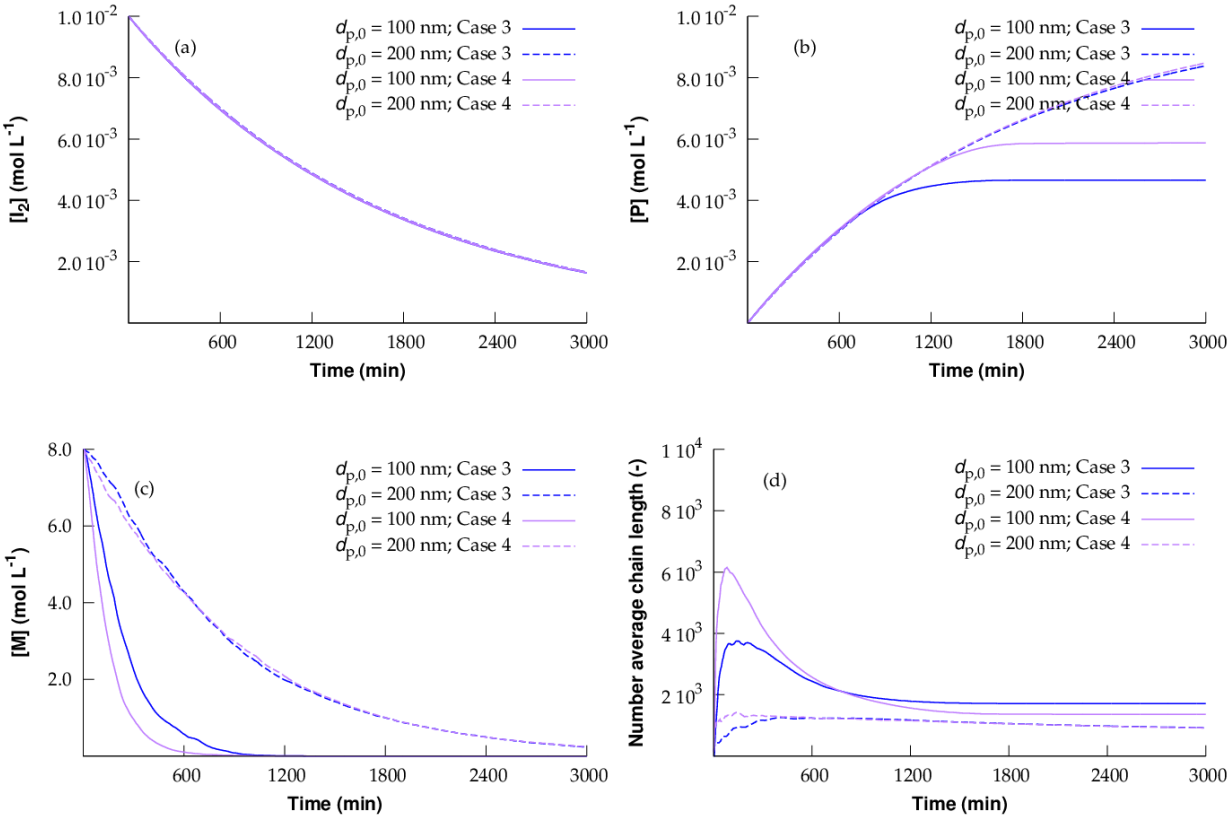

Figure 6. Importance of exit and entry of macroradicals by comparing case 3 (blue lines; exit and entry of initiator radicals and monomeric radicals formed by chain transfer) and case 4 (purple lines; case 3 + exit/entry of macroradicals) in Table 2; critical chain length above which radicals can no longer exit is 5 (Table 1); temporal evolution of (a) the monomer concentration, (b) concentration of 'dead' polymer, (c) monomer concentration, and (d) 'dead' polymer number average chain length; model parameters: Table 1; initial conditions: see caption Figure 3.

Importance of exit and entry of monomer molecules

As illustrated in Figure 3 (c), Figure 5 (c) and Figure 6 (c) (case 2-4; all with exit/entry of radicals but not with exit/entry of monomer molecules), a particle size dependent evolution of the monomer concentration is obtained due to the different exit/entry rate of radicals from/to particles of a different size. This leads in practice to a driving force for monomer transport, which is accounted for in case 5 in Table 2 (exit/entry of I, M^* and R_i ($i \leq 5$) and monomer molecules). The effect on the miniemulsion characteristics is displayed in Figure 7, with focus on the comparison between results for case 4 (purple lines; exit/entry of I, M^* and R_i ($i \leq 5$)) and case 5 (black lines; case 4 + exit/entry of monomer).

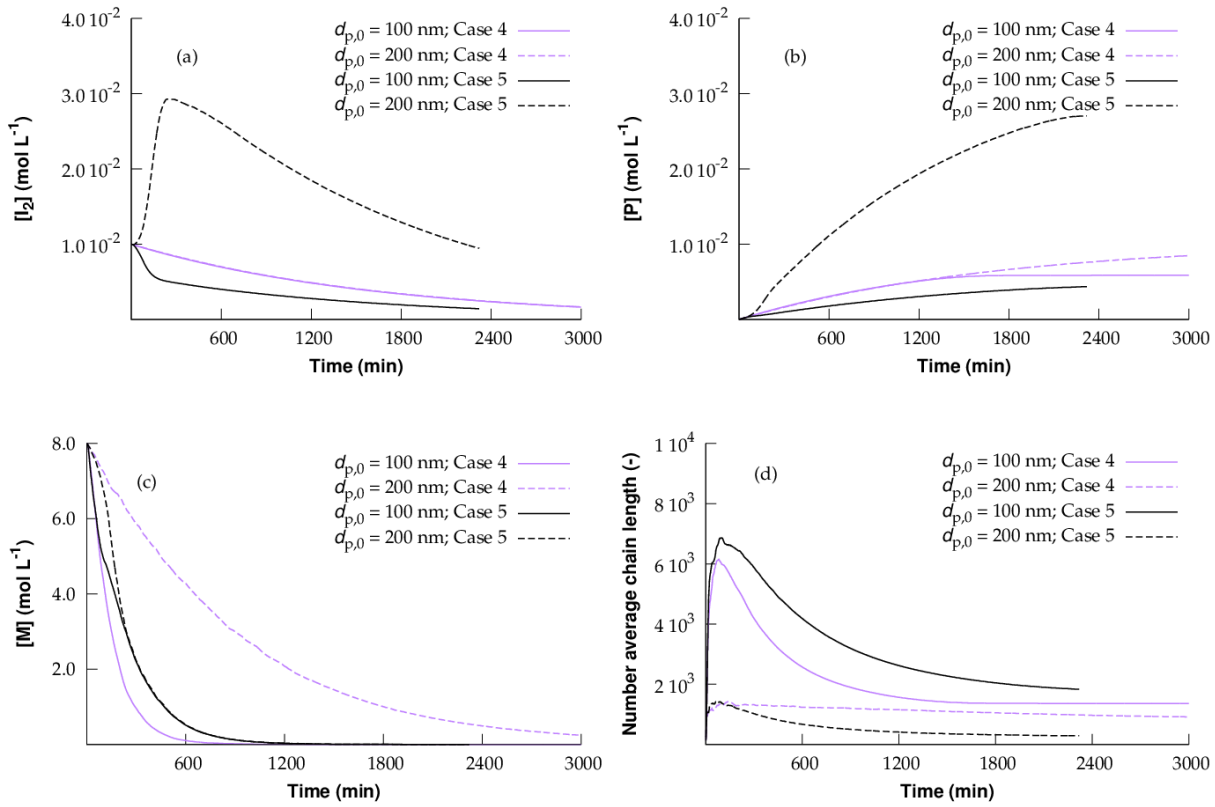

Figure 7. Importance of exit and entry of monomer molecules by comparing case 4 (purple lines; exit/entry of *I*, *M** and R_i ($i \leq 5$)) to case 5 (black lines; case 4 + exit/entry of monomer molecules) in Table 2; temporal evolution of (a) the initiator concentration, (b) concentration of 'dead' polymer, (c) monomer concentration, and (d) 'dead' polymer number average chain length; model parameters: Table 1; initial conditions: see caption Figure 3; as monomer mass transfer is accounted for in case 5 a dynamic particle size distribution (PSD) different from the initial bimodal one is obtained (Figure 8). The black lines in this figure represent thus at any time the average contribution for the particles originally having a size of 100 and 200 nm.

It follows that this monomer transfer is fast enough so that similar monomer concentrations per particle size are obtained (almost coinciding black lines in Figure 7 (c)). Based on the comparison with the lines for case 4 (no exit/entry monomer), overall monomer is transferred from particles with $d_{p,0}$ = 200 nm to particles with $d_{p,0}$ = 100 nm, leading to a decrease of the (volume average) diameter of the $d_{p,0}$ = 200 nm particles and an increase of the (volume average) diameter of the $d_{p,0}$ = 100 nm particles, as illustrated in Figure 8 (a). This explains the decrease in initiator concentration for the $d_{p,0}$ = 100 nm particles (diluting) and the increase in initiator concentration for the $d_{p,0}$ = 200 nm (concentrating) particles going from case 4 to case 5 (Figure 7 (a)). Analogously, the same observations are made for the 'dead' polymer

concentration (Figure 7 (b)). As with monomer transfer the monomer concentration in the $d_{p,0}$ = 100 nm particles is higher in case 5 compared to case 4, higher x_n values are obtained for these particles (Figure 7 (c)). Accordingly, the lower monomer concentration for the $d_{p,0}$ = 200 nm particles in case 5 leads to lower x_n values.

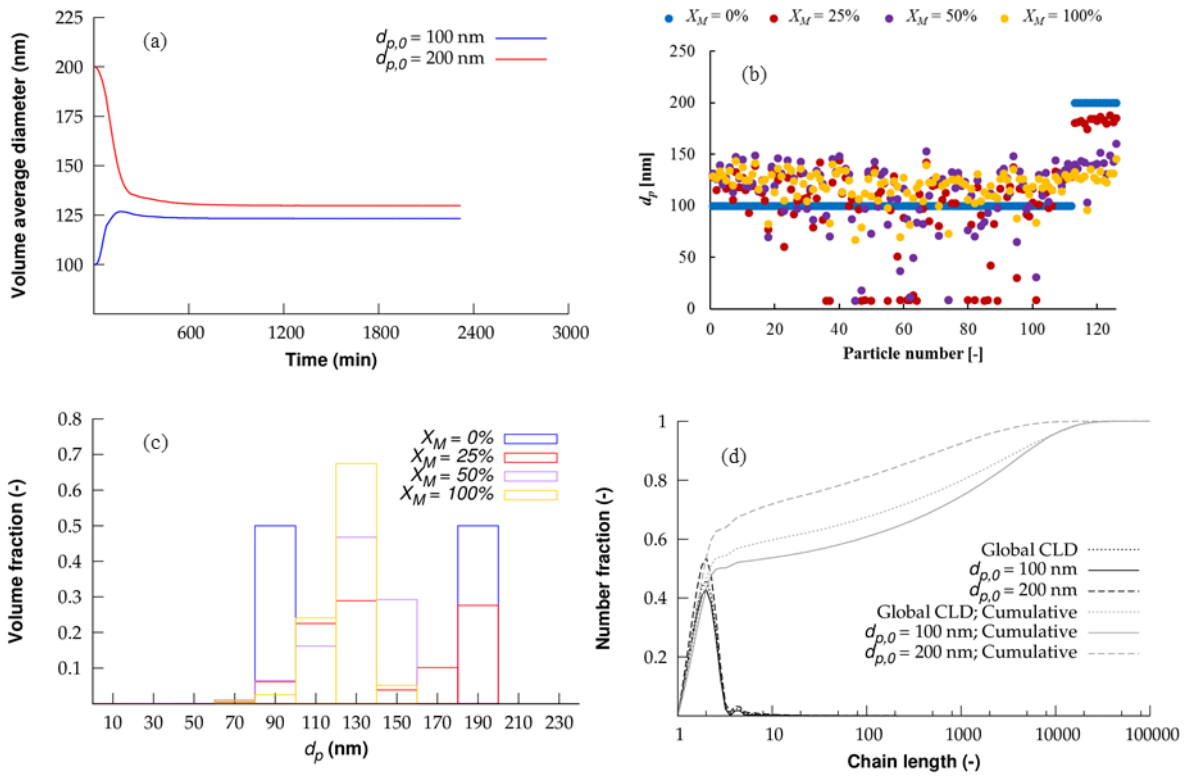

Figure 8. (a) Evolution of the volume average diameter for the particles with $d_{p,0}$ = 100 nm (blue line) and $d_{p,0}$ = 200 nm (red line) for case 5 (exit/entry of radicals I, M^* and R_i ($i \leq 5$) + exit/entry of M); (b) d_p of the individual particles in case 5 at a monomer conversion X_m of 0% (blue symbols; bimodal initialization with $d_{p,0}$ = 100 and 200 nm), 25% (red symbols), 50% (purple symbols) and 100% (yellow symbols); from this subplot the particle size distributions (PSDs) depicted in (c) are obtained; (d) chain length distributions (CLDs) for case 5 at X_M = 100%; conditions: caption Figure 3.

Importantly, as monomer transport takes place between the organic and aqueous phase, the PSD becomes dynamic and, hence, for case 5 (with monomer transport) the *k*MC model highlights contributions of much more particle sizes than just the two initial ones, as confirmed in Figure 8 (b) displaying the diameter of individual particles at a monomer conversion (X_M) of 0, 25, 50, and 100%. It follows that after 25% monomer conversion (red symbols) the theoretical bimodal initial PSD (X_M = 0%, blue symbols) is perturbed, with some particles having a higher d_p due

to a net monomer supply, while other particles have a lower d_p as they supplied monomer to other particles through multiple interactions between the aqueous and organic phase. Note that some $d_{p,0}$ = 100 nm particles did not undergo any significant polymerization, as detectable with the *k*MC model. Such particles only supplied monomer to other particles, explaining the very low d_p contributions (red symbols) in Figure 8 (b). In agreement with Figure 8 (a), it can also be noted that globally the diameter of particles with initially a particle diameter of 100 nm increases, while the diameter of particles with initially a particle diameter of 200 nm decreases. It can be further observed in Figure 8 (b) that the PSD progressively narrows (less scatter in y-direction) if the monomer conversion increases to 50% (purple symbols) and 100% (yellow symbols), consistent with the work of Jansen *et al.*[54] This can also be seen in Figure 8 (c), in which the actual PSD is given in the form of a histogram. Figure 8 (d) represents the final CLDs for particles with $d_{p,0}$ = 100 nm and $d_{p,0}$ = 200 nm and the corresponding global and cumulative ones. Clearly, the global CLD is influenced by the PSD evolution as both original populations give rise to different contributions.

Importance of exit and entry of initiator molecules

As monomer transport in case 5 (exit/entry of I, M^*, R_i ($i \leq 5$), and M) makes that globally small particles become larger and large particles become smaller, a decrease of the initiator concentration in the small particles and an increase in the large particles is theoretically obtained (Figure 7 (a)). These gradients in initiator concentration imply that mass transfer of initiator molecules needs to be also accounted for, which is done in case 6 in Table 2 (case 5 + exit/entry of I_2). To highlight this extra complexity Figure 9 is included, highlighting differences between case 5 (black lines) and case 6 (orange lines).

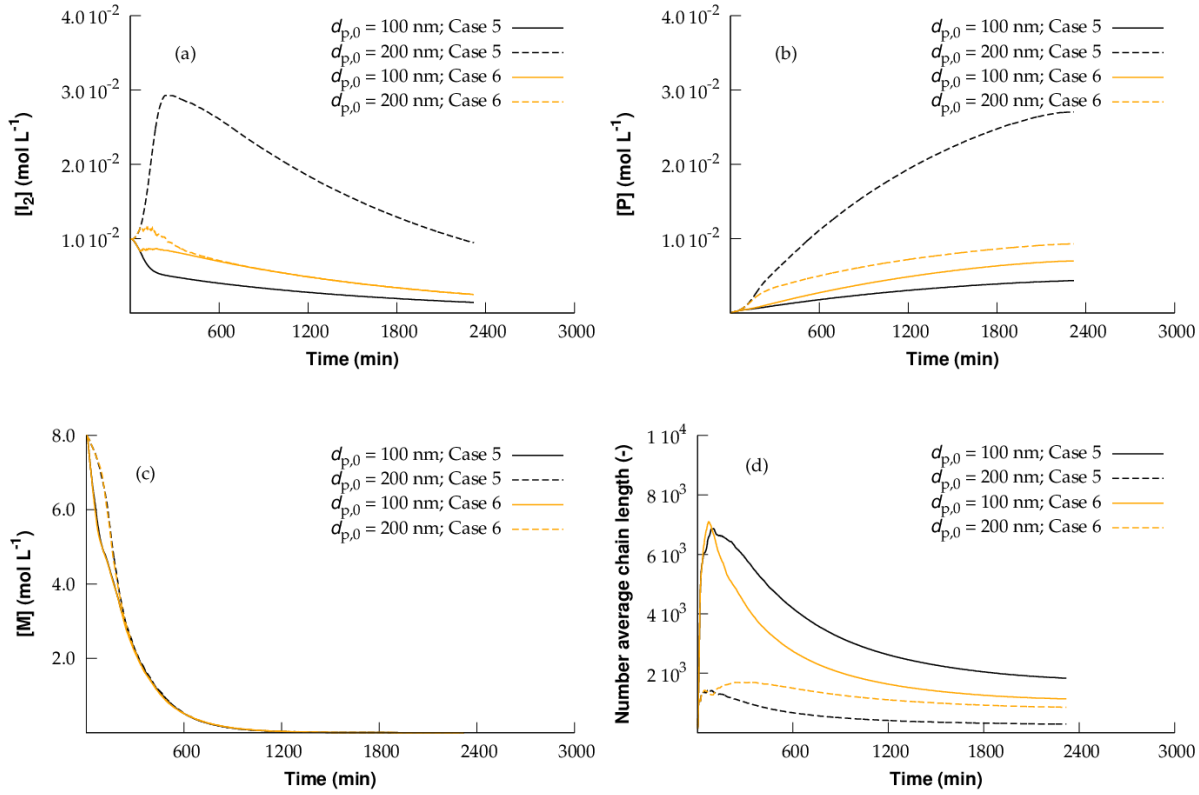

Figure 9. Importance of exit and entry of initiator molecules by comparing case 5 (exit/entry of radicals *I*, *M**, R_i ($i \leq 5$) and *M*) and case 6 (case 5 + exit/entry of initiator molecules I_2); temporal evolution of (a) the initiator concentration, (b) concentration of 'dead' polymer, (c) monomer concentration, and (d) 'dead' polymer number average chain length; model parameters: Table 1; initial conditions: see caption Figure 3.

If mass transfer of initiator molecules is considered (case 6), the temporal evolution of the initiator concentration (Figure 9 (a)) is almost the same for the particles with $d_{p,0}$ = 100 and 200 nm. Similarly, also the difference between the evolution of the 'dead' polymer concentrations for both initial particle sizes is more similar in case 6 compared to case 5 (Figure 9 (b)). While no significant effect of phase transfer of initiator molecules on the temporal evolution of the monomer concentration (Figure 9 (c)) is observed, the higher initiator concentration for the $d_{p,0}$ = 100 nm particles in case 6 (higher located orange full line) leads to a faster initiator dissociation and thus a faster termination. These increases explain the lower x_n values in case 6 compared to case 5 (Figure 9 (d); lower located orange full line). For the $d_{p,0}$ = 200 nm particles, the initiator concentration is lower in case 6 compared to case 5 and, hence, the reverse is true implying higher x_n values for the $d_{p,0}$ = 200 nm particles in case 6 compared to case 5. Overall

it is thus clear that this complex case with several exit/entries leads to partial homogenization but still the temporal evolution of the polymer properties such as x_n (Figure 9 (d)) are largely different for particles of different initial size, highlighting the need of the *k*MC model developed. The latter is also confirmed in Figure 10 in which the final PSD (a) and CLD (b) are shown; the final PSD is clearly very different from the initial one (blue bars in Figure 8 (c)).

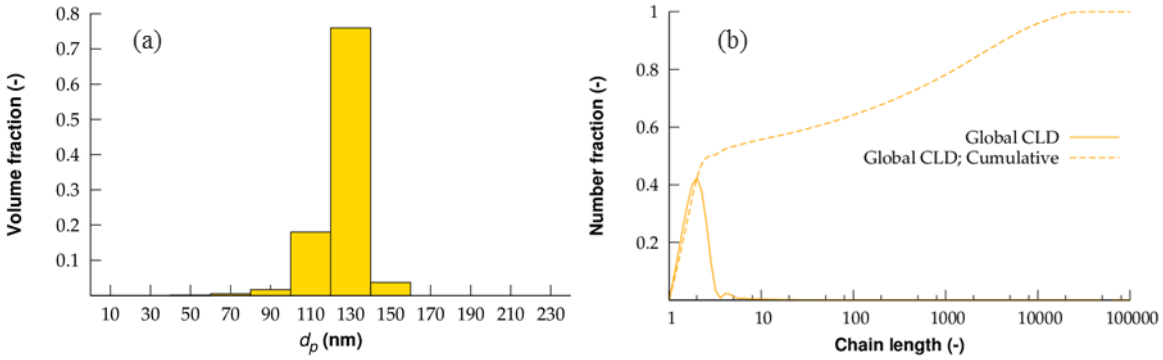

Figure 10. Particle size distribution (a) and overall chain length distribution (so for all particles and the aqueous phase) at full monomer conversion (X_M = 100%) for case 6; model parameters: Table 1; initial conditions: see caption Figure 3. The PSD and CLD evolution are coupled, with the final PSD being clearly different than the initial one (blue bars in Figure 8 (c)).

Importance of apparent termination kinetics

In the last case (case 7 in Table 2), also chain length and monomer conversion dependent apparent termination kinetics are considered (Equation (S5)-(S9) in Appendix E). The importance of these apparent kinetics is evaluated in Figure 11 by a comparison of the miniemulsion characteristics of case 6 (yellow lines; all exit/entry phenomena + intrinsic termination rate coefficients) and case 7 (cyan lines). Limited changes are observed, which can be explained by the selected process conditions leading to a low average number of radicals per particle. Recent work of the Devlaminck *et al.*[86] demonstrated that diffusional limitations on termination are likely only relevant in miniemulsion if at one point a zero-one kinetic behavior is obtained with $\bar{n}$ equal to 0.5. This threshold value of 0.5 is not exceeded in the present work, consistent with the limited impact of diffusional limitations on termination in Figure 11.

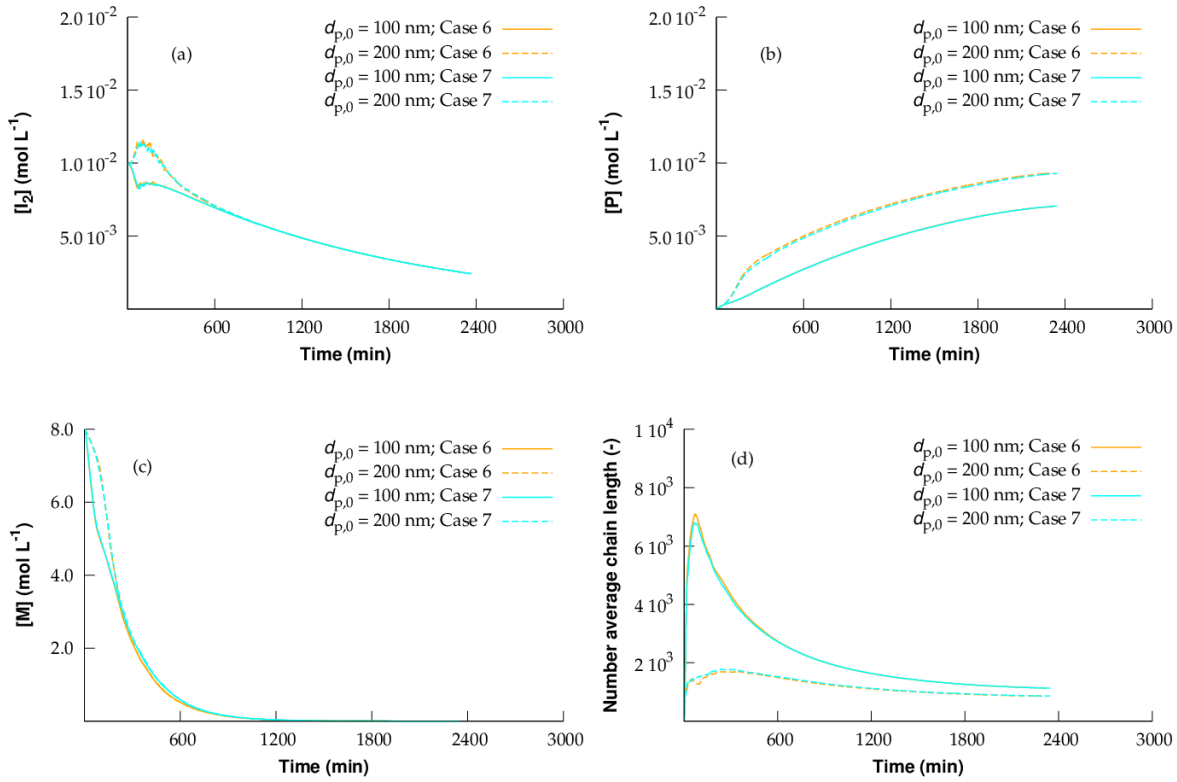

Figure 11. Importance of conversion and chain length dependent termination by comparing case 6 (all exit/entry phenomena) and case 7 all exit/entry phenomena + apparent termination rate coefficients); temporal evolution of (a) the initiator concentration, (b) concentration of 'dead' polymer, (c) monomer concentration, and (d) 'dead' polymer number average chain length; model parameters: Table 1; initial conditions: see caption Figure 3; a limited effect is observed as the conditions are in the regime of a low average radical number per particle.

6.4 Conclusions

A novel kinetic Monte Carlo (*k*MC) modeling tool has been presented, allowing the simulation of miniemulsion free radical polymerization (FRP) explicitly taking into account the evolution of the particle size distribution (PSD) and its interaction with the evolution of the chain length distribution (CLD). In this model, the number of radicals and the monomer concentration in each individual particle are tracked, hence, the model does not make use of an average particle monomer concentration at any time as done in previous studies, including those based on the conventional Smith-Ewart approach. Moreover, exit/entry of both radicals and monomer is accounted for between the particles and the aqueous phase, considering a diffusion-based approach.

To highlight the consistency of the developed *k*MC model with the emulsion field it is demonstrated for a simplified intrinsic FRP reaction scheme with a water-soluble initiator that the conventional Smith-Ewart kinetics are obtained if a downsized version of the *k*MC model is used. Analogously to the Smith-Ewart model the particle monomer concentrations are averaged out in the downsized *k*MC model. In contrast, if the *k*MC model accounts for the monomer fluctuations over the particles a different evolution of the monomer conversion and average chain length characteristics is obtained, highlighting the relevance of the present work.

This relevance is further demonstrated for the description of the miniemulsion kinetics considering a detailed FRP reaction scheme with micro-scale diffusional limitations on termination and an oil-soluble initiator. Radical exit and entry rates have been shown to strongly effect the miniemulsion polymerization kinetics, with acceptable monomer conversions and polymer chain lengths only explainable due to the occurrence of such meso-scale interphase mass transfer phenomena. Moreover, the radical exit and entry rates depend on the particle size, leading to different monomer concentrations in particles of different size. These monomer fluctuations are counteracted by monomer phase transfer, leading to a time dependent PSD, which in turn affects the evolution of the CLD, highlighting the need for the coupled calculation of both distributions.

On a longer term the modeling platform can be further improved at its individual scales, with in particular focus on the description of mass transfer phenomena combining diffusion and thermodynamic based methods, benefiting from recent meso-scale emulsion work.

6.5 References

1. U. C. Palmiero, J. Singh and D. Moscatelli, *Curr. Org. Chem.*, 2018, **22**, 1285-1296.
2. L. Hlalele, D. R. D'hooge, C. J. Durr, A. Kaiser, S. Brandau and C. Barner-Kowollik, *Macromolecules*, 2014, **47**, 2820-2829.
3. C. I. Holdsworth, Z. F. Jia and M. J. Monteiro, *Polymer*, 2016, **106**, 200-207.
4. F. Brandl, M. Drache and S. Beuermann, *Polymers*, 2018, **10**.
5. S. Hamzehlou, M. Aguirre, J. R. Leiza and J. M. Asua, *Macromolecules*, 2017, **50**, 7190-7201.
6. S. C. Thickett and R. G. Gilbert, *Polymer*, 2007, **48**, 6965-6991.
7. C. S. Chern, *Prog. Polym. Sci.*, 2006, **31**, 443-486.
8. J. M. Asua, *J. Polym. Sci. Pol. Chem.*, 2004, **42**, 1025-1041.
9. D. R. D'hooge, P. H. M. Van Steenberge, M. F. Reyniers and G. B. Marin, *Prog. Polym. Sci.*, 2016, **58**, 59-89.
10. M. F. Cunningham, *Prog. Polym. Sci.*, 2008, **33**, 365-398.
11. J. Jennings, G. He, S. M. Howdle and P. B. Zetterlund, *Chem. Soc. Rev.*, 2016, **45**, 5055-5084.
12. J. M. Asua, *Prog. Polym. Sci.*, 2002, **27**, 1283-1346.
13. P. B. Zetterlund, *Polym. Chem.*, 2011, **2**, 534-549.
14. P. B. Zetterlund and M. Okubo, *Macromolecules*, 2006, **39**, 8959-8967.
15. Y. Kagawa, P. B. Zetterlund, H. Minami and M. Okubo, *Macromol. Theory Simul.*, 2006, **15**, 608-613.
16. A. Butte, G. Storti and M. Morbidelli, *Macromolecules*, 2000, **33**, 3485-3487.
17. B. Charleux, *Macromolecules*, 2000, **33**, 5358-5365.
18. H. Tobita and F. Yanase, *Macromol. Theory Simul.*, 2007, **16**, 476-488.
19. M. Nomura, J. Ikoma and K. Fujita, *Acs Symposium Series*, 1992, **492**, 55-71.
20. M. Nomura and K. Fujita, *Polym. React. Eng.*, 1994, **2**, 317-345.
21. P. C. Mork and Y. Makame, *J. Polym. Sci. Pol. Chem.*, 1997, **35**, 2347-2354.
22. J. A. Alduncin, J. Forcada and J. M. Asua, *Macromolecules*, 1994, **27**, 2256-2261.
23. J. A. Alduncin, J. Forcada, M. J. Barandiaran and J. M. Asua, *J. Polym. Sci. Pol. Chem.*, 1991, **29**, 1265-1270.
24. C. Costa, S. A. S. Timmermann, J. C. Pinto, P. H. H. Araujo and C. Sayer, *Macromol. React. Eng.*, 2013, **7**, 221-231.
25. C. Autran, J. C. de la Cal and J. M. Asua, *Macromolecules*, 2007, **40**, 6233-6238.
26. T. G. T. Jansen, J. Meuldijk, P. A. Lovell and A. M. van Herk, *J. Polym. Sci. Pol. Chem.*, 2016, **54**, 2731-2745.
27. G. Lichti, R. G. Gilbert and D. H. Napper, *J. Polym. Sci. Pol. Chem.*, 1980, **18**, 1297-1323.

28. G. Arzamendi, C. Sayer, N. Zoco and J. M. Asua, *Polym. React. Eng.*, 1998, **6**, 193-223.
29. A. Butte, G. Storti and M. Morbidelli, *Macromol. Theory Simul.*, 2002, **11**, 37-52.
30. M. Wulkow and J. R. Richards, *Ind. Eng. Chem. Res.*, 2014, **53**, 7275-7295.
31. Y. Shang, G. R. Shan and P. J. Pan, *Macromolecular Chemistry and Physics*, 2015, **216**, 884-893.
32. C. A. Capeletto, C. Costa, C. Sayer and P. H. H. Araujo, *Aiche J.*, 2017, **63**, 2128-2140.
33. L. Bentein, D. R. D'hooge, M. F. Reyniers and G. B. Marin, *Polymer*, 2012, **53**, 681-693.
34. P. H. M. Van Steenberge, D. R. D'hooge, M. F. Reyniers, G. B. Marin and M. F. Cunningham, *Macromolecules*, 2014, **47**, 7732-7741.
35. W. V. Smith and R. H. Ewart, *The Journal of Chemical Physics*, 1948, **16**, 592-599.
36. H. M. Vale and T. F. McKenna, *Prog. Polym. Sci.*, 2005, **30**, 1019-1048.
37. N. Sheibat-Othman, H. M. Vale, J. M. Pohn and T. F. L. McKenna, *Macromol. React. Eng.*, 2017, **11**, 32.
38. A. H. Alexopoulos, P. Pladis and C. Kiparissides, *Ind. Eng. Chem. Res.*, 2013, **52**, 12285-12296.
39. O. Kammona, P. Pladis, C. E. Frantzikinakis and C. Kiparissides, *Macromol. Chem. Phys.*, 2003, **204**, 983-999.
40. A. Hosseini, A. E. Bouaswaig and S. Engell, *Chem. Eng. Sci.*, 2013, **88**, 108-120.
41. P. B. Zetterlund, *Macromol. Theory Simul.*, 2010, **19**, 11-23.
42. Y. Sugihara and P. B. Zetterlund, *ACS Macro Lett.*, 2012, **1**, 692-696.
43. H. Tobita, Y. Takada and M. Nomura, *Macromolecules*, 1994, **27**, 3804-3811.
44. H. Tobita, Y. Takada and M. Nomura, *J. Polym. Sci. Pol. Chem.*, 1995, **33**, 441-453.
45. G. Arzamendi and J. R. Leiza, *Ind. Eng. Chem. Res.*, 2008, **47**, 5934-5947.
46. L. X. Nie, W. L. Yang, H. D. Zhang and S. K. Fu, *Polymer*, 2005, **46**, 3175-3184.
47. Y. W. Luo and B. Yu, *Polym.-Plast. Technol. Eng.*, 2004, **43**, 1299-1321.
48. J. A. Rawlston, J. Guo, F. J. Schork and M. A. Grover, *J. Polym. Sci. Pol. Chem.*, 2008, **46**, 6114-6128.
49. J. Stubbs, R. Carrier and D. C. Sundberg, *Macromol. Theory Simul.*, 2008, **17**, 147-162.
50. M. Drache, K. Brandl, R. Reinhardt and S. Beuermann, *Phys. Chem. Chem. Phys.*, 2018, **20**, 10796-10805.
51. M. Do Amaral, S. Van Es and J. M. Asua, *J. Polym. Sci. Pol. Chem.*, 2004, **42**, 3936-3946.
52. U. C. Palmiero, A. Agostini, S. Gatti, M. Sponchioni, V. Valenti, L. Brunel and D. Moscatelli, *Macromolecules*, 2016, **49**, 8387-8396.
53. H. A. Zayas, N. P. Truong, D. Valade, Z. F. Jia and M. J. Monteiro, *Polym. Chem.*, 2013, **4**, 592-599.

54. T. G. T. Jansen, J. Meuldijk, P. A. Lovell and A. M. van Herk, *Macromol. React. Eng.*, 2015, **9**, 19-31.
55. M. Nomura, H. Tobita and K. Suzuki, in *Polymer Particles*, ed. M. Okubo, Springer-Verlag Berlin, Berlin, 2005, vol. 175, pp. 1-128.
56. H. F. Hernandez and K. Tauer, *Macromol. React. Eng.*, 2009, **3**, 375-397.
57. H. F. Hernandez and K. Tauer, *Ind. Eng. Chem. Res.*, 2008, **47**, 9795-9811.
58. J. M. Asua and J. C. De La Cal, *J. Appl. Polym. Sci.*, 1991, **42**, 1869-1877.
59. V. S. Rodriguez, J. M. Asua, M. S. Elaasser and C. A. Silebi, *J. Polym. Sci. Pt. B-Polym. Phys.*, 1991, **29**, 483-500.
60. I. A. Maxwell, J. Kurja, G. H. J. Vandoremaele and A. L. German, *Makromolekulare Chemie-Macromolecular Chemistry and Physics*, 1992, **193**, 2065-2080.
61. J. Ugelstad and P. C. Mork, *Advances in Colloid and Interface Science*, 1980, **13**, 101-140.
62. J. Delgado and M. S. Elaasser, *Makromolekulare Chemie-Macromolecular Symposia*, 1990, **31**, 63-87.
63. J. Delgado, M. S. Elaasser, C. A. Silebi, J. W. Vanderhoff and J. Guillot, *J. Polym. Sci. Pt. B-Polym. Phys.*, 1988, **26**, 1495-1517.
64. V. S. Rodriguez, J. Delgado, C. A. Silebi and M. S. Elaasser, *Ind. Eng. Chem. Res.*, 1989, **28**, 65-74.
65. J. M. Asua, *European Polymer Journal*, 2018, **106**, 30-41.
66. F. K. Hansen and J. Ugelstad, *J. Polym. Sci. Pol. Chem.*, 1978, **16**, 1953-1979.
67. J. L. Gardon, *Journal of Polymer Science Part a-1-Polymer Chemistry*, 1968, **6**, 623-641.
68. I. A. Penboss, R. G. Gilbert and D. H. Napper, *Journal of the Chemical Society-Faraday Transactions I*, 1986, **82**, 2247-2268.
69. P. H. M. Van Steenberge, D. R. D'hooge, M. F. Reyniers and G. B. Marin, *Chem. Eng. Sci.*, 2014, **110**, 185-199.
70. D. J. G. Devlaminck, P. H. M. Van Steenberge, L. De Keer, M. F. Reyniers and D. R. D'hooge, *Polym. Chem.*, 2017, **8**, 6948-6963.
71. Y. W. Marien, P. H. M. Van Steenberge, C. Barner-Kowollik, M. F. Reyniers, G. B. Marin and D. R. D'hooge, *Macromolecules*, 2017, **50**, 1371-1385.
72. G. B. Desmet, Y. W. Marien, P. H. M. Van Steenberge, D. R. D'hooge, M. F. Reyniers and G. B. Marin, *Polym. Chem.*, 2017, **8**, 7143-7150.
73. Y. W. Marien, P. H. M. Van Steenberge, K. B. Kockler, C. Barner-Kowollik, M. F. Reyniers, G. B. Marin and D. R. D'hooge, *Polym. Chem.*, 2017, **8**, 3124-3128.
74. S. K. Fierens, S. Telitel, P. H. M. Van Steenberge, M. F. Reyniers, G. B. Marin, J. F. Lutz and D. R. D'hooge, *Macromolecules*, 2016, **49**, 9336-9344.
75. D. R. D'hooge, P. H. M. Van Steenberge, M. F. Reyniers and G. B. Marin, *Polymers*, 2014, **6**, 1074-1095.

76. P. H. M. Van Steenberge, D. R. D'hooge, Y. Wang, M. J. Zhong, M. F. Reyniers, D. Konkolewicz, K. Matyjaszewski and G. B. Marin, *Macromolecules*, 2012, **45**, 8519-8531.
77. D. R. D'hooge, *Macromol. Rapid Commun.*, 2018, **39**, 5.
78. I. A. Maxwell, B. R. Morrison, D. H. Napper and R. G. Gilbert, *Macromolecules*, 1991, **24**, 1629-1640.
79. D. T. Gillespie, *J. Phys. Chem.*, 1977, **81**, 2340-2361.
80. D. R. D'hooge, M. F. Reyniers and G. B. Marin, *Macromol. React. Eng.*, 2013, **7**, 362-379.
81. D. S. Achilias, *Macromol. Theory Simul.*, 2007, **16**, 319-347.
82. A. D. Peklak and A. Butte, *Macromol. Theory Simul.*, 2006, **15**, 546-562.
83. J. B. L. de Kock, B. Klumperman, A. M. van Herk and A. L. German, *Macromolecules*, 1997, **30**, 6743-6753.
84. Y. N. Zhou and Z. H. Luo, *Macromol. React. Eng.*, 2016, **10**, 516-534.
85. G. Johnston-Hall and M. J. Monteiro, *J. Polym. Sci. Pol. Chem.*, 2008, **46**, 3155-3173.
86. D. J. G. Devlaminck, P. H. M. Van Steenberge, M.-F. Reyniers and D. R. D'hooge, *Macromolecules*, 2018, **51**, 9442-9461.
87. M. C. Griffiths, J. Strauch, M. J. Monteiro and R. G. Gilbert, *Macromolecules*, 1998, **31**, 7835-7844.
88. M. Nomura and K. Fujita, *Makromolekulare Chemie-Rapid Communications*, 1989, **10**, 581-587.
89. J. M. Asua, E. D. Sudol and M. S. Elaasser, *J. Polym. Sci. Pol. Chem.*, 1989, **27**, 3903-3913.
90. L. Xie and Z. H. Luo, *Ind. Eng. Chem. Res.*, 2017, **56**, 4690-4702.

Chapter 7: Kinetic Monte Carlo modeling for the coupled simulation of the chain length and particle size distribution in miniemulsion copolymerization of styrene and N-vinylcaprolactam

Summary

Kinetic Monte Carlo modeling is applied for the coupled simulation of the chain length and particle size distribution (CLD/PSD) in isothermal batch miniemulsion copolymerization of styrene and N-vinylcaprolactam (VCL), which is an interesting polymerization system in view of *e.g.* drug delivery applications. A polymerization temperature of 333 K and the oil-soluble initiator 2,2′-azobis(2-methylpropionitrile) is considered. It is theoretically shown that the disparate monomer reactivity ratios lead to a consecutive dominant incorporation of styrene and VCL. Moreover, a strong effect of the initial (Gaussian) PSD is observed, with much higher polymerization rates if the PSD shifts to lower particles sizes. Overall, a very dynamic PSD evolution is simulated, with a negative skewing at low monomer conversions and a uniformization of the PSD as the monomer conversion increases.

7.1 Introduction

Thermo-responsive crosslinked polymer nanoparticles or nanogels have unique capabilities as pharmaceutical carriers as they allow the controlled release of a potent substance at well-defined physiological temperatures.[1, 2] The most popular thermoresponsive polymers for nanogel application are poly(N-vinylcaprolactam), pVCL, and poly(N-isopropylacrylamide), pNIPAM.[3-5] As such these polymers display a lower critical solution temperature (LCST) in water around body temperature, which implies that below this temperature they are water-soluble and above that temperature phase segregation takes place.[6] Crosslinked particles based

on these polymers, *i.e.* nanogels, display a volume phase transition temperature (VPTT), *i.e.* they collapse upon increasing the temperature from T < VPTT to T > VPPT, allowing the release of a drug, as illustrated in Figure 1 (a). Recently, significant attention is paid to pVCL (Figure 1 (b)) as this polymer has a more beneficial biocompatibility compared to pNIPAM.[3, 7]

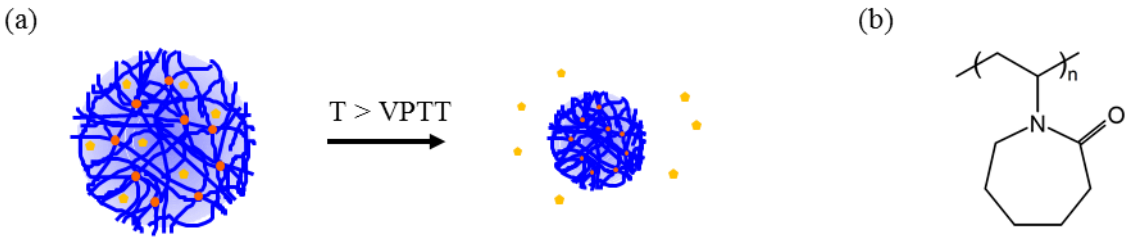

Figure 1. (a) Collapsing of a drug-loaded thermo-responsive nanogel when heated over the volume phase transition temperature (VPTT) leading to the release of a potent substance (yellow symbols); crosslinking points: orange symbols; (b) Chemical structure of poly(N-vinylcaprolactam), pVCL, which can be the blue polymer in (a).

The most frequently used method for the synthesis of pVCL nanogels is dispersion/precipitation polymerization.[8-10] There one starts from a homogeneous mixture, *i.e.* the monomer (here N-vinylcaprolactam, VCL) dissolved in water. Polymerization is initiated by a water-soluble initiator. As the oligomers start to grow they become increasingly water-insoluble (as T > LCST) and, hence, these oligomers precipitate, leading to (precursor) particles. At this point, the system becomes heterogeneous with the particles dispersed in the continuous aqueous phase. Polymerization now takes place both in water and in the particles which leads to particle growth. In addition, aggregation of (precursor) particles leads to particle growth and further polymerization in the water phase can occur as long as water-soluble initiator is present. By adding a crosslinker to the initial reaction mixture, *e.g.* N,N-methylenebis-(acrylamide), chemically crosslinked nanoparticles that can reversibly swell and collapse around the VPPT are obtained.[9, 10]

Alongside dispersion/precipitation polymerization a limited number of studies have used mini- or microemulsion polymerization for the synthesis of pVCL nanogels. For example, Medeiros

et al.[11] synthesized pVCL nanogels via water-in-oil (*i.e.* inverse) miniemulsion polymerization. By using hexadecane as the continuous phase, Span 80 (sorbitan monoleate) as an oil-soluble surfactant, NaCl salt as a lipophobe to prevent Ostwald ripening and N,N-methylenebis-(acrylamide) as a crosslinker, nanogels with a diameter in the range of *ca*. 200 – 600 nm were obtained, starting from a monomer droplet population. On the other hand, Crespy *et al*.[12] performed 'direct' oil-in-water miniemulsion polymerization of VCL with toluene as an organic solvent and sodium dodecyl sulfate (SDS) as surfactant. As a last example, Shah *et al*.[13] synthesized copolymer nanoparticles of VCL and methyl methacrylate (MMA) via oil-in-water microemulsion polymerization, thus starting from micelles and monomer droplets, and leading to stable, non-crosslinked particles of less than 50 nm in average diameter.

Crucial for (mini)emulsion based nanogel production is the need for an on spec (co)polymer composition, crosslinking density, and particle size distribution (PSD), as these properties determine key nanogel features such as the VPTT, the swelling degree (and hence the loading capacity), and the rheological behavior.[1, 8, 14, 15] Limited focus has however been put on a systematic understanding of the relation of reaction conditions and the final nanogel properties. Typically (mini/micro)emulsion studies are also focused on homopolymerization conditions and/or a limited number of experimental variables and responses.[11-13]

Due to the high number of variables it is recommended to apply multi-scale modeling in which at the micro-scale the interplay of chemistry and viscosity is grasped in a given reaction locus (*e.g.* polymer particle) and at the meso-scale interphase mass phenomena (*e.g.* exit and entry of radicals) are included.[16] Ideally, model parameters are determined by careful parameter estimation to bulk and emulsion polymerization data.[17-19] Recent work of Marien *et al*.[20] on radical miniemulsion homopolymerization has indicated that advanced kinetic Monte Carlo (*k*MC) modeling is ideally suited to handle the interactive evolution of the chain length distribution (CLD) and PSD. Only by particle by particle tracking of the reaction and mass

transfer events it becomes possible to capture the correlation between chain and particle growth. Notably this work highlighted the limitations of the conventional Smith-Ewart approach to model miniemulsion polymerization kinetics. Monomer transport needs to be accounted for and an average monomer concentration per particle cannot be simply assumed.

A next logical step is to evaluate if the developed *k*MC model can also be applied for radical miniemulsion copolymerization and can support the design of *e.g.* nanogel synthesis. In the present work, the main characteristics of miniemulsion copolymerization of VCL with a hydrophobic comonomer are therefore simulated. Focus is on a polymerization temperature of 333 K and the oil-soluble initiator 2,2′-azobis(2-methylpropionitrile), AIBN. For simplicity, the addition of the crosslinker is not included in the simulation results and all model parameters are literature based, with some simplifications due to lack of literature data. Incorporation of certain amounts of the hydrophobic comonomer allows to tune the VPPT and to facilitate the miniemulsion formation. For illustration purposes, styrene is considered as a hydrophobic comonomer in view of the availability of benchmarked model parameters for styrene.

It is theoretically shown that the disparate monomer reactivity ratios induce a consecutive dominant incorporation of styrene and VCL. Moreover, a strong effect of the initial (Gaussian) PSD is observed, with higher polymerization rates if this PSD shifts to lower particles sizes. Overall, a very dynamic PSD evolution is simulated, with a negative skewing at low monomer conversions and a uniformization of the PSD as the monomer conversion further increases.

7.2 Model development

In the present work, the kinetic Monte Carlo (*k*MC) model developed by Marien *et al*.[20] allowing to track particle by particle reaction and interphase mass transfer events in miniemulsion free radical homopolymerization (see Chapter 6) is extended to copolymerization. Focus is on copolymerization of styrene and VCL at 333 K, for which for

simplicity a terminal model is assumed, *i.e.* the reactivity of a radical is assumed to depend only on the terminal unit.[21, 22] 2,2′-Azobis(2-methylpropionitrile), AIBN, is used as an oil-soluble radical initiator. The simulated number of particles is sufficiently high for numerical accuracy.

A listing of all reaction and mass transfer events considered in the *k*MC model and their corresponding rate coefficients is shown in Table 1 (the label A refers to styrene and B to VCL; for particle size dependent coefficients the value at 100 nm is reported). It follows that a basic FRP reaction scheme, consisting of dissociation, chain initiation, propagation, chain transfer to monomer, and termination, is considered with a further distinction based on the reaction locus being the organic phase or water. It should be noted that limited kinetic information is available for radical polymerization of VCL. In particular, to the best of our knowledge, no absolute homopropagation rate coefficients are available for VCL. Hence, homopropagation rate coefficients for VCL are approximated by the ones reported for N-vinylpyrrolidone,[23] which belongs to the same family of vinyl lactams. Notably N-vinylpyrrolidone has a pronounced solvent effect attributed to intermolecular interactions leading to a hindered internal rotational motion in the transition structure. A 20-fold increase in the homopropagation rate coefficient is for instance observed at 303 K from bulk to dilute aqueous solution conditions.[23] This solvent effect is taken into account in the current work, as envisaged by the higher propagation rate coefficients for VCL in the aqueous phase compared to the ones for the organic phase (Table 1).

Cross-propagation rate coefficients are calculated from literature data[24] on the reactivity ratios. Disparate reactivity ratios have been reported in literature[24] ($r_A = k_{p,AA}/k_{p,AB} = 21.2$, $r_B = k_{p,BB}/k_{p,BA} = 0.026$), indicating a tendency to induce a consecutive dominant incorporation of A and B.[21, 25] Due to the lack of literature data, chain transfer to monomer coefficients (or the ratio of chain transfer to monomer rate coefficients to propagation rate coefficients) for VCL are approximated by the ones for N-vinylpyrrolidone.[26]

To account for a representative description of the gel-effect apparent chain length and monomer conversion dependent termination rate coefficients pertaining to standard styrene homopolymerization are used in all cases, again bearing in mind that with VCL such parameters are lacking. The apparent termination rate coefficients are explicitly linked to each termination couple taking into account the actual chain lengths of the two radicals and the polymer mass fraction corresponding to the reaction locus in which the two radicals reside, *i.e*. no average $<k_{t,app}>$ is used. The individual apparent termination coefficients are calculated using Equation (S5)-(S9) in Appendix E.[27]

Entry and exit rate coefficients are calculated in agreement with the emulsion field[28-34] (formulas: see footnotes Table 1). In agreement with Marien *et al.*[20] entry and exit phenomena of non-compartmentalized species (*i.e.* the comonomers and initiator) are described via lumped events, see Equation (S1)-(S4) in Appendix E. Globally these equations reflect that the system strives for the establishment of equilibrium. The latter is reflected by partitioning coefficients (Γ values) for which literature based data are considered.[10, 35] Moreover, possible diffusional limitations on entry and exit of oligomers are accounted for via Equation (S10) in Appendix E.[36] It should be stressed that the scope of the current work is theoretical and the results must be interpreted in the following way. In case the model parameters in Table 1 are considered then the model outcome is as predicted in the present work.

Table 1. Reactions and phase transfer events for the simulation of batch isothermal (T = 333 K) miniemulsion copolymerization of styrene ('A' label) and N-vinylcaprolactam ('B' label) initiated by 2,2′-azobis(2-methylpropionitrile), AIBN; the reported *k* values for entry and exit events corresponds to a particle diameter of 100 nm (formulas: see footnotes).

Event	Equation	k (d_p = 100 nm)	Ref.
Reactions in particles			
Dissociation[a]	$I_{2,p} \xrightarrow{f_p, k_{d,p}} 2\, I_p$	1.3 10^{-5} s^{-1}	37
Chain initiation	$I_p + M_{A,p} \xrightarrow{k_{iIA,p}} R_{1,A,p}$	3.4 10^{3} L mol^{-1} s^{-1}	b,38
	$I_p + M_{B,p} \xrightarrow{k_{iIB,p}} R_{1,B,p}$	2.2 10^{4} L mol^{-1} s^{-1}	b,23
	$M^*_{A,p} + M_{A,p} \xrightarrow{k_{iM^*_A A,p}} R_{1,A,p}$	3.4 10^{3} L mol^{-1} s^{-1}	b,23
	$M^*_{A,p} + M_{B,p} \xrightarrow{k_{iM^*_A B,p}} R_{1,B,p}$	1.6 10^{2} L mol^{-1} s^{-1}	b,24, 38
	$M^*_{B,p} + M_{A,p} \xrightarrow{k_{iM^*_B A,p}} R_{1,A,p}$	8.5 10^{6} L mol^{-1} s^{-1}	b,23, 24
	$M^*_{B,p} + M_{B,p} \xrightarrow{k_{iM^*_B B,p}} R_{1,B,p}$	2.2 10^{4} L mol^{-1} s^{-1}	b,23
Propagation	$R_{i,A,p} + M_{A,p} \xrightarrow{k_{pAA,p}} R_{i+1,A,p}$	3.4 10^{2} L mol^{-1} s^{-1}	38
	$R_{i,A,p} + M_{B,p} \xrightarrow{k_{pAB,p}} R_{i+1,B,p}$	1.6 10^{1} L mol^{-1} s^{-1}	c,24, 38
	$R_{i,B,p} + M_{A,p} \xrightarrow{k_{pBA,p}} R_{i+1,A,p}$	8.5 10^{4} L mol^{-1} s^{-1}	c,23, 24
	$R_{i,B,p} + M_{B,p} \xrightarrow{k_{pBB,p}} R_{i+1,B,p}$	2.2 10^{3} L mol^{-1} s^{-1}	23
Chain transfer to monomer	$R_{i,A,p} + M_{A,p} \xrightarrow{k_{trM,AA,p}} P_{i,p} + M^*_{A,p}$	1.8 10^{-2} L mol^{-1} s^{-1}	d,39
	$R_{i,A,p} + M_{B,p} \xrightarrow{k_{trM,AB,p}} P_{i,p} + M^*_{B,p}$	1.4 10^{-1} L mol^{-1} s^{-1}	d,26, 39
	$R_{i,B,p} + M_{A,p} \xrightarrow{k_{trM,BA,p}} P_{i,p} + M^*_{A,p}$	1.4 10^{-1} L mol^{-1} s^{-1}	d,26, 39
	$R_{i,B,p} + M_{B,p} \xrightarrow{k_{trM,BB,p}} P_{i,p} + M^*_{B,p}$	1.1 10^{0} L mol^{-1} s^{-1}	d,26
Termination	$R_{i,p} + R_{j,p} \xrightarrow{k_{t,app,p,i,j}} P_{i+j,p}$	1.0 10^{9} L mol^{-1} s^{-1}	e,40
Reactions in water			
Dissociation[a]	$I_{2,w} \xrightarrow{f_w, k_{d,w}} 2\, I_w$	1.3 10^{-5} s^{-1}	37
Chain initiation	$I_w + M_{A,w} \xrightarrow{k_{iIA,w}} R_{1,A,w}$	3.4 10^{3} L mol^{-1} s^{-1}	b,38
	$I_w + M_{B,w} \xrightarrow{k_{iIB,w}} R_{1,B,w}$	3.3 10^{5} L mol^{-1} s^{-1}	b,23
	$M^*_{A,w} + M_{A,w} \xrightarrow{k_{iM^*_A A,w}} R_{1,A,w}$	3.4 10^{3} L mol^{-1} s^{-1}	b,23
	$M^*_{A,w} + M_{B,w} \xrightarrow{k_{iM^*_A B,w}} R_{1,B,w}$	1.6 10^{2} L mol^{-1} s^{-1}	b,24, 38
	$M^*_{B,w} + M_{A,w} \xrightarrow{k_{iM^*_B A,w}} R_{1,A,w}$	1.3 10^{7} L mol^{-1} s^{-1}	b,23, 24
	$M^*_{B,w} + M_{B,w} \xrightarrow{k_{iM^*_B B,w}} R_{1,B,w}$	3.3 10^{5} L mol^{-1} s^{-1}	b,23
Propagation	$R_{i,A,w} + M_{A,w} \xrightarrow{k_{pAA,w}} R_{i+1,A,w}$	3.4 10^{2} L mol^{-1} s^{-1}	38
	$R_{i,A,w} + M_{B,w} \xrightarrow{k_{pAB,w}} R_{i+1,B,w}$	1.6 10^{1} L mol^{-1} s^{-1}	c,24, 38
	$R_{i,B,w} + M_{A,w} \xrightarrow{k_{pBA,w}} R_{i+1,A,w}$	1.3 10^{6} L mol^{-1} s^{-1}	c,23, 24
	$R_{i,B,w} + M_{B,w} \xrightarrow{k_{pBB,w}} R_{i+1,B,w}$	3.3 10^{4} L mol^{-1} s^{-1}	23
Chain transfer to monomer	$R_{i,A,w} + M_{A,w} \xrightarrow{k_{trM,AA,w}} P_{i,w} + M^*_{A,w}$	1.8 10^{-2} L mol^{-1} s^{-1}	d,39
	$R_{i,A,w} + M_{B,w} \xrightarrow{k_{trM,AB,w}} P_{i,w} + M^*_{B,w}$	5.3 10^{-1} L mol^{-1} s^{-1}	d,26, 39
	$R_{i,B,w} + M_{A,w} \xrightarrow{k_{trM,BA,w}} P_{i,w} + M^*_{A,w}$	5.3 10^{-1} L mol^{-1} s^{-1}	d,26, 39

Table 1 continued

	$R_{i,B,w} + M_{B,w} \xrightarrow{k_{trM,BB,w}} P_{i,w} + M^*_{B,w}$	1.6 10^1 L mol^{-1} s^{-1}	d,26
Termination	$R_{i,w} + R_{j,w} \xrightarrow{k_{t,app,w}{}^{i,j}} P_{i+j,w}$	1.0 10^9 L mol^{-1} s^{-1}	e,40
Phase transfer events			
Entry of I_2	$I_{2,w} \xrightarrow{k_{entry,I}} I_{2,p}$	6.0 10^6 L mol^{-1} s^{-1}	f
Entry of I	$I_w \xrightarrow{k_{entry,I}} I_p$	6.0 10^6 L mol^{-1} s^{-1}	f
Entry of M_A	$M_{A,w} \xrightarrow{k_{entry,M_A}} M_{A,p}$	6.0 10^6 L mol^{-1} s^{-1}	f
Entry of M_B	$M_{B,w} \xrightarrow{k_{entry,M_B}} M_{B,p}$	6.0 10^6 L mol^{-1} s^{-1}	f
Entry of M_A *	$M^*_{A,w} \xrightarrow{k_{entry,M^*_A}} M^*_{A,p}$	6.0 10^6 L mol^{-1} s^{-1}	f
Entry of M_B *	$M^*_{B,w} \xrightarrow{k_{entry,M^*_B}} M^*_{B,p}$	6.0 10^6 L mol^{-1} s^{-1}	f
Entry of R_i	$R_{i,w} \xrightarrow{k_{entry,R}} R_{i,p}$	6.0 10^6 L mol^{-1} s^{-1} [c]	f
Exit of I_2	$I_{2,p} \xrightarrow{k_{exit,I_2}} I_{2,w}$	1.7 10^{-1} s^{-1}	g
Exit of I	$I_p \xrightarrow{k_{exit,I}} I_w$	2.4 10^0 s^{-1}	g
Exit of M_A	$M_{A,p} \xrightarrow{k_{exit,M_A}} M_{A,w}$	7.0 10^{-2} s^{-1}	g
Exit of M_A *	$M^*_{A,p} \xrightarrow{k_{exit,M^*_A}} M^*_{A,w}$	7.0 10^{-2} s^{-1}	g
Exit of M_B	$M_{B,p} \xrightarrow{k_{exit,M_B}} M_{B,w}$	7.6 10^{-1} s^{-1}	g
Exit of M_B *	$M^*_{B,p} \xrightarrow{k_{exit,M^*_B}} M^*_{B,w}$	7.6 10^{-1} s^{-1}	g
Exit of R_i ($i \leq i_{sol}$)	$R_{i,p} \xrightarrow{k_{exit,R}} R_{i,w}$	2.4 10^0 s^{-1} [c]	g

[a] Initiator efficiency f; for illustration purposes, a constant value equal to 0.6 is used for all reaction loci.[41]

[b] Chain initiation rate coefficient assumed 10 times higher than the long chain limit for macropropagation.[42]

[c] Reactivity ratios $r_A = k_{p,AA}/k_{p,AB} = 21.2$, $r_B = k_{p,BB}/k_{p,BA} = 0.026$.[24]

[d] Same chain transfer to monomer ratios $C_{trM} = k_{trM}/k_p$ assumed for the organic and aqueous phase; hence, higher chain transfer to monomer rate coefficients for VCL in the aqueous phase as higher propagation rate coefficient due the reported solvent effect for the analogue N-vinylpyrrolidone;[23] .$C_{trM,AA} = k_{trM,AA}/k_{p,AA} = 5.3\ 10^{-5}$ (ref:[39]), $C_{trM,BB} = k_{trM,BB}/k_{p,BB} = 4.8\ 10^{-4}$ (ref:[26]); $k_{trM,AB} = k_{trM,BA} = (k_{trM,AA}\, k_{trM,BB})^{0.5}$.

[e] Chain length and monomer conversion dependent termination rate coefficients are considered to account for a gel-effect,[40] see Equations (S5)-(S9) in Appendix E; $k_{t,app}$ (1,1) is reported here; due to lack of literature data for VCL termination rate coefficients, the termination reactivity assumed independent of terminal unit. The diffusivity is described based on styrene units.

[f] $k_{entry,Z} = C_{entry,Z}\, N_A\, D_{Z,w}\, d_p$ (references[28-34]) with $Z = I_2$, I, M_A, M_B, M_A*, M_B*, or R and $C_{entry,Z} = 10^{-4}$ and $D_{I2/I/M/M^*,} = D_{R,w}$ (i = 1) = 10^{-7} dm^2 s^{-1}; $D_{R,w}$(i): Eq (S10) in Appendix E (ref [36]).

[g] $k_{exit,Z} = C_{exit,Z}\, D_{Z,p}\, d_p^{-2}$ with $C_{exit,Z} = 6\, C_{entry,Z}\, D_{Z,w}\, \pi^{-1}\, \Gamma_Z^{-1}\, D_{Z,p}^{-1}$ (references[28-34]); $D_{R,p}$ (i = 1) = 10^{-7} dm^2 s^{-1}; $D_{R,p}(i)$: Eq (S10) in Appendix E (ref [36]); $\Gamma_{I_2} = 115$, $\Gamma_I = 8$ (intermediate literature value), $\Gamma_{M_A} = \Gamma_{M_A^*} = 273$, $\Gamma_{M_B} = \Gamma_{M_B^*} = 25$, $\Gamma_{R_i}(i \leq i_{sol}) = 8$, $\Gamma_{R_i}(i > i_{sol}) = \infty$; i_{sol} = 7 (intermediate value for styrene and VCL).

7.3 Results and discussion

The evolution of the typical (average) copolymerization characteristics for a miniemulsion polymerization with an initial fraction of styrene/VCL monomer A/B ($f_{A/B,0}$) equal to 0.5 and a Gaussian initial PSD with a volume average diameter equal to 100 nm (see Figure 3; top left) are shown in Figure 2. Following initial conditions are considered with the subscripts *p* and *w* referring to the particles (organic phase) and the water phase: $[AIBN]_{p,0}$ = 1.0 10^{-2} mol L^{-1}, $[AIBN]_{w,0}$ = 8.7 10^{-5} mol L^{-1}, $[A]_{p,0}$ = 4.3 mol L^{-1}, $[A]_{w,0}$ = 2.9 10^{-2} mol L^{-1}, $[B]_{p,0}$ = 4.1 mol L^{-1}, $[B]_{w,0}$ = 3.5 10^{-1} mol L^{-1}; and volume fraction of the aqueous phase: 0.3.

The evolution of the conversion of monomer A (styrene; full blue line; X_A), monomer B (VCL; dotted red line; X_B) and the total monomer conversion (*i.e.* based on both A and B; dashed black line; X_{tot}) are shown in Figure 2 (a). A faster increase of X_A is observed, in agreement with the high value of r_A ($r_A = k_{p,AA}/k_{p,AB}$ = 21.2) and the low value of r_B ($r_B = k_{p,BB}/k_{p,BA}$ = 0.026). Such reactivity ratios imply that radicals with both terminal unit A and B preferentially add to monomer A, hence, most radicals have a terminal A unit and mostly homopropagation of A occurs. At high reactions times (t > 400 min), a pronounced increase in X_B is observed as almost all A monomer has been consumed and homopropagation of B becomes the dominant propagation mode. Due to the higher value of $k_{p,BB}$ compared to $k_{p,AA}$ a faster increase in X_{tot} is observed for these high reaction times (t > 400 min).

The evolution of the fraction of monomer molecules of type A (f_A; full blue line) and B (f_B; full red line) is shown in Figure 2 (b) together with the evolution of the fraction of monomer units incorporated on average in the 'dead' polymer of type A (F_A; dashed blue line) and B (F_B; dashed red line). In agreement with the faster increase in X_A for t < 400 min (Figure 2 (a)), F_A >> F_B for t < 400 min and a decrease of f_A and increase of f_B are observed for these reactions times. Once almost all A monomer has been consumed (t > 400 min), the fraction of B on

average in the 'dead' polymer increases to its final value with as expected $F_B = F_A = f_{A,0} = f_{B,0} = 0.5$.

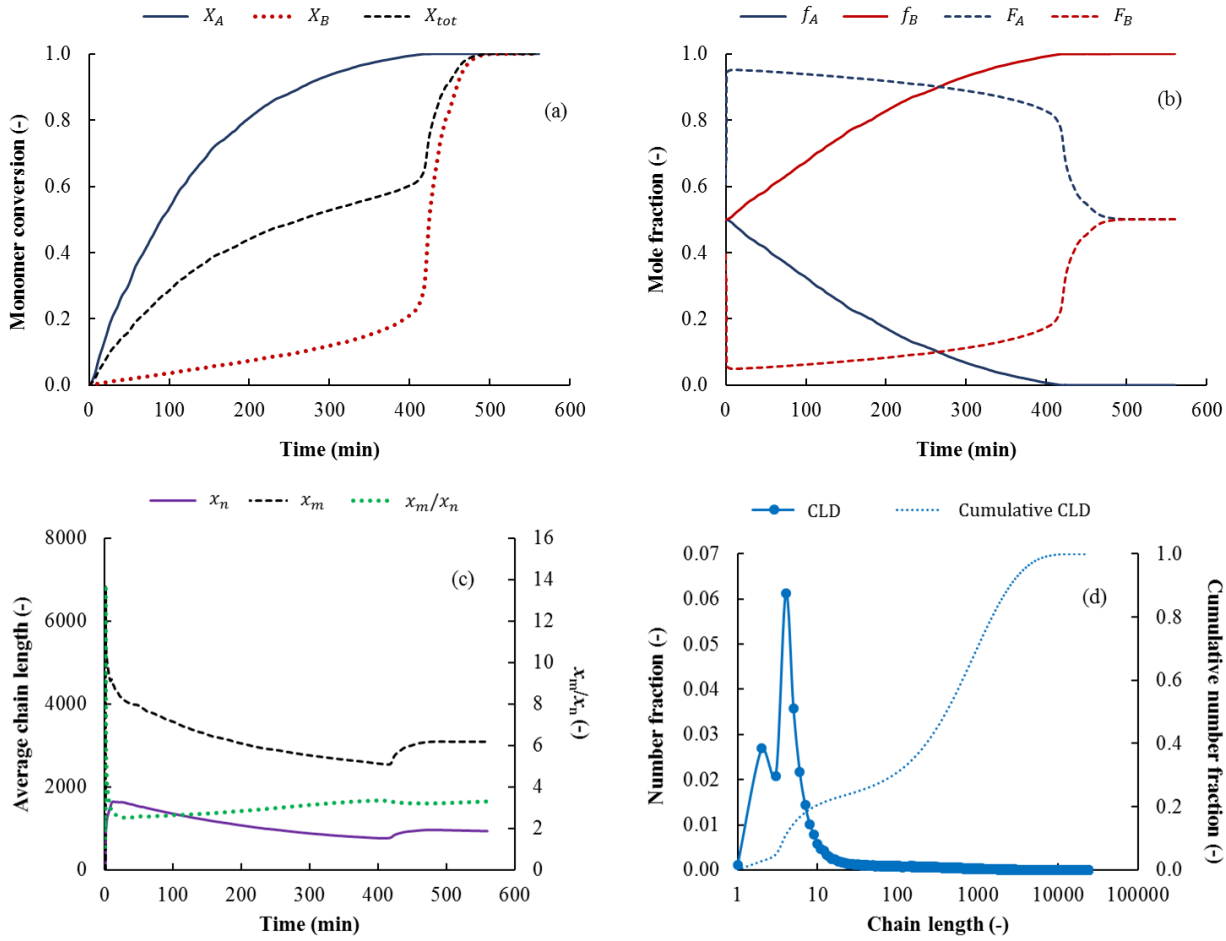

Figure 2. Simulation results for the batch isothermal miniemulsion copolymerization of styrene (A; molar fraction at start = $f_{A,0} = 0.5$) and N-vinylcaprolactam (B; molar fraction at start = $f_{B,0} = 0.5$) initiated by 2,2′-azobis(2-methylpropionitrile), AIBN; initial PSD and its evolution: see Figure 3; (a): conversion of monomer A (full blue line), monomer B (dotted red line) and the total monomer conversion (*i.e.* based on both A and B; dashed black line); (b): fraction of monomer molecules of type A (f_A; full blue line) and type B (f_B; full red line); fraction of units on average in the 'dead' polymer of type A (F_A; dashed blue line) and type B (F_B; dashed red line); (c): number (x_n; full purple line) and mass (x_m; dashed black line) average chain length of the 'dead' polymer and the corresponding dispersity (x_m/x_n; dotted green line); (d): final CLD and corresponding cumulative distribution; Initial conditions: T = 333 K, $[AIBN]_{p,0} = 1.0\ 10^{-2}$ mol L^{-1}, $[AIBN]_{w,0} = 8.7\ 10^{-5}$ mol L^{-1}, $[A]_{p,0} = 4.3$ mol L^{-1}, $[A]_{w,0} = 2.9\ 10^{-2}$ mol L^{-1}, $[B]_{p,0} = 4.1$ mol L^{-1}, $[B]_{w,0} = 3.5\ 10^{-1}$ mol L^{-1}; volume fraction aqueous phase: 0.3; model parameters: Table 1; simulated number of particles: 127.

Figure 2 (c) shows the evolution of the 'dead' polymer number (x_n; full purple line) and mass (x_m; dashed black line) average chain length and the corresponding dispersity (x_m/ x_n; dotted green line). In agreement with work on homopolymerization,[20] a maximum in x_n and x_m is

observed for low reaction times. At low reaction times the only termination events taking place are between radicals originating from the same particle (*cf*. oil-soluble initiator). Hence, due to a strong confined space effect,[43-46] initially only 'dead' polymers of very short chain length are formed. For larger times, also termination after entry of a radical to a particle containing a single radical can take place, leading to the formation of 'dead' polymer with much higher chain lengths and an increase of the (cumulative) x_n value. This increase in x_n is however counteracted by the decreasing monomer concentration (*cf*. Figure 2 (a)), which lowers the propagation rate, and, hence, the additional chain lengths, explaining the observed maximum. It can also be noted that the shift from initially forming only very short 'dead' polymer chains to also forming longer 'dead' polymer chains also leads to a maximum in the dispersity (full green line). Closer inspection reveals that a strong variation in the dispersity values is obtained, highlighting the relevance of the developed model which fully reflects time dependencies. Furthermore, a slight increase in x_n and x_m can be observed at high reaction times (t > 400 min), which can be explained by the depletion of almost all A monomer at these reaction times and the higher value of $k_{p,BB}$ compared to $k_{p,AA}$.

Figure 2 (d) shows the number CLD (full blue line) and its cumulative distribution (dotted blue line) at the end of the polymerization (X_{tot} = 1). Due to a strong confined space effect at low times,[43-46] a large fraction (*ca*. 20%) of the 'dead' polymer chains has a very short chain length (< 10). In particular, there is a dominant contribution of chain length 2 and 4, as can be envisaged from the two peaks. The fraction of large polymer chain lengths (chain length 100-10000) can be attributed to particles in which a single radical grows to high chain lengths due to absence of a second radical for termination.[20, 43]

The evolution of the PSD corresponding to the conditions of Figure 2 is shown in Figure 3. In agreement with Jansen *et al*.,[47] at a total monomer conversion of 25%, a negatively skewed distribution is observed. This skew is due to the presence of droplets/particles that did not

undergo any significant polymerization and, hence, only supplied monomer to other particles, which leads to particles with sizes larger than initially present (Figure 3; top left vs. top right). As the polymerization rate is lower in larger particles,[20] the large particles eventually supply monomer to particles of small and intermediate size in which polymerization is faster, leading to a narrowing of the PSD when the monomer conversion further increases to 50% (Figure 3; bottom left) and 100% (Figure 3; bottom right).

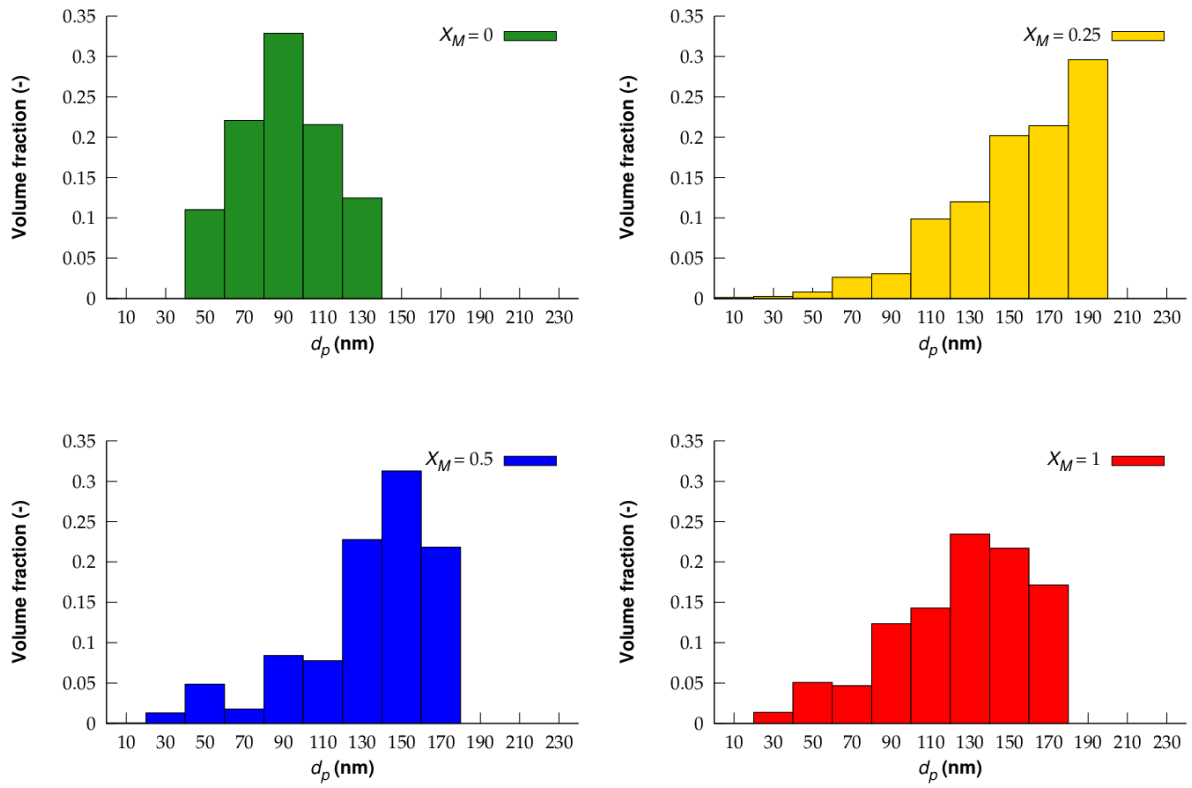

Figure 3. Evolution of the particle size distribution (PSD) corresponding to Figure 2; volume-weighted PSD at a total monomer conversion (*i.e.* based on both comonomers) of 0% (*i.e.* the initial PSD; top left; Gaussian), 25% (top right), 50% (bottom left) and 100% (*i.e.* the final PSD; bottom right); initial conditions: see caption Figure 2; model parameters: see Table 1; corresponding overall chain length distributions (CLDs) at X_M = 1 is shown in Figure 2 (d).

The effect of the initial PSD on the evolution of the copolymerization characteristics of Figure 2 is studied in Figure 4 by considering a Gaussian initial PSD with average diameter $\overline{d_{p,0}}$ = 200 nm (Figure 5; top left) instead of $\overline{d_{p,0}}$ = 100 nm as before (Figure 2 and 3). For $\overline{d_{p,0}}$ = 200 nm the (co)monomer conversions (Figure 4 (a)) show a similar trend as for $\overline{d_{p,0}}$ = 100 nm (same

lines as in Figure 2). However, a significantly slower increase in monomer conversion is observed, in agreement with the larger time scale for radical entry and larger time between two dissociation events for smaller particles, leading to a delayed termination. Analogously, a similar but slower evolution of f_A, f_B, F_A and F_B is observed in Figure 4 (b). As can be envisaged from Figure 4 (c), a more pronounced maximum for x_n and x_m at low reaction times (< 100 min) is observed for the smaller particles. The difference between the average chain length characteristics however narrows as the reaction time increases, as is also the case under homopolymerization conditions.[20] A significant effect of the initial PSD can however still be observed for the final CLD. Consistent with a delayed termination in smaller particles, a higher contribution of high chain length (*e.g.* > 100) is observed for $\overline{d_{p,0}}$ = 100 nm (dotted blue line), as can be envisaged from the lower cumulative number fraction at a chain length of *e.g.* 100.

For completeness, the evolution of the PSD corresponding to Figure 4 (case with $\overline{d_{p,0}} = 200$ nm) is shown in Figure 5. As in Figure 3, a negative skewing is observed at low (Figure 5; top right) and intermediate (Figure 5; bottom left) monomer conversions and a uniformization occurs toward high monomer conversion (Figure 4; bottom right).

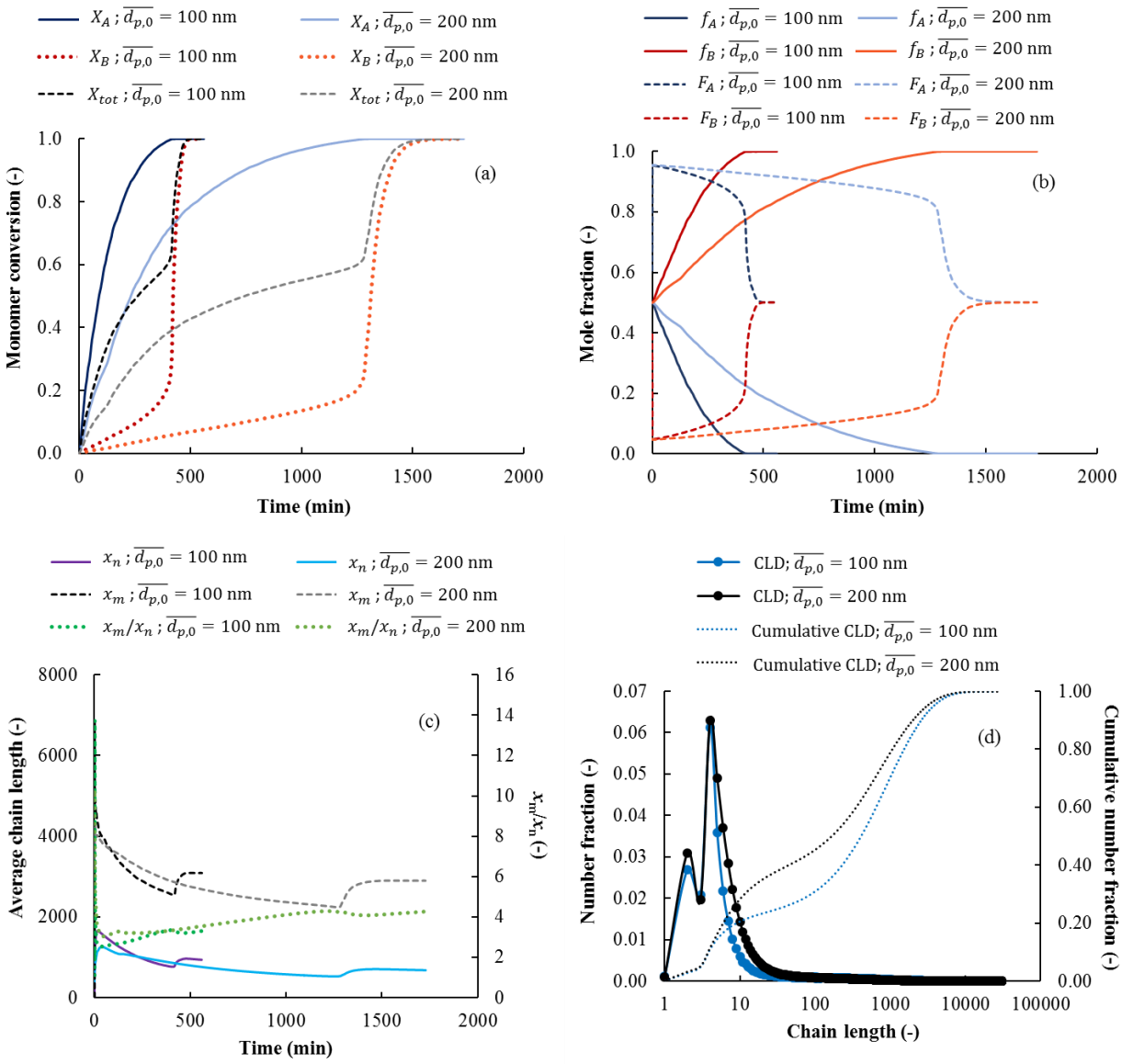

Figure 4. Effect of the initial PSD on the simulation results of Figure 2; initial conditions: see caption Figure 2; model parameters: see Table 1.

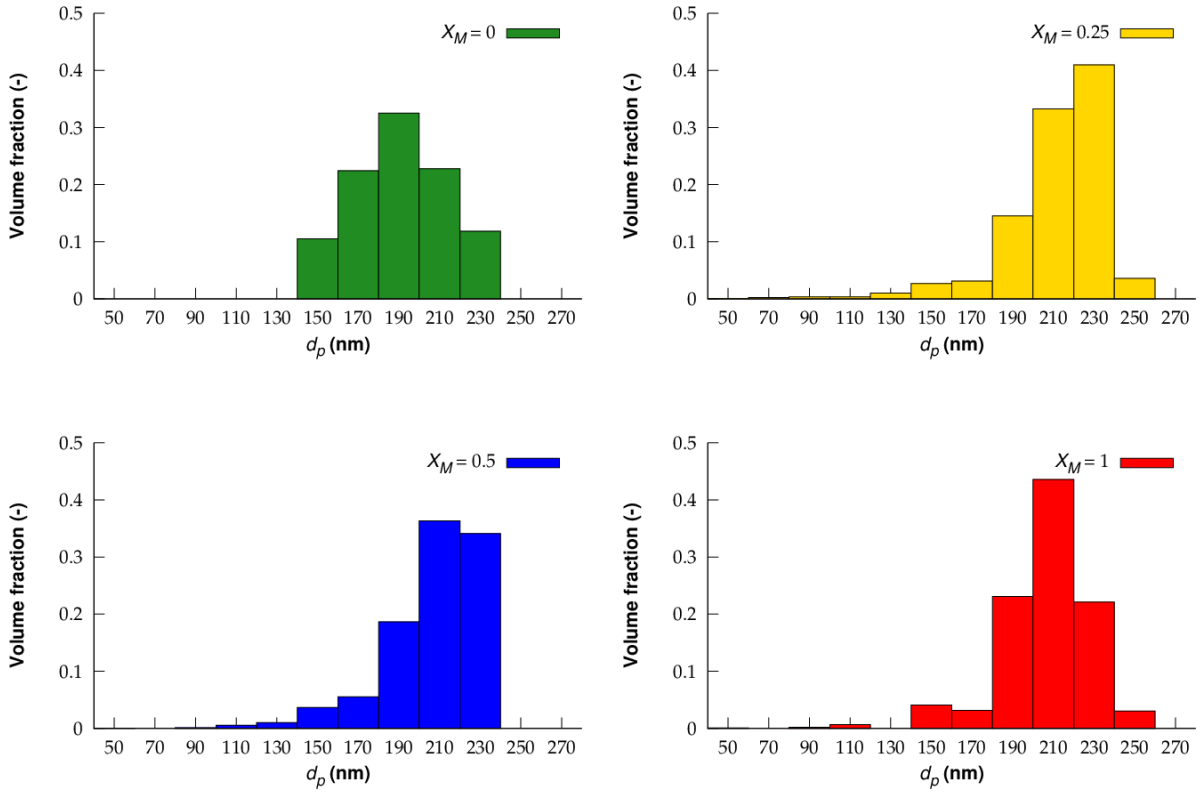

Figure 5. Evolution of the particle size distribution (PSD) corresponding to Figure 4 (the case of a Gaussian initial PSD with average diameter $\overline{d_{p,0}}$ = 200 nm); volume-weighted PSD at a total monomer conversion (*i.e.* based on both comonomers) of 0% (*i.e.* the initial PSD; top left), 25% (top right), 50% (bottom left) and 100% (*i.e.* the final PSD; bottom right); initial conditions: see caption Figure 2; model parameters: see Table 1.

7.4 Conclusions

A kinetic Monte Carlo model for the simulation of isothermal batch miniemulsion copolymerization has been developed. Reaction and interphase mass transfer events of initiator, monomer-molecules and initiator-derived, monomeric and oligomeric radicals are tracked particle by particle. The model allows the interactive and joint simulation of the micro-scale characteristics such as the chain length distribution and copolymer composition and meso-scale characteristics such as the particle size distribution.

Miniemulsion copolymerization of styrene and N-vinylcaprolactam (VCL) initiated by 2,2′-azobis(2-methylpropionitrile) has been selected as a case study, taking into account the opportunities VCL copolymer nanoparticles offer for *e.g.* controlled drug delivery.

The evolution of the (co)monomer conversions, the fraction of the comonomers in the reaction mixture and incorporated on average in the polymer chains, and the number and mass average chain lengths are consistent with the disparate monomer reactivity ratios of styrene and VCL. The effect of the initial PSD has been studied by comparing the evolution of the copolymerization characteristics obtained with an initial Gaussian PSD with a volume-average diameter of 100 nm and 200 nm. Similar but much slower evolving trends for the monomer conversions and copolymer compositions are obtained for the latter case, highlighting the strong interaction between the PSD (meso-scale) and the polymerization kinetics (micro-scale).

In agreement with previous experimental work, investigation of the temporal evolution of the PSD demonstrated a negative skewing of the PSD at low and intermediate conversions due to droplets/particles that did not undergo any significant polymerization and, hence, only supplied monomer to other particles. Toward higher monomer conversions, a more uniform PSD is obtained.

The presented modeling tool unveils unprecedented insight into dispersed phase copolymerization and will help the design of tailored nanoparticles for *e.g.* drug delivery applications on a longer term.

7.5 References

1. A. V. Kabanov and S. V. Vinogradov, *Angew. Chem.-Int. Edit.*, 2009, **48**, 5418-5429.
2. M. J. Kettel, K. Schaefer, A. Pich and M. Moeller, *Polymer*, 2016, **86**, 176-188.
3. J. Liu, A. Debuigne, C. Detrembleur and C. Jerome, *Adv. Healthc. Mater.*, 2014, **3**, 1941-1968.
4. G. Y. Liu and Z. S. An, *Polym. Chem.*, 2014, **5**, 1559-1565.
5. D. R. D'hooge, M. Vachaudez, F. J. Stadler, M. F. Reyniers, O. Coulembier, C. Bailly, P. Dubois and G. B. Marin, *European Polymer Journal*, 2013, **49**, 2344-2355.
6. N. A. Cortez-Lemus and A. Licea-Claverie, *Prog. Polym. Sci.*, 2016, **53**, 1-51.
7. H. Vihola, A. Laukkanen, L. Valtola, H. Tenhu and J. Hirvonen, *Biomaterials*, 2005, **26**, 3055-3064.
8. A. Pich and W. Richtering, in *Chemical Design of Responsive Microgels*, eds. A. Pich and W. Richtering, Springer Berlin Heidelberg, Berlin, Heidelberg, 2011, pp. 1-37.
9. H. J. M. Wolff, M. Kather, H. Breisig, W. Richtering, A. Pich and M. Wessling, *ACS Appl. Mater. Interfaces*, 2018, **10**, 24799-24806.
10. F. A. L. Janssen, M. Kather, L. C. Kroger, A. Mhamdi, K. Leonhard, A. Pich and A. Mitsos, *Ind. Eng. Chem. Res.*, 2017, **56**, 14545-14556.
11. S. F. Medeiros, A. M. Santos, H. Fessi and A. Elaissari, *J. Polym. Sci. Pol. Chem.*, 2010, **48**, 3932-3941.
12. D. Crespy, S. Zuber, A. Turshatov, K. Landfester and A. M. Popa, *J. Polym. Sci. Pol. Chem.*, 2012, **50**, 1043-1048.
13. S. Shah, A. Pal, R. Gude and S. Devi, *European Polymer Journal*, 2010, **46**, 958-967.
14. X. M. Ma, J. Y. Xi, X. B. Huang, M. Zhao and X. Z. Tang, *Mater. Lett.*, 2004, **58**, 3400-3404.
15. B. H. Tan and K. C. Tam, *Advances in Colloid and Interface Science*, 2008, **136**, 25-44.
16. D. R. D'hooge, P. H. M. Van Steenberge, M. F. Reyniers and G. B. Marin, *Prog. Polym. Sci.*, 2016, **58**, 59-89.
17. D. J. G. Devlaminck, P. H. M. Van Steenberge, M.-F. Reyniers and D. R. D'hooge, *Macromolecules*, 2018, **51**, 9442-9461.
18. D. J. G. Devlaminck, P. H. M. Van Steenberge, L. De Keer, M. F. Reyniers and D. R. D'Hooge, *Polym. Chem.*, 2017, **8**, 6948-6963.
19. Y. N. Zhou and Z. H. Luo, *Macromol. React. Eng.*, 2016, **10**, 516-534.
20. Y. W. Marien, P. H. M. Van Steenberge, D. R. D'hooge and G. B. Marin, *Macromolecules*, 2019, **52**, 1408-1423.
21. S. K. Fierens, P. H. M. Van Steenberge, M. F. Reyniers, D. R. D'Hooge and G. B. Marin, *React. Chem. Eng.*, 2018, **3**, 128-145.
22. S. K. Fierens, P. H. M. Van Steenberge, M. F. Reyniers, G. B. Marin and D. R. D'Hooge, *Aiche J.*, 2017, **63**, 4971-4986.

23. M. Stach, I. Lacik, D. Chorvat, M. Buback, P. Hesse, R. A. Hutchinson and L. Tang, *Macromolecules*, 2008, **41**, 5174-5185.
24. C. Hagiopol, *Copolymerization: toward a systematic approach*, Springer Science+Business Media New York, 1999.
25. J. Asua, *Polymer Reaction Engineering*, John Wiley & Sons, 2008.
26. S. Santanakrishnan, L. Tang, R. A. Hutchinson, M. Stach, I. Lacik, J. Schrooten, P. Hesse and M. Buback, *Macromol. React. Eng.*, 2010, **4**, 499-509.
27. G. Johnston-Hall and M. J. Monteiro, *J. Polym. Sci. Pol. Chem.*, 2008, **46**, 3155-3173.
28. S. C. Thickett and R. G. Gilbert, *Polymer*, 2007, **48**, 6965-6991.
29. M. Nomura, H. Tobita and K. Suzuki, in *Polymer Particles*, ed. M. Okubo, Springer-Verlag Berlin, Berlin, 2005, vol. 175, pp. 1-128.
30. H. F. Hernandez and K. Tauer, *Macromol. React. Eng.*, 2009, **3**, 375-397.
31. H. F. Hernandez and K. Tauer, *Ind. Eng. Chem. Res.*, 2008, **47**, 9795-9811.
32. J. M. Asua and J. C. De La Cal, *J. Appl. Polym. Sci.*, 1991, **42**, 1869-1877.
33. P. H. M. Van Steenberge, D. R. D'hooge, M. F. Reyniers, G. B. Marin and M. F. Cunningham, *Macromolecules*, 2014, **47**, 7732-7741.
34. L. Bentein, D. R. D'hooge, M. F. Reyniers and G. B. Marin, *Polymer*, 2012, **53**, 681-693.
35. Y. Shang, G. R. Shan and P. J. Pan, *Macromolecular Chemistry and Physics*, 2015, **216**, 884-893.
36. M. C. Griffiths, J. Strauch, M. J. Monteiro and R. G. Gilbert, *Macromolecules*, 1998, **31**, 7835-7844.
37. J. W. Breitenbach and A. Schindler, *Monatsh Chem*, 1952, **83**, 724–730.
38. M. Buback, R. G. Gilbert, R. A. Hutchinson, B. Klumperman, F. D. Kuchta, B. G. Manders, K. F. Odriscoll, G. T. Russell and J. Schweer, *Macromolecular Chemistry and Physics*, 1995, **196**, 3267-3280.
39. D. Kukulj, T. P. Davis and R. G. Gilbert, *Macromolecules*, 1998, **31**, 994-999.
40. G. Johnston-Hall and M. J. Monteiro, *Macromolecules*, 2008, **41**, 727-736.
41. C. Autran, J. C. de la Cal and J. M. Asua, *Macromolecules*, 2007, **40**, 6233-6238.
42. J. P. A. Heuts and G. T. Russell, *European Polymer Journal*, 2006, **42**, 3-20.
43. P. B. Zetterlund and M. Okubo, *Macromolecules*, 2006, **39**, 8959-8967.
44. Y. Kagawa, P. B. Zetterlund, H. Minami and M. Okubo, *Macromol. Theory Simul.*, 2006, **15**, 608-613.
45. P. B. Zetterlund, *Polym. Chem.*, 2011, **2**, 534-549.
46. H. Tobita and F. Yanase, *Macromol. Theory Simul.*, 2007, **16**, 476-488.
47. T. G. T. Jansen, J. Meuldijk, P. A. Lovell and A. M. van Herk, *Macromol. React. Eng.*, 2015, **9**, 19-31.

Chapter 8: General conclusions and future outlook

8.1 General conclusions

Many polymer products used in every-day life, ranging from commodity materials to high-tech materials for *e.g.* controlled drug delivery applications, are produced via radical polymerization. Notably, the macroscopic material properties of the associated polymer products are strongly determined by micro- and meso-scale characteristics that have a distributed nature, such as the chain length or molar mass distribution (CLD/MMD) on the micro-scale (*i.e.* the level of molecules) and the particle size distribution (PSD) on the meso-scale (*i.e.* the level of particles). Often these distributions display multimodality. A detailed overview of the origin and possible advantages multimodality offers for (dispersed phase) radical polymerizations has been given is **Chapter 1**, together with an overview of the state-of-the-art for the modeling of these distributions.

In this PhD thesis, kinetic Monte Carlo (*k*MC) modeling, which is a powerful stochastic technique allowing to track individual reaction and phase transfer events in chemical processes, has been applied for the accurate simulation of multimodal CLD/MMD and PSD encountered in radical polymerizations. In a first part of this PhD thesis, *k*MC modeling has been applied to pulsed laser polymerization (PLP), which is a frequently used technique for the determination of individual (intrinsic) rate coefficients. In **Chapter 2**, it has been demonstrated that the *k*MC simulation of complete experimental multimodal PLP MMDs allows to obtain information beyond only information on the conventional propagation reactivity from the location of the inflection points. In particular, it has been demonstrated that the success of 2,2-dimethoxy-2-phenylacetophenone (DMPA) as a photoinitiator for PLP can be attributed to the disparate reactivities of the DMPA radical fragments, leading to sharper peaks and, hence, a more facile identification of the inflection points. Moreover, the crucial role of diffusional limitations on

termination has been illustrated. Only if chain length dependent termination kinetics are accurately accounted for, an excellent agreement between the simulated and experimental MMD can be obtained. Next, the developed *k*MC model for PLP has been applied in **Chapter 3** to develop a novel methodology for the estimation of the photodissociation quantum yield, which, up until now, was a difficult parameter to estimate. By performing regression analysis to the ratio of the peak heights in the PLP MMD, a reliable estimation for the DMPA photodissociation quantum yield has been obtained. The *k*MC model has also been applied to the estimation of the backbiting (and tertiary propagation) rate coefficient from low temperature PLP experiments (**Chapter 4**) and the β-scission rate coefficient from high temperature acrylate PLP experiments (**Chapter 5**). It should be noted that due to the higher activation energy of β-scission this stepwise approach is affordable. A variation of both the laser pulse frequency and solvent volume fraction has been proposed to obtain reliable and robust estimates for the backbiting and β-scission rate coefficient. By using the saturated analogue of the monomer as solvent, solvent effects could be ruled out in acrylate PLP.

In the second part of this PhD thesis, focus has shifted to dispersed phase radical polymerization. In view of the expected stronger interaction between the micro- and meso-scale in emulsion polymerization compared to suspension polymerization focus has been on the former polymerization technique. For illustration purposes miniemulsion polymerization was studied in the absence of morphological aspects such as phase separation in the polymer particles. In **Chapter 6**, a novel detailed *k*MC model in which reaction and interphase mass transfer events are tracked particle by particle has been developed for isothermal batch miniemulsion free radical homopolymerization. A joint and interactive prediction of the CLD and PSD evolution has been demonstrated for the first time, considering literature parameters for all model parameters. The relevance of each radical polymerization reaction and each mass transfer event in view of striving for the establishment of partitioning has been highlighted. It

has been also illustrated that the conventional Smith-Ewart deterministic modeling methodology with average monomer concentrations per particle and an average particle size is inaccurate as monomer fluctuations between particles matter and the organic phase kinetics are particle size dependent. This model has been extended and applied to miniemulsion copolymerization of styrene and N-vinylcaprolactam (VCL) in **Chapter 7**. Notably, the initial PSD has been demonstrated to have a large effect on the evolution of the copolymerization characteristics, with lower polymerization rates as the initial PSD shifts to higher particle sizes. A consecutive dominant incorporation of styrene and VCL has been simulated, in agreement with the disparate monomer reactivity ratios. Moreover, the *k*MC simulations indicated a very dynamic evolution of the PSD, again highlighting the need for the simultaneous simulation of both CLD and PSD. Importantly, the obtained insights will aid the design of copolymer VCL nanogel particles for *e.g.* drug delivery applications, also benefiting from the experimental knowledge acquired during a research stay in the group of Prof. Pich at DWI Leibniz Institute for Interactive Materials/ RWTH Aachen University.

8.2 Future outlook

8.2.1 Pulsed laser polymerization research axis

A novel alternative method for the estimation of the backbiting, tertiary propagation and β-scission rate coefficient from bulk and/or solution low frequency inflection point data has been developed in this PhD thesis. While this PhD thesis was being finalized, a large experimental data set has been obtained at the Laboratory for Chemical Technology (LCT) for PLP of *n*-butyl acrylate, allowing the reliable estimation of Arrhenius parameters for these reactions. On a longer term, the method can also be applied to other acrylates, for which, to date, no kinetic information on backbiting, tertiary propagation and β-scission is available. This would then allow to investigate whether acrylates display a trend or family type behavior for these reactions.

Moreover, in view of the applications of pVCL nanoparticles and the absence of reliable absolute propagation rate coefficients for VCL, propagation rate coefficients for VCL are currently being measured at LCT. On a longer term, a comparison with other vinyl lactams can be made, allowing to investigate if a trend or family type behavior can be detected.

Finally, as the model developments presented in this PhD thesis allow not only the simulation of inflection points but also of complete PLP-SEC traces, regression analysis to (parts of) complete SEC traces could be considered in future work in order to obtain even more kinetic information from PLP experiments.

8.2.2 Emulsion polymerization research axis

A novel *k*MC modeling tool allowing the joint and interactive CLD and PSD calculation for isothermal batch miniemulsion homo- and copolymerization has been developed in this PhD thesis. A first challenge to allow a further exploitation of this modeling tool is the extension to the industrial macro-emulsion polymerization process, in which initially larger monomer droplets are present than in a miniemulsion polymerization and also (monomer-swollen) micelles are present. Hence, for a macro-emulsion polymerization *e.g.* also homogeneous nucleation leading to (precursor) particles, coagulation of precursor particles and breakage of monomer droplets need to be taken into account.

A second challenge to allow a further exploitation of the developed modeling tool is the consideration of morphology aspects due to polymer phase separation inside polymer particles. Hence, depending on the phase separation mechanism, *e.g.* radial gradients in polymer composition need to be taken into account.

A final challenge is the refinement of the meso-scale model and the more reliable determination of meso-scale model parameters. Ideally, micro-scale model parameters are first determined via regression to dedicated bulk/solution polymerization data obtained *e.g.* via PLP. In a next step,

meso-scale model parameters are to be determined via regression to emulsion polymerization data.

Appendix A: Supporting Information for Chapter 2

A.1 Model details

A.1.1 Photodissociation kinetics

The generated amount of DMPA photoinitiator radical fragments per pulse ($\Delta[R_0]$) is calculated explicitly (Equation (2) in Chapter 2), based on the principles introduced by Odian,[1] who reported a derivation for the rate of photodissociation (mol L^{-1} s^{-1}) as a function of the intensity delivered by the light source (I_{0*}; W dm^{-2}):

$$r_d = \Phi \frac{I_{0*}\lambda}{hcN_A L}[1 - \exp(-2.303\varepsilon[DMPA]L)] \quad \text{(S.1)}$$

in which Φ is the quantum yield for photodissociation, λ the wavelength of the laser, ε the molar absorptivity of the photoinitiator (dm^2 mol^{-1}), L the optical path length (dm), h the Planck constant (J s), c the speed of light (dm s^{-1}), [DMPA] (mol L^{-1}) the DMPA concentration at the selected time t (s), and N_A the Avogadro constant (mol^{-1}). The quantum yield is the probability of the photoinitiator to dissociate upon absorption of a photon. Note that no (chemical) efficiency factor f is used since all reactions with I species are explicitly accounted for, hence, f is taken equal to one.

Equation (S.1) follows from the following mathematical manipulations. Focusing only on a unit cell in the reaction mixture at distance D (dm) the corresponding photodissociation rate (r_d) at t (s) can be calculated from:

$$r_d = \Phi\, r_a \quad \text{(S.2)}$$

in which r_a is the rate at which photons are absorbed (mol dm^{-3} s^{-1}), at t and D. The rate of photon absorption r_a can be related to the intensity of the absorbed light I (mol $(dm)^{-2}$ s^{-1}):

$$r_a = -\frac{dI}{dD} \quad \text{(S.3)}$$

in which I can be calculated using the Bouguer-Lambert-Beer law:

$$I = I_0 \exp(-\alpha[DMPA]D) \tag{S.4}$$

in which I_0 is the incident light intensity at the outer surface (mol dm^{-2} s^{-1}), and α the absorption coefficient of DMPA (dm^2 mol^{-1}). It should be noted that alternatively, the molar absorptivity ε can be used which is related to α by:

$$\alpha = \varepsilon \ln 10 = 2{,}303\ \varepsilon \tag{S.5}$$

Hence, by combining the above equations r_a follows from:

$$r_a = -\frac{dI}{dD} = 2{,}303\ \varepsilon\ [DMPA] I_0 \exp(-2.303\ \varepsilon\ [DMPA]D) \tag{S.6}$$

In addition, the light intensity I_0 can be expressed in J dm^{-2} s^{-1} (I_{0*}), The latter can be accounted for by insertion of a conversion factor, *i.e.* $N_A h\, c/\lambda$ which is the energy of a mole of photons:

$$r_a = 2{,}303\ \varepsilon\ [DMPA]\left(\frac{I_{0*}\lambda}{N_A h\ c}\right)\exp(-2.303\ \varepsilon\ [DMPA]D) \tag{S.7}$$

Upon integration (D from 0 to L) and dividing by L the average rate of photon absorption ($<r_a>$) is obtained, which can be used for the whole (still small) sample at least to a first approximation:

$$< r_a >= \frac{I_{0*}\lambda}{hcN_A L}[1 - \exp(-2.303\varepsilon[DMPA]L)] \tag{S.8}$$

Furthermore, I_{0*} can be expressed as a function of the laser pulse energy (E_{pulse}):

$$I_{0*} = \frac{E_{pulse}}{\Omega \Delta t_{pulse}} \tag{S.9}$$

with Ω the optical cross-sectional area and Δt_{pulse} the duration of the pulse. Since the change in DMPA concentration during a pulse can assumed to be negligible, $\Delta[R_0]$ can thus be calculated by multiplying r_d (Equation (S.2) for the entire sample (*i.e.* r_a replaced by $<r_a>$) with Δt_{pulse} and multiplying by two, since two radicals are formed per dissociation event.

$$\Delta[R_0] = 2\Phi \frac{E_{pulse}\lambda}{hcN_AV}[1 - \exp(-2.303\varepsilon[\mathrm{DMPA}]L)] \quad \text{(S.10)}$$

which is Equation (2) in Chapter 2.

A.1.2 Chain length dependent propagation kinetics

Chain length dependent propagation kinetics are accounted based on the work of Heuts and Russell:[2]

$$k_p(i) = k_p\left[1 + C_1\exp(-\frac{\ln(2)}{i_{1/2}}i)\right] \quad \text{(S.11)}$$

Note that in Equation (S.4) *i* refers to the chain length (0 for an initiator-derived radical), in contrast to the equation as originally reported by Heuts and Russell,[2] in which *i* = 1 for an initiator-derived radical. In this work, C_1 = 10 and $i_{1/2}$ = 1. These values have been reported by Haven *et al.*[3] for the modeling of so-called single unit monomer insertion (SUMI) reactions, considering acrylate monomers (*n*-butyl acrylate, *t*-butyl acrylate and 2-ethylhexyl acrylate), and allowed the representative simulation of product distributions.

A.1.3 SEC broadening

For the simulated log-MMDs, SEC broadening is accounted for according to the method proposed by Buback *et al.*,[4] which is based on the principles described by Tung[5] and Billiani[6]. The log-MMD as observed after SEC broadening, $w_{SEC}(\log M)$, is expressed as the convolution of the unbroadened log-MMD $w(\log \mathrm{M})$ with a Gaussian distribution with SEC broadening parameter $\sigma_v b$:

$$w_{SEC}(\log M) = \frac{1}{(2\pi)^{0.5}\sigma_v b}\int_0^{+\infty} \exp(-\frac{(\log(M) - \log(\widetilde{M}))^2}{2(\sigma_v b)^2})w(\log \widetilde{M})\, dlog(\widetilde{M}) \quad \text{(S.12)}$$

In this work, $\sigma_v b$ is taken equal to 0.051, in agreement with typical values reported in literature.[7, 8]

A.2 Concentration profiles of β-scission and termination products

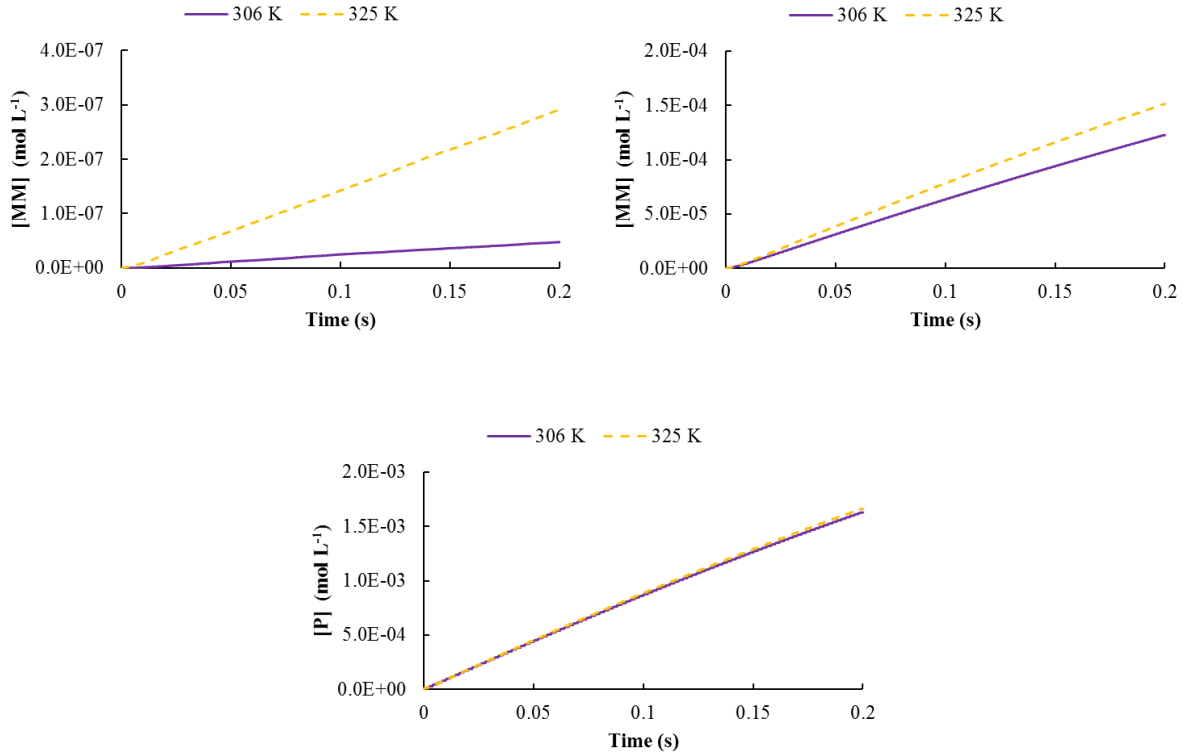

Figure S1. Top: concentration profiles for macromonomer formed via β-scission (left) and disproportionation (right); bottom: concentration profile for termination products (disproportionation and recombination); initial conditions: Figure 3 (left; Chapter 2); model parameters; Table 1 (Chapter 2).

Figure S1 shows the concentration of macromonomer formed via β-scission (top left) and disproportionation (top right), and the total concentration of termination products (bottom; both disproportionation and recombination) at 306 and 325 K. It follows that the concentration of macromonomer formed via β-scission is three orders of magnitude smaller than the concentration of termination products. Hence, β-scission products do not significantly contribute to the PLP-SEC trace. Only a small fraction of the termination products (9 % at 325 K, 7 % at 306 K; molar basis) correspond to macromonomers formed via disproportionation. Due this low fraction of macromonomers and also taking into account that macromonomer propagation is slower than conventional propagation, macromonomer propagation can be neglected.

A.3 Further illustration of the strength of *k*MC modeling to visualize the chain growth of the different radical types

A.3.1 Radical concentration traces up to the final pulse (extension of Figure 6 (right) and Figure 7 in Chapter 2)

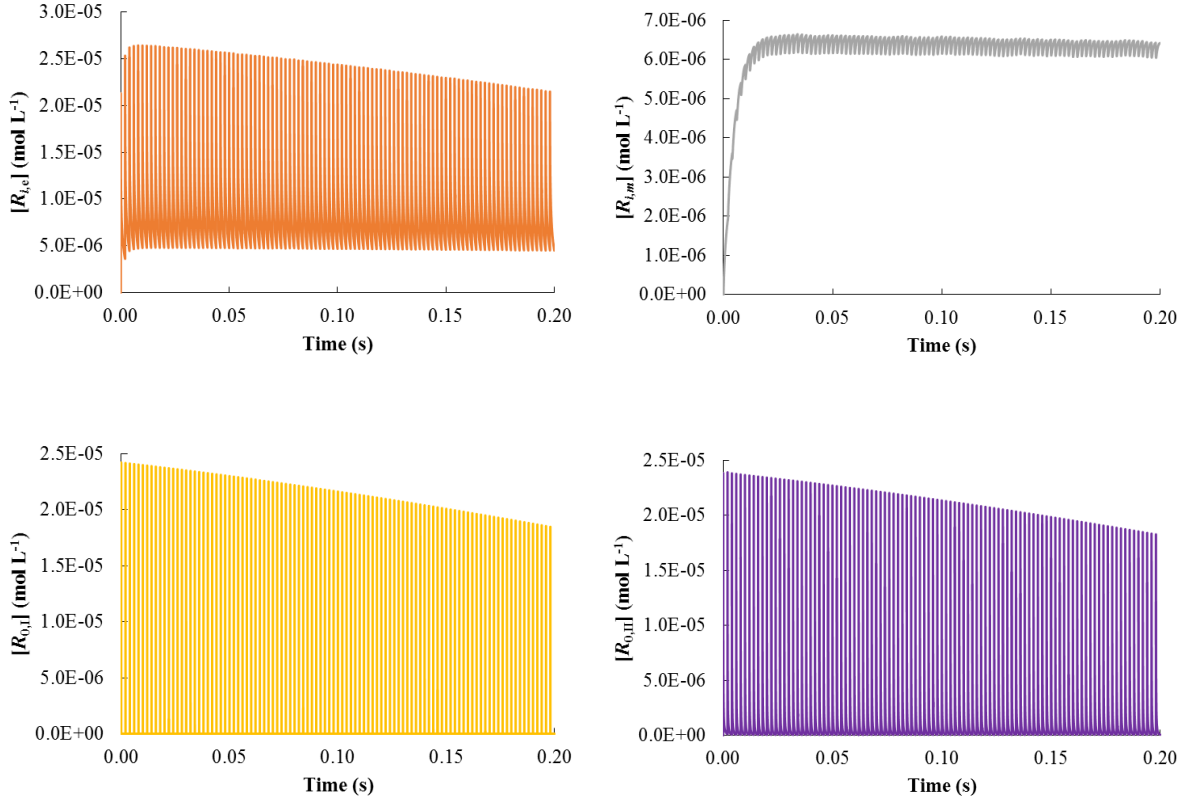

Figure S2. Temporal evolution of the concentrations of the different radical types ([$R_{i,e}$] (top left), [$R_{i,m}$] (top right), [$R_{0,I}$] (bottom left) and [$R_{0,II}$] (bottom right) up to the final pulse (*i.e.* extension of Figure 7 in Chapter 2 in which focus is only on the first 10 pulses)

A.3.2 Comparison of actual concentrations and approximate ones after application of the PSSA

Under the assumption of negligible intermolecular chain transfer and termination, the pseudo-steady state approximation (PSSA) for the ECR and MCR concentration can be expressed as:[9]

$$k_{bb}\sum_{i=3}^{\infty}[R_{i\geq 3,e}] = k_{p,m}[M]_0[R_m] \qquad \text{(S.13)}$$

Defining x_{ECR} and x_{MCR} as the fraction of macroradicals being secondary of nature (ECR; $i \geq 3$) and tertiary (MCR), and taking into account that:

$$x_{ECR} + x_{MCR} = 1 \tag{S.14}$$

allows to obtain the PSSA based fractions by solving Equation (S.13) and (S.14) to x_{ECR} and x_{MCR}:[9]

$$x_{ECR}^{PSSA} = \frac{k_{p,m}[M]_0}{k_{bb} + k_{p,m}[M]_0} \tag{S.15}$$

$$x_{MCR}^{PSSA} = \frac{k_{bb}}{k_{bb} + k_{p,m}[M]_0} \tag{S.16}$$

in which the monomer concentration is assumed equal to the initial one, an acceptable assumption since the monomer conversion is limited in PLP experiments (*ca.* < 5%).

In Figure S3, it is shown that x_{ECR} and x_{MCR} calculated from the concentrations as obtained by the *k*MC simulations (no PSSA assumed; rate coefficients are listed Table 1 in Chapter 2) do not reach the PSSA based fractions (Equation (S.15) and Equation (S.16)) within a dark period. Since a relatively high frequency is applied (500 s^{-1}), new ECRs are already generated before the PSSA based concentrations can be reached.

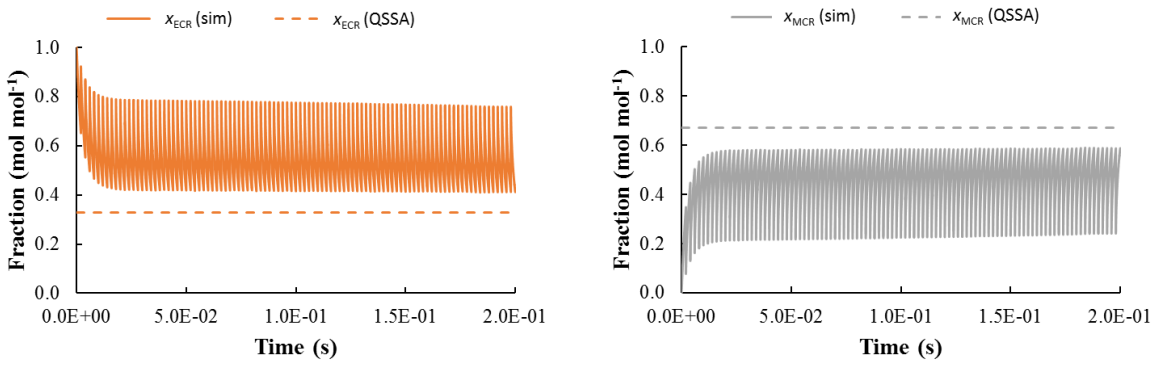

Figure S3. Illustration of the approximate nature of PSSA based ECR and MCR concentrations; full line: actual fraction; dashed line: PSSA based fraction obtained via Equation (S.14) and (S.15); conditions: Figure 3 (left) in Chapter 2.

A.3.3 Visualization of the chain growth in between pulses

As mentioned in Chapter 2, the chain growth in between two pulses can be visualized by considering the log-MMD of the ECRs (full blue line) and MCRs (dotted yellow line) at different times. In Figure S4, focus is on the chain growth in between the 50th and 51st pulse (*i.e.* $49\Delta t \leq t \leq 50\Delta t$); the log-MMD at three times is shown, namely at $(1/3)\Delta t$ (top left), $(2/3)\Delta t$ (top right) and just before the 51st pulse (bottom). Radicals originating from the previous pulses can clearly be distinguished in the higher molar mass regions, which is additionally illustrated in Figure S4 (left) in which the ECR log-MMDs of the three subfigures of Figure S3 are now all in the same plot. The conversion of ECRs to MCRs via backbiting can be inferred from Figure S3, considering the increase in importance of MCRs originating from the last laser pulse at increasing time. A more pronounced (longer) fronting is observed at higher times, as also shown in Figure S4 (right) in which all subfigures are included in the same plot. Due to the low reactivity of the MCRs, the peak corresponding to MCRs formed after a time Δt can be detected in the MCR log- MMD at times in between two pulses (Figure S3 (top left/ right)).

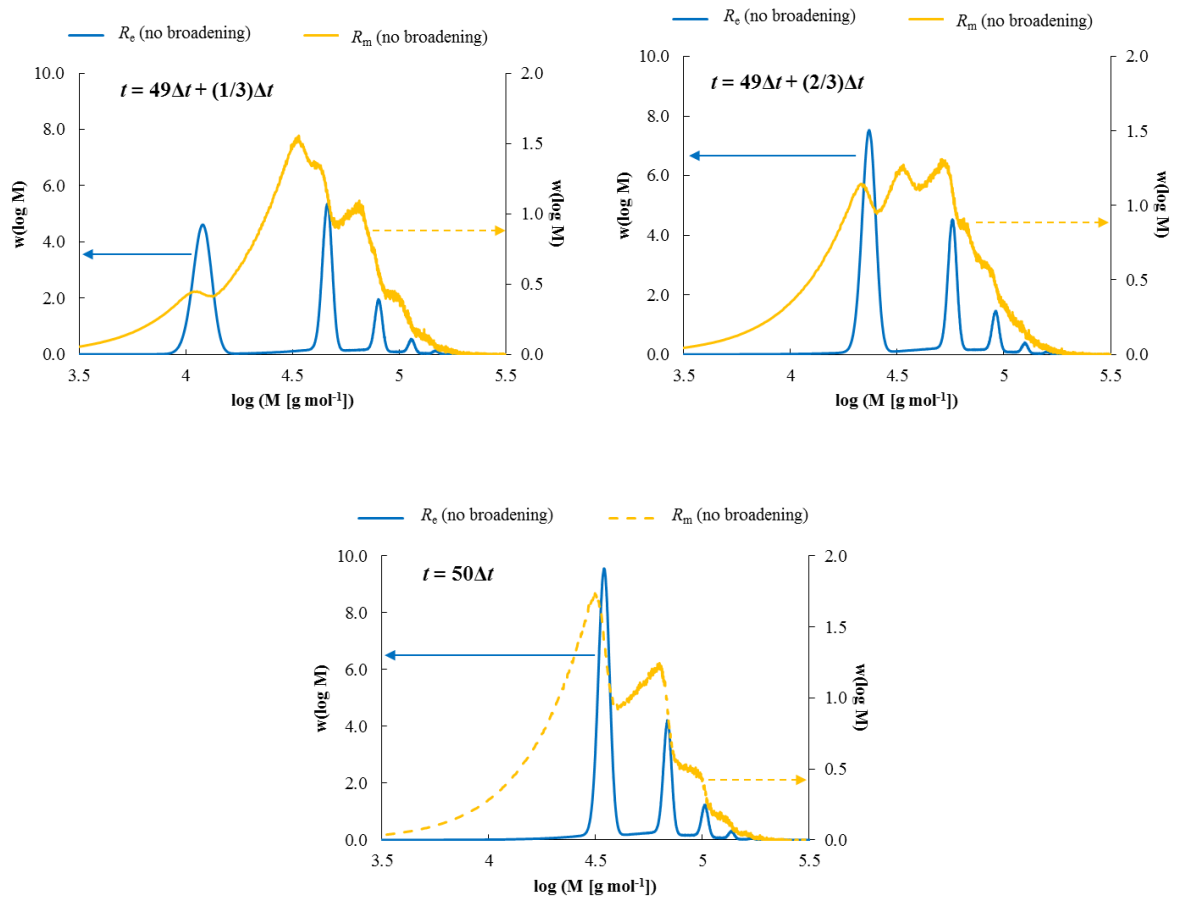

Figure S4. Simulated log-MMD without SEC-broadening for the ECRs (full blue line) and MCR (dashed yellow line) at different times (top left: $t = 49\Delta t + (1/3)\Delta t$, top right: $t = 49\Delta t + (2/3)\Delta t$, bottom: $t = 50\Delta t = 0.1$ s (same as in Figure 8 in Chapter 2); same conditions as in Figure 3 (left; Chapter 2); model parameters are listed in Table 1 of Chapter 2.

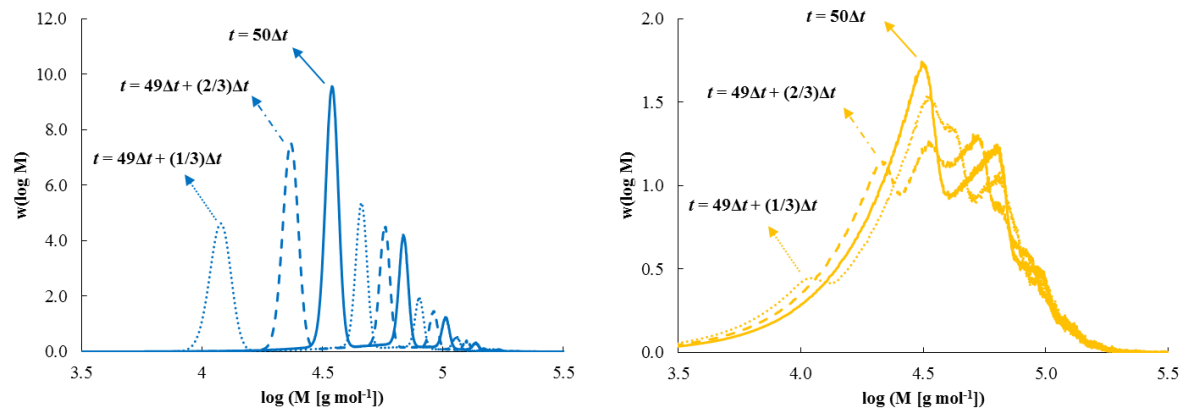

Figure S5. Simulated log-MMD without SEC-broadening for the ECRs/MCRs at different times (dotted blue line: $t = 49\Delta t + (1/3)\Delta t$*;* dashed blue line: $t = 49\Delta t + (2/3)\Delta t$*;* full blue line: $t = 50\Delta t = 0.1$ s (same as in Figure 8 in Chapter 2); same conditions as in Figure 3 (left; Chapter 2); model parameters are listed in Table 1 of Chapter 2.

A.4 References

1. G. Odian, *Principles of Polymerization*, Wiley, 2004.
2. J. P. A. Heuts and G. T. Russell, *European Polymer Journal*, 2006, **42**, 3-20.
3. J. J. Haven, J. Vandenbergh, R. Kurita, J. Gruber and T. Junkers, *Polym. Chem.*, 2015, **6**, 5752-5765.
4. M. Buback, M. Busch and R. A. Lammel, *Macromol. Theory Simul.*, 1996, **5**, 845-861.
5. L. H. Tung and J. R. Runyon, *J. Appl. Polym. Sci.*, 1969, **13**, 2397-&.
6. J. Billiani, G. Rois and K. Lederer, *Chromatographia*, 1988, **26**, 372-376.
7. A. N. Nikitin, R. A. Hutchinson, M. Buback and P. Hesse, *Macromolecules*, 2007, **40**, 8631-8641.
8. P. Drawe and M. Buback, *Macromol. Theory Simul.*, 2016, **25**, 74-84.
9. C. Plessis, G. Arzamendi, J. M. Alberdi, A. M. van Herk, J. R. Leiza and J. M. Asua, *Macromol. Rapid Commun.*, 2003, **24**, 173-177.

Appendix B: Supporting Information for Chapter 3

B.1 Experimental details for the measurement of the ratio of PLP-SEC peak heights

An overview of all initial conditions for PLP of *n*-butyl acrylate (*n*BuA) and the corresponding experimental results for the ratio of the peak heights of the SEC trace is given in Table S1. For each pulse energy, an experimentally recorded SEC trace is shown in Figure S1.

Table S1: Experimental results for PLP of *n*BuA at 306 K and varying E_{pulse}; initial conditions: $[DMPA]_0 = 3\ 10^{-3}$ mol L^{-1}, $[nBuA]_0 = 6.91$ mol L^{-1}, $\nu = 500\ s^{-1}$.

Entry	E_{pulse} [mJ]	Number of pulses [-]	h_1/h_2
1	1.5	200	0.895
2	2.5	100	0.989
3	3.5	80	1.228
4	4.5	65	1.419
5	6	40	1.626

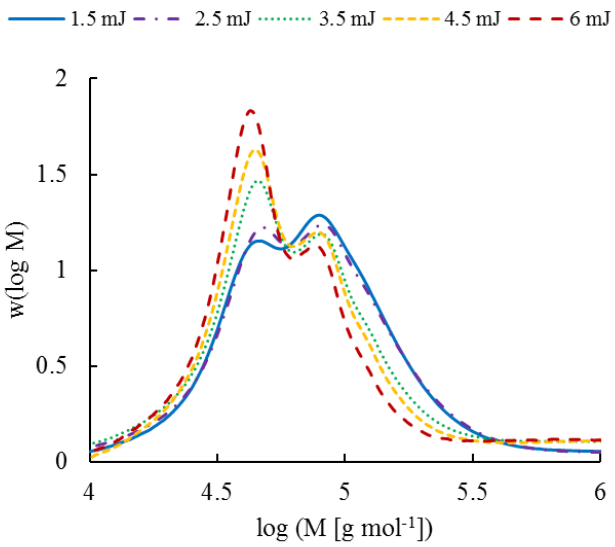

Figure S1: Experimentally recorded SEC traces for PLP of *n*BuA at various pulse energies; conditions: see Table S1.

B.2 Model details for the simulation of the ratio of PLP-SEC peak heights

B.2.1 Reactions and model parameters

In Table S2 the reactions considered in the kinetic Monte Carlo (*k*MC) model to simulate the PLP-SEC trace and, hence, the PLP-SEC peak heights are listed. The model parameters for the *in silico* testing of the method with the parameters having values reflecting typical orders of magnitude (column 3) and the parameters for the *in silico* application to MMA (column 5) are also shown. Similarly, the parameter are given for the actual application of the method to PLP of *n*BuA (column 4). The concentration of radicals generated at the laser pulses, $\Delta[R_0]$, is calculated via Equation (2; main text) with the input value of Φ for the theoretical evaluation and the value estimated via regression analysis to the peak heights of *n*BuA PLP at 306 K given in entry 1 of Table S2. For each laser pulse, $\Delta[R_0]$ is calculated taking into account the decreasing photoinitiator concentration.

Note that intermolecular chain transfer can be neglected at the low monomer conversions considered in this work.[1-4] Moreover, due to the low temperature (306 K), β-scission of MCRs can safely be neglected.[1, 5] In addition, as illustrated by the coinciding lines in Figure S2 (full green line: $k_{trM,e}$ = 0 L mol^{-1} s^{-1}, $k_{trM,m}$ = 0 L mol^{-1} s^{-1}; dotted black line: $k_{trM,e}$ = 8.0 10^{-1} L mol^{-1} s^{-1}, $k_{trM,m}$ = 2.8 10^{-3} L mol^{-1} s^{-1} (ref. [6])), chain transfer to monomer can also be neglected in the present work.

It should be further reminded, as explained in the main text, that the current modeling strategy with an explicit treatment of the chemical reactions with the DMPA radical fragments does not require the introduction of a chemical initiator efficiency.

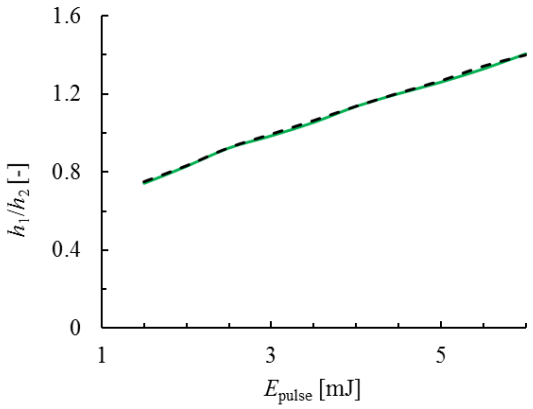

Figure S2: Illustration of the negligible effect of chain transfer to monomer on h_1/h_2 for PLP of *n*BuA under the conditions considered in this work (Table S1); full green line: $k_{trM,e}$ = 0 L mol^{-1} s^{-1}, $k_{trM,m}$ = 0 L mol^{-1} s^{-1}; dotted black line: $k_{trM,e}$ = 7.9 10^{-1} L mol^{-1} s^{-1},[6] $k_{trM,m}$ = 2.7 10^{-3} L mol^{-1} s^{-1};[6] model parameters: Table S2 (column 4).

Chain length dependent (apparent) termination kinetics are taken into account and expressed as:

$$k_t^{app}(i,i) = k_t^{app}(1,1)i^{-\alpha s} \qquad i \leq i_c \tag{S.1}$$

$$k_t^{app}(i,i) = k_t^{app}(1,1)i_c^{-\alpha_S+\alpha_L}i^{-\alpha_L} \qquad i > i_c \tag{S.2}$$

$$k_t^{app}(i,j) = [k_t^{app}(i,i)k_t^{app}(j,j)]^{0.5} \tag{S.3}$$

with α_S, α_L and i_c equal to 0.85, 0.16 and 30 (theoretical evaluation (Figure 2, 3 in the main text) and application to *n*BuA (Figure 4 in the main text); parameters *cf.* ref. [7]) or α_S, α_L and i_c equal to 0.65, 0.15 and 100 (*in silico* application to MMA (Figure S3); parameters *cf.* ref. [8]).

Non-instantaneous quenching at the end of a PLP experiment is accounted for in agreement with ref.[9]

Table S2. Basic reaction scheme to simulate low temperature PLP initiated by DMPA, including a listing of the model parameters used for the theoretical evaluation of the method (only orders of magnitude) and the actual application to *n*BuA at 306 K, for which intermolecular chain transfer and *β*-scission can be neglected based on literature data[1-5], and for which chain transfer to monomer can also be neglected, as demonstrated above. The model parameters for the *in silico* application to PLP of MMA are also listed.

Reaction	Equation	Theoretical evaluation (Figure 2, 3) Φ [-] or k [(L mol^{-1}) s^{-1}]	*n*BuA 306 K (Figure 4) Φ [-] or k [(L mol^{-1}) s^{-1}]	MMA 306 K (Figure S3) Φ [-] or k [(L mol^{-1}) s^{-1}]
Photodissociation[a]	$DMPA \xrightarrow{h\nu,\Phi} R^{\mathrm{I}}_{0,\mathrm{e}} + R^{\mathrm{II}}_{0,\mathrm{e}}$	0.5	0.42 (this work; estimated)	0.42
Chain initiation[b]	$R^{\mathrm{I}}_{0,\mathrm{e}} + M \xrightarrow{k_{\mathrm{p,I}}} R_{1,\mathrm{e}}$	10^4	2.0 10^4	4.1 10^2
Propagation	$R_{\mathrm{i,e}} + M \xrightarrow{k_{\mathrm{p,e}}} R_{\mathrm{i+1,e}}$	10^4	2.0 10^4 [10]	4.1 10^2 [11]
	$R_{\mathrm{i,m}} + M \xrightarrow{k_{\mathrm{p,m}}} R_{\mathrm{i+1,e}}$	10^1	1.4 10^1 [7]	-
Backbiting ($i \geq 3$)	$R_{\mathrm{i,e}} \xrightarrow{k_{\mathrm{bb}}} R_{\mathrm{i,m}}$	10^2	1.9 10^2 [7]	-
Termination[c] ($i, j \geq 0$)	$R_{\mathrm{i,e}} + R_{\mathrm{j,e}} \xrightarrow{k^{\mathrm{app}}_{\mathrm{t,ee}}(i,j)} P_{\mathrm{i(+j)}}(+P_{\mathrm{j}})$	10^9	9.6 10^8 [7]	1.5 10^9 [8,d]
	$R_{\mathrm{i,e}} + R_{\mathrm{j,m}} \xrightarrow{k^{\mathrm{app}}_{\mathrm{t,em}}(i,j)} P_{\mathrm{i(+j)}}(+P_{\mathrm{j}})$	10^8	3.1 10^8 [7]	-
	$R_{\mathrm{i,m}} + R_{\mathrm{j,m}} \xrightarrow{k^{\mathrm{app}}_{\mathrm{t,mm}}(i,j)} P_{\mathrm{i(+j)}}(+P_{\mathrm{j}})$	10^6	2.0 10^6 [7]	-

[a]: dissociation into a benzoyl and dimethoxy benzyl radical; $\Delta[R_0]$ calculated via Equation (2; main text), with both for the theoretical validation and the actual application to PLP of *n*BuA ε = 280 L mol^{-1} cm^{-1}, λ = 351 nm, V = 0.2 mL and L = 0.52 cm (*cf.* Experimental Section (main text)).
[b]: $k_{\mathrm{p,I}}$ can be taken equal to the plateau value for propagation with long ECRs, no propagation of $R_{0,\mathrm{II}}$ (*cf.* ref. [9])
[c]: chain length dependent (apparent) termination rate coefficients are considered (Equation (S.1) - (S.3); parameters: ref. [7, 8]); $k^{\mathrm{app}}_{\mathrm{t}}(1,1)$ is reported, taking into account a correction with a factor 2, as indicated by *e.g.* Derboven *et al.*;[12] fraction termination by recombination (δ) in agreement with literature data (column 3,4: δ_{ee} = 0.9, δ_{em} = 0.3, δ_{mm} = 0.1 *cf.* ref [5, 13]; column 5: δ_{ee} = 0.25 *cf.* ref. [14]); i, j = 0: $R^{\mathrm{I//II}}_{0,\mathrm{e}}$ (hence termination of the propagating and non-propagating radical also taken into account)
[d]: $k^{\mathrm{app}}_{\mathrm{t,ee}}(1,1)$ determined from its value at 353 K as reported in ref. [8] and an E_{a} of 9 kJ mol^{-1} in agreement with ref. [15]

B.2.2 Correction for SEC broadening

In agreement with the method described in previous work,[16] the simulated log-MMD $w(\log M)$ is corrected according to the following formula to account for SEC broadening:

$$w_{SEC}(\log M) = \frac{1}{(2\pi)^{0.5}\sigma_v b}\int_0^{+\infty} \exp\left(-\frac{(\log(M) - \log(\widetilde{M}))^2}{2(\sigma_v b)^2}\right) w(\log \widetilde{M})\, dlog(\widetilde{M}) \quad \text{(S.4)}$$

In this work, the SEC broadening parameter $\sigma_v b$ is taken equal to 0.05, in agreement with typical values reported in literature.[9, 17, 18]

B.3 *In silico* application to PLP of MMA

In order to test if the method yields the same estimate for Φ_{diss} for other monomers, the method is applied to *in silico* PLP data of MMA at 306 K (all conditions are listed in the caption of Figure S3; in order to increase the intensity of the SEC signal, multiple samples at identical conditions may be combined before SEC analysis). These data are obtained via *k*MC simulations using the model parameters as listed in Table S2 (5th column) and a value of 0.42 for Φ_{diss} (*cf*. value estimated from PLP data of *n*BuA). In a subsequent step this data is superimposed with a random error determined via Gaussian sampling with standard deviation σ = 0.3 to mimic an experimental error of *ca*. 10%. By performing a regression analysis to the latter data an estimate for Φ_{diss} of 0.43 ± 0.07 (95% confidence interval) is obtained, with the corresponding fit shown in Figure S3. Since the obtained estimate (Φ_{diss} = 0.43) is very close to the estimate obtained via regression analysis to PLP data of *n*BuA (Φ_{diss} = 0.42), it has been demonstrated that in case accurate monomer-specific model parameters are used, the obtained estimate for Φ_{diss} does not depend on the selected monomer.

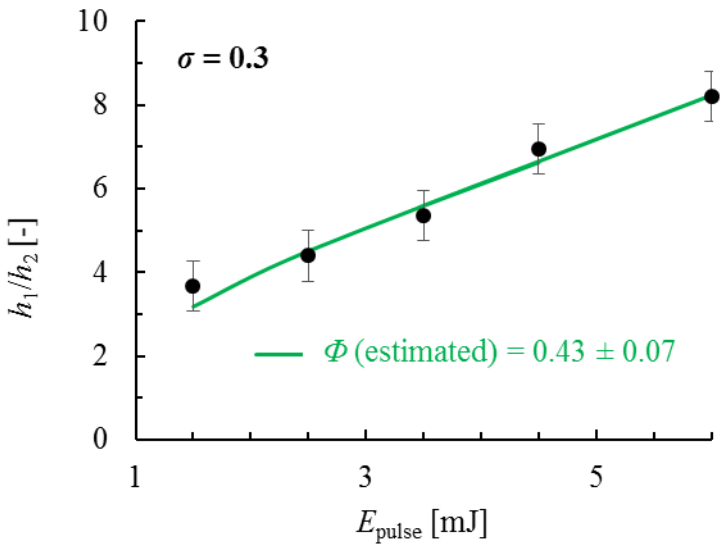

Figure S3. *In silico* application to PLP of MMA; symbols: data generated using a *k*MC model with an input value of 0.42 for Φ_{diss} (*cf.* value estimated from PLP data of *n*BuA) and all other model parameters as in Table S2 (5th column), superimposed with a random error (Gaussian sampling with standard deviation σ = 0.6 (*i.e.* an error of *ca.* 10%); full line: model after regression analysis; conditions: T = 306 K, $\nu = 10\ s^{-1}$, $[DMPA]_0 = 0.3$ mmol L^{-1}, sample volume: 0.2 mL (optical path length: 0.52 cm), N_{pulse} = 225 (1.5 mJ), 150 (2.5 mJ), 120 (3.5 mJ), 100 (4.5 mJ), 70 (6mJ).

B.4 Sensitivity to the apparent termination reactivity

As for any method, the accuracy of the presented approach is affected by the accuracy of the model parameters. In particular, the method is most sensitive to the apparent termination reactivity $k_{t,app}$ (*i*,*j*). In this section, the effect a large error on $k_{t,app}$ (*i*,*j*) has on the estimate for Φ_{diss} is investigated.

To this purpose, a regression analysis to the same data as in Figure 3 (left; main text), *i.e.* h_1/h_2 data obtained via simulation with an input value of 0.5 for Φ_{diss} and the model parameters as listed in Table S2 (column 3) and superimposed with a Gaussian error mimicking an experimental error of *ca.* 10%, is performed. However, in the regression analysis $k_{t,app}$ (*i*,*j*) is increased with 50% compared to Table S2 (column 3). Hence, a large error of 50% is considered in this case study. An estimate of 0.34 ± 0.04 (95% confidence interval) is obtained. The overestimation of $k_{t,app}$ (*i*,*j*) thus leads to an underestimation of Φ_{diss}. Importantly, such inaccuracies can be detected by applying the method to another monomer for which extensively

studied rate coefficients are available. Indeed, provided that accurate monomer-specific model parameters are used, the same value of Φ_{diss} is obtained.

B.5 References

1. J. Barth, M. Buback, P. Hesse and T. Sergeeva, *Macromol. Rapid Commun.*, 2009, **30**, 1969-1974.
2. C. Farcet, J. Belleney, B. Charleux and R. Pirri, *Macromolecules*, 2002, **35**, 4912-4918.
3. P. Derboven, P. H. M. Van Steenberge, J. Vandenbergh, M. F. Reyniers, T. Junkers, D. R. D'hooge and G. B. Marin, *Macromol. Rapid Commun.*, 2015, **36**, 2149-2155.
4. N. Ballard, S. Hamzehlou and J. M. Asua, *Macromolecules*, 2016, **49**, 5418-5426.
5. A. N. Nikitin, R. A. Hutchinson, W. Wang, G. A. Kalfas, J. R. Richards and C. Bruni, *Macromol. Reac. Eng.*, 2010, **4**, 691-706.
6. S. Maeder and R. G. Gilbert, *Macromolecules*, 1998, **31**, 4410-4418.
7. J. Barth, M. Buback, P. Hesse and T. Sergeeva, *Macromolecules*, 2010, **43**, 4023-4031.
8. G. Johnston-Hall, M. H. Stenzel, T. P. Davis, C. Barner-Kowollik and M. J. Monteiro, *Macromolecules*, 2007, **40**, 2730-2736.
9. Y. W. Marien, P. H. M. Van Steenberge, C. Barner-Kowollik, M.-F. Reyniers, G. B. Marin and D. R. D'hooge, *Macromolecules*, 2017, **50**, 1371-1385.
10. J. M. Asua, S. Beuermann, M. Buback, P. Castignolles, B. Charleux, R. G. Gilbert, R. A. Hutchinson, J. R. Leiza, A. N. Nikitin, J. P. Vairon and A. M. van Herk, *Macromol. Chem. Phys.*, 2004, **205**, 2151-2160.
11. S. Beuermann, M. Buback, T. P. Davis, R. G. Gilbert, R. A. Hutchinson, O. F. Olaj, G. T. Russell, J. Schweer and A. M. van Herk, *Macromol. Chem. Phys.*, 1997, **198**, 1545-1560.
12. P. Derboven, D. R. D'hooge, M.-F. Reyniers, G. B. Marin and C. Barner-Kowollik, *Macromolecules*, 2015, **48**, 492-501.
13. S. Hamzehlou, N. Ballard, Y. Reyes, A. Aguirre, J. M. Asua and J. R. Leiza, *Polym. Chem.*, 2016, **7**, 2069-2077.
14. A. N. Nikitin and R. A. Hutchinson, *Macromol. Theory Simul.*, 2007, **16**, 29-42.
15. J. Barth and M. Buback, *Macromol. Rapid Commun.*, 2009, **30**, 1805-1811.
16. M. Buback, M. Busch and R. A. Lammel, *Macromol. Theory Simul.*, 1996, **5**, 845-861.
17. A. N. Nikitin, R. A. Hutchinson, M. Buback and P. Hesse, *Macromolecules*, 2007, **40**, 8631-8641.
18. P. Drawe and M. Buback, *Macromol. Theory Simul.*, 2016, **25**, 74-84.

Appendix C: Supporting Information for Chapter 4

C.1 Experimental details for the measurement of the inflection points

In this section, an overview of the experimental results is given. In Table S1, all the initial conditions and the corresponding results for the inflection points are listed. Typical PLP-SEC traces are shown in Figure S1 with an indication of the inflection points (black circles).

Table S1. Experimental results for PLP of *n*BuA at 303 K for varying solvent volume fraction and laser pulse frequency; initial conditions: $[DMPA]_0$ = 2.5 10^{-3} mol L^{-1}, E_{pulse} = 1.5 10^{-3} J; solvent: butyl propionate

Entry	Volume fraction solvent [-]	Frequency [s^{-1}]	Number of pulses [-]	$k_{p,app}$ [L mol^{-1} s^{-1}]
1	0	10	25	4366
2	0	20	35	7820
3	0	40	45	8913
4	0	60	55	9873
5	0.5	10	35	3727
6	0.5	20	45	4575
7	0.5	40	65	6218
8	0.5	60	75	7816
9	0.75	10	50	2858
10	0.75	20	65	4193
11	0.75	40	85	5179
12	0.75	60	95	7152

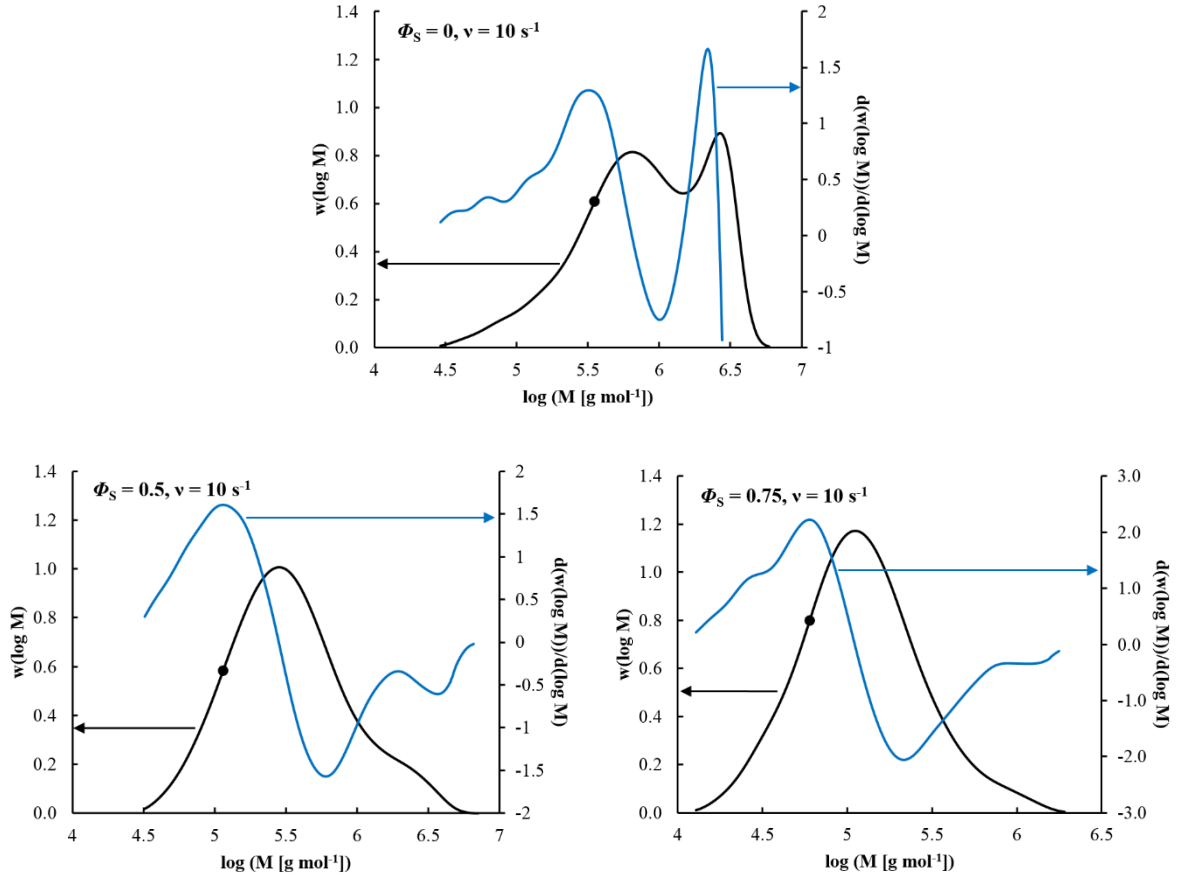

Figure S1. Typical measured PLP-SEC traces (full black line) and their corresponding first derivative (full blue line) for PLP of *n*BuA at 303 K for varying solvent volume fraction (Φ_S = 0, 0.5, 0.75) and a laser pulse frequency ν = 10 s^{-1}; black circle: inflection point (*i.e.* maximum of first derivative) used for $k_{p,app}$ determination (Equation (2) in the main text); initial conditions: $[DMPA]_0$ = 2.5 10^{-3} mol L^{-1}, E_{pulse} = 1.5 10^{-3} J; solvent: butyl propionate (see also Table S1).

C.2 Model details for the calculation of the inflection points

C.2.1 Reactions and model parameters for the basic PLP model

An overview of the reactions considered in the kinetic Monte Carlo (*k*MC) model to calculate the inflection points and thus to obtain the simulated input for the regression analysis is provided in Table S2 (basic reaction scheme). In the same table, the model parameters for the theoretical evaluation of the method (parameters: only typical orders of magnitude) and the application to the actual experimental data (*cf.* Table S1) are included.

Table S2. Basic reaction scheme to simulate low temperature PLP of *n*BuA initiated by DMPA, including a listing of the model parameters used for the theoretical evaluation of the method (only orders of magnitude) and the actual application to *n*BuA at 303 K; intermolecular chain transfer, *β*C-scission and macromonomer addition neglected based on literature data.[1, 2] Chain transfer to monomer and solvent can be also neglected, as demonstrated in Section 3.

Reaction	Equation	Theoretical evaluation $\Delta[R_0]$ [mol L^{-1}], k [(L mol^{-1}) s^{-1}]	*n*BuA 303 K $\Delta[R_0]$ [mol L^{-1}], k [(L mol^{-1}) s^{-1}]
Photodissociation[a]	$DMPA \xrightarrow{\Delta[R_0]} R^{\mathrm{I}}_{0,\mathrm{e}} + R^{\mathrm{II}}_{0,\mathrm{e}}$	10^{-4}	$2\ 10^{-5}$
Chain initiation[b]	$R^{\mathrm{I}}_{0,\mathrm{e}} + M \xrightarrow{k_{\mathrm{p,I}}} R_{1,\mathrm{e}}$	10^{4}	$1.8\ 10^{4}$
Propagation	$R_{\mathrm{i,e}} + M \xrightarrow{k_{\mathrm{p,e}}} R_{\mathrm{i+1,e}}$	10^{4}	$1.8\ 10^{4}$ [3]
	$R_{\mathrm{i,m}} + M \xrightarrow{k_{\mathrm{p,m}}} R_{\mathrm{i+1,e}}$	10^{2}	$1.2\ 10^{1}$ [4]
Backbiting ($i \geq 3$)	$R_{\mathrm{i,e}} \xrightarrow{k_{\mathrm{bb}}} R_{\mathrm{i,m}}$	10^{3}	$1.7\ 10^{2}$
Termination[c] ($i, j \geq 0$)	$R_{\mathrm{i,e}} + R_{\mathrm{j,e}} \xrightarrow{k^{\mathrm{app}}_{\mathrm{t,ee}}(i,j)} P_{\mathrm{i(+j)}}(+P_{\mathrm{j}})$	10^{9}	$9.3\ 10^{8}$ [4]
	$R_{\mathrm{i,e}} + R_{\mathrm{j,m}} \xrightarrow{k^{\mathrm{app}}_{\mathrm{t,em}}(i,j)} P_{\mathrm{i(+j)}}(+P_{\mathrm{j}})$	10^{8}	$6.1\ 10^{8}$ [4]
	$R_{\mathrm{i,m}} + R_{\mathrm{j,m}} \xrightarrow{k^{\mathrm{app}}_{\mathrm{t,mm}}(i,j)} P_{\mathrm{i(+j)}}(+P_{\mathrm{j}})$	10^{6}	$1.9\ 10^{6}$ [4]

[a]: dissociation into a benzoyl and dimethoxy benzyl radical; $\Delta[R_0]$ of the first laser pulse is reported (Equation (S.3))
[b]: $k_{\mathrm{p,I}}$ can be taken equal to the plateau value for propagation with long ECRs, no propagation of $R_{0,\mathrm{II}}$ (*see* Subsection 2.1)
[c]: chain length dependent (apparent) termination rate coefficients according to the composite k_t model are considered (see Subsection 2.1); $k_t^{\mathrm{app}}(1,1)$ is reported, taking into account a correction with a factor 2, as indicated by *e.g.* Derboven *et al.*;[5] fraction termination by recombination (δ) in agreement with literature data ($\delta_{\mathrm{ee}} = 0.9$, $\delta_{\mathrm{em}} = 0.3$, $\delta_{\mathrm{mm}} = 0.1$) [2, 6]; $i, j = 0$: $R^{\mathrm{I/II}}_{0,\mathrm{e}}$

In what follows, specific attention is focused on the kinetic parameters for photodissociation, chain initiation, and termination. In Section 3 it is demonstrated that the reactions included are indeed sufficient for the reliable calculation of the inflection points.

The generated amount of photoinitiator radical fragments per pulse ($\Delta[R_0]$) is calculated explicitly.[7] The rate of photodissociation (mol L^{-1} s^{-1}) as a function of the intensity delivered by the light source (I_0; W dm^{-2}) is calculated as:

$$r_{diss} = \Phi_{diss} \frac{I_0 \lambda}{hcN_A L} [1 - \exp(-2.303 \varepsilon [DMPA] L)] \quad \text{(S.1)}$$

with Φ_{diss} the quantum yield for photodissociation (0.95;[8] also see subsection 3.1.1), λ the wavelength of the laser (351 10^{-7} cm), ε the molar absorptivity of the photoinitiator (280 L mol^{-1} cm^{-1}), L the optical path length (0.78 cm), h the Planck constant (6.63 10^{-34} J s), c the speed of light (3 10^{9} dm s^{-1}) , and N_A the Avogadro constant (6.02 10^{23} mol^{-1}). The intensity (I_0) can be expressed as a function of the laser pulse energy (E_{pulse}; 1.5 10^{-3} J):

$$I_0 = \frac{E_{pulse}}{\Omega \Delta t_{pulse}} \tag{S.2}$$

with Ω the optical cross-sectional area (3.85 10^{-3} dm^2) and Δt_{pulse} the duration of the pulse. Since the change in DMPA concentration during a pulse can assumed to be negligible (initial [DMPA] = 2.5 10^{-3} mol L^{-1}), $\Delta[R_0]$ can be calculated by multiplying r_{diss} (Equation (S.1)) with Δt_{pulse}, taking into account a factor 2 (two radicals formed per dissociation reaction):

$$\Delta[R_0] = 2\Phi_{diss} \frac{E_{pulse}\lambda}{hcN_A \Omega \mathrm{L}} [1 - \exp(-2.303\varepsilon[\mathrm{DMPA}]L)] \tag{S.3}$$

In agreement with earlier kinetic analysis of single pulse-pulsed laser polymerization (SP-PLP) experiments,[9] and based on literature data,[10-13] in the present work, the difference in chain initiation reactivity of the DMPA radical initiator fragments (entry 2 in Table S2) is taken into account. No further decomposition needs to be taken into account due to the selected low polymerization temperature of 303 K.[9]

Chain length dependent termination kinetics - either caused intrinsically or by diffusional limitations - are evaluated via the composite k_t model.[14-17] For the low monomer conversion ranges as encountered during PLP, it suffices to consider:

$$k_t^{app}(i,i) = k_t^{app}(1,1) i^{-\alpha_S} \qquad i \leq i_c \tag{S.4}$$

$$k_t^{app}(i,i) = k_t^{app}(1,1) i_c^{-\alpha_S + \alpha_L} i^{-\alpha_L} \qquad i > i_c \tag{S.5}$$

in which α_S and α_L express the chain length dependence for short and long radicals, and i_c is the cross-over chain length. The values as reported by Barth *et al.*[4] are used, *i.e.* $\alpha_S = 0.85$, $\alpha_L = 0.16$, and $i_c = 30$.

C.2.2 Correction for SEC broadening

When designing and interpreting PLP-SEC experiments, it has to be taken into account that axial dispersion during analysis leads to a broadening. Buback *et al.*[18] have proposed a procedure to account for this experimental broadening, based on principles suggested by Tung[19] and Billiani.[20]

Tung[19] proposed to express the chromatogram *f* as the convolution of the chromatogram in case no experimental broadening would occur, *h*, with a broadening function *G*:

$$f(v) = \int_0^{+\infty} G(v - \tilde{v})h(\tilde{v})d\tilde{v} \tag{S.6}$$

According to Billiani[20] the broadening function can be represented by a Gaussian distribution with variance σ_v^2:

$$G(v - \tilde{v}) = \frac{1}{\sigma_v\sqrt{2\pi}}\exp(-\frac{(v - \tilde{v})^2}{2\sigma_v^2}) \tag{S.7}$$

Shortt[21] demonstrated that the relation between the broadened MMD $w_{SEC}(\log M)$ and the chromatogram *f(v)* is given by:

$$w_{SEC}(log\, M) = -\frac{f(v)}{d(\log M)/dv} \tag{S.8}$$

Analogously, the relation between *w(log M)*, with *M* representing the molar mass, and the chromatogram *h(v)*, with *w(log M)*and *h(v)* both representing the case no broadening occurs, is given by:

$$w(log\,M) = -\frac{h(v)}{d(\log M)/dv} \tag{S.9}$$

If the relation between the elution volume *v* and *log M* is linear:

$$log\,M = a - bv \tag{S.10}$$

it follows that:

$$\frac{d(\log M)}{dv} = -b \tag{S.11}$$

Substituting (S.11) into (S.8) and (S.9), respectively, yields:

$$f(v) = b\,w_{SEC}(log\,M) \tag{S.12}$$

$$h(v) = b\,w(log\,M) \tag{S.13}$$

Finally, substituting (S.7), (S.12), and (S.13) into (S.6), yields:

$$w_{SEC}(\log M) = \frac{1}{(2\pi)^{0.5}\sigma_v b}\int_0^{+\infty} \exp\left(-\frac{(\log(M) - \log(\widetilde{M}))^2}{2(\sigma_v b)^2}\right) w(\log\,\widetilde{M})\,dlog(\widetilde{M}) \tag{S.14}$$

Equation (S.14) has the important implication that broadening is assumed Gaussian with respect to *log*(*M*) and, hence, larger chain lengths will SEC-broaden exponentially. The SEC broadening parameter ($\sigma_v b$) can be determined via regression to the SEC-measured MMD for a narrow polystyrene standard. It can be expected that this leads to an upper limit for the broadening parameter, as this value also reflects the width of the MMD of the polystyrene standard. It has been opted in the present work to use the literature value of 4 10^{-2}.[22]

C.3 Robustness of the alternative method

In the present section, the robustness of the alternative method is illustrated. Via a sensitivity analysis it is first demonstrated that a correct calculation of inflection points does not imply the need of a detailed model with highly accurate kinetic parameters. Next it is shown that the method can in principle be applied for the simultaneous estimation of the backbiting and mid-

chain radical propagation rate coefficient, indicating that a lack of knowledge on the latter does not lead to a failure of the method.

C.3.1 Sensitivity of $k_{p,app}$ to the model parameters

C.3.1.1 Photodissociation

In this work, $\Delta[R_0]$ is fundamentally calculated via Equation (S.3) by substituting the values for the experimental parameters (E_{pulse} = 1.5 10^{-3} J, [DMPA] = 2.5 10^{-3} mol L^{-1}, λ = 351 10^{-7} cm, Ω = 3.85 10^{-3} dm^2, L = 0.78 cm), the physical constants (h = 6.63 10^{-34} J s, c = 3 10^9 dm s^{-1}, N_A = 6.02 10^{23} mol^{-1}) and physicochemical coefficients (ε = 280 L mol^{-1} cm^{-1} and Φ_{diss} = 0.95). It should be noted that Φ_{diss} has been also reported equal to 0.52;[23] in contrast to the value reported by Allonas *et al.*[8] (Φ_{diss} = 0.95). For Φ_s = 0 and ν = 10 s^{-1} the effect of such a variation in Φ_{diss} (and thus $\Delta[R_0]$) on the PLP-SEC trace and in particular on the position of the inflection point is shown to be negligible in Figure S2 (full purple line: Φ_{diss} = 0.95, L_1 = 3778; dashed yellow line: Φ_{diss} = 0.52, L_1 = 3851).

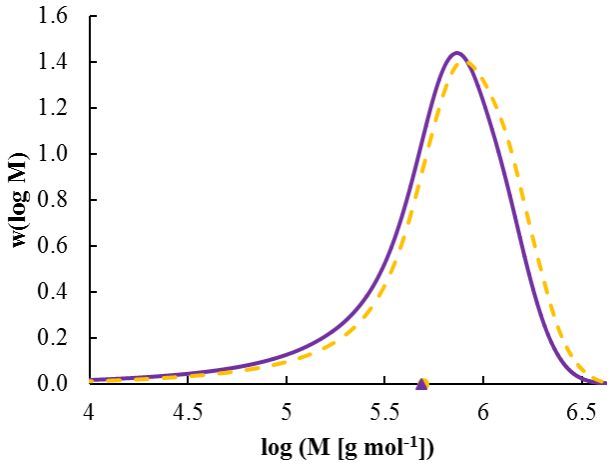

Figure S2. Theoretical illustration of the negligible effect of a possible variation of Φ_{diss} on the PLP-SEC trace (full purple line: Φ_{diss} = 0.95; dashed yellow line: Φ_{diss} = 0.52) and in particular on the inflection point (symbols) for Φ_s = 0 and ν = 10 s^{-1}; initial conditions: Table S1; model parameters: Table S2.

C.3.1.2 Chain transfer to monomer

In principle the estimated parameter values could depend on the chain transfer to monomer rate coefficients $k_{trM,e}$ (transfer from an ECR) and $k_{trM,m}$ (transfer from an MCR). In Figure S3 it is theoretically demonstrated that at the temperature considered in this study (303 K), chain transfer to monomer has a negligible effect on the PLP-SEC trace (dashed yellow line: $k_{trM,e}$ = 6.9 10^{-1} L mol^{-1} s^{-1} and $k_{trM,m}$ = 2.3 10^{-3} L mol^{-1} s^{-1} (literature values[24]), L_1 = 3528; full purple line: $k_{trM,e}$ = $k_{trM,m}$ = 0 L mol^{-1} s^{-1}, L_1 = 3778) and in particular on the position of the inflection point (symbols in Figure S3), even under the conditions of the highest importance of chain transfer to monomer, *i.e.* highest monomer concentration (Φ_S = 0) and lowest frequency (ν = 10 s^{-1}) considered in this study.

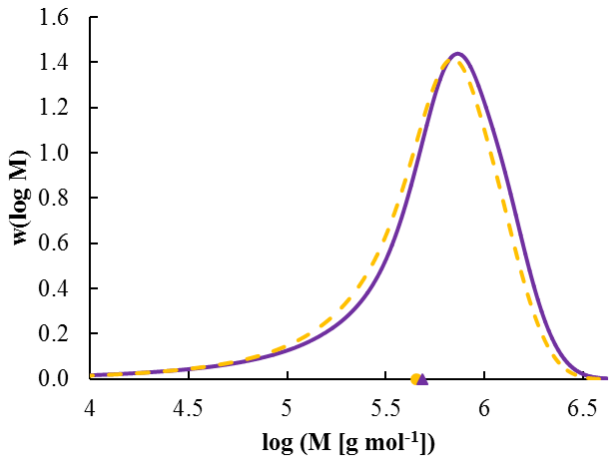

Figure S3. Theoretical illustration of the negligible effect of chain transfer to monomer on the PLP-SEC trace and in particular on the inflection point at 303 K; transfer to monomer accounted for (dashed yellow line; $k_{trM,e}$ and $k_{trM,m}$ from ref.[24]) and neglected (full purple line; $k_{trM,e}$ = $k_{trM,m}$ = 0 L mol^{-1} s^{-1}); Φ_S = 0, ν = 10 s^{-1} (*i.e.* conditions corresponding to the highest importance of chain transfer to monomer); initial conditions: Table S1; model parameters: Table S2.

C.3.1.3 Chain transfer to solvent

In addition to chain transfer to monomer, chain transfer to solvent can occur. In order to investigate the effect of this chain transfer reaction on the PLP-SEC trace and in particular on the inflection point, simulations with the coefficient of chain transfer to solvent (C_{trS}) based on literature data are performed. C_{trS} is assessed by the value for chain transfer from poly(ethyl

acrylate) radicals to ethyl acetate at 353 K (C_{trS} = 8.9 10^{-5}).[25] The value of C_{trS} at 353 K is converted to the value at 303 K using for simplicity the activation energy of the rate coefficient of chain transfer to monomer (C_{trM}), which yields a value for C_{trS} of 3.9 10^{-5}. In Figure S4, the PLP-SEC trace for C_{trS} = 3.9 10^{-5} (dashed yellow line; L_1 = 465) and C_{trS} = 0 (full blue line; L_1 = 496) is shown, with the inflection pointed indicated by a symbol. It is clear that at 303 K, chain transfer to solvent has a negligible effect on the PLP-SEC trace and thus on the inflection point, even under the conditions of the highest importance of chain transfer to solvent, *i.e.* highest solvent volume fraction (Φ_S = 0.75) and lowest frequency (ν = 10 s^{-1}) considered in this study. Hence, chain transfer to solvent can safely be neglected in the present work and no accurate rate coefficients need to be known for the reliable estimation of k_{bb} and $k_{p,m}$. In addition, in general, the temperature and frequencies can always be regulated to avoid a possible impact.

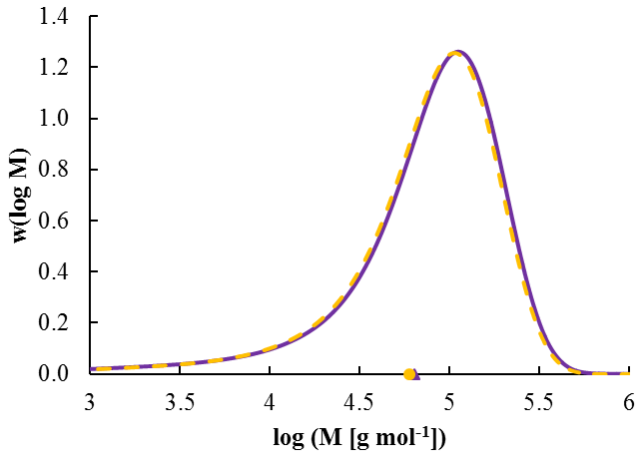

Figure S4. Theoretical illustration of the negligible effect of chain transfer to solvent on the PLP-SEC trace and in particular on the inflection point at 303 K; transfer to solvent accounted for (dashed yellow line; C_{trS} based on ref[25]) and neglected (full purple line; C_{trS} = 0 L mol^{-1} s^{-1}); Φ_S = 0.75, ν = 10 s^{-1} (*i.e.* conditions corresponding to the highest importance of chain transfer to solvent); initial conditions: Table S1; model parameters: Table S2.

C.3.1.4 Termination

Finally, the estimated parameter value for k_{bb} (and $k_{p,m}$) could depend on the apparent termination reactivities. In Figure S5 it is demonstrated for Φ_S = 0 and ν = 10 s^{-1} that a significant variation of the termination reactivity (variation of $k_t(1,1)$ by a factor 2) results in a shift of the PLP-SEC trace (full purple line: literature value for $k_t(1,1)$,[4] L_1 = 3778; dotted blue line: k_t (1,1) x 2, L_1 = 3638; dashed yellow line: k_t (1,1) : 2, L_1 = 3913); the variation of the position of the inflection point is however negligible. Note that for a general monomer always a quick tuning of this parameter can be performed by considering the shift of the complete trace.

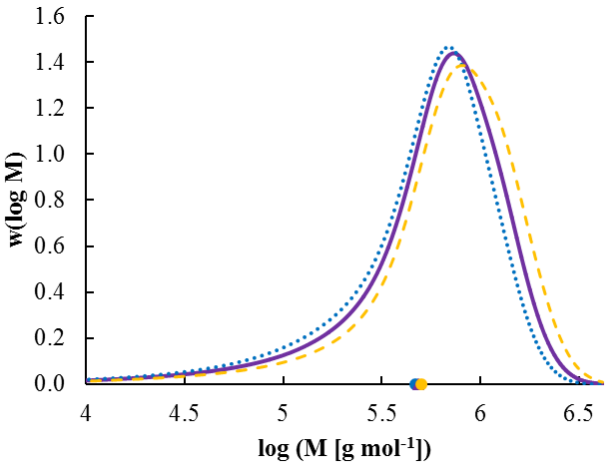

Figure S5. Theoretical illustration of the limited effect of the termination reactivity on the position of the inflection point (symbols) for Φ_S = 0 and ν = 10 s^{-1}; full purple line: literature value for $k_t(1,1)$,[4] dotted blue line: k_t (1,1) x 2, dashed yellow line: k_t (1,1) : 2; initial conditions: Table S1; model parameters: Table S2.

C.3.2 Simultaneous estimation of k_{bb} and $k_{p,m}$

In the main text, the high accuracy of the method to estimate bulk k_{bb} values provided that $k_{p,m}$ is accurately known is demonstrated (Figure 1). In this section, it is theoretically illustrated that in addition to k_{bb}, $k_{p,m}$ can also be accurately estimated provided that sufficient PLP-SEC inflection point data are available.

In agreement with the main text (Figure 1 (left)), regression analysis of *in silico* $k_{p,app}$ data perturbed by a Gaussian error with a standard deviation of 400 L mol^{-1} s^{-1} (*i.e.* a relative error

of *ca*. 10%) is performed, however this time aiming at the estimation of both k_{bb} and $k_{p,m}$. For all rate coefficients typical orders of magnitude are again used (Table S2). A k_{bb} and $k_{p,m}$ value of 1012 s^{-1} and 102 L mol^{-1} s^{-1} are obtained with the corresponding fits shown in Figure S6 (full lines). The obtained estimates (1012 ± 307 s^{-1} and 102 ± 40 L mol^{-1} s^{-1}) are thus very close to the implemented and to be estimated value of 1000 s^{-1} and 100 L mol^{-1} s^{-1} (Table S2); statistical analysis indicates a correlation coefficient of 0.83, which is sufficiently low highlighting the limited correlation between the parameters. Large individual 95% confidence intervals are however obtained as only a small data set is considered. Hence, in case both parameters need to be estimated for an actual experimental data set it can be concluded that this set needs to be larger, in particular in case of high experimental errors.

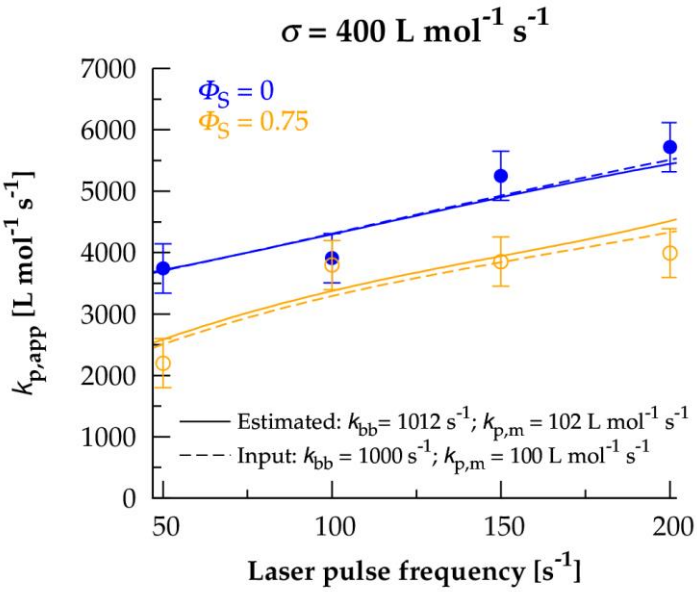

Figure S6. Potential of the method to estimate both k_{bb} and $k_{p,m}$ for acrylate radical polymerization from $k_{p,app}$ data (Equation 2); symbols: generated data with the *k*MC model (dashed lines), superimposed with an artificial error with a standard deviation σ (same as in Figure 1 (left) in the main text; model parameters: Table S2; full lines: fits after regression analysis.

C.4 References

1. J. Barth, M. Buback, P. Hesse and T. Sergeeva, *Macromol. Rapid Commun.*, 2009, **30**, 1969-1974.
2. A. N. Nikitin, R. A. Hutchinson, W. Wang, G. A. Kalfas, J. R. Richards and C. Bruni, *Macromol. Reac. Eng.*, 2010, **4**, 691-706.
3. J. M. Asua, S. Beuermann, M. Buback, P. Castignolles, B. Charleux, R. G. Gilbert, R. A. Hutchinson, J. R. Leiza, A. N. Nikitin, J. P. Vairon and A. M. van Herk, *Macromol. Chem. Phys.*, 2004, **205**, 2151-2160.
4. J. Barth, M. Buback, P. Hesse and T. Sergeeva, *Macromolecules*, 2010, **43**, 4023-4031.
5. P. Derboven, D. R. D'hooge, M.-F. Reyniers, G. B. Marin and C. Barner-Kowollik, *Macromolecules*, 2015, **48**, 492-501.
6. S. Hamzehlou, N. Ballard, Y. Reyes, A. Aguirre, J. M. Asua and J. R. Leiza, *Polym. Chem.*, 2016, **7**, 2069-2077.
7. G. Odian, *Principles of Polymerization*, Wiley, 2004.
8. X. Allonas, J. Lalevee and J. P. Fouassier, *Journal of Photochemistry and Photobiology a-Chemistry*, 2003, **159**, 127-133.
9. M. Buback, M. Busch and C. Kowollik, *Macromol. Theory Simul.*, 2000, **9**, 442-452.
10. H. Fischer, R. Baer, R. Hany, I. Verhoolen and M. Walbiner, *J. Chem. Soc.-Perkin Trans. 2*, 1990, 787-798.
11. C. Barner-Kowollik, P. Vana and T. P. Davis, *J. Polym. Sci. Pol. Chem.*, 2002, **40**, 675-681.
12. Z. Szablan, T. M. Lovestead, T. P. Davis, M. H. Stenzel and C. Barner-Kowollik, *Macromolecules*, 2007, **40**, 26-39.
13. Z. Szablan, T. Junkers, S. P. S. Koo, T. M. Lovestead, T. P. Davis, M. H. Stenzel and C. Barner-Kowollik, *Macromolecules*, 2007, **40**, 6820-6833.
14. G. B. Smith, G. T. Russell and J. P. A. Heuts, *Macromol. Theory Simul.*, 2003, **12**, 299-314.
15. G. Johnston-Hall and M. J. Monteiro, *J. Polym. Sci. Pol. Chem.*, 2008, **46**, 3155-3173.
16. C. Barner-Kowollik and G. T. Russell, *Prog. Polym. Sci.*, 2009, **34**, 1211-1259.
17. J. B. L. de Kock, B. Klumperman, A. M. van herk and A. L. German, *Macromolecules*, 1997, **30**, 6743-6753.
18. M. Buback, M. Busch and R. A. Lammel, *Macromol. Theory Simul.*, 1996, **5**, 845-861.
19. L. H. Tung and J. R. Runyon, *J. Appl. Polym. Sci.*, 1969, **13**, 2397-&.
20. J. Billiani, G. Rois and K. Lederer, *Chromatographia*, 1988, **26**, 372-376.
21. D. W. Shortt, *J Liq Chromatogr*, 1993, **16**, 3371-3391.
22. A. N. Nikitin, R. A. Hutchinson, M. Buback and P. Hesse, *Macromolecules*, 2007, **40**, 8631-8641.
23. U. Muller and C. Vallejos, *Angewandte Makromolekulare Chemie*, 1993, **206**, 171-191.

24. S. Maeder and R. G. Gilbert, *Macromolecules*, 1998, **31**, 4410-4418.
25. J. Brandrup, *Polymer Handbook (4th Edition)*, John Wiley & Sons, 2005.

Appendix D: Supporting Information for Chapter 5

D.1 Experimental details for the application of the proposed method

This section describes the details of the bulk *n*-butyl acrylate (*n*BuA) PLP experiments at 413 K. Typical SEC traces with the corresponding derivative at the outer pulse laser frequencies of the considered range are shown in Figure S1. These SEC traces are used to determine the apparent propagation rate coefficient ($k_{p,app}$; Equation (1) in Chapter 5; i=1) by locating the (first) inflection point of the log-MMD plot.

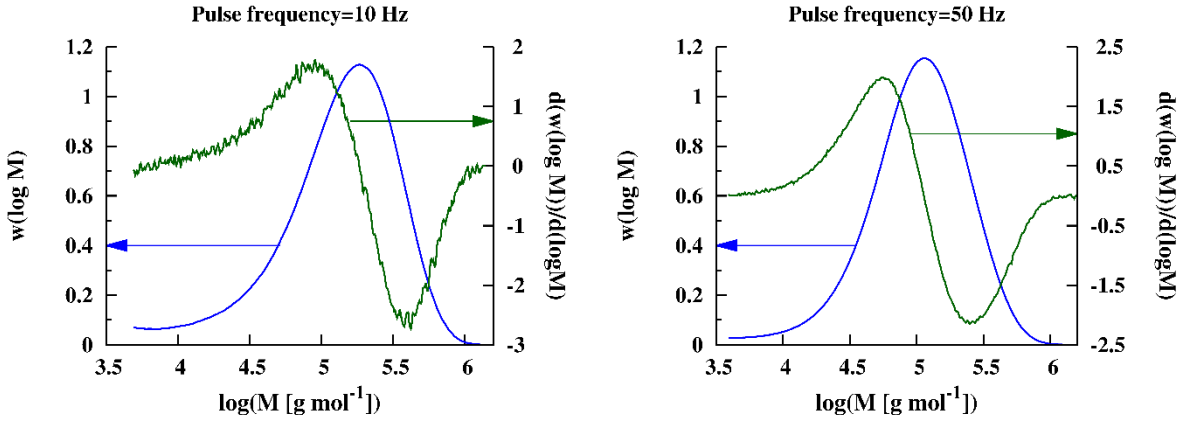

Figure S1. Experimental PLP-SEC trace (full blue line) and corresponding first derivative (full green line) for PLP of *n*BuA at 413 K under bulk conditions and a frequency of 10 Hz (left) and 50 Hz (right); initial conditions: $[\mathrm{DMPA}]_0 = 2.5 \times 10^{-3}$ mol L^{-1} and $\mathrm{E}_{\mathrm{pulse}} = 1.5 \times 10^{-3}$ J. Number of pulses: 20 at frequency of 10 Hz and 60 at frequency of 50 Hz.

D.2 Correction for SEC broadening

The log-MMD as obtained via size exclusion chromatography shows broadening.[1] In this work, SEC broadening is accounted for based on the method proposed by Buback *et al.*[2] For a more detailed description and derivation the reader is referred to previous work.[3,4] The log-MMD after SEC broadening is calculated as:

$$w_{SEC}(\log\ \mathrm{M}) = \frac{1}{(2\pi)^{0.5}(\sigma_v b)} \int_0^{+\infty} \exp\left(-\frac{\left(\log(M) - \log(\tilde{M})\right)^2}{2(\sigma_v b)^2} \right) w(\log \tilde{M})\ d\log(\tilde{M}) \qquad \text{(S1)}$$

In this work $\sigma_v b$ is taken equal to 0.04, in agreement with literature data.[1,5]

D.3 Kinetic modeling details

The reaction scheme and the corresponding literature-based Arrhenius parameters for PLP of *n*BuA at high temperature are shown in Table 1 in Chapter 5. Thermal self-initiation and macropropagation reactions are neglected based on Figure 1 in Chapter 5 and the discussion in this section.

D.3.1 Photodissociation kinetics

The concentration of initiator radicals generated at each laser pulse ($\Delta[R]_0$) is calculated via:[6,7]

$$\Delta[R]_0 = 2\Phi_{\text{diss}} \frac{E_{\text{pulse}}\lambda}{h\,c\,N_{\text{A}}\,\Omega\,l}\left[1-\exp\left(-2.303\,\varepsilon\,[\text{DMPA}]\,l\right)\right] \tag{S2}$$

in which Φ_{diss} is the photodissociation quantum yield (0.42[6]), E_{pulse} the laser pulse energy ($1.5\times10^{-3}\,\text{J}$), λ the laser wavelength ($351\times10^{-9}\,\text{m}$), h the Planck constant ($6.63\times10^{23}\,\text{J s}$), c the speed of light ($3\times10^{9}\,\text{m s}^{-1}$), N_{A} the Avogadro constant ($6.02\times10^{23}\,\text{mol}^{-1}$), Ω the optical cross-sectional area ($3.85\times10^{-5}\,\text{m}^2$), l the optical path length ($1.04\times10^{-2}\,\text{m}$), ε the molar absorptivity of the photoinitiator ($28\,\text{m}^2\,\text{mol}^{-1}$), and [DMPA] the concentration of the photoinitiator.

D.3.2 Negligible impact of macromonomer propagation under PLP conditions

The macromonomers formed via β-scission can propagate with end-chain and mid-chain radicals, adding additional complexity to the kinetics of *n*-butyl acrylate free radical polymerization. To investigate the effect of macromonomer propagation on the PLP kinetics, simulations were carried out considering the macromonomer propagation reaction and its rate coefficient was varied from minimum to maximum values as reported in the literature.[8] For simplicity and to even enlarge a possible effect, the macropropagation rate coefficient for MCRs

is taken equal to the one for ECRs. The effect is although negligible as shown in Figure S2-Figure S4.

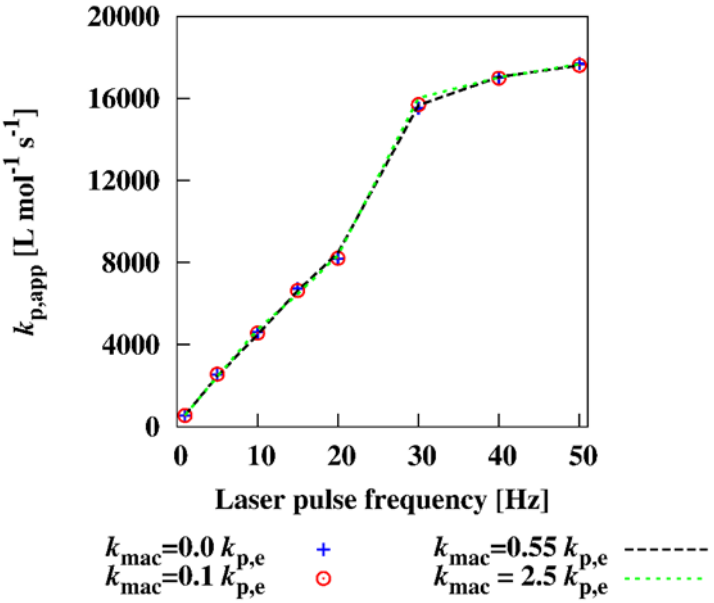

Figure S2. Effect of the macromonomer propagation reactivity on the apparent propagation rate coefficient ($k_{p,app}$; Equation (1) in Chapter 5; i=1) in bulk PLP of *n*-butyl acrylate. Simulations were carried out by changing the macromonomer propagation rate coefficient (k_{mac}). Other parameters as in Table 1 in Chapter 5; T = 413 K. For simplicity and to enlarge a possible effect, the macropropagation rate coefficient for MCRs is taken equal to the one for ECRs.

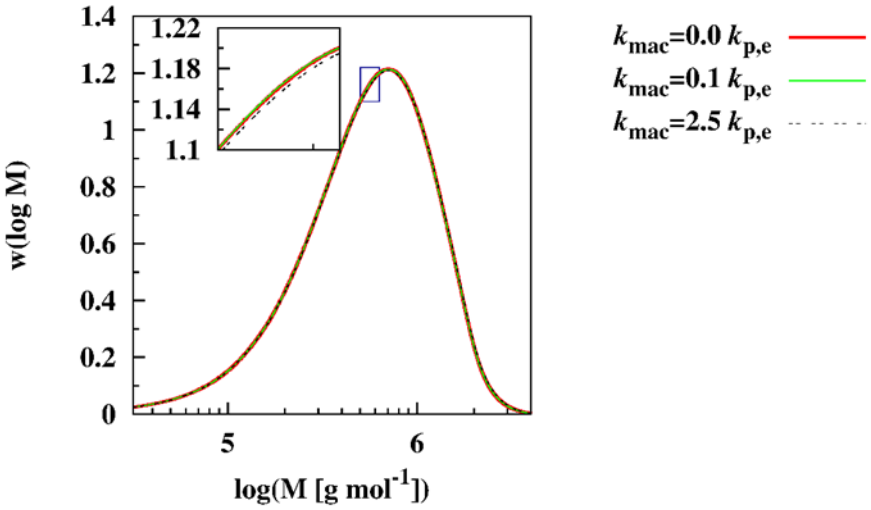

Figure S3. Corresponding log-MMD for Figure S2 at a frequency =10 Hz (also Figure 1 (right) in Chapter 5).

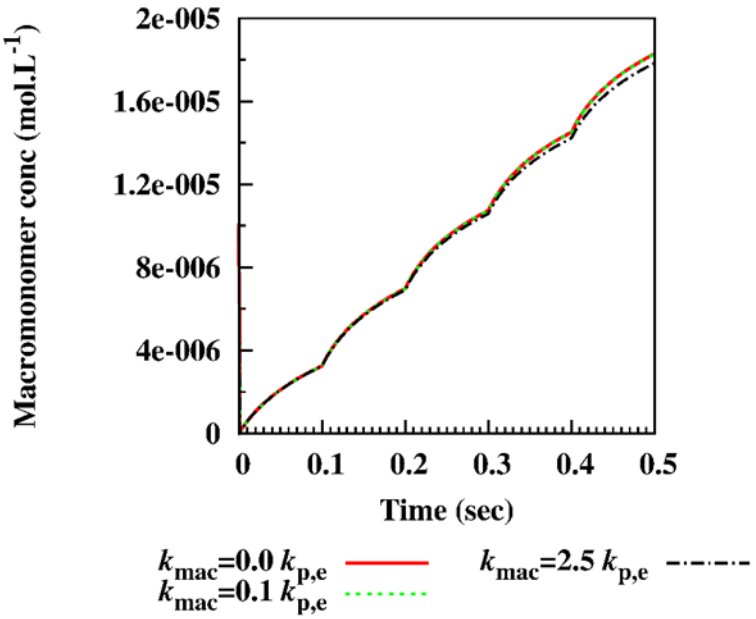

Figure S4. Corresponding macromonomer concentrations for Figure S3.

D.3.3 Chain length dependencies

Chain length dependent propagation kinetics are accounted based on (details in reference 6; based on the work of Heuts and Russell [9]).

$$k_p(i) = k_p\left[1 + C_1\exp(-\frac{\ln(2)}{i_{1/2}}i)\right] \qquad \text{(S3)}$$

Here i refers to the chain length (0 for an initiator-derived radical), in contrast to the equation as originally reported in which i = 1 for an initiator-derived radical.

Chain length dependent termination kinetics are evaluated via the composite k_t model. For the low monomer conversion ranges as encountered during PLP, it suffices to consider:

$$k_t^{app}(i,i) = k_t^{app}(1,1)i^{-\alpha_S} \qquad i \le i_c \qquad \text{(S4)}$$

$$k_t^{app}(i,i) = k_t^{app}(1,1)i_c^{-\alpha_S+\alpha_L}i^{-\alpha_L} \qquad i > i_c \qquad \text{(S5)}$$

in which α_S and α_L express the chain length dependence for short and long radicals, and i_c is the cross-over chain length (details in reference 5).

D.4 Extra information related to the sensitivity of $k_{p,app}$ to k_β (related to Figure 2 and 3 in Chapter 5)

In this section the sensitivity of $k_{p,app}$ to k_β at varying reaction conditions is investigated.

D.4.1 Effect of the temperature on the sensitivity of $k_{p,app}$ to k_β

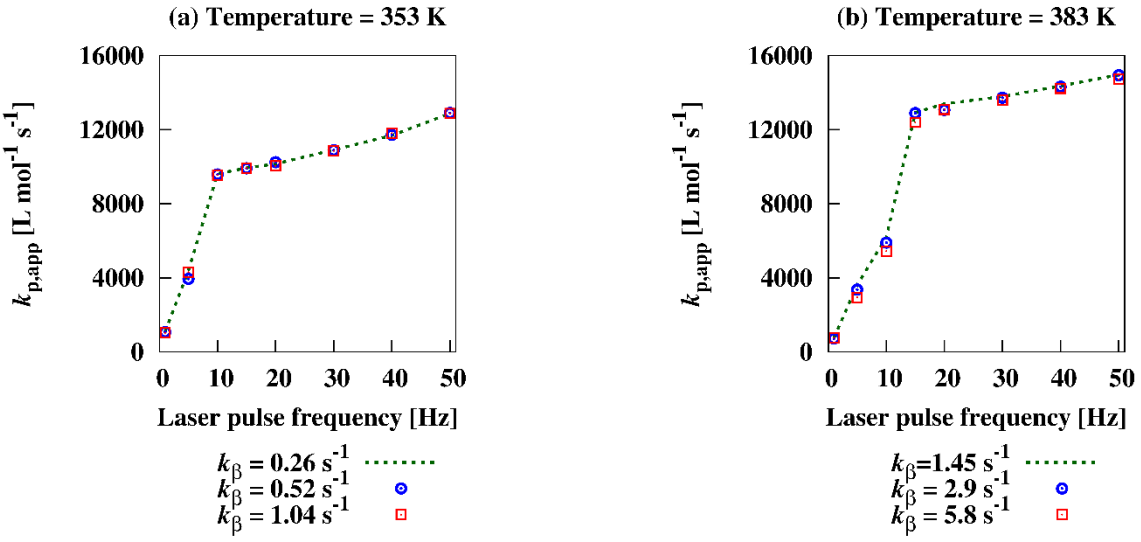

Figure S5. Effect of the temperature on the sensitivity of $k_{p,app}$ to k_β in PLP of *n*-butyl acrylate; (a) 353 K and (b) 383 K. Reference k_β = 0.52 s^{-1} at 353 K and reference k_β = 2.9 s^{-1} at 383 K. Simulation conditions: ϕ_s=0; other parameters: Table 1 in Chapter 5.

D.4.2 Effect of the solvent volume fraction on the sensitivity of $k_{p,app}$ to k_β

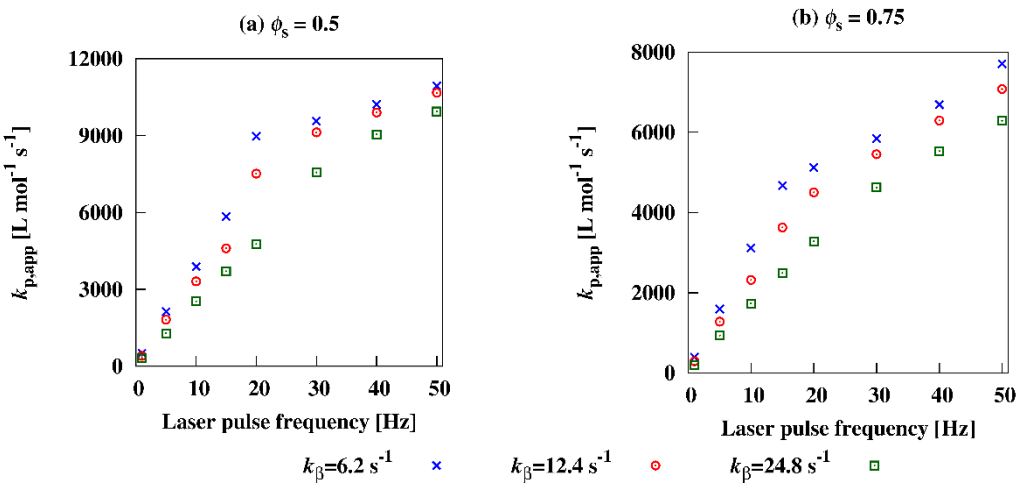

Figure S6. Sensitivity of $k_{p,app}$ to k_β in PLP of *n*-butyl acrylate at varying solvent volume fractions as observed via *k*MC simulations. (a) ϕ_s=0.5 and (b) ϕ_s=0.75. Simulation conditions: 413 K, k_β= 12.41 s^{-1}; other parameters: Table 1 in Chapter 5.

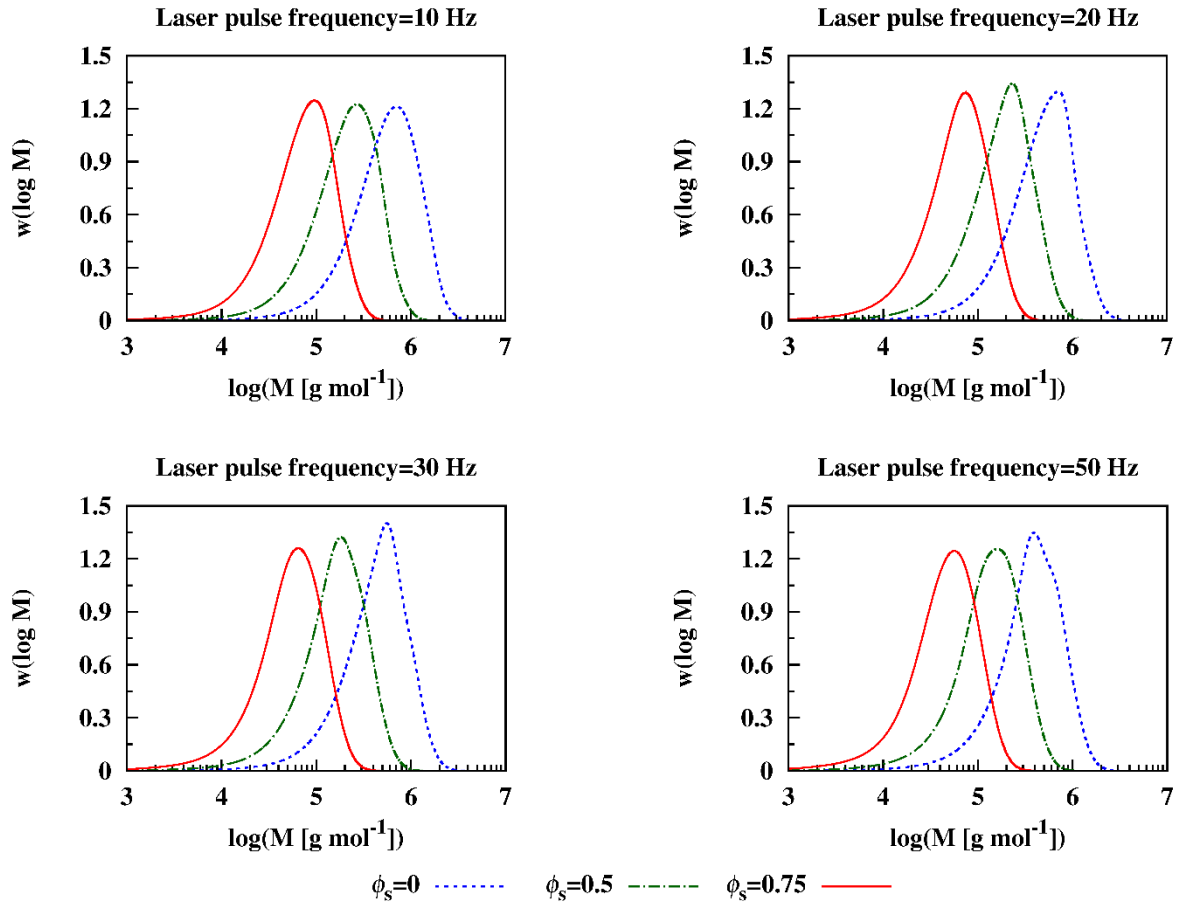

Figure S7. Effect of the solvent volume fraction on the simulated log-MMD in PLP of *n*-butyl acrylate at selected laser pulse frequencies. Simulation conditions: 413 K, k_β= 12.4 s^{-1}; other parameters: Table 1 in Chapter 5.

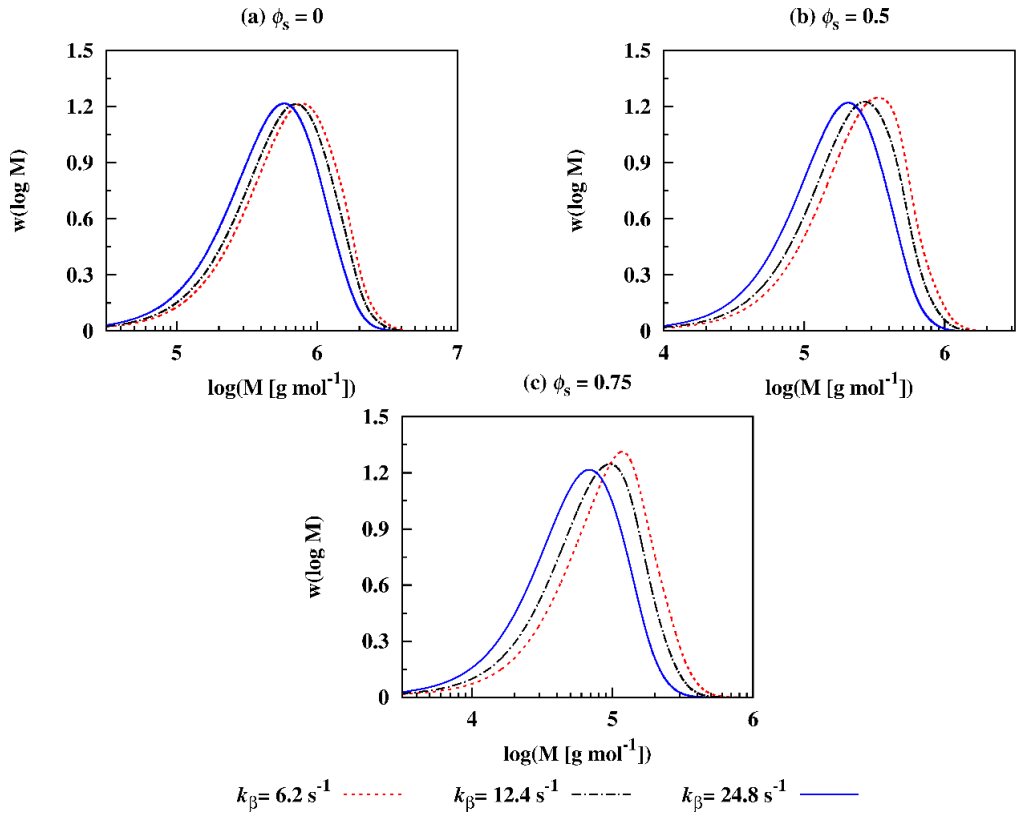

Figure S8. Effect of k_β on the simulated log-MMD at varying solvent volume fractions. (a) ϕ_s=0, (b) ϕ_s=0.5 and (c) ϕ_s=0.75. Simulation conditions: Temperature=413 K; frequency=10 Hz*;* other parameters: Table 1 in Chapter 5.

D.5 References

1 A. N. Nikitin, R. A. Hutchinson, M. Buback and P. Hesse, *Macromolecules*, 2007, **40**, 8631–8641.

2 M. Buback, M. Busch and R. a Liimmel, *Macrolol. theory simul*, 1996, **861**, 845–861.

3 Y. W. Marien, P. H. M. Van Steenberge, K. B. Kockler, C. Barner-Kowollik, M.-F. Reyniers, D. R. D'hooge and G. B. Marin, *Polym. Chem.*, 2016, **7**, 6521–6528.

4 Y. W. Marien, P. H. M. Van Steenberge, C. Barner-Kowollik, M. F. Reyniers, G. B. Marin and D. R. D'hooge, *Macromolecules*, 2017, **50**, 1371–1385.

5 P. Drawe and M. Buback, *Macromol. Theory Simulations*, 2016, **25**, 74–84.

6 Y. W. Marien, P. H. M. Van Steenberge, K. B. Kockler, C. Barner-Kowollik, M.-F. Reyniers, G. B. Marin and D. R. D'hooge, *Polym. Chem.*, 2017, **8**, 3124–3128.

7 G. Odian, *Principles of Polymerization*, John Wiley and Sons, Inc., 4th edn., 2004.

8 W. Wang, A. N. Nikitin and R. A. Hutchinson, *Macromol. Rapid Commun.*, 2009, **30**, 2022–2027.

9 J. P. A. Heuts and G. T. Russell, *Eur. Polym. J.*, 2006, **42**, 3–20.

Appendix E: Supporting Information for Chapter 6

E.1 Modeling methodology of the *k*MC simulation tool for the interactive calculation of the CLD and PSD in batch isothermal miniemulsion FRP

A flow chart illustrating the modeling methodology for batch isothermal miniemulsion FRP is shown in Figure S1. The code requires as input (**step 0**) a list with all reactions and mass transfer events and the corresponding kinetic and diffusion parameters (here Table 1 of the main text). In addition, the initial concentration of the initiator and the monomer in the organic and aqueous phase need to be specified. Moreover, the initial droplet size distribution (i), which is here the initial particle size distribution, as well as the initial number of droplets/particles in the simulation volume (ii), and the volume fraction of the organic phase (iii) need to be given as input. Finally, the time up to which one wants to simulate the miniemulsion kinetics needs to be mentioned.

Next, in **step 1**, from (i) and (ii) the initial volume of each particle is calculated. From the former and (iii) the initial volume occupied by the organic and aqueous phase in the simulation volume is calculated. From these volumes and the given values for the initial concentration of I_2 and M in the organic and aqueous phase, the initial number of I_2 and M molecules in both phases are calculated.

This allows to calculate – analogously to bulk simulations[1] - the individual and overall microscopic Monte Carlo rates (*i.e.* rates in s^{-1}) with increasing time for all reactions and mass transfer events (**step 2)**. From a random number r_1 and the total microscopic rate the time τ in between two events is calculated in agreement with the pioneering method of Gillespie.[2] In a next step, the microscopic rates are converted into probabilities, which – upon selection of a second random number r_2 - allows to determine which reaction or mass transfer event takes place (**step 3**), again in agreement with the method of Gillespie.[2] It should be noted that for the

calculation of the total microscopic rate and for determining which reaction or mass transfer event takes place, mass transfer of I_2 and M are not taken into account. Due to the typically very large number of I_2 and M molecules in each reaction locus, sampling of individual mass transfer events of I_2 and M would lead to a too large computational cost. Hence, it is more recommendable to only update I_2 and M at certain time instances (see step 6).

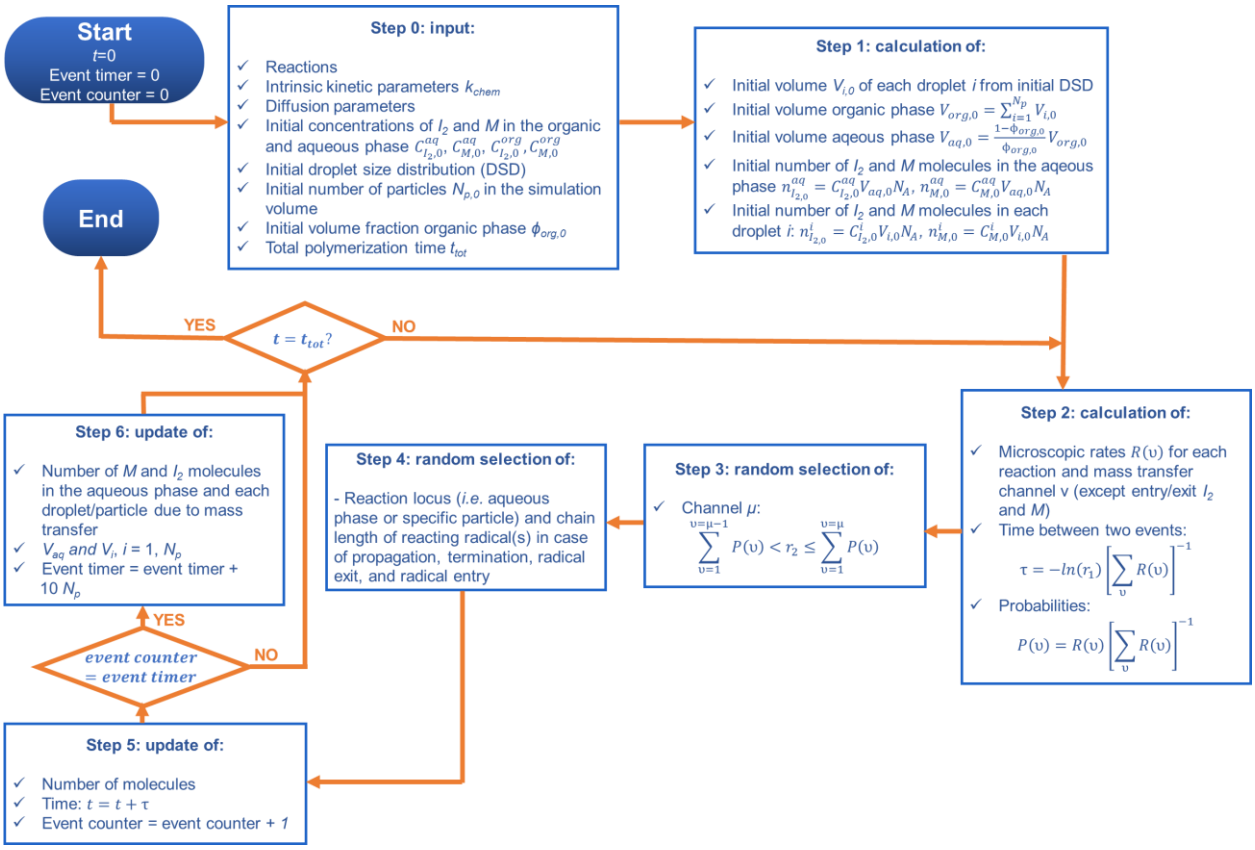

Figure S1. Flow chart illustrating the *k*MC simulation strategy and extensions compared to *k*MC modeling of bulk/solution polymerization to allow for an explicit calculation of the chain length and particle size distribution in minemulsion radical polymerization.

If a particle is involved then the locus of the selected event (*i.e.* the specific particle) is determined based on the individual probabilities of the selected event in each locus and a third random number (**step 4**). In case the selected event involves one or two macroradicals (*i.e.* in case of propagation, termination, entry or exit of a macroradical), the chain length of the reacting radical(s) is determined based on a fourth random number, and in case of diffusion limitations, also based on the chain length dependent microscopic rates. The selection of the

specific particle and/or chain length(s) of the reacting radical(s) follows selection procedures as developed in previous work on bulk/solution polymerization.[1] The number of the reacting species in the locus of the event is updated in a next step (**step 5**).

Then it is evaluated whether the number of events that has taken place since the last time that the number of I_2 and M molecules have been updated is equal to x (*e.g.*10) times the number of droplets/particles in the simulation volume, *i.e.* if on average approximately x (*e.g.* 10) events have taken place per particle. If this is the case, the number of I_2 and M molecules at the current time t_i (t_{i-1} is the time I_2 and M were previously updated) is updated at follows (**step 6**):

$$n_{I_2}(i,t_i) = n_{I_2}(i,t_{i-1}) + \left[R_{entry,I_2}(i,t_{i-1}) - R_{exit,I_2}(i,t_{i-1})\right][t_i - t_{i-1}],\ i = 1,..N_p \quad \text{(S1)}$$

$$n_M(i,t_i) = n_M(i,t_{i-1}) + \left[R_{entry,M}(i,t_{i-1}) - R_{exit,M}(i,t_{i-1})\right][t_i - t_{i-1}],\ i = 1,..N_p \quad \text{(S2)}$$

$$n_{I_{2,aq}}(t_i) = n_{I_2}(1,t_{i-1}) + \left[\sum_{i=1}^{N_p} R_{exit,I_2}(i,t_{i-1}) - \sum_{i=1}^{N_p} R_{entry,I_2}(i,t_{i-1})\right][t_i - t_{i-1}] \quad \text{(S3)}$$

$$n_{M,aq}(t_i) = n_M(1,t_{i-1}) + \left[\sum_{i=1}^{N_p} R_{exit,M}(i,t_{i-1}) - \sum_{i=1}^{N_p} R_{entry,M}(i,t_{i-1})\right][t_i - t_{i-1}] \quad \text{(S4)}$$

with $n_{I_2}(i,t_i)$ and $n_M(i,t_i)$ the number of I_2 and M molecules in particle i (N_p particles in total) at time t_i, $n_{I_{2,aq}}(t_i)$ and $n_{M,aq}(t_i)$ the number of I_2 and M molecules in the aqueous phase at time t_i and $R_{entry,I_2/M}(i,t_{i-1})$ and $R_{exit,I_2/M}(i,t_{i-1})$ the microscopic entry/exit rate (*i.e.* in s^{-1}) of I_2/M from/to particle i at time t_{i-1}.

Next it is evaluated if the actual time is equal to the desired total simulation time t_{tot}. If not, the algorithm returns to step 2 and, if, yes, the simulation is stopped and the complete output can be generated.

E.2 Additional *k*MC modeling details

E.2.1 Calculation of apparent chain length and monomer conversion dependent termination rate coefficients (macroscopic rate coefficiens)

The composite k_t model[3] as accessible via reversible addition fragmentation chain transfer – chain length dependent – termination (RAFT-CLD-T) experiments was used to describe the apparent chain length and monomer conversion dependent termination rate coefficients. The apparent termination rate coefficient for termination between two radicals of chain length *i*, $k_{t,app}(i,i)$, is calculated via:

$i < i_{gel}$

$$k_{t,app}(i,i) = k_t(1,1)i^{-\alpha_S} \qquad i < i_{SL} \qquad \text{(S5)}$$

$$k_{t,app}(i,i) = k_t(1,1){i_{SL}}^{\alpha_L-\alpha_S}i^{-\alpha_L} \qquad i \geq i_{SL} \qquad \text{(S6)}$$

$i \geq i_{gel}$

$$k_{t,app}(i,i) = k_t(1,1){i_{gel}}^{\alpha_{gel}-\alpha_S}i^{-\alpha_{gel}} \qquad i < i_{SL} \qquad \text{(S7)}$$

$$k_{t,app}(i,i) = k_t(1,1){i_{SL}}^{\alpha_L-\alpha_S}{i_{gel}}^{\alpha_{gel}-\alpha_L}i^{-\alpha_{gel}} \qquad i \geq i_{SL} \qquad \text{(S8)}$$

Typical values[3] are used for the model parameters (m_p: mass fraction of the polymer):

$\alpha_S = 0.5$

$\alpha_L = 0.15$

$\alpha_{gel} = m_p - 0.1$

$i_{SL} = 30$

$i_{gel} = 3{m_p}^{-2}$

The apparent termination rate coefficient for termination between a radical of chain length *i* and chain length *j*, $k_{t,app}(i,j)$, is approximated via:[4]

$$k_{t,app}(i,j) = \left(k_{t,app}(i,i)\, k_{t,app}(j,j)\right)^{0.5} \qquad \text{(S9)}$$

It should be noted that in the *k*MC model each termination possibility is considered individually, i.e. no lumping of all termination possibilities is performed and an average $<k_{t,app}>$ is thus not used. Indeed, $k_{t,app}(i,j)$ is calculated for each individual termination possibility based on the chain length of the two radicals and the volume and the polymer mass fraction of the reaction locus (*i.e.* the aqueous phase or a specific particle) in which the two radicals of the termination possibility are present.

E.2.2 Calculation of chain length dependent diffusion coefficients for entry and exit of macroradicals

The diffusion coefficient of macroradicals having a chain length i, $D_R(i)$, is assessed via:[5]

$$D_R(i) = \frac{D_M}{i^{0.664+2.2m_p}} \tag{S10}$$

with D_M the diffusion coefficient of the monomer and m_p the mass fraction of polymer. For the calculation of the diffusion coefficient in the aqueous phase, m_p is taken equal to zero.

E.3 Time scales of reactions and mass transfer events

Table S1. Formulas for the time scales τ in the beginning of a miniemulsion polymerization process ($[M] \approx [M]_0$) reported in Table 1 of the main text; only in case 7 there is chain length dependent termination so that the formula should be calculated with the average apparent termination rate coefficient.

Event	Equation	Formula τ
Reactions in particles		
Dissociation	$I_{2,p} \xrightarrow{k_{d,p}} 2\ I_p$	$\frac{1}{k_{d,p}}$
Chain initiation	$I_p + M_p \xrightarrow{k_{i,p}} R_{1,p}$	$\frac{1}{k_{i,p}[M]_0}$
	$M_p^* + M_p \xrightarrow{k_{i,p}} R_{1,p}$	$\frac{1}{k_{i,p}[M]_0}$
Propagation	$R_{i,p} + M_p \xrightarrow{k_{p,p}} R_{i+1,p}$	$\frac{1}{k_{p,p}[M]_0}$
Chain transfer to monomer	$R_{i,p} + M_p \xrightarrow{k_{trM,p}} M_p^*$	$\frac{1}{k_{trM,p}[M]_0}$
Termination [a]	$R_{i,p} + R_{j,p} \xrightarrow{k_{t,app,p}} P_{i+j,p}$	$\frac{\pi d_p^3 N_A}{6\ k_{t,app,p}(1,1)}$
Reactions in water		
Dissociation	$I_{2,p} \xrightarrow{k_{d,w}} 2\ I_p$	$\frac{1}{k_{d,w}}$
Chain initiation	$I_w + M_w \xrightarrow{k_{i,w}} R_{1,w}$	$\frac{1}{k_{i,w}[M]_0}$
	$M_w^* + M_w \xrightarrow{k_{i,w}} R_{1,w}$	$\frac{1}{k_{i,w}[M]_0}$
Propagation	$R_{i,w} + M_w \xrightarrow{k_{p,w}} R_{i+1,w}$	$\frac{1}{k_{p,w}[M]_0}$
Chain transfer to monomer	$R_{i,w} + M_w \xrightarrow{k_{trM,w}} M_w^*$	$\frac{1}{k_{trM,w}[M]_0}$
Termination [a]	$R_{i,w} + R_{j,w} \xrightarrow{k_{t,app,w}} P_{i+j,w}$	$\frac{V_w N_A}{k_{t,app,w}(1,1)}$
Transfer of radicals		
Entry of I [c]	$I_w \xrightarrow{k_{entry,I}} I_p$	$\frac{V_w}{C_{entry,I} D_{I,w} d_p}$
Entry of M^* [c]	$M_w^* \xrightarrow{k_{entry,M^*}} M_p^*$	$\frac{V_w}{C_{entry,M^*} D_{M^*,w} d_p}$
Entry of R_i [c]	$R_{i,w} \xrightarrow{k_{entry,R}} R_{i,p}$	$\frac{V_w}{C_{entry,R} D_{R,w} d_p}$
Exit of I [e]	$I_p \xrightarrow{k_{exit,I}} I_w$	$\frac{d_p^2}{C_{exit,I} D_{I,p}}$
Exit of M^* [e]	$M_p^* \xrightarrow{k_{exit,M^*}} M_w^*$	$\frac{d_p^2}{C_{exit,M^*} D_{M^*,p}}$
Exit of R_i [e]	$R_{i,p} \xrightarrow{k_{exit,R}} R_{i,w}$	$\frac{d_p^2}{C_{exit,R} D_{R,p}}$

E.4 Conventional Smith-Ewart equations to benchmark the novel kMC modeling tool upon its simplification with a single particle size and a constant particle monomer concentration; intrinsic case

The novel *k*MC modeling tool is benchmarked to a conventional (deterministic) Smith-Ewart model for intrinsic miniemulsion FRP kinetics with a water-soluble initiator and a simplified reaction scheme. The model assumes a Maxwell-Morrison entry mechanism, *i.e.* entry is irreversible (no exit takes place) and entry only takes place once a radical reaches a certain chain length (here 4). In addition, chain transfer to monomer and diffusional limitations are not taken into account. More importantly, an average particle size and monomer concentration in the particles are considered. Termination by recombination is considered. The differential equations for this conventional Smith-Ewart model are discussed below.

E.4.1 $\bar{n}$ and monomer conversion vs. time evolution

For the considered model, the temporal evolution of the number of particles containing *k* radicals, N_k, is expressed by:

$$\frac{dN_k}{dt} = k_{entry,R_4}[R_4]_w N_{k-1} - k_{entry,R_4}[R_4]_w N_k + \frac{k_t(1,1)}{V_p N_A}\frac{(k+2)(k+1)}{2}N_{k+2} - \frac{k_t(1,1)}{V_p N_A}\frac{k(k-1)}{2}N_k \quad \text{(S11)}$$

The temporal evolution of the aqueous phase concentrations in expressed by (note: initiator efficient f = 1 here; N_p is the total number of particles, which is assumed constant; V_w is the volume of the aqueous phase):

$$\frac{d[I_2]_w}{dt} = -k_{d,w}[I_2]_w \quad \text{(S12)}$$

$$\frac{d[I]_w}{dt} = 2k_{d,w}[I_2]_w - k_{i,w}[I]_w[M]_w \quad \text{(S13)}$$

$$\frac{d[M]_w}{dt} = -\left(k_{i,w}[I]_w + k_{p,w}\sum_{i=1}^{3}[R_i]_w\right)[M]_w \tag{S14}$$

$$\frac{d[R_1]_w}{dt} = k_{i,w}[I]_w[M]_w - k_{p,w}[R_1]_w[M]_w \tag{S15}$$

$$\frac{d[R_2]_w}{dt} = k_{p,w}[R_1]_w[M]_w - k_{p,w}[R_2]_w[M]_w \tag{S16}$$

$$\frac{d[R_3]_w}{dt} = k_{p,w}[R_2]_w[M]_w - k_{p,w}[R_3]_w[M]_w \tag{S17}$$

$$\frac{d[R_4]_w}{dt} = k_{p,w}[R_3]_w[M]_w - k_{entry,R_4}[R_4]_w\frac{N_p}{V_w N_A} \tag{S18}$$

After numerical integration of Equation (S11)-(S18) the average number of radicals per particle, $\bar{n}$, can be calculated via:

$$\bar{n} = \frac{\sum_{k\geq 1} kN_k}{N_p} \tag{S19}$$

The temporal evolution of the average monomer concentration in the particles follows from:

$$\frac{d[M]_p}{dt} = -k_{p,p}[M]_p\frac{\bar{n}}{V_p N_A} \tag{S20}$$

From Equation (S14) and (S20) the evolution of the monomer conversion can be determined via:

$$\frac{dX_M}{dt} = -\frac{1}{[M]_{p,0}V_{org} + [M]_{w,0}V_w}\left(V_{org}\frac{d[M]_p}{dt} + V_w\frac{d[M]_w}{dt}\right) \tag{S21}$$

E.4.*2 Moment equations for the calculation of the x_n and x_m versus time evolutions*

For the calculation of the x_n and x_m versus time evolutions, the temporal evolution of the first and second order moment of the chain length distribution (CLD) of the macroradicals ($\lambda_{i,p}$; i = 1, 2) and 'dead' polymer molecules ($\mu_{i,p}$; i = 1, 2) in the particles needs to be determined. Since

no chain length and monomer conversion dependency of the termination rate coefficient is taken into account for the benchmark, $k_t(1,1)$ is large (10^9 L mol^{-1} s^{-1}) and small particles (d_p= 50 nm) are considered, termination in the particles can be assumed to be instantaneous. Hence, it can be assumed particles contain either contain zero or one radical. The zeroth moment of the macroradical CLD in the particles is equal to:

$$\lambda_{0,p} = N_p \bar{n} \tag{S22}$$

The temporal evolution of the first moment of the macroradical CLD in the particles, $\lambda_{1,p}$, is expressed by:

$$\frac{d\lambda_{1,p}}{dt} = k_{p,p}[M]_p \lambda_{0,p} + k_{entry,R_4}[R_4]_w N_0 4 - k_{entry,R_4}[R_4]_w N_1 \frac{\lambda_{1,p}}{\lambda_{0,p}} \tag{S23}$$

The last term of Equation (S23) expresses that upon entry of a radical to a particle containing one radical, which on average has a chain length of $\frac{\lambda_{1,p}}{\lambda_{0,p}}$, termination takes place instantaneously. Note that $N_1 = N_p \bar{n}$ and $N_0 = N_p(1 - \bar{n})$.

Analogously, the temporal evolution of the second order moment of the macroradical CLD follows from:

$$\frac{d\lambda_{2,p}}{dt} = k_{p,p}[M]_p \lambda_{0,p} + 2k_{p,p}[M]_p \lambda_1 + k_{entry,R_4}[R_4]_w N_0 16 - k_{entry,R_4}[R_4]_w N_1 \frac{\lambda_{2,p}}{\lambda_{0,p}} \tag{S24}$$

As termination takes places instantaneously upon entry of a radical to a particle already containing a radical, the temporal evolution of the zeroth order moment of the 'dead' polymer CLD in the particles is expressed by:

$$\frac{d\mu_{0,p}}{dt} = k_{entry,R_4}[R_4]_w N_1 \tag{S25}$$

From Equation (S23) and (S24) it follows that the temporal evolution of the first and second order moment of the 'dead' polymer CLD in the particles is given by (neglecting the contribution of the radical with chain length 4 to the total chain length):

$$\frac{d\mu_{1,p}}{dt} = k_{entry,R_4}[R_4]_w N_1 (\frac{\lambda_{1,p}}{\lambda_{0,p}}) \tag{S26}$$

$$\frac{d\mu_{2,p}}{dt} = k_{entry,R_4}[R_4]_w N_1 (\frac{\lambda_{2,p}}{\lambda_{0,p}}) \tag{S27}$$

After integration of Equation (S23)-(S27) the temporal evolution of x_n and x_m is obtained via:

$$x_n = \frac{\mu_{1,p}}{\mu_{0,p}} \tag{S28}$$

$$x_m = \frac{\mu_{2,p}}{\mu_{1,p}} \tag{S29}$$

E.5 Additional simulation results in support of the main text

E.5.1 kMC simulations results for miniemulsion FRP with a water-soluble initiator accounting for monomer fluctuations over the particles, thus a particle dependent monomer concentration

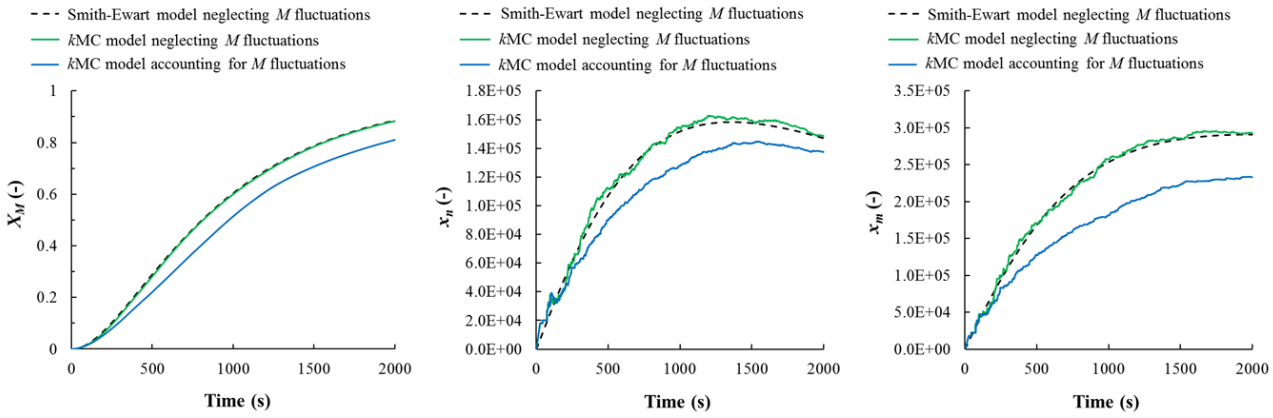

Figure S2. Importance of monomer fluctuations over the particles for the evolution of the monomer conversion X_M, and the "dead" polymer number and mass average chain length x_n and x_m. *k*MC simulations results neglecting monomer fluctuations (full green line; same as in Figure 2 of the main text) and accounting for monomer fluctuations (full blue line); for completeness, the simulation results obtained with the Smith-Ewart model are also included (dashed black line; same as in Figure 2 of the main text); conditions and parameters: see caption Figure 2 (main text). As the blue lines deviate from the other two lines (that coincide) it is clear that monomer fluctuations need to be accounted for.

E.5.2 Number of radicals in individual particles for case 1 and case 2

The evolution of the number of radicals in two individual particles, one with $d_{p,0}$ = 100 nm and one with $d_{p,0}$ = 200 nm, is shown for $0 \leq t \leq 10^3$ s in Figure S3 for case 1 and in Figure S4 for case 2 in Table 2 (conditions caption Figure 3 in the main text).

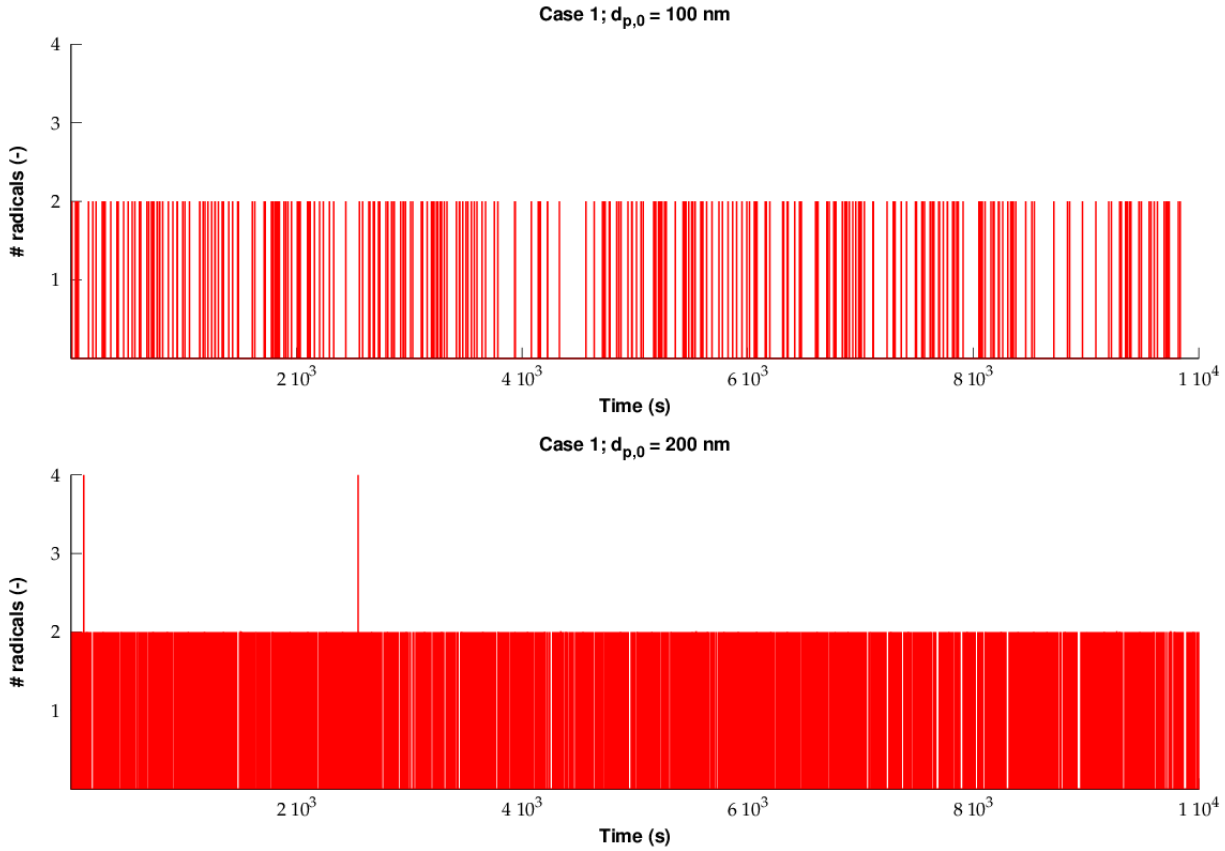

Figure S3. Evolution of the number of radicals in two individual particles, one with $d_{p,0}$ = 100 nm (top) and one with $d_{p,0}$ = 200 nm (bottom) in case 1 (no exit/entry) in Table 2; conditions caption Figure 3.

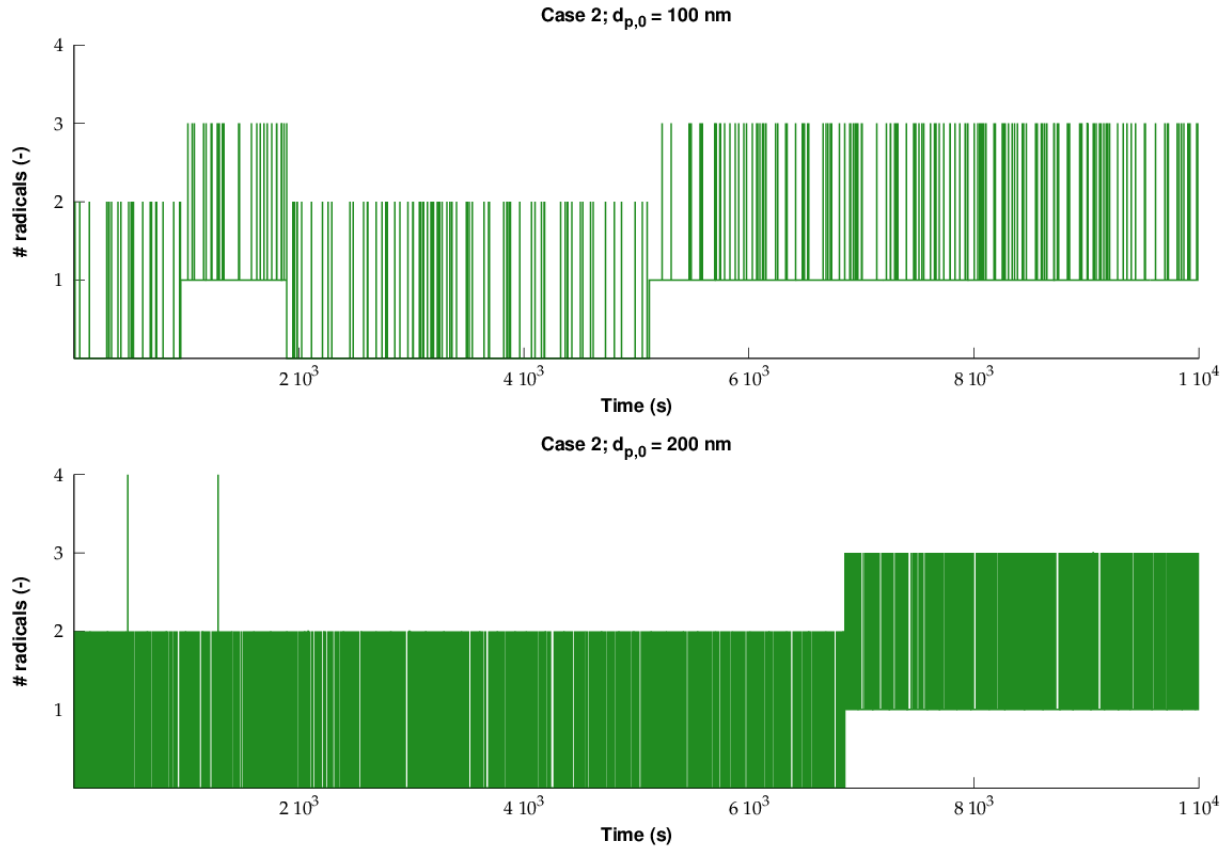

Figure S4. Evolution of the number of radicals in two individual particles, one with $d_{p,0}$ = 100 nm (top) and one with $d_{p,0}$ = 200 nm (bottom) in case 2 (with exit/entry of *I*) in Table 2; conditions: caption Figure 3.

E.6 References

1. P. H. M. Van Steenberge, D. R. D'hooge, M. F. Reyniers and G. B. Marin, *Chem. Eng. Sci.*, 2014, **110**, 185-199.
2. D. T. Gillespie, *J. Phys. Chem.*, 1977, **81**, 2340-2361.
3. G. Johnston-Hall and M. J. Monteiro, *J. Polym. Sci. Pol. Chem.*, 2008, **46**, 3155-3173.
4. P. Derboven, D. R. D'Hooge, M. F. Reyniers, G. B. Marin and C. Barner-Kowollik, *Macromolecules*, 2015, **48**, 492-501.
5. M. C. Griffiths, J. Strauch, M. J. Monteiro and R. G. Gilbert, *Macromolecules*, 1998, **31**, 7835-7844.

Appendix F: Glossary

***β*-scission**: reaction in which a mid-chain radical is converted into an end-chain radical and a macromonomer via the scission of a β C-C bond.

Apparent rate coefficient: rate coefficient related to the observed kinetics, *i.e.* rate coefficient determined by the intrinsic chemical rate coefficient and transport phenomena.

Backbiting: also referred to as intramolecular chain transfer; reaction in which the radical center of an end-chain radical is transferred a few monomer units from the chain end resulting in a mid-chain radical; typically the unit is transferred three units from the chain end via a six membered ring transition state, *i.e.* 1:5-intramolecular chain transfer.

Chain length of a polymer molecule: the number of repeating units (coming from the monomer(s)) in a polymer molecule.

Chain transfer: reaction leading to transfer of the radical center within a species or between two species.

Dead polymer molecule: polymer molecule without end group functionality.

Emulsion polymerization: polymerization in which an organic phase is dispersed in an aqueous medium in the presence of a surfactant or stabilizer; polymerization can take place in the aqueous phase and in polymer nanoparticles (d_p = 10-500 nm); types of emulsion polymerization are macro-, micro- and mini-emulsion polymerization.

End-chain radical: radical for which the radical center is located at the end of the chain, *i.e.* on the last repeating unit.

Dispersity of the molar mass distribution of the polymer: ratio of the mass to number average molar mass; measure for the broadness of the molar mass distribution of the polymer.

Inflection point: point at which a curve crosses its tangent, *i.e.* the curve changes from being concave to convex; can be identified via the location of the extrema of the curve's derivative.

Kinetic Monte Carlo: stochastic modeling technique in which reaction and mass transfer events are sampled using random numbers.

Macro-emulsion: A type of emulsion polymerization in which large monomer droplets (> 1 μm), (monomer swollen) micelles (5-10 nm), and polymer nanoparticles (d_p = 10-500 nm) are initially present.

Micro-emulsion: A type of emulsion polymerization in which only small monomer droplets (< 100 nm) and (monomer swollen) micelles (5-10 nm) are initially present.

Mid-chain radical: radical for which the radical center is located in the middle of the chain.

Miniemulsion: A type of emulsion polymerization in which only small monomer droplets/particles (< 500 nm), as formed under high shear conditions with (co)stabilizer, are initially present.

Monomer conversion: monomer consumed with respect to initial amount.

Multimodal distribution: a distribution with two or more modes that appear as distinct peaks; in case of two peaks, referred to as bimodal.

Nanogel: crosslinked polymer nanoparticle; typically possesses responsiveness (*e.g.* thermoresponsiveness).

Number chain length distribution of the polymer: number fraction of polymer molecules as a function of chain length.

Number molar mass distribution of the polymer: number fraction of polymer molecules as a function of molar mass.

Particle size distribution: fraction of particles based on their number, surface area or volume as a function of particle diameter.

Partition coefficient: ratio of the concentration of a species in two phases which are in contact at equilibrium; in emulsion polymerization: ratio of the concentration in the organic and aqueous phase.

Photodissociation quantum yield: fraction of the photoinitiator molecules that are excited via photon absorption that result in dissociation.

Photoinitiator: initiator which dissociates under the influence of light (typically UV light).

Propagation of a radical: reaction leading to chain growth, *i.e*, addition to monomer.

Pulsed laser polymerization: polymerization in which a mixture of monomer, photoinitiator and possibly solvent is irradiated by laser pulses with a certain frequency; from the size exclusion chromatography trace, rate coefficients can be determined.

Radical entry: interphase transfer phenomena in which a radical is transferred from a particle to the aqueous phase; also referred to as absorption.

Radical exit: interphase transfer phenomena in which a radical is transferred from the aqueous phase to a particle; also referred to as desorption.

Rate coefficient: the coefficient of proportionality for the calculation of a reaction rate.

Reversible addition-fragmentation chain transfer polymerization – chain length dependent – termination (RAFT-CLD-T): technique to determine the monomer and chain length dependence of the apparent termination rate coefficient.

Size exclusion chromatography trace (SEC trace): distribution obtained via size exclusion chromatography, which is an analysis technique that separates polymer molecules based on their chain length; typically, a broadened distribution of the molar mass distribution on logarithmic scale (*i.e.* the log-MMD) is obtained.

Skewness of the molar mass distribution of the polymer: measure for the molar mass distribution of the polymer being symmetric or asymmetric.

Termination of radicals: reaction leading to the formation of (a) dead polymer molecule(s) with the disappearance of two radical reactive centers.

Thermoresponsivness: the ability to react on a temperature change; *e.g.* the reversible swelling/deswelling of a nanogel.